ISBN 978-91-628-7258-8
LUNFD6/(NFFL-7226)2007

Azimuthal Correlations in Dijet Events from Deep Inelastic Positron-Proton Scattering at HERA

Thesis submitted for the degree of
Doctor of Philosophy
by

Magnus Hansson

LUND
UNIVERSITY

DEPARTMENT OF PHYSICS
LUND, 2007

Organization
LUND UNIVERSITY
Department of Physics
Lund University
Box 118
SE-221 00 Lund
SWEDEN

Document name
DOCTORAL DISSERTATION

Date of issue
23 August 2007

CODEN
LUNFD6/(NFFL-7226)2007

Author(s)
Magnus Hansson

Sponsoring organization

Title and subtitle
Azimuthal Correlations in Dijet Events from Deep Inelastic Positron-Proton Scattering at HERA

Abstract

Correlations in the azimuthal angle between dijets produced in deep inelastic e^+p scattering events, collected by the H1 experiment during 1999-2000, have been investigated. Cross sections are presented as a function of the azimuthal separation between the two jets in the hadronic center of mass frame, $\Delta\phi^*$, in different regions of the photon virtuality Q^2 and in different regions of the Bjorken scaling variable x_{Bj}. The results are compared to the predictions of QCD models implementing LO matrix elements, matched parton showers and hadronisation as well as to NLO di-jet (α_s^2) and NLO three-jet (α_s^3) parton level calculations corrected for hadronisation effects. Also, a fit of the unintegrated gluon density is presented, in which a first attempt to constrain the intrinsic transverse momentum distribution is performed.

Key words:
Azimuthal Correlations, Jets, Dijets, Parton Dynamics, Low-x, HERA, H1

Classification system and/or index terms (if any)

Supplementary bibliographical information:

Language
English

ISSN and key title:

ISBN
978-91-628-7258-8

Recipient's notes

Number of pages
164

Price

Security classification

Distribution by (name and address)

Magnus Hansson
Department of Physics
Div. of Experimental High-Energy Physics
Box 118
SE-221 00 Lund, SWEDEN

I, the undersigned, being the copyright owner of the above-mentioned dissertation, hereby grant to all reference sources permission to publish and disseminate the abstract of the above-mentioned dissertation.

Signature Magnus Hansson **Date** 23 August 2007

Contents

Populärvetenskaplig sammanfattning

Det mänskliga ögat kan, i bästa fall, upplösa detaljer ner till några tiondels millimeter, d.v.s. ungefär tjockleken av ett hårstrå. Vill man se ännu finare detaljer får man ta till något hjälpmedel, t.ex. ett förstoringsglas, eller - ännu bättre - ett mikroskop. Lägger man ett hårstrå under ett bra mikroskop kan man upplösa strukturer mindre är en miljondels meter, d.v.s. samma storleksordning som celler. Men vi vet att all materia i världen - luften du andas, marken du står på och inte minst du själv - är uppbyggd av *atomer*. För att "se" atomerna måste vi byta teknik. Hittills har vi använt ögat för att registera det ljus som reflekterats av hårstrået och därefter passerat mikroskopets linser. Utan att vi tänker på det registrerar ögat en mängd egenskaper hos ljuset: hur mycket ljus som reflekteras, vilken färg (d.v.s energi eller våglängd) ljuset har, vilka vinklar ljuset sprids i o.s.v. All denna information bearbetas av hjärnan och ger dig en uppfattning om hur hårstrået ser ut. Men oberoende av hur stora och fina mikroskop man lyckas bygga så når man ändå till slut en gräns för de detaljer man kan observera, vilken bestäms av det synliga ljusets våglängd. Ett föremål som är mindre än våglängden hos det ljus som det belyses med kan inte observeras eftersom föremålet inte är stort nog för att sprida ljuset. Detta kan liknas vid en boll som flyter i vattnet. Om bollen är mindre än avståndet mellan vågorna kommer de inte att påverkas av bollens närvaro. Men om bollen däremot är större än avståndet mellan vågorna kommer de att störas och bilda andra vågmönster på vattnet. För att komma vidare i vår strävan att observera mindre detaljer måste vi alltså ersätta det synliga ljuset med ljus av kortare våglängder som t.ex. röntgenstrålar. Eftersom vi inte kan se röntgenstrålarna måste vi också ersätta ögat med någon typ av detektor t.ex. en sensor liknande de som finns i digitalkameror.

I de flesta tillämpningar beskriver man ljus som en elektromagnetisk vågrörelse, medan t.ex. elektronen betraktas som en partikel. Men i kvantmekaniken finns det ingen tydlig gräns mellan vad som skall anses vara en vågrörelse respektive en partikel, utan det beror helt och hållet på i vilket sammanhang de förekommer. Alltså kan även partiklar beskrivas som vågor och ersätta det vi normalt kallar för ljus, för att belysa föremål som skall studeras. Elektronen är liten och lätt, och är en av de fundamentala partiklar som bygger upp atomen. Genom att skjuta elektroner med hög hastighet (hög energi - kort våglängd) mot hårstrået och sedan detektera i vilka riktningar och med vilka energier elektronerna sprids kan vi upplösa detaljer mindre än en miljarddels meter. Med sådana så kallade elektronmikroskop kan man alltså "se" strukturen hos atomerna i hårstrået. För att kunna se in i atomerna - atomkärnan och dess beståndsdelar *protonen* och *neutronen* - behövs mycket höga energier hos elektronerna, vilket kräver särskilda partikelacceleratorer.

Partikelacceleratorn *HERA* i Hamburg och detektorerna kring denna anläggning kan beskrivas som världens största elektronmikroskop, där HERA-acceleratorn utgör ljuskällan och detektorerna själva mikroskopet. Men till skillnad från vanliga elektronmikroskop där provet (hårstrået) ligger stilla så accelereras provet (protonen) i HERA till mycket höga energier, vilket gör att vi kan ”se” in i protonerna; upplösningen är en miljarddels miljarddels meter, eller 0,000000000000000001 meter. Protonerna består av *kvarkar*, vilka tillsammans med elektronerna tillhör de mest grundläggande beståndsdelar vi känner till. De tre ”huvudkvarkarna” i protonen hålls samman av en kraft som kallas den starka kraften, vilken förmedlas av *gluoner* (från engelskans ”glue”, d.v.s. ”klister”) som hela tiden strålas ut och absorberas av kvarkarna och håller dem samman. Men det är mer komplicerat än så. Gluonerna kan nämligen, på grund av en kvantmekanisk effekt, splittras upp i två gluoner eller ett kvark-antikvark[1] par. Dessa gluoner kan i sin tur splittras upp i nya gluoner och kvark-antikvark par, medan kvarkarna och antikvarkarna kan stråla ut ännu fler gluoner o.s.v. Det finns dock en gräns för hur länge sådana så kallade *virtuella partiklar* kan existera, eftersom de har ”lånat” energi från vakuum, och denna energi måste betalas tillbaka inom en viss tid. Detta kan antingen ske genom en växelverkan med en yttre partikel eller genom att de virtuella partiklarna åter annihilerar, d.v.s. förintas.

För att kunna dra några slutsatser om protonens uppbyggnad måste vi detektera elektronen och mäta dess energi och spridningsvinkel, på samma sätt som ögat registrerar ljusets färg och spridningsvinkel när du tittar på t.ex. ett hårstrå. En sådan detektor har byggts av *H1-kollaborationen*, vilken består av ca. 400 fysiker och ingenjörer från 12 länder. När en elektron kolliderar med en proton vid så höga energier träffas en av kvarkarna så hårt att den försöker frigöra sig från protonen. På grund av den starka kraftens speciella egenskaper tillåts kvarkarna inte att bli fria, och fria kvarkar har heller aldrig observerats. Det som sker när den träffade kvarken flyger iväg i en annan riktning än resten av protonen är att det starka kraftfältet spänns ut och spricker upp på ett sådant sätt att nya konfigurationer av kvarkar och antikvarkar uppstår och bildar hadroner, som kan observeras i detektorn. Hadroner är ett gemensamt namn för alla partiklar som är uppbyggda av kvarkar. Dessa hadroner utgör en partikelskur, eller en jet, med ungefär samma energi och riktning som den ursprungliga kvarken. Genom att studera sådana partikeljettar kan man få värdefull information om kvarkarnas egenskaper. I sådana kollisioner spricker resten av protonen också upp och flera kvarkar och gluoner kan slås ut, vilka bildar jettar i olika riktningar. För att få maximal information om protonens uppbyggnad måste man alltså detektera både den spridda elektronen och alla partiklar som bildas i kollisionen. H1-detektorn är därför uppbyggd för att kunna identifiera och mäta energier och vinklar för många olika sorters partiklar.

I den här avhandligen presenteras en analys där jag har undersökt en speciell typ av kollisioner som ger upphov till minst två jettar. Dessa jettar kommer ofta från en gluon som splittrats upp i ett kvark-antikvark par, och genom att undersöka egenskaper för de två jettarna kan man få information om gluonen som splittrades upp. Dessutom kan man ta reda på om, och i så fall hur, den strålat ut andra gluoner innan den splittrades upp. Detta i sin tur ger information om hur den starka kraften fungerar. Teoretiska beräkningar av fenomen som styrs av den starka kraften görs med *kvantkromodynamiken* (eng. Quantum Chromo Dynamics, QCD) och kan vara väldigt komplicerade, vilket medför att approximationer ofta måste göras. Olika approximationer ger olika förutsägelser för hur sannolikt det är att två jettar ska bildas i kollisioner, och vilka egenskaper (energier, vinklar etc.) de i så fall

---

[1] De flesta partiklar har en motsvarande antipartikel med exakt samma massa men motsatt laddning.

har. Resultaten från analysen har givit fördjupad insikt i det dynamiska förloppet enligt vilket partonerna splittras upp och har påvisat nödvändigheten av en modellbeskrivning av den starka kraftens egenskaper som skiljer sig från den gängse. Ett mycket viktigt resultat är att energispektret hos de partoner som produceras i uppsplittringsprocesserna har kunnat bestämmas för första gången i en sådan mätning. För att kunna ange partonernas energispektrum med ännu högre precision kommer resultat från mätningar av ytterligare observabler att inkluderas i bestämningen framöver.

Introduction

The past century has revealed many secrets concerning the fundamental particles and their interactions. The story of the strong interaction began with the famous scattering experiment of Rutherford in 1911 [1, 2]. Using α-particles from a radioactive source to hit a metal foil, he could show that the atom consists of a positively charged nucleus and negative electrons. Later it was found that the nucleus in turn consists of positively charged protons and neutral neutrons. By studying the scattering of electrons, with energies up to 190 MeV, against a hydrogen gas, Hofstadter *et al.* [3, 4] in 1955 discovered that the protons in fact are not pointlike, but have their charge distributed in a volume of about $0.7 \cdot 10^{-15}$ m in diameter. In the late 1960's, the Stanford Linear Accelerator (SLAC) was able to accelerate electrons to energies as high as 20 GeV, and these were scattered against a liquid H_2 target. At such high energies, far beyond what had been previously possible, the scattered electrons can probe deep into the inner structure of the proton, a process called Deep Inelastic Scattering (DIS). The experiments at SLAC led to the identification of pointlike quarks as the constituents of the proton (the Quark Parton Model, QPM) and later to the formulation of Quantum Chromo Dynamics (QCD) in the 1970's [5–7].

The experiments leading to these revolutionary discoveries were all fixed-target scattering experiments. In 1992, however, the world's first (and so far only) electron - proton collider, HERA[2] at the DESY[3] laboratory in Hamburg, was put into operation. By colliding 27 GeV electrons and 920 GeV protons, HERA provided much higher center-of-mass energies than previously obtained, which significantly improved the measuring resolution and extended the kinematic range coverage by several orders of magnitude. The precision measurements carried out at the HERA collider have given further insight and a deeper knowledge about the properties of the constituents of the proton, the quarks and gluons, and the theory describing the strong interactions, QCD, in which the gluons are the carriers of the strong force.

The picture we have today is that the proton consists of three valence quarks bound together by gluons, which are constantly emitted and absorbed by the valence quarks. Moreover, each of these gluons can "borrow" energy from the vacuum and fluctuate into two gluons or a quark-antiquark pair, called sea quarks. These gluons can in turn split up into new gluons and sea quarks while the quarks and anti-quarks can emit more gluons, and so on. The sea quarks and gluons created in such fluctuations, or splittings, can only exist for a short time, and must eventually pay back the borrowed energy by annihilating. The

---

[2] HERA, Hadron Elektron Ring Anlage, can accelerate both electrons and positrons. Since the analysis presented in this thesis is insensitive to the choice of either e^- or e^+, we will not distinguish between them and the generic name electron will be used for both electrons and positrons.

[3] Deutsches Elektronen-Synchrotron.

proton can thus be thought of as three valence quarks surrounded by a cloud of quarks, anti-quarks and gluons which are constantly created and destroyed. The behaviour (dynamics) of the gluons and quarks (which is the equivalent of asking: "what does the proton look like?") is explained by QCD in the region where the theory is applicable. But, since so far analytic calculations have only been performed to a limited extent due to the complexity of the parton dynamics, approximations must be used. Such approximations describe how a parton splits into two new partons in a sequence of splittings. One of these approximations is named DGLAP [8–11] (after the initials of the originators) and assumes that in each splitting the propagating partons are ordered in virtuality, or four-momentum squared. The DGLAP approximation has worked extremely well so far, and has successfully described various observables measured at HERA. It is, however, expected that DGLAP will fail when targeting certain corners of the phase space, where other non-DGLAP approximations are designed to work.

In this thesis, a study of deep inelastic scattering events is presented. In such collisions, the electron interacts with the constituents of the proton. Because of the large momentum transferred in the collision, the interacting quark will change its flight direction and try to escape the proton. If the scattered quark is a sea quark it has been produced through quantum fluctuations, and depending on the complexity of the fluctuations it might be accompanied by additional partons, created in a so-called initial state (and/or final state) cascade. However, (anti-)quarks and gluons are never observed directly, due to the special properties of the strong force. As the strong field between the escaping partons and the rest of the proton is stretched out, it will break up and new configurations of quarks and anti-quarks will be formed, resulting in a collimated flow of new hadrons, which can be observed in the detector. Such collimated flows of hadrons are called jets, and are believed to reflect the properties of the original (anti-)quarks or gluons. The full scattering process is illustrated by a schematic diagram in Figure 1.14. In this analysis, events with at least two jets are selected. Such events, called dijet events, are already at leading order in the strong coupling constant (α_s) directly sensitive to both the quark and gluon content of the proton, and are thus suitable for testing various aspects of QCD. The aim of the analysis presented here is to investigate regions where predictions based on the DGLAP approximation fail to describe the experimental data. In the DGLAP approximation, the transverse momentum k_T of the interacting gluon is restricted due to ordering in virtuality of the propagating partons in the initial state cascade. However, this approximation is not valid at small values of the longitudinal momentum fraction of the interacting gluon, x_g, and new dynamics with non-ordering in virtuality of the initial state cascade is expected. In this region, the k_T of the interacting gluon is not restricted, but can take any kinematically allowed value. The azimuthal angle $\Delta\phi^*$ between the two jets in a dijet event is directly sensitive to the k_T of the interacting gluon and is thus an appropriate observable when trying to distinguish between DGLAP and non-DGLAP parton evolutions. Dijet cross sections as a function of $\Delta\phi^*$ can also be used to constrain the unintegrated (k_T dependent) gluon densities which are used in non-DGLAP parton evolutions. The event sample used in this analysis is a factor three larger than that used in the previous H1 analysis concerning azimuthal correlations [12], and, due to an improved description of the hadronic final state, the cross sections are presented differentially in $\Delta\phi^*$ for the first time in H1. Also, a fit of the unintegrated gluon density is presented, in which a first attempt to constrain the intrinsic transverse momentum distribution is performed.

The structure of this thesis is as follows: in Chapter 1 an introduction to DIS and QCD is given; kinematic variables are defined, and different orders of DIS processes are discussed, including alternative ways of approximating higher order QCD radiation. Also, the Monte Carlo event generators and fixed order QCD programs, used for correcting the measured data for detector effects and QED radiation and for comparing with the data, are explained. The HERA accelerator and the H1 detector, where special attention is payed to the detector components used in the analysis, are presented in Chapter 2. The DIS and dijet selections together with basic control plots are given in Chapter 3, while migrations, corrections, efficiencies, systematic errors and the final results of the measurement are presented in Chapter 4. Chapter 5 describes how the unintegrated gluon density is determined by a fit to the dijet cross sections presented in Chapter 4 in combination with dijet cross sections from an earlier H1 measurement.

Chapter 1

Introduction to DIS and QCD

1.1 Introduction to Deep Inelastic Scattering

Within the Standard Model [13], lepton-nucleon interactions are mediated either by γ, Z^0 (neutral current interactions) or $W^{\pm}$ (charged current interactions) bosons. At HERA energies, where electrons with energy 27.6 GeV collide with 920 GeV protons, Z^0 and $\mathrm{W}^{\pm}$ exchange can mostly be neglected since such processes are suppressed due to the high masses of the exchange particles. Since a large momentum transfer between the electron and the proton implies a small wavelength of the exchanged boson, it also means a high resolution. If the momentum transfer is much larger than the proton mass ($\sim$ 1 GeV), the wavelength of the photon is small enough for it to resolve the structure of the proton, and the photon then interacts with the constituents (partons) of the proton. Such scatterings are always inelastic, i.e. the proton breaks up in the collision. They are therefore called Deep Inelastic Scattering (DIS) events. In contrast, events where the momentum transfer is smaller than the proton mass are called photoproduction events.

Figure 1.1 shows an electron with four-momentum P_e scattering off a proton with four-momentum P_p via the exchange of a virtual photon with four-momentum q. After the scattering, the electron is left with a four-momentum $P_e^{'}$ and the proton breaks up into a Hadronic Final State (HFS) with an invariant mass squared $W^2 > m_p^2$.

It is useful to define some Lorentz invariant variables characterizing the event:

- The virtuality Q^2 of the photon is defined as

  $$Q^2 \equiv -q^2 = -(P_e - P_e^{'})^2.$$

  Since the photon is spacelike, $Q^2 > 0$.

- Bjorken-x, defined as

  $$x_{Bj} \equiv \frac{Q^2}{2P_p \cdot q},$$

  which, in lowest order of the strong coupling α_s, can be interpreted as the fractional momentum of the proton carried by the interacting parton.

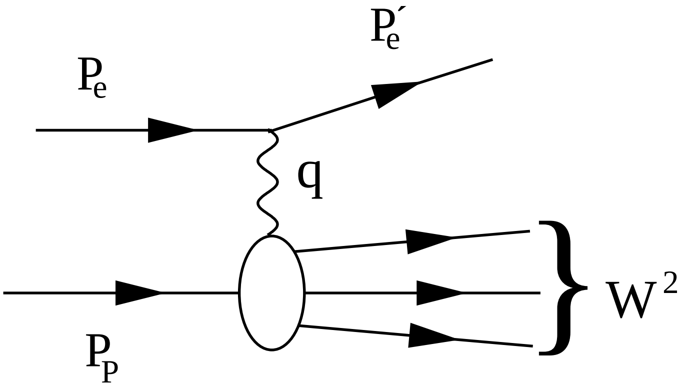

Figure 1.1: *A schematic view of a neutral current electron-proton scattering.*

- The inelasticity
$$y \equiv \frac{P_p \cdot q}{P_p \cdot P_e},$$
which, in the rest frame of the proton, is the fractional energy of the incoming electron carried by the photon.
- The invariant mass W of the hadronic final state,
$$W^2 \equiv (P_p + q)^2.$$
- The invariant mass squared, s, of the system,
$$s \equiv (P_p + P_e)^2.$$

However, these variables are not all independent. Neglecting the proton mass, we get

$$Q^2 = x_{Bj} y s$$

and

$$W^2 = Q^2 \cdot \frac{1 - x_{Bj}}{x_{Bj}}.$$

Hence, only three of the five variables listed above are independent. Also, since s is a constant, only two variables, for example x_{Bj} and Q^2, need to be determined in order to completely define the kinematics of the inclusive[1] DIS event.

Neglecting Z^0 and $W^\pm$ exchange and the proton mass, the differential DIS cross section can be written as

$$\frac{d^2\sigma}{dx_{Bj} dQ^2} = \frac{4\pi\alpha^2}{x_{Bj} Q^4} \left(y^2 x_{Bj} F_1(x_{Bj}, Q^2) + (1-y) F_2(x_{Bj}, Q^2) \right). \tag{1.1}$$

Here, α is the fine structure constant and F_1 and F_2 are structure functions parameterizing the partonic structure of the proton. The absorption of transversely polarized photons

---

[1] Inclusive means integrating over all HFS configurations.

is described by F_1 while longitudinally polarized photon interactions are described by $F_L = F_2 - 2x_{Bj}F_1$. Equation (1.1) can then be written as

$$\frac{d^2\sigma}{dx_{Bj}dQ^2} = \frac{4\pi\alpha^2}{x_{Bj}Q^4}\left(\frac{-y^2}{2}F_L(x_{Bj},Q^2) + (1 - y + \frac{y^2}{2})F_2(x_{Bj},Q^2)\right). \tag{1.2}$$

For processes where Q^2 is small, F_L can normally be neglected since longitudinally polarized photons are suppressed. The term $\frac{4\pi\alpha^2}{x_{Bj}Q^4}$ in Equations (1.1) and (1.2) is the classical Rutherford formula for a pointlike particle scattering off a pointlike target, while the structure functions are corrections due to the structure of the proton [14].

1.2 QPM and the Leading Order DIS Process

The Quark Parton Model (QPM) [15, 16] postulates that the proton consists of partons, identified as three valence quarks (uud) which carry the quantum numbers of the proton, and quark-antiquark pairs. The model is defined in the infinite momentum frame, $P_p \to \infty$, where the proton is Lorentz contracted to a disk and the partons, which are assumed to be pointlike, are time dilated such that they are effectively free. In the QPM, DIS processes are thus elastic, incoherent scatterings of electrons off free quarks, as shown in Figure 1.2, and as a consequence, the structure functions are independent of the scale Q^2,

$$F_i(x_{Bj},Q^2) \to F_i(x_{Bj}),$$

a phenomenon called scaling. Also, if quarks have spin 1/2, then $F_L = 0$ and the Callan-Gross relation [17] is valid:

$$F_2(x_{Bj}) = 2x_{Bj}F_1(x_{Bj}).$$

In the QPM

$$F_2(x_{Bj}) = \sum_{i=q} e_i^2 x_{Bj} f_i(x_{Bj}), \tag{1.3}$$

where e_i and $f_i(x_{Bj})$ are the charge and parton density function (PDF) of parton i, respectively. The PDF can be interpreted as the probability distribution of finding a parton i in the proton carrying a fraction x_{Bj} of the proton energy.

The scaling behaviour of the structure functions was first observed in 1969 [18, 19] (for $x_{Bj} \sim 0.25$), and the Callan-Gross relation was confirmed the same year [20, 21], giving strong support for the QPM. However, later experiments [22–25] found that the structure functions do, in fact, depend on Q^2. Recent data [26] showing this scaling violation (and the scaling at $x_{Bj} \sim 0.25$) is shown in Figure 1.3. Also, it seemed that only about 50% of the proton momentum was carried by the quarks. The theory of Quantum Chromo Dynamics (QCD), in which the QPM process (Figure 1.2) is the lowest order approximation, offers solutions to these problems.

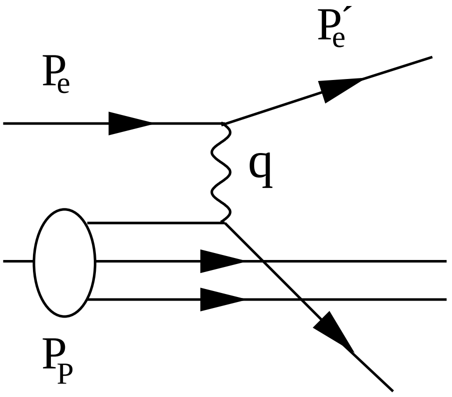

Figure 1.2: *A schematic view of the QPM process. The electron scatters off a free quark via the exchange of a photon.*

1.3 Perturbative Quantum Chromo Dynamics

The theory of strong interactions, QCD, introduces a new gauge boson, called the gluon, as mediator of the strong force, and the concept of colour degree of freedom. The gluons couple to all particles carrying this colour charge, and the strength of the coupling is denoted α_s. The colour charge can have three values: red, green and blue, and correspondingly for anti-colours: anti-red, anti-green and anti-blue. Quarks (anti-quarks) carry one of these colours (anti-colours), while the gluons themselves carry one colour and one anti-colour, making gluon self-interactions possible. Hence, in QCD, the QPM process is corrected for real and virtual gluons and quarks. In perturbative QCD (pQCD), this is done by expanding amplitudes in a perturbation series in α_s. For a given observable, the first non-zero term in this expansion is called the Leading Order (LO) term, the following term is Next-to Leading Order (NLO) and so on. For inclusive DIS, the LO term corresponds to the QPM process and is thus of zeroth order in α_s, $\mathcal{O}(\alpha_s^0)$, while the NLO term is $\mathcal{O}(\alpha_s^1)$. For dijet production, the LO term is of $\mathcal{O}(\alpha_s^1)$, while the NLO term is $\mathcal{O}(\alpha_s^2)$, see Section 1.9.

When including for example the virtual loop corrections of Figure 1.4, ultraviolet divergencies appear. They arise because the momentum of a virtual quark or gluon is unrestricted, making the loop integral divergent as the momentum $P \to \infty$. These divergencies can be regularized and absorbed into α_s, using renormalization. In the renormalization procedure[2], a new scale is introduced, on which α_s (and the coefficients in the perturbative expansion) becomes dependent. This renormalization scale, μ_r, is an arbitrary parameter of QCD, and physical quantities should not depend on it. However, cross sections calculated as truncated series in α_s, will depend on μ_r through the dependence of α_s on the scale (running of $\alpha_s(\mu_r)$), meaning that a choice of μ_r must be made. Most often the hardest scale in the process is chosen, e.g. $\mu_r^2 = Q^2$. The scale dependence of $\alpha_s(\mu_r)$ is determined by

$$\mu_r^2 \frac{\partial \alpha_s}{\partial \mu_r^2} = \beta(\alpha_s) = -\frac{\beta_0}{4\pi}\alpha_s^2 - \frac{\beta_1}{(4\pi)^2}\alpha_s^3 + ... \tag{1.4}$$

---

[2] There are different ways of performing renormalization, e.g. the MS and $\overline{MS}$ schemes.

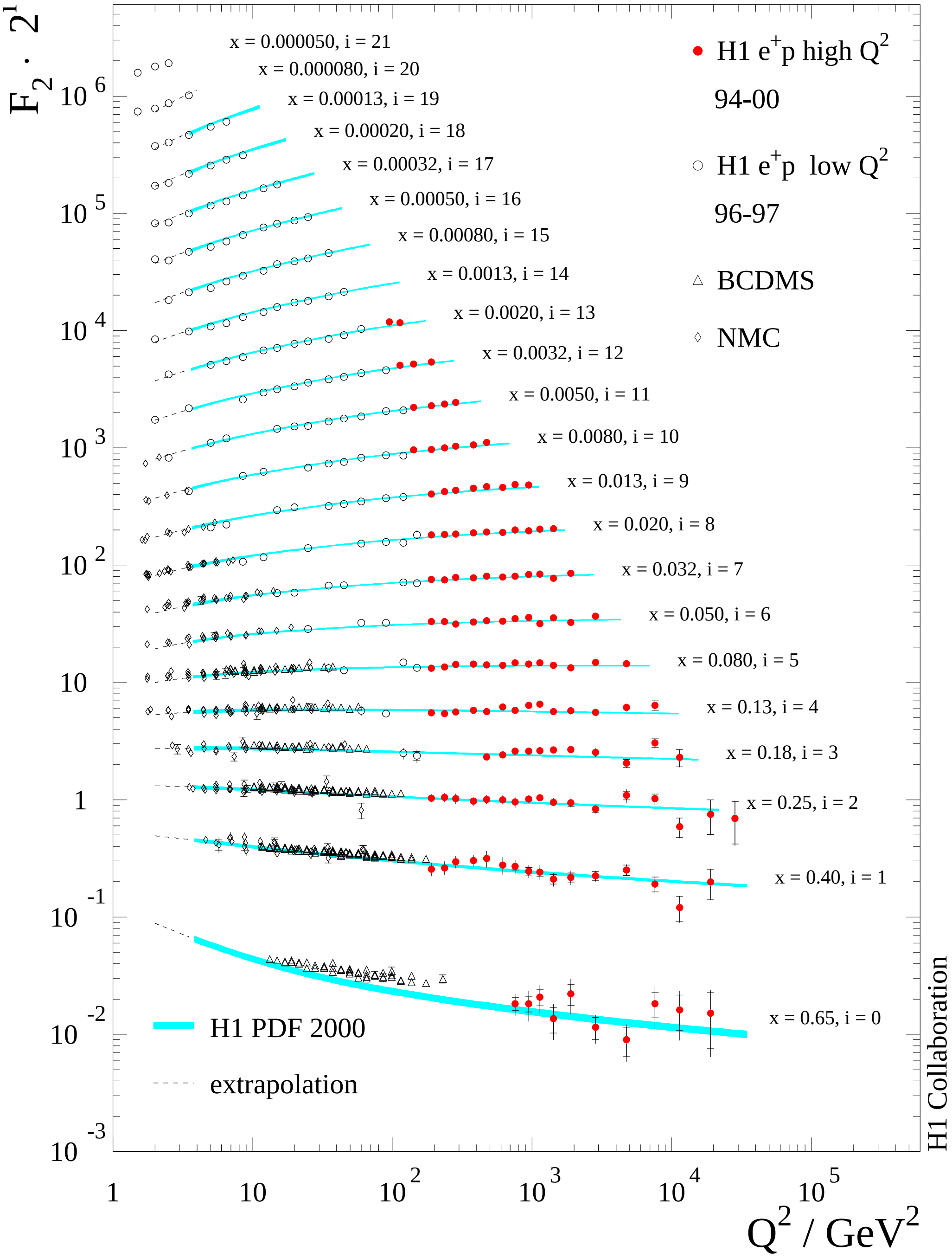

Figure 1.3: *The proton structure function* F_2 *for different values of* x_{Bj} *(denoted* x *in the figure) as a function of* Q^2*, showing scaling at* $x_{Bj} \sim 0.25$ *and scaling violation at smaller and larger* x_{Bj}*. Also shown are Standard Model predictions from a QCD fit to the data, where the shaded bands indicate the theoretical errors, and an extrapolation (broken line) to lower* Q^2 *values than the starting value of the fit. The figure is taken from [26].*

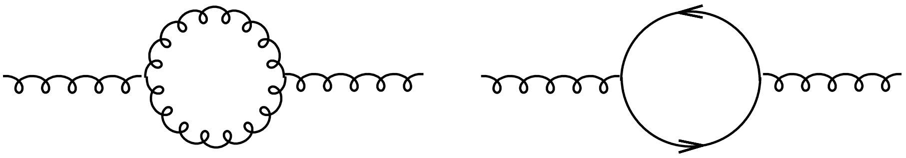

Figure 1.4: *Virtual loop corrections giving rise to ultraviolet divergencies.*

where

$$\begin{aligned}\beta_0 &= 11 - \frac{2}{3}n_f \\ \beta_1 &= 102 - \frac{38}{3}n_f\end{aligned}$$

and n_f being the number of active flavours, i.e. the number of quarks with $m_q^2 << \mu_r^2$. Equation (1.4) describes how α_s depends on the scale μ_r, but does not give any absolute value of α_s at any scale. Hence, α_s has to be determined experimentally by measuring various observables sensitive to the strong coupling. The values of α_s obtained at the energy of the measurement can then be transformed to any other scale using Equation (1.4). The scale chosen for comparison of α_s from different measurements is by convention the mass of the Z^0 boson, $\mu_0 = M_Z$. With this experimental input, α_s is completely determined at all scales by Equation (1.4). In the one-loop approximation (only considering the first term in Equation (1.4)), the solution becomes

$$\alpha_s(\mu_r^2) = \frac{\alpha_s(\mu_0^2)}{1 + \alpha_s(\mu_0^2)\frac{\beta_0}{4\pi}ln\left(\frac{\mu_r^2}{\mu_0^2}\right)}. \qquad (1.5)$$

Here, we see that at large μ_r^2, $\alpha_s(\mu_r^2)$ becomes small, meaning that partons probed at a large scale (small distances) will behave as free particles, a property called asymptotic freedom. However, as μ_r^2 becomes smaller, α_s becomes larger, and eventually the expansion cannot converge. As a consequence of this, pQCD breaks down at small scales $\mu_r \approx 200$ MeV.

The current world average value of the strong coupling constant is [27]

$$\alpha_s(M_Z^2) = 0.1176 \pm 0.0020.$$

1.4 Factorization

With the introduction of QCD and the possibility of gluon emissions, the number of possible DIS processes increases dramatically. Although the relative contribution of the process decreases with a factor α_s for each added gluon, these higher order corrections are crucial when doing precision measurements or studying exclusive observables. However, the addition of gluons introduces divergencies in the perturbative calculations, originating from gluons that are collinear to the radiating parton, i.e. when the transverse momentum of the gluon approaches zero, $k_{T,g} \rightarrow 0$. Just as the ultraviolet divergencies could be absorbed into the running of α_s, with the introduction of a renormalization scale μ_r, these collinear

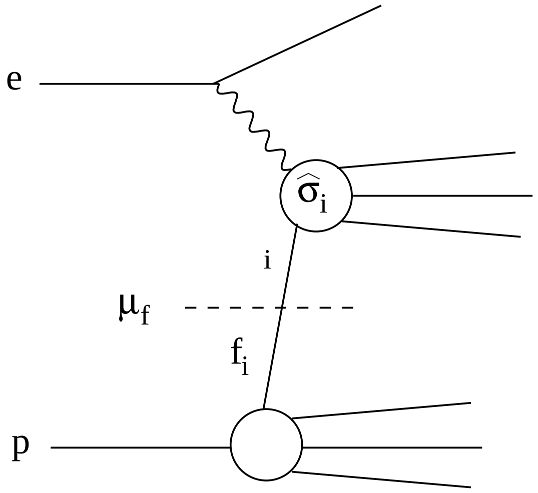

Figure 1.5: *Schematical interpretation of factorization: the scale* μ_f *separates the perturbative* ($\hat{\sigma}_i$) *and non-perturbative* (f_i) *part of the cross section.*

divergencies can be absorbed into parton density functions (PDFs) with the introduction of a cut-off parameter μ_f, on which the PDFs become dependent (running of the PDFs). The PDFs describe, in LO, the probability of finding a specific parton inside a hadron (in this case the proton), and are completely process independent. The scale μ_f can be interpreted as the scale (or transverse momentum k_T) separating (factorizing) the perturbative and non-perturbative parts of the cross section, schematically shown in Figure 1.5. Hence, all partons with $k_T < \mu_f$ are included in the PDF, while partons with with $k_T > \mu_f$ are taken care of perturbatively. Therefore, the scale μ_f is called the factorization scale. Exactly how the PDFs depend on the factorization scale is described by so called evolution equations, which will be discussed in the next section.

The most common way to separate the perturbative and the non-perturbative parts of the cross section is by applying **collinear factorization**, in which the partons are approximated to be collinear with the proton [28]. Then, the *ep* cross section can be written as

$$\sigma(ep \to e^{'}X) = \sum_i \int_0^1 \frac{dx}{x} f_i(x, \mu_f^2) \cdot \hat{\sigma}_i, \tag{1.6}$$

where f_i is the process independent parton density function and $\hat{\sigma}_i$ is the perturbatively calculable partonic cross section. The function $f_i(x, \mu_f^2)$ can be interpreted as the density of partons of type i carrying a longitudinal momentum fraction x probed at a scale μ_f^2. Note that $x = x_{Bj}$ only in LO DIS. The collinear approximation, in combination with the DGLAP approximation (see Section 1.5), has been successfully applied to F_2 and various jet cross sections [29]. However, when x becomes small the collinear approximation is expected to lose its validity. An alternative approach is then to use **$\mathbf{k_T}$-factorization** in which the *ep* cross section can be written as

$$\sigma(ep \to e^{'}X) = \sum_i \int \frac{dx}{x} dk_T^2 \mathcal{F}_i(x, k_T) \hat{\sigma}_i. \tag{1.7}$$

Here, both the partonic cross section $\hat{\sigma}$ and the so called unintegrated parton density

$\mathcal{F}(x, k_T)$ depend on k_T so that the kinematics of the partons are properly taken into account.

In the factorization procedure, one is, to some extent, free to choose which finite terms that are absorbed into the PDFs in addition to the infinite ones. For example, in the (collinear) DIS scheme, all finite terms are absorbed into the PDFs, such that

$$F_2(x, Q^2) = \sum_{i=q,\bar{q}} e_i^2 x f_i(x, Q^2) \tag{1.8}$$

which is similar to Equation (1.3) except that here F_2 and f_i depend on Q^2. In the $\overline{MS}$ scheme, however, only some finite terms are absorbed, so that Equation (1.8) is only true in LO. Since the PDFs are different in these schemes, also $\hat{\sigma}$ is scheme dependent.

1.5 Higher Order DIS Processes and Evolution Equations

As already mentioned, the LO DIS process ($\mathcal{O}(\alpha_s^0)$) is a simple quark-photon scattering and is completely independent of QCD. The next term in the expansion series, the Next-to-Leading Order (NLO) term is of $\mathcal{O}(\alpha_s)$ and corresponds to the processes with one gluon emission, i.e. QCD-Compton (QCD-C) and Boson-Gluon Fusion (BGF), seen in Figure 1.6. Also, the virtual corrections shown in Figure 1.7 need to be included. Separately, these diagrams diverge, but when added the divergencies exactly cancel. Due to the complexity of the calculations and the rapidly increasing number of contributing diagrams, the full set of NNLO DIS matrix elements has not yet been calculated.

In addition to the partonic cross section $\hat{\sigma}$, one must also have the PDF at the factorization scale μ_f. Although it is not possible to calculate the size and shape of the PDFs in pQCD, it is possible to derive so called evolution equations that predict the scale dependence of the PDFs. Once a starting PDF has been chosen at some starting scale $\mu_{f,0}^2$, its size and shape at any other scale μ_f^2 can be determined by these equations. (This is in analogy to Equation (1.4) which determines α_s at any scale μ_r^2 once a starting value has been chosen at some starting scale $\mu_{r,0}^2$.)

The evolution equations describe how a mother parton is split into two daughter partons, one of which is emitted whereas the other continues as a propagator parton. This propagator is then split into two daughters and so on, creating a parton ladder as illustrated in Figure 1.8. Hence, evolution equations can be used to approximate higher order emissions beyond what has been calculated analytically. Three different evolution equations, derived under different approximations and valid in different phase space regions, are presented below.

1.5.1 DGLAP Evolution

The DGLAP [8–11] evolution equation is of the form

$$\frac{df_j(x, \mu_f^2)}{d \ln \mu_f^2} = \frac{\alpha_s(\mu_f^2)}{2\pi} \sum_i \int_x^1 \frac{dx'}{x'} f_i(x', \mu_f^2) P_{i \to j,k}(z) \tag{1.9}$$

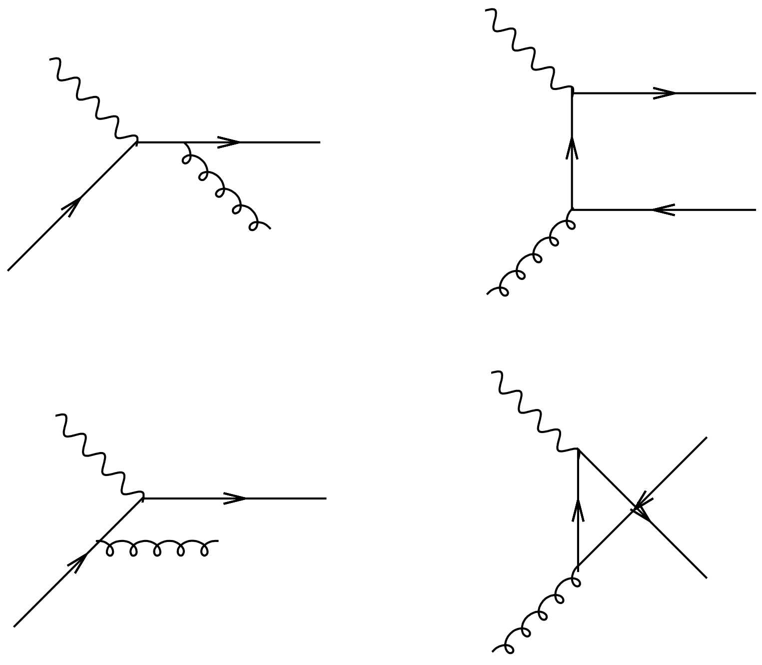

a) b)

Figure 1.6: *The first order real corrections to the QPM process, a) QCD-Compton and b) Boson-Gluon Fusion.*

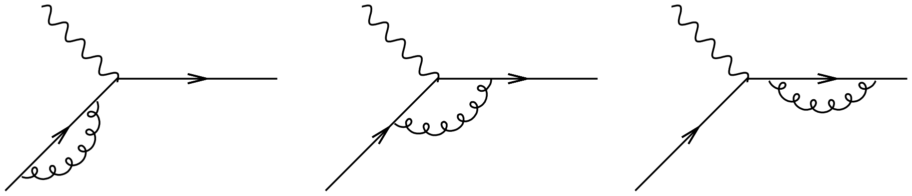

Figure 1.7: *The $\mathcal{O}(\alpha_s)$ virtual corrections to the QPM process.*

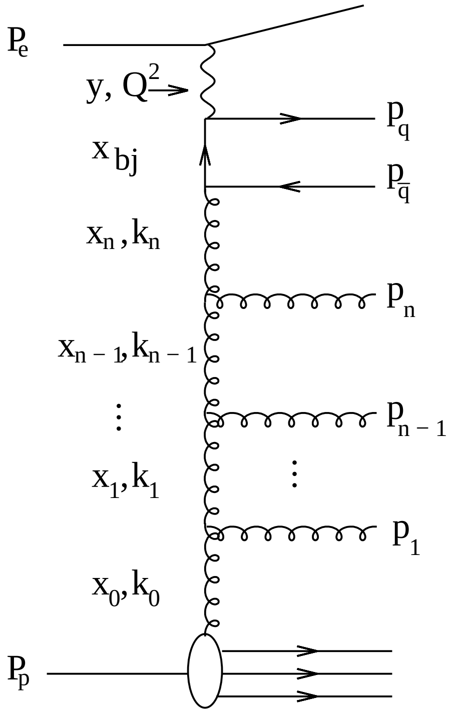

Figure 1.8: *Parton ladder created by gluon emissions.* x_i *and* k_i *are the longitudinal momentum fractions and four-vectors of the propagator gluons, respectively, while* p_i *are the four-vectors of the emitted gluons.*

where $f_i(x, \mu_f^2)$ is the PDF and $P_{i \to j,k}(z)$ describes the probability that a parton i is split into two partons j and k with fractions $z = \frac{x}{x'}$ and $1 - z$ of the original parton momentum, respectively. The possible splittings (in QCD) are $q \to qg$, $g \to q\bar{q}$ and $g \to gg$. For example, the probability that a gluon splits into two gluons is in LO given by

$$P_{g \to g,g}(z) = \frac{1}{1-z} - 2 + z(1-z) + \frac{1}{z} \tag{1.10}$$

where the terms $\frac{1}{1-z}$ and $\frac{1}{z}$ are called the singular terms, since they give infinite contributions when $z \to 1$ and $z \to 0$, respectively. The Equation (1.9) thus describes the change in the probability of finding a parton of type j with momentum fraction x as we increase the scale μ_f^2. This is the scaling violation mentioned in Section 1.2.

The DGLAP equation in lowest order resums terms of the form $(\alpha_s \ln(\frac{\mu_f^2}{\mu_{f,0}^2}))^n$, where n denotes the order of the term, in the expansion of the cross section. These so-called Leading Log (LL) terms correspond to parton ladder diagrams where the virtualities of the propagator gluons are strongly ordered (see Figure 1.8 and put $Q^2 \sim \mu_f^2$),

$$\mu_f^2 \gg |k_n^2| \ldots \gg |k_1^2| \gg |k_0^2|. \tag{1.11}$$

Here, k_i is the four momentum of parton i. This means that in each splitting $i \to i+1, j$ one can approximate $k_0^2 = k_1^2 = \ldots\ k_i^2 = 0$ compared to k_{i+1}^2, and since $k_i^2 = m_i^2$ these partons are considered to be massless. Since $|k^2| = \frac{k_T^2}{1-x}$, the ordering in virtuality implies that also the transverse momenta of the propagator partons are strongly ordered (at small x) according to

$$\mu_f^2 \gg |k_{Tn}^2| \ldots \gg |k_{T1}^2| \gg |k_{T0}^2| \tag{1.12}$$

where $k_{Ti} = (0, k_{xi}, k_{yi}, 0)$. In the collinear approximation one approximates $k_{T0}^2 = k_{T1}^2 = \ldots k_{Ti}^2 = 0$ such that the PDF and the partonic cross section is independent of k_T, as seen in Equation 1.9. The DGLAP approximation is only valid in the region where x is not too small and μ_f^2 is large, such that the terms $(\alpha_s \ln(\frac{\mu_f^2}{\mu_{f,0}^2}))^n$ will dominate the cross section.

1.5.2 BFKL Evolution

The BFKL [30–32] evolution equation resums the terms $(\alpha_s \ln(\frac{1}{x}))^n$ in the expansion, and is thus only valid at small x_{Bj} and moderate scales. It is of the form

$$\frac{d\mathcal{G}(x, k_T^2)}{d\ln(\frac{1}{x})} = \int dk_T'^2 \mathcal{G}(x, k_T'^2) \cdot K(k_T^2, k_T'^2), \tag{1.13}$$

where the function K is the splitting kernel equivalent to P in Equation (1.9). Following the convention in [33], the parton density is now labeled $\mathcal{G}$. In deriving the BFKL equation, strong ordering in longitudinal fractional momentum is assumed,

$$x_0 \gg x_1 \ldots \gg x_n \gg x_{Bj}. \tag{1.14}$$

This implies that the emitted gluons will take a large fraction of the propagator momentum. However, there is no ordering in k^2 or k_T^2, so the collinear approximation can not be used, and the incoming partons of the matrix elements must be taken off-shell (the particles can have a virtual mass). Due to this non-ordering, a parton carries out a "random walk" in k_T and can diffuse into the non-perturbative region. This is avoided by introducing a lower cut-off $k_{T,0}$ in the integral of Equation (1.13). Another important consequence of the non-ordering in k_T is that unintegrated parton densities (uPDFs) must be used in (1.13), i.e. they must depend on k_T. The uPDFs can be related to the (integrated) parton densities by

$$xf(x, \mu_f^2) \approx \int_0^{\mu_f^2} \frac{dk_T'^2}{k_T'^2} \mathcal{G}(x, k_T'^2).$$

It is not a strict equality, because the integration over k_T is performed up to the factorization scale μ_f while there can still be a tail in the uPDF with $k_T > \mu_f$.

1.5.3 CCFM Evolution

The CCFM [34–37] evolution equation is valid both at large and small x, since it resums terms of both the form $(\alpha_s \ln(\frac{1}{x}))^n$ and $(\alpha_s \ln(\frac{1}{1-x}))^n$. This means that at large x the CCFM evolution will be DGLAP-like, and at small x it will be BFKL-like. The CCFM evolution includes angular ordering in the initial state cascade in order to account for coherence effects, which means that the angles ξ of the emitted partons with respect to the propagator increases as one moves towards the hard interaction,

$$\Xi \gg \xi_n \ldots \gg \xi_1 \gg \xi_0, \tag{1.15}$$

where the maximum allowed angle Ξ is set by the quark box,

$$p_q + p_{\bar{q}} = \Upsilon(P_p + \Xi P_e) + \vec{Q}_t.$$

This is written in the Sudakov (or lightcone) variables, where p_q, $p_{\bar{q}}$, P_e and P_p are the four momenta of the produced quarks, the electron and the proton, respectively (see Figure 1.8), Υ and $\Upsilon\Xi$ are the positive and negative light-cone momentum fractions of the quark pair, and $\vec{Q}_t$ is the sum of the transverse momentum vectors of the quark pair. The momenta of the emitted gluons i can be written similarly,

$$p_i = \upsilon_i(P_p + \xi_i P_e) + p_{ti}, \ \xi_i = \frac{p_{ti}^2}{s\upsilon_i^2}, \tag{1.16}$$

where $\upsilon_i = (x_{i-1} - x_i)$ is the momentum fraction of the emitted gluon, p_{ti} is the transverse momentum of the gluon, and $s = (P_p + P_e)^2$ is the squared center of mass energy. Here, it is assumed that all particles are massless. The CCFM equation is written as

$$\bar{q}^2 \frac{d}{d\bar{q}^2} \frac{x\mathcal{A}(x, k_T^2, \bar{q}^2)}{\Delta_s(\bar{q}^2, \mu_0^2)} = \int dz \frac{d\phi}{2\pi} \frac{\tilde{P}(z, k_T^2, (\bar{q}/z)^2)}{\Delta_s(\bar{q}^2, \mu_0^2)} x'\mathcal{A}(x', k_T'^2, (\bar{q}/z)^2) \tag{1.17}$$

where

$$\bar{q}_i = \frac{p_{ti}}{1 - z_i} = x_{i-1}\sqrt{s\xi_i} \tag{1.18}$$

is the rescaled transverse momenta of the emitted gluons, $z_i = \frac{x_i}{x_{i-1}}$ and $\mathcal{A}(x, k_T^2, \bar{q}^2)$ is the unintegrated gluon density function (uGDF) which now depends on two scales, k_T and $\bar{q}$. In CCFM, $\bar{q}$ plays the role of factorization scale. In this formalism, (1.15) becomes

$$\bar{q}_i > z_{i-1}\bar{q}_{i-1}. \tag{1.19}$$

When $z \to 1$ we have $\bar{q}_i > \bar{q}_{i-1}$, i.e. ordering in rescaled transverse momentum, which means that the evolution is DGLAP-like. In the limit $z \to 0$ the angular ordering gives no restrictions on $\bar{q}$. Also, (1.14) holds because of the definition of z. This means that the evolution is BFKL-like.

The Sudakov form factor Δ_s appearing in Equation (1.17) describes the probability that there are no emissions from the starting scale μ_0^2 to the maximum rescaled transverse momentum $\bar{q}_{max}^2$. Most often, only the singular terms in the CCFM splitting function are considered

$$\tilde{P}_{g\to gg}(z, k_T^2, (\bar{q}/z)^2) = \frac{\bar{\alpha}_s(q_i^2(1 - z_i)^2)}{1 - z_i} + \frac{\bar{\alpha}_s(k_{Ti}^2)}{z_i}\Delta_{ns}(z_i, k_{Ti}^2, q_i^2), \tag{1.20}$$

where the non-Sudakov form factor Δ_{ns} originates from the fact that, in CCFM and BFKL, all virtual corrections in the gluon vertex are automatically taken into account, see Figure 1.9.

1.5.4 The Colour Dipole Model

The Colour Dipole Model (CDM) [38–41] offers an alternative way of simulating higher order QCD radiation. The basic idea is that dipoles are spanned between $q\bar{q}$-, qg-, $\bar{q}g$- and

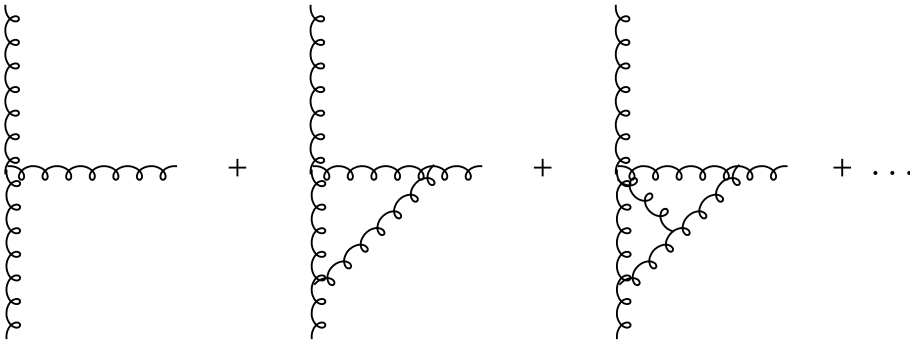

Figure 1.9: *Virtual corrections included by the non-Sudakov form factor* Δ_{ns}.

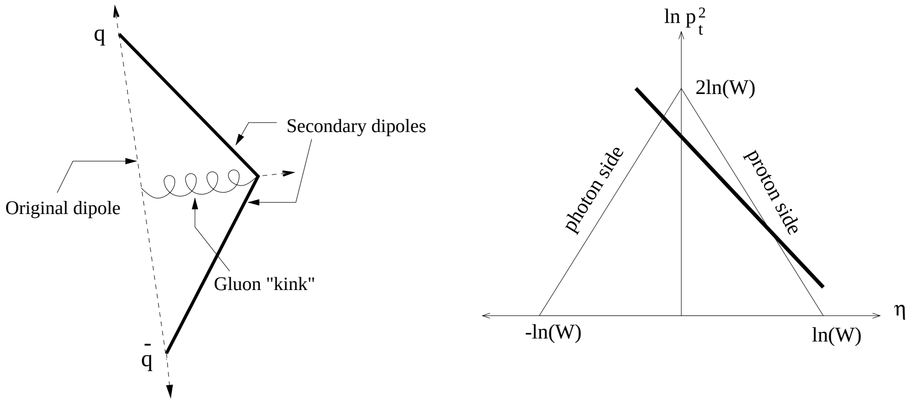

a) b)

Figure 1.10: *In a) is shown a schematic picture of a dipole spanned by a* $q\bar{q}$ *pair. The dipole radiates a gluon, which creates two new dipoles between the* qg *and the* $\bar{q}g$ *pairs, while the original dipole is destroyed. The triangle in b) shows the allowed phase space for radiation from a dipole of energy* W *in* $ln(p_t^2) - \eta$ *space. The thick line indicates the modified phase space due to the spatial extension of the proton.*

gg-pairs and these dipoles emit gluons independently. Any gluon emission from a dipole will produce a kink in the original dipole resulting in two new dipoles, see Figure 1.10 a). In DIS, the first dipole is stretched between the proton remnant and the struck quark, meaning that all radiation will take place between these. Hence, the CDM does not distinguish between initial and final state radiation.

QCD radiation from a dipole of energy W is restricted by

$$p_t \cdot cosh(\eta) < \frac{W}{2}$$

where p_t and $\eta = -\ln(\tan(\theta/2))$ is the transverse momentum and pseudo-rapidity in the dipole center of mass system of the emitted gluon. For dipoles spanned between pointlike particles, this can be visualized as a triangle in $ln(p_t^2) - \eta$ space, as seen in Figure 1.10 b). However, the phase space is somewhat modified (thick line) if one of the particles has a spatial extension, as is the case in ep-collisions.

The CDM produces radiation that is non-ordered in transverse momentum k_T [42–45], like BFKL and CCFM.

1.5.5 The Resolved Photon Model

The resolved photon model includes the possibility for the photon to fluctuate into a $q\bar{q}$-pair, thus acquiring a hadronic structure. The $q\bar{q}$-pair may either be on-shell, i.e. a vector meson, or off-shell. Assuming massless quarks, the fluctuation time is characterized by the virtuality Q^2 of the photon, $t_f \sim \frac{1}{|Q|}$. If there is a second hard scale in the process, for example a high E_T jet, the interaction time will be $t_i \sim \frac{1}{|E_T|}$. Since the hadronic structure of the photon will be significant if $t_f \gtrsim t_i$, it follows that resolved photons will become important when $E_T^2 \gtrsim Q^2$. Of course, this will most often be the case in photoproduction events where the photons are quasi-real ($Q^2 \sim 0$ GeV^2). Because of the second hard scale in the process, two gluon ladders may be evolved: one on the photon side towards the hard matrix element, and one from the proton side, see Figure 1.11. Even if both these ladders are evolved using DGLAP, the ordering in k_T will be broken.

In analogy to the proton, a structure function for the photon may be defined as[3]

$$F_2^\gamma(x_\gamma, \mu_f^2) = \sum_i e_i^2 x_\gamma f_i^\gamma(x_\gamma, \mu_f^2), \tag{1.21}$$

where x_γ is the longitudinal momentum fraction of the photon carried by the parton, μ_f is the factorization scale, e is the electric charge and $f_i^\gamma(x_\gamma, \mu_f^2)$ is the probability of finding a parton of type i with longitudinal momentum fraction x_γ in the photon when probed at a scale μ_f. Also, unintegrated parton densities for the photon may be used for example in the CCFM scheme.

---

[3] This is in the DIS scheme.

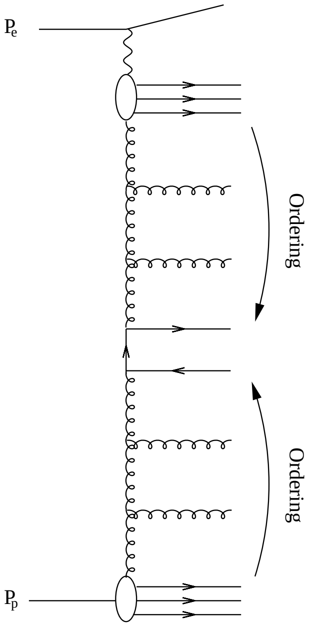

Figure 1.11: *In the resolved photon model two DGLAP ladders are evolved, one from the photon side and one from the proton side, thus breaking the* k_T*-ordering.*

1.6 Hadronization and Fragmentation

As already mentioned, pQCD calculations are only applicable when the scale μ_r is large, such that $\alpha_s(\mu_r^2)$ is small, and the perturbative series converge. At these small distances, the partons behave more or less like free particles inside the hadron. At smaller scales, or larger distances ($\sim$ 1 fm), the quarks may not escape as free particles, but are confined in the colourless hadrons with integer charges, that are observed in nature. The bridge between the "parton level", where pQCD predictions are made, and the "hadron level" which is observed[4], must thus be made using phenomenological models.

There are a number of different hadronization/fragmentation models, for example Independent Fragmentation [46, 47], Cluster Fragmentation [48, 49] and String Fragmentation [50–54]. The latter one, which is implemented in the MC generators used in this thesis, will briefly be described below.

In the Lund String Model, the colour field between a quark and an anti-quark is compressed to a tube because of gluon self-interactions. Due to this string-like structure, the energy density per unit length in the string is constant $\kappa = 1$ GeV/fm. Therefore, if the two quarks are moving away from each other, the potential energy in the string will increase linearly with the distance (neglecting the Coulomb interaction), and when the stored energy is large enough, the string breaks, creating a $q\bar{q}$-pair using a tunnelling mechanism, see Figure 1.12. The probability of creating a $q\bar{q}$ pair with mass m and transverse momentum p_T is

$$exp(-\frac{\pi(m^2 + p_T^2)}{\kappa})$$

---

[4] Actually, what is observed are tracks and clusters on the "detector level", which are then corrected to the "hadron level".

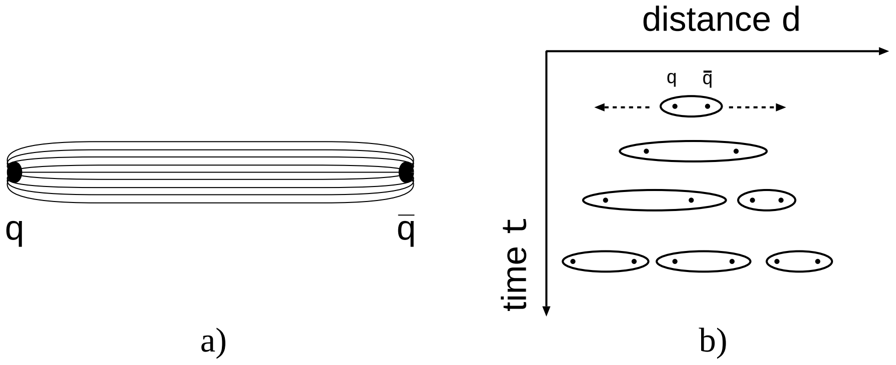

Figure 1.12: *a) A schematic picture of a string between a quark and an anti-quark. b) A quark and an anti-quark moves away from each other, stretching a string between them. When the potential energy in the string is large enough, the string breaks up and a $q\bar{q}$-pair is created. This procedure continues until the energy is too low to produce new $q\bar{q}$-pairs.*

resulting in a suppression of heavy quark production $u : d : s : c \approx 1 : 1 : 0.3 : 10^{-11}$. The fragmentation process continues until there is no energy left to create new $q\bar{q}$-pairs.

Baryons may be produced either by combining quarks and anti-quarks from $q\bar{q}$ splittings to qqq and $\bar{q}\bar{q}\bar{q}$ states, or by allowing diquark pairs $(qq, \bar{q}\bar{q})$ to be created when the string breaks. These diquarks (anti-diquarks) can then be combined with a quark (anti-quark) to form a baryon (anti-baryon).

1.7 Jet Production and Reconstruction

In the fragmentation procedure, a parton may hadronize into many final state particles, thereby “hiding” the underlying partonic event. However, it is expected that the hadrons are collimated in the direction of the original parton, especially if the original parton is hard (has a large k_T). The properties of such a collimated flow of particles, called a jet, are therefore expected to reflect the properties of the original parton. A good correlation between the “parton level” and the “hadron level” is essential for making experimental tests of pQCD. There is no unique procedure for grouping hadrons into jets, and many models exists, for example the JADE [55] and the CONE [56] algorithms. The one used in this thesis is the longitudinally invariant inclusive k_T algorithm [57–59], which is infrared safe to all orders (i.e. the results are stable with respect to soft gluons) [60] and has smaller hadronization corrections than other jet algorithms [61].

1.7.1 The Inclusive k_T Algorithm

The inclusive k_T algorithm takes as input a list of objects, or protojets, for example partons, hadrons, or combined objects (clusters and/or tracks, see Section 2.3) depending on which level it is applied. This list is then iterated, and in each iteration, a “distance” is calculated for each pair of protojets, and also a “distance” between each protojet and the proton direction. Either two protojets are combined into one protojet or a protojet is removed from the list of protojets and added to the list of jets depending on which distance is the smallest. Because of this procedure, the number of protojets are decreasing and the number of jets are increasing for each iteration. When there are no protojets left, the algorithm returns the list of jets. The iteration procedure may be summarized as follows:

1. For each pair of protojets $\{i, j\}$, the distance parameter
$$d_{i,j} = min(E_{T,i}^2, E_{T,j}^2) \cdot \left((\eta_i - \eta_j)^2 + (\phi_i - \phi_j)^2\right)$$
is calculated.

2. For each protojet, the distance between the protojet and the beam direction is calculated as
$$d_i = E_{T,i}^2 R^2.$$
R defines the radius of a cone in the (η,ϕ) plane, and most often $R = 1$ is chosen [59].

3. Find the minimum of all $\{d_{i,j}, d_i\}$. If the minimum is one of $d_{i,j}$, then the protojets i and j are merged into a new protojet k according to some recombination scheme (see Section 1.7.2). Of course, protojets i and j are removed from the list and jet k is added. If d_i is the minimum, then protojet i is removed from the list of protojets and added to the list of jets. The procedure is then repeated starting from step 1.

1.7.2 Recombination Schemes

There are many possibilities of combining the four-vectors of two protojets into one. For example, one can consider the protojets as real particles and simply add the four-vectors,
$$P_k = P_i + P_j.$$
In this scheme, sometimes called the **E-scheme**, the resulting (proto-)jet k has a mass $m_k \neq 0$. To preserve the longitudinal boost invariance, the rapidity $\frac{1}{2} ln \frac{E+P_z}{E-P_z}$ of the (proto-)jets must be used when calculating the distance parameter $d_{i,j}$ instead of the pseudorapidity $\eta = -ln(tan(\theta/2))$. Also, E_T, η and ϕ have to be recalculated from the four-vectors in each step. Computationally, it can be more convenient to use a recombination scheme where the (proto-)jets are constructed using E_T, η and ϕ directly. This is done in the **$\mathbf{E_T}$ recombination scheme** [62], where the scalar transverse energies are added, while η and ϕ are weighted with E_T and added according to
$$E_{T,k} = E_{T,i} + E_{T,j}$$
$$\eta_k = \frac{E_{T,i}\eta_i + E_{T,j}\eta_j}{E_{T,k}}$$
$$\phi_k = \frac{E_{T,i}\phi_i + E_{T,j}\phi_j}{E_{T,k}}.$$
Here, the invariance under longitudinal boosts is preserved because the (proto-)jets k are massless. There are also other possibilities, for example adding the four-vectors and then rescaling either the energy E or the momentum $|\bar{P}|$ such that the resulting four-vector is massless. Of course, different recombination schemes will give different jet properties, and which scheme to apply is a matter of convention. In this analysis, the E_T recombination scheme has been used.

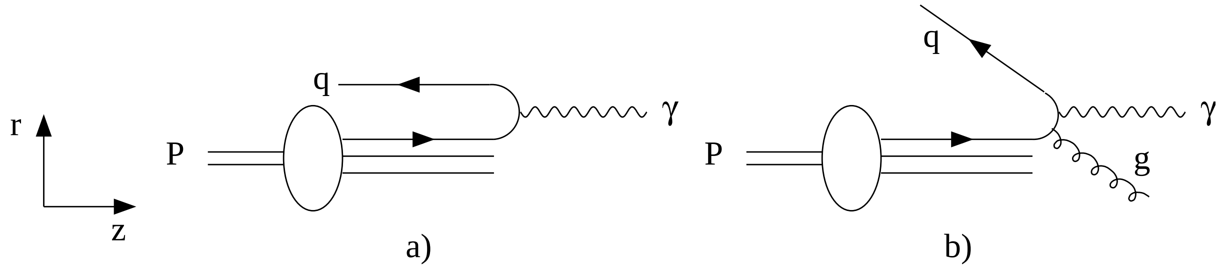

Figure 1.13: *Jet production in the HCM frame: a) the QPM diagram and b) the QCD-C process.*

1.7.3 The Hadronic Center of Mass Frame

In the laboratory frame, where the electron and the proton collide head-on, the hadronic final state must balance the transverse momentum of the scattered electron. However, the influence of the scattered electron can be removed with a boost to the Hadronic Center of Mass (HCM) frame, where the photon collides head-on with the proton,

$$P_\gamma + P_p = 0.$$

Hence, in LO (if the intrinsic k_T of the partons are neglected) the photon collides with a quark which back-scatters with a transverse momentum[5] $E_T^* = 0$, see Figure 1.13 a). (In the HCM frame, transverse momenta are perpendicular to the proton direction, which defines the z-axis.) In NLO, for example the QCD-C process shown in Figure 1.13 b), the photon and the incoming quark are collinear while the gluon and the outgoing quark, i.e. the produced jets, are emitted back-to-back. In higher order processes, the parton involved in the hard scattering may receive a non-zero transverse momentum from additional initial state gluon emissions, such that the dijet system (for example the two hardest jets) no longer need to balance in transverse momentum. Non back-to-back jets can of course also be produced if the scattered quark emits gluons after the hard collision. This means that, in the HCM frame, the dijet configuration is directly sensitive to the underlying QCD process.

The k_T-algorithm was originally constructed for the Breit frame (sometimes called the brick wall frame), defined by

$$P_\gamma + 2xP_p = 0.$$

In lowest order, the quark has a four-momentum xP_p, meaning that in the Breit frame the photon has exactly twice the four-momentum of the quark, but with opposite sign. The quark thus back-scatters, leaving the collision with the same four-momentum as it had before the collision, but in the opposite direction. The Breit frame and the HCM frame are very similar, in fact, they are only separated by a longitudinal boost. Since the k_T-algorithm used here is invariant under longitudinal boosts, it can also be applied in the HCM frame.

---

[5] In this thesis, variables in the HCM frame are labeled with a *.

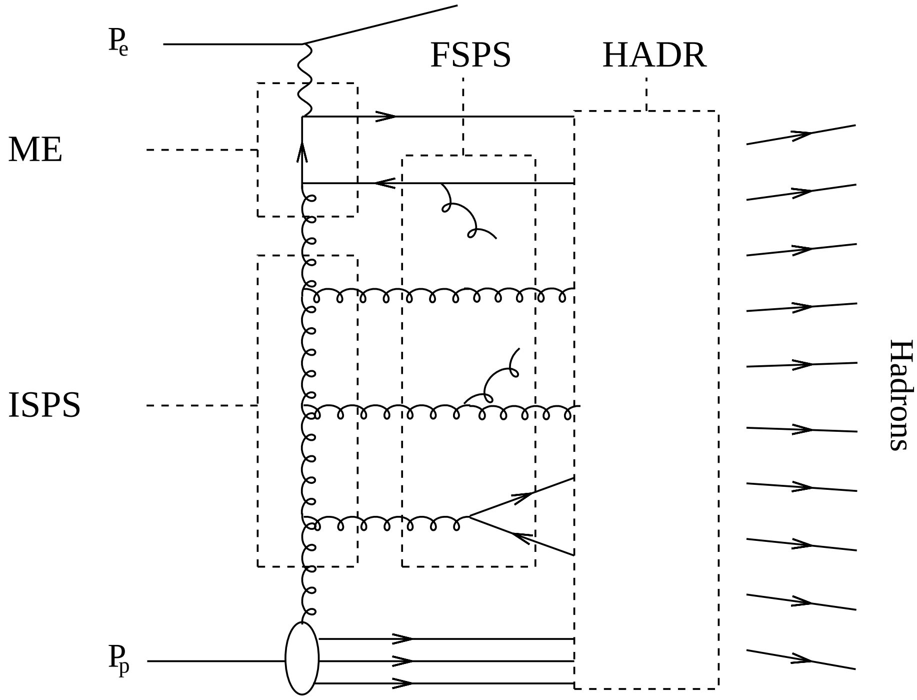

Figure 1.14: *A schematic picture showing the separate parts describing a DIS event: Matrix Element (ME), Initial and Final State Parton Showers (ISPS, FSPS) and Hadronization (HADR).*

1.8 Monte Carlo Event Generators

The description of a DIS event may be separated in different parts such as the matrix element, initial and final state parton showers and hadronization, schematically shown in Figure 1.14. Monte Carlo (MC) Event Generators, in which all these parts are implemented and treated independently from each other, produce complete DIS events which can undergo the same analysis procedure as the data. In this way, one can study effects of using different evolution equations for parton showers, hadronization effects, the effects of using different quark masses and PDFs etc. Also, by running the simulated events through a detector simulation one can obtain detector correction factors which can be applied to data, see Section 4.2. Below, a short description of the MC generators used in this thesis is given. The parameters and the PDFs used in the MC generators are summarized Table 1.1.

RAPGAP

RAPGAP [63] uses LO matrix elements and evolves the parton ladder according to the LL DGLAP equation. QED radiation is included using HERACLES [64], while hadronization is made using the Lund string model as implemented in JETSET [65,66]. In addition, RAPGAP can simulate diffractive DIS and photoproduction events, and offers the possibility of using resolved photons in DIS.

CASCADE

The program CASCADE [67,68] uses the CCFM equation for producing the parton ladder, and thus uses (LO) off-shell ME and unintegrated parton densities. Presently, only gluon densities are used in the evolution. In addition to ep collisions, pp, $p\bar{p}$, γp and $\gamma\gamma$ collisions are implemented. JETSET/PYTHIA [69] is used for hadronization. In this analysis, two different unintegrated gluon densities are used: A0 [70] and J2003 set2 [71]. They have been fitted to the same F_2 data and describe these data equally well. However, they differ on a number of points, e.g. that A0 was evolved using a splitting function including only the singular terms, see Equation (1.20), while for J2003 set2 also non-singular terms were included [71, 72]. In addition, they have slightly different starting distributions and treat the soft regions differently, see Chapter 5.

ARIADNE
ARIADNE [73] simulates parton showers according to the colour dipole model. While the QCD-C process is naturally included in the model, the BGF matrix element is included explicitly. ARIADNE needs to be used in combination with another MC program, for example RAPGAP or LEPTO, which takes care of the hard interactions, hadronization etc.

LEPTO
LEPTO [74] generates LL Parton Showers according to the DGLAP equation convoluted with LO matrix elements, while JETSET is used for hadronization. LEPTO also includes options for producing rapidity gaps without pomeron exchange. QED corrections are however not included, but can be taken into account using DJANGO [75], which is an interface between LEPTO and HERACLES.

PHOJET
The PHOJET [76, 77] generator is in this thesis used for simulating photoproduction events, in order to estimate the background contribution from such processes. PHOJET also includes hadron-hadron, photon-hadron and photon-photon processes, where the hadrons can be either protons, antiprotons, neutrons or pions.

1.9 Fixed Order QCD Calculations

In this thesis the measured data are compared to NLO 2-jet and NLO 3-jet calculations using the program NLOJET++ [78]. This program can be used to calculate LO 2-jet, NLO 2-jet, LO 3-jet, NLO 3-jet and LO 4-jet cross sections in DIS. Although it makes use of the Monte Carlo technique, it should not be confused with the Monte Carlo generators described previously. The NLO programs do not approximate higher order corrections using parton showers and do not include hadronization, but instead calculate the matrix elements of the LO and NLO processes in such a way that the infrared and virtual divergencies cancel.

1.9.1 LO 2-jet Cross Section

The diagrams contributing to the LO dijet cross section are shown in Figure 1.6. The QCD-Compton (QCD-C) process (Figure 1.6 (a)) is initiated by the quark densities in the proton, while the Boson Gluon Fusion (BGF) process depends on the gluon density. At small values of x the gluon density dominates the proton, meaning that the largest contribution to the LO dijet cross section comes from BGF. The matrix elements for BGF diverge if one of the partons is collinear to the initial gluon, or if one of the partons is

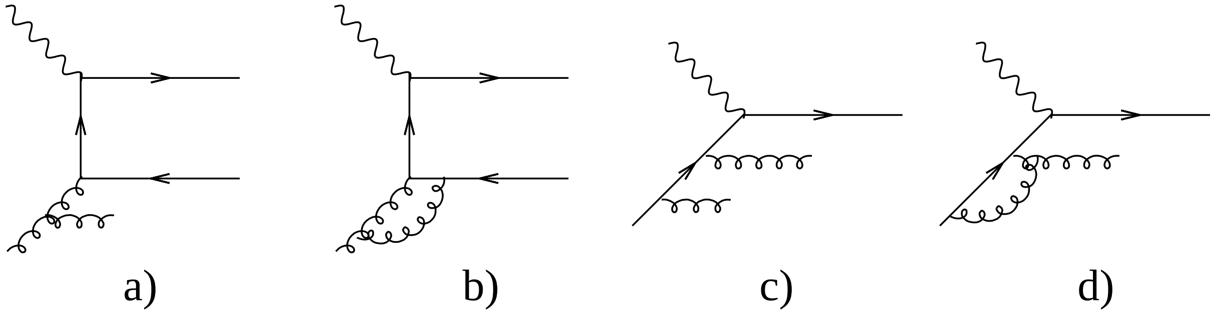

Figure 1.15: *NLO dijet cross section corrrections to BGF (a,b), and QCD-C (c,d).*

soft. Also the QCD-C ME is divergent if the emitted gluon is collinear to the incoming or scattered quark, or if one of the outgoing partons is soft. All these divergencies are, however, connected to the regions $E_T^* \to 0$ or $\eta^* \to \infty$, and can hence be avoided by requiring a minimum transverse momentum $E_T^* > 0$ for the partons. Because of energy and momentum conservation, the two outgoing partons will be emitted back-to-back in the HCM frame ($\Delta\phi^* = 180°$).

1.9.2 NLO 2-jet Cross Section

In next-to leading order, the dijet cross section includes contributions from additional real and virtual gluons; four examples are shown in Figure 1.15. Separately, these diagrams diverge. The virtual contributions diverge because the momenta of the virtual gluons can take any value, and the real contributions diverge when the gluons are either collinear with one of the quarks, or when the gluon energy $E_g \to 0$. However, the divergencies from the virtual contributions exactly cancel the divergencies from the real contributions, leaving the resulting cross sections finite.

It has been shown [79–81] that this cancellation, however, is incomplete if one applies symmetric E_T^* cuts to the two jets. With symmetric cuts, one can have configurations where the two jets are back-to-back and have the same (but opposite) E_T^*. On the parton level this corresponds to two back-to-back partons, so any gluon radiation is excluded. If the two partons are slightly decorrelated, soft gluon radiation is allowed but kinematically constrained. As a consequence, some of the contribution from the virtual diagram that should have been cancelled by the real diagram is left uncancelled. This leads to unphysical behaviour, e.g. that the dijet cross section with symmetric cuts, $E_{T1}^*, E_{T2}^* > E_{T,MIN}^*$, is smaller than the dijet cross section with asymmetric cuts $E_{T1}^* > E_{T,MIN}^* + \Delta$ and $E_{T2}^* > E_{T,MIN}^*$ for small values of Δ (in [12, 80] this was shown to be true for $\Delta < 1$ GeV) even though the phase space is larger for the case with symmetric cuts. Of course, this behaviour is not seen for the measured data. The remedy for this is, from the theoretical side, to perform a full resummation of the cross section, or, from the experimental side, to apply an asymmetric cut such that the NLO 2-jet cross section calculation gives resonable results [82, 83]. However, it has been argued [84] that even asymmetric cuts will not be sufficient to completely solve this problem. In this analysis, symmetric cuts have been applied because NLO dijet cross section calculations including full resummation have recently been performed for the first time [81].

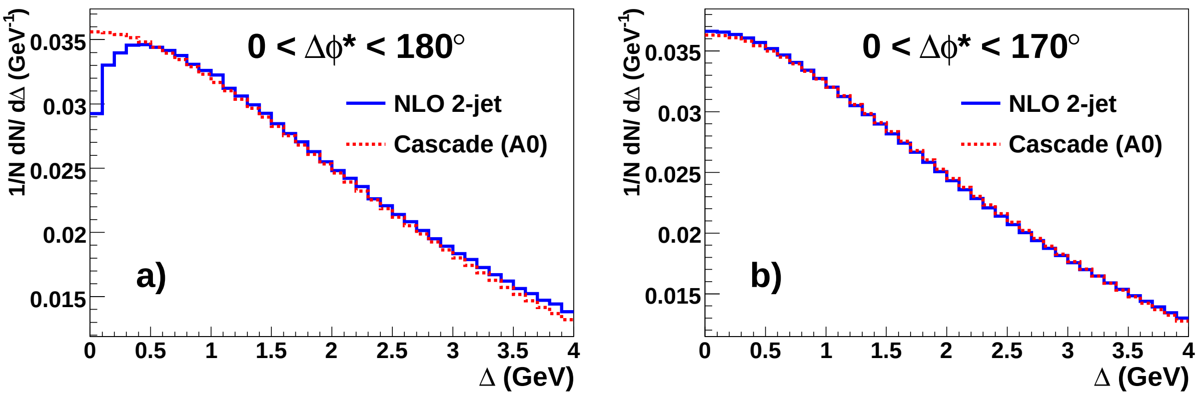

Figure 1.16: *The figure shows an NLO 2-jet calculation of the number of dijet events with jet cuts* $E^*_{T1} > (5 + \Delta)$ *GeV and* $E^*_{T2} > 5$ *GeV as a function of* Δ *compared to the prediction of* CASCADE *for (a)* $0 < \Delta\phi^* < 180°$ *and (b)* $0 < \Delta\phi^* < 170°$. *The distributions are normalised to the total number of dijet events.*

The NLO 2-jet cross section will, however, not be calculated correctly by the NLOJET++ program if symmetric cuts are applied. This will only be a problem in the bin $170 < \Delta\phi^* < 180°$, where the two jets are back-to-back, since for smaller $\Delta\phi^*$ we have an implicit asymmetric cut on the jets. Hence, for $\Delta\phi^* < 170°$ the NLO 2-jet cross section will not suffer from these incomplete cancellations. This problem is illustrated in Figure 1.16 where the number of dijets as a function of Δ, defined above, has been calculated in NLO and using CASCADE in the angular ranges $0 - 180°$ and $0 - 170°$, respectively.

1.9.3 NLO 3-jet Cross Section

The NLO 3-jet cross section is calculated by using the diagrams in Figure 1.17 (here, only the BGF diagrams are shown). In the leading order diagram, Figure 1.17 (a), there are three hard partons which could produce three jets in the final state, and in (b) and (c) this diagram is corrected with a soft or virtual gluon.

Additional complications arise when calculating NLO 3-jet cross sections but only demanding two jets, as done in this analysis. The problematic configuration is when we have two hard jets which are back-to-back in ϕ^*, i.e. $\Delta\phi^* \approx 180°$. Here, any additional gluon is forced to be soft, giving an infrared divergence. This divergence should be cancelled by the diagram with two virtual gluons shown in Figure 1.18. This, however, is not included in the NLO 3-jet calculation (had it been included, it would be a NNLO 2-jet calculation) which thus diverges in this phase space region.

The NLO calculations are made on the parton level, i.e. the particles involved are quarks and gluons. To be able to compare with data, one must either correct the calculations for hadronization effects and the data for detector effects and QED radiation, so that both the calculations and the data are given on the hadron level, or correct the data for hadronization effects so that the measurement is presented on the parton level. In this analysis, the data are corrected to the hadron level, and the NLO calculations are thus

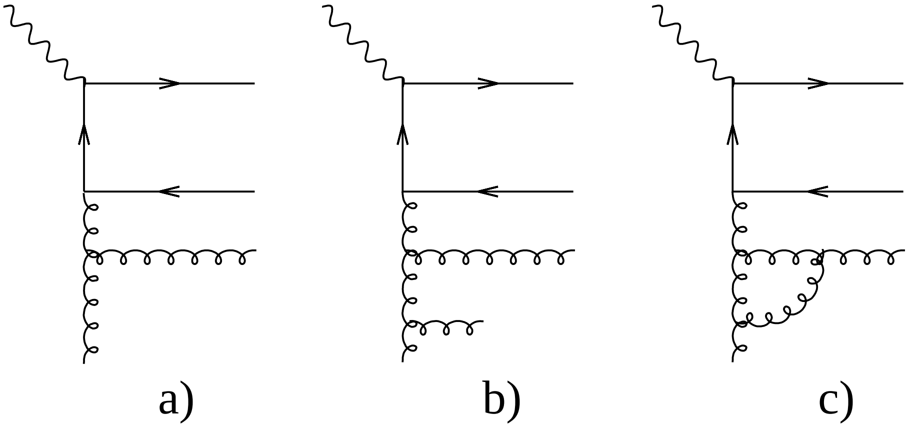

Figure 1.17: *Diagrams contributing to the NLO 3-jet cross section: leading order (a), and NLO corrections (b) and (c).*

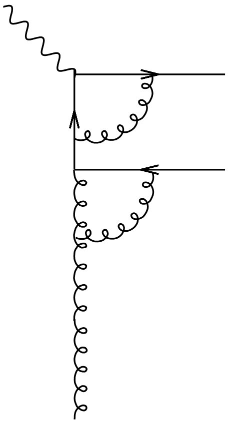

Figure 1.18: *Example of a virtual correction included in a NNLO 2-jet calculation, but not in the NLO 3-jet calculations.*

corrected for hadronization effects. This is done using Monte Carlo event generators, by simulating events with and without fragmentation/hadronization and taking the ratio of these as a correction factor applied to the NLO calculations,

$$C_{Hadr} = \frac{\sigma_{Hadr}}{\sigma_{NoHadr}}.$$

	LEPTO/ARIADNE	CASCADE	RAPGAP	NLOJET++
Version	6.51/4.10	1.2007	3.1	2.0
Parameters	Tuning from [85]	Default	Default	–
Proton PDF	CTEQ6L [86]	A0 J2003 set2	CTEQ6L	CTEQ6M [86]
Photon PDF	–	–	SaS-G 1D [87] (RES only)	–
μ_r^2	P_T^2	$\hat{s}+ < P_{T,Dijets}^2 >$	$Q^2+ < P_{T,Dijets}^2 >$	$\left(\frac{P_{T,1}+P_{T,2}}{2}\right)^2$
μ_f^2	P_T^2	$\hat{s} + Q_t^2$	$Q^2+ < P_{T,Dijets}^2 >$	$\left(\frac{P_{T,1}+P_{T,2}}{2}\right)^2$

Table 1.1: *Summary of the parameters and the PDFs used in the Monte Carlo event generators and the fixed order calculations in this analysis.* $< p_{T,Dijets}^2 >$ *is the mean squared transverse momentum of the dijet system from the matrix element,* Q_t *is the vectorial sum of the transverse momentum of the quark pair, while* $P_{T,i}$ *denote the transverse momentum of the selected jet* i.

1.10 Azimuthal Correlations in Dijet Events

In the HCM frame, the photon and the proton collide head-on. Using collinear factorization, the interacting gluon in the leading order BGF process will not have any transverse momentum k_T, which means that the photon and the gluon collide head-on. Due to energy and momentum conservation, the two outgoing quarks will be emitted back-to-back, i.e. with $\Delta\phi^* = 180°$. In higher order processes, the outgoing quarks can emit final state radiation, leading to a decorrelation of the produced jets ($\Delta\phi^* < 180°$). Configurations with $\Delta\phi^* < 180°$ can also occur when the interacting gluon emits initial state radiation, and thereby acquires a transverse momentum. The azimuthal angle $\Delta\phi^*$ between the two jets is related to the transverse momentum k_T of the interacting gluon according to

$$k_T^2 = P_{T,1}^{*2} + P_{T,2}^{*2} + 2P_{T,1}^*P_{T,2}^*cos(\Delta\phi^*),$$

where $P_{T,i}^*$ is the transverse momentum of the jets $i = 1, 2$ in the HCM frame.

In the DGLAP approximation, the propagator gluons are ordered in virtuality, leading to an ordering in transverse momentum

$$\mu_f^2 \gg |k_{Tn}^2| \ldots \gg |k_{T1}^2| \gg |k_{T0}^2| \tag{1.22}$$

as described in Section 1.5. The k_T of the interacting gluon is thus restricted by μ_f. In BFKL and CCFM, there is no such restriction, since the propagator gluons are ordered in x and ξ, respectively. The gluons can in these evolution schemes have any kinematically allowed k_T, leading to more decorrelation of the dijets, on the average, compared to

DGLAP. A measurement of the azimuthal correlations in dijet events could thus be sensitive to different parton dynamics in the initial state cascade. Also, in the k_T-factorization approach the interacting gluon can have a non-zero k_T already in leading order, since unintegrated PDFs are used. This means that the azimuthal correlations are sensitive to different uPDFs, and may be used to further constrain the intrinsic k_T distribution of the gluons.

Dijet azimuthal correlations has been measured previously in ep-collisions [12, 88, 89] and in $p\bar{p}$-collisions [90, 91]. For theoretical discussions, see e.g. [92–107].

Chapter 2

HERA and the H1 Experiment

This chapter gives an introduction to the HERA facility and presents an overview of the H1 detector and its components, especially those important for the analysis presented in this thesis.

2.1 The HERA Collider

The HERA collider, situated at the DESY research laboratory in Hamburg, Germany, is the only electron-proton collider in the world, and with a circumference of 6.3 km it is also one of the largest accelerators existing. It consists of two separate storage rings, accelerating electrons/positrons and protons to 27.6 GeV and 920 GeV, respectively. This corresponds to a center of mass energy $\sqrt{s} \approx 318$ GeV. Before 1998, the proton beam energy was 820 GeV. A schematic view of the HERA facility is shown in Figure 2.1. Also shown is the system of pre-accelerators used to produce and accelerate the electron- and proton bunches before they are injected in HERA. During data taking, there are up to 220 bunches colliding with 96 ns intervals, giving a bunch crossing rate of 10.4 MHz.

HERA hosts three experiments: H1, ZEUS and HERMES, which are situated in the North, South and East Hall, respectively. H1 and ZEUS are collider experiments with main physics interests of measuring the proton structure, investigating the properties of QCD and searching for new physics. HERMES, however, uses only the (polarized) electron beam on a polarized gas target (H_2, D, ^3He, ^4He) which is injected into the beampipe. The main objective concerns the spin properties of the proton. Until 2003, a fourth experiment, HERA-B, operated in the West Hall. HERA-B was designed to study B-physics and especially the CP violation in B-decays, and used the proton beam on a fixed wire target.

After more than 15 years of operation, HERA was shut down on June 30, 2007.

2.2 The H1 Experiment

The H1 detector, shown in Figure 2.2, is designed to measure the energy and momentum of the final state particles from the electron-proton interactions. It consists of layers of

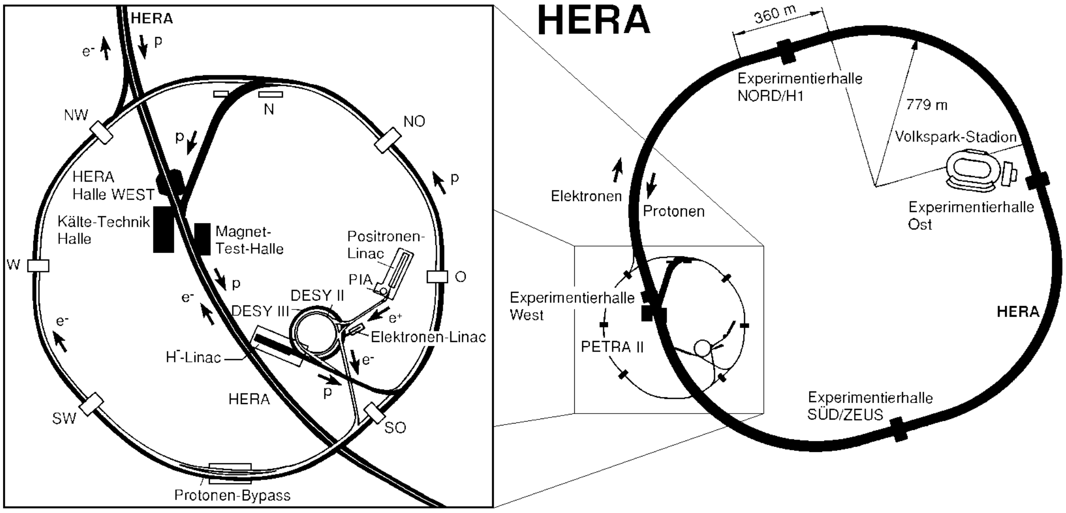

Figure 2.1: *A schematic view of the HERA facility (right), also showing the system of pre-accelerators (left).*

detector components positioned concentrically around the beampipe $\boxed{1}$. Surrounding the interaction point are the tracking detectors $\boxed{2}$ which enable momentum measurements of charged particles travelling in the 1.15 T solenoidal magnetic field provided by the superconducting coil $\boxed{6}$. (Another superconducting coil $\boxed{7}$ compensates for this field such that the beam is not distorted.) Next, there are the electromagnetic $\boxed{4}$ and hadronic $\boxed{5}$ Liquid Argon (LAr) calorimeters measuring the total energy of the particles. Some particles, mostly muons, may escape the inner parts of the detector and enter the muon chambers $\boxed{9}$ and the instrumented iron $\boxed{10}$ in which energy leakage from the LAr calorimeter may be detected.

Because of the asymmetric energies of the electron and proton beams, the center of mass will be boosted in the proton direction, which also defines the z-direction in the righthanded H1 coordinate system, giving more activity in this region. Therefore, the detector has finer granularity and more detector components in the forward (proton) direction. The backward (electron) direction is covered by the Spaghetti Calorimeter (SPACAL) $\boxed{12}$, making electron tagging at larger angles possible.

In the following subsections, the detector components relevant for this thesis will be described. A detailed description of the H1 detector can be found in [108, 109].

2.2.1 The Tracking System

The tracking system, shown in Figure 2.3, consists of three major components: the Central Tracking Detector (CTD), the Forward Tracking Detector (FTD) and the Backward Drift Chamber (BDC). Three kinds of detector types are used: drift chambers, Multi-Wire Proportional Chambers (MWPC) and semiconductors. The drift chambers provide precision measurements of tracks and, since the particle trajectories are bent in the magnetic field, the transverse momenta and charges of the particles can be determined from the curvature of these tracks. The MWPCs have worse spatial resolution than the drift chambers, but are

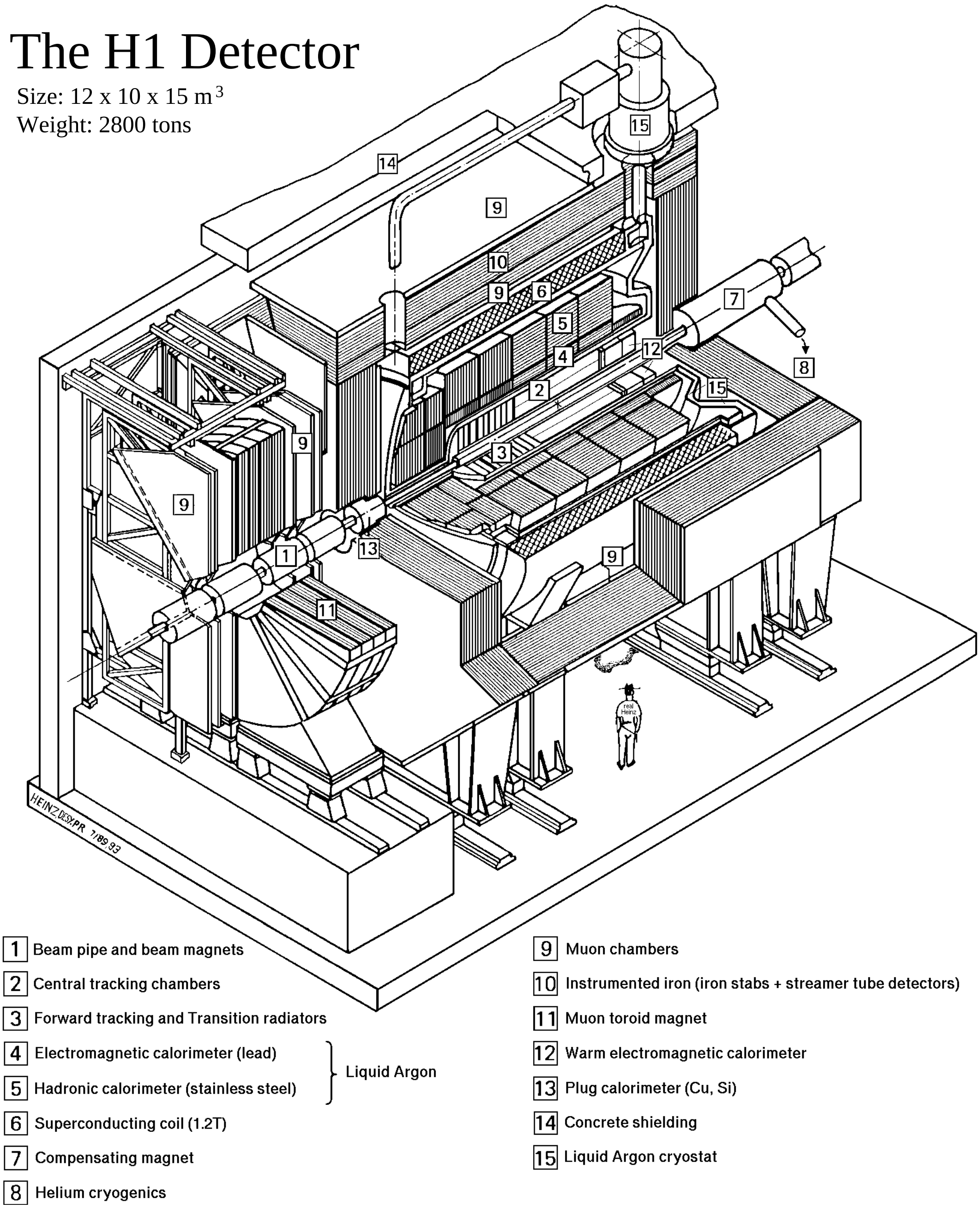

Figure 2.2: *A schematic view of the H1 detector.*

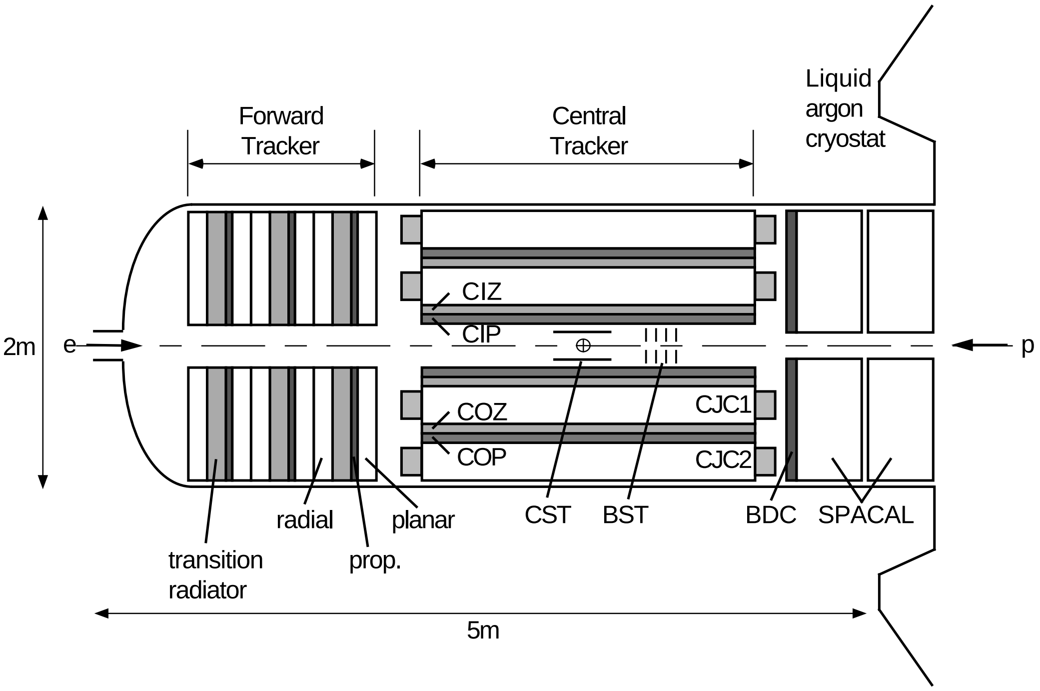

Figure 2.3: *A side view of the tracking system in the H1 detector. Also shown is the SPACAL calorimeter.*

instead faster, and are therefore suitable for triggering purposes. Semiconductors, which are used in the central (CST) and backward (BST) silicon trackers are more accurate than both the drift chambers and the MWPCs. On the other hand, they are much more expensive, and thus only used in a small volume close to the beampipe. The silicon trackers are essential components when identifying secondary vertices from the decay of short-lived particles.

The Central Trackers

The main detectors of the central tracking system are the two Central Jet Chambers, CJC1 and CJC2. These two drift chambers, covering polar angles of $11 < \theta < 169°$ and $26 < \theta < 154°$ respectively, have anode sense wires[1] in the z-direction and by measuring the drift time, a resolution of 170 μm in the (r,ϕ) plane is achieved. The z coordinate can be determined with a resolution of about 22 mm from the ratio of the measured charges at both ends of the sense wires (charge division method).

Two other drift chambers, the Central Inner and Outer z-chambers (CIZ and COZ) have wires perpendicular to the beam axis, giving a z coordinate resolution of 300 μm and a resolution of about 30-60 mm in the (r,ϕ) plane. Using the complementary information from the CJC1, CJC2, CIZ and COZ, one can achieve a momentum resolution of

$$\frac{\sigma_p}{p^2} < 0.01\ \mathrm{GeV}^{-1}.$$

The Central Inner and Outer Proportional chambers (CIP and COP) are used for a fast

---

[1] CJC1 and CJC2 have 720 and 1920 sense wires, respectively.

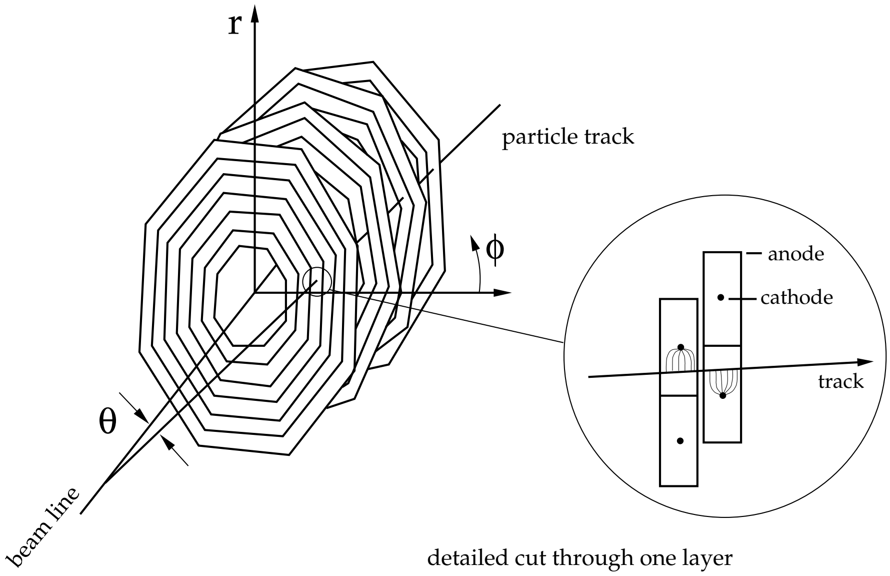

Figure 2.4: *The backward drift chamber consists of four octagonal double-layers (left), where the drift cells of the two layers are staggered by half a drift distance (right).*

determination of the interaction time and the position of the z-vertex. This information is used by the first level trigger system (see Section 2.2.5).

The Backward Drift Chamber
The Backward Drift Chamber (BDC) covers the polar angle region $153 < \theta < 178°$ and, in this analysis, is used for determining the azimuthal and polar angles of the scattered electron (ϕ_e and θ_e). As seen in Figure 2.4, the BDC consists of four octagonal double-layers with wires perpendicular to the radial vector. This allows a precise determination of the polar angle; the resolution is $\sigma_\theta < 1$ mrad. Each layer is rotated 11.25° in ϕ with respect to the next one, which gives a spatial resolution in the $r-\phi$ -plane $\sigma_{r-\phi} = 0.8$ mm. The drift cells are shifted by half a drift cell to resolve left-right ambiguities.

The Forward Trackers
Particle tracking in the forward region is managed by the forward trackers, which cover the polar angles $5 < \theta < 25°$. Like the central tracking system, the FTD consists of both drift chambers and MWPCs. The FTD is split up in three identical layers, each one consisting of two drift chambers, one MWPC, used for triggering, and one transition radiation detector. One of the drift chambers has wires parallel to each other and perpendicular to the beampipe (called planar in Figure 2.3) and one has wires strung radially. The obtained momentum resolution is $\frac{\sigma_p}{p^2} = 0.03$ GeV^{-1} while the spatial resolution is $\sigma_{x,y} \leqslant 200\mu$m.

2.2.2 Calorimeters

The Liquid Argon Calorimeter
Most particles except muons, neutrinos and most of the beam remnant are absorbed in the LAr calorimeter (Figure 2.5), covering polar angles $4 < \theta < 154°$. It consists of an electromagnetic part, with a thickness of 20-30 radiation lengths, and an hadronic part,

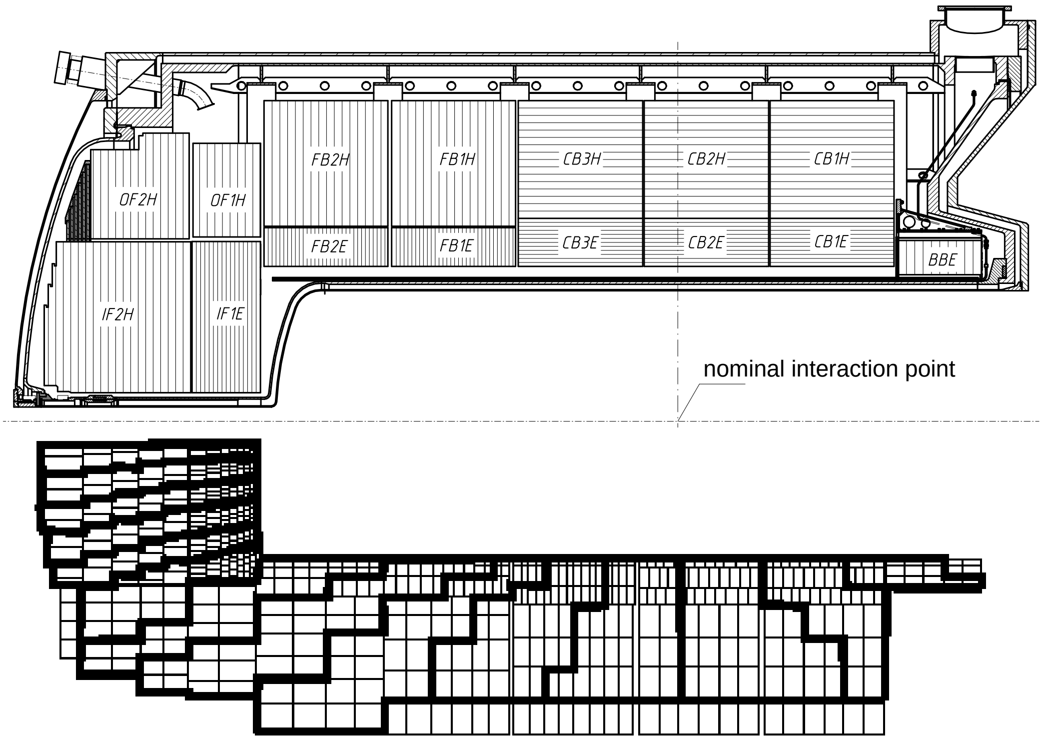

Figure 2.5: *A side view of the Liquid Argon calorimeter, showing the absorber plate structure (upper) and the cell structure and the Big Tower segments used for triggering (lower).*

4.7-8 nuclear interaction lengths thick, depending on the impact angle of the particle. In both parts, liquid Argon is the active material, while lead and iron are used as passive materials in the electromagnetic and hadronic part, respectively. The LAr calorimeter is further split up into 8 wheels which in turn consists of individual cells. In total, there are 45000 cells with dimensions $4 \times 4 \times 4$ cm^3 and $10 \times 10 \times 10$ cm^3 in the electromagnetic and hadronic part, respectively. The achieved electromagnetic resolution is

$$\frac{\sigma_{em}}{E} \approx \frac{0.11}{\sqrt{E[\text{GeV}]}} \oplus 0.01 \tag{2.1}$$

while the hadronic energy resolution is

$$\frac{\sigma_{had}}{E} \approx \frac{0.5}{\sqrt{E[\text{GeV}]}} \oplus 0.02, \tag{2.2}$$

where $\oplus$ means addition in quadrature.

The Spaghetti Calorimeter

The SPACAL, using scintillating fibres and lead as active and passive material, respectively, covers polar angles $153 < \theta < 178°$ and can therefore be used for detecting the scattered electron in events with $1 \lesssim Q^2 \lesssim 100$ GeV^2. Like the LAr calorimeter, the SPACAL consists of an electromagnetic and an hadronic part, both 25 cm thick, corresponding to 28 radiation lengths and 2 interaction lengths, respectively. This makes it possible to effectively separate electrons from pions, which otherwise may be misidentified as the scattered electron, see

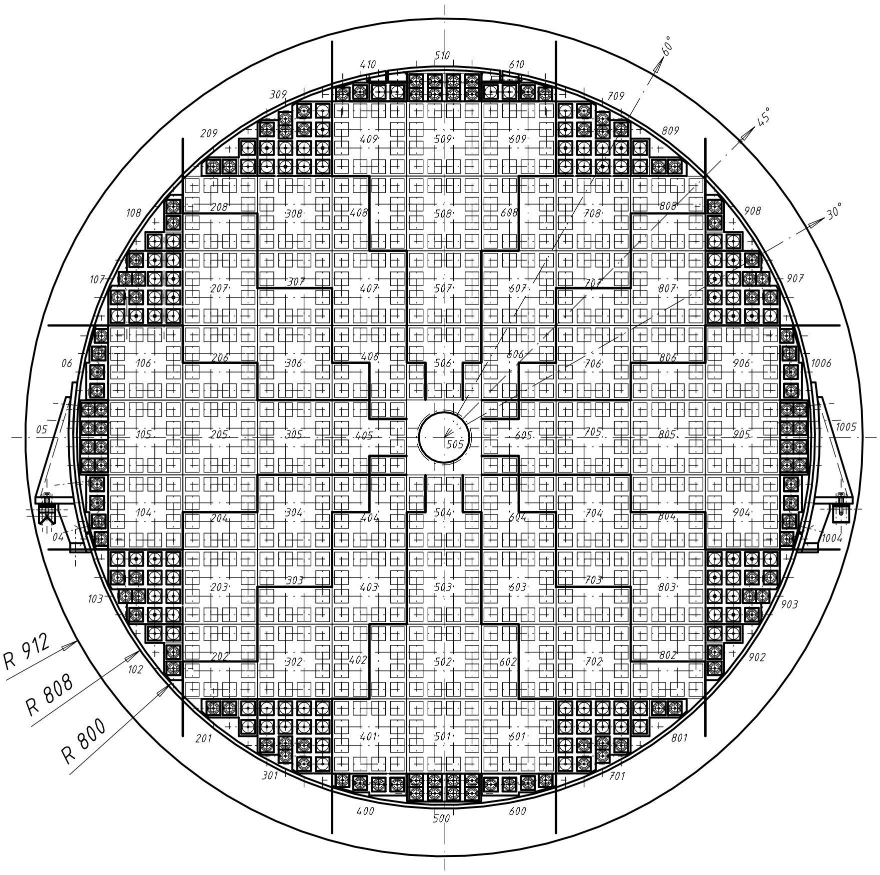

Figure 2.6: *A cross-section of the electromagnetic part of the SPACAL. Also shown are the supermodules, with 4 × 4 cells in each, and the VETO layers (the white area surrounding the beam pipe).*

Section 3.2.4. The electromagnetic part consists of 1192 cells, $4.05 \times 4.05 \times 25$ cm^3, while the hadronic part has 136 cells, $12 \times 12 \times 25$ cm^3, see Figure 2.6. Also shown in the figure are the supermodules, consisting of 4×4 cells, and the VETO layer close to the beam pipe. High activity in this layer indicates that some energy may have leaked out of the detector, meaning that the energy measurement may be wrong. The obtained energy resolutions are

$$\frac{\sigma_{em}}{E} \approx \frac{0.07}{\sqrt{E[\mathrm{GeV}]}} \oplus 0.01$$

and

$$\frac{\sigma_{had}}{E} \approx \frac{0.56}{\sqrt{E[\mathrm{GeV}]}}.$$

2.2.3 The Time of Flight System

The Time of Flight (ToF) system is used for rejecting background events, originating from beam interactions with gas in the beam pipe (the vacuum in the beam pipe is $\sim 10^{-10}$

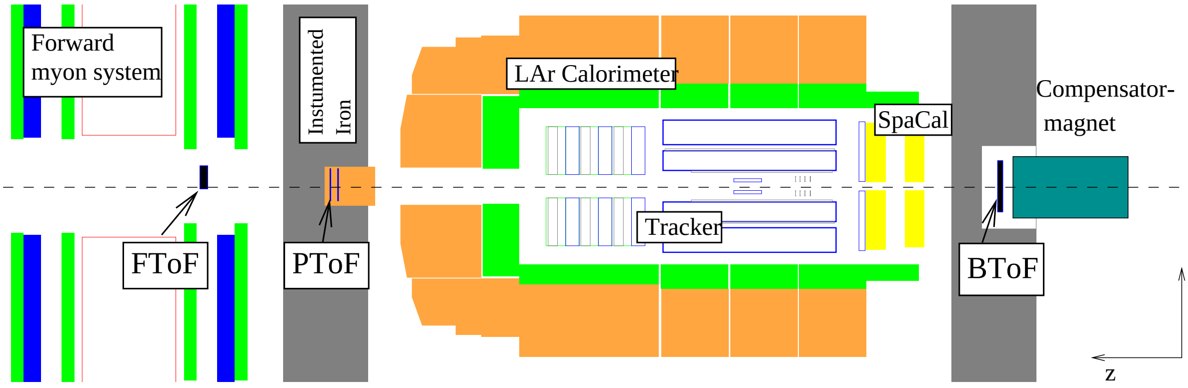

Figure 2.7: *A schematic zy-view of the H1 detector, indicating the position of the Backward (BToF), Forward (FToF) and Plug (PToF) Time of Flight systems.*

kPa) and with the beam pipe itself. It consists of three scintillators (Backward, Forward and Plug ToF at $z = -275$ cm, $z = 790$ cm and $z = 540$ cm, respectively, see Figure 2.7) and two scintillator veto walls ($z = -810$ cm and $z = -650$ cm), giving a time resolution of about 1 ns. Using this information together with knowledge of the exact bunch crossing rate, one is able to reject events outside the time window characteristic for e-p collisions.

2.2.4 The Luminosity System

The luminosity system, shown in Figure 2.8, measures the rate of the Bethe-Heitler process $ep \rightarrow ep\gamma$, and since the cross section of this process is very accurately known, one indirectly measures the luminosity. The electrons, having lost some energy in the process, are deflected by a bending magnet and escapes the beam pipe through a window at $z = -27.9$ m, thus hitting the Electron Tagger (ET) at $z = -33.4$ m. The photons leave the beampipe at $z = -92.3$ m, where the beam pipe bends upwards, and hit the Photon Detector (PD) located at $z = -102.8$ m. In front of the PD is a lead Filter (F), protecting the PD from synchrotron radiation, and a Veto Counter (VC) which makes it possible to determine whether the photon has showered in the lead filter. Using this technique, the luminosity during 1999-2000 has been determined with a precision of 1.5%.

2.2.5 The Trigger System

Although the bunch crossing rate at HERA is about 10.4 MHz, the rate of e-p interactions is much smaller. However, the rate of background events, originating from beam-gas and beam-wall interactions, from synchrotron radiation and from cosmic radiation, is several orders of magnitude larger than the e-p event rate. Reading out the whole detector for each event and then selecting the “good” events would result in a very large dead time. Instead, a four level trigger system is used for filtering out the actual e-p events from the background using increasingly sophisticated methods, thus minimizing the dead time.

Level 1
The first level in the trigger system uses 192 trigger elements combined into 128 subtriggers.

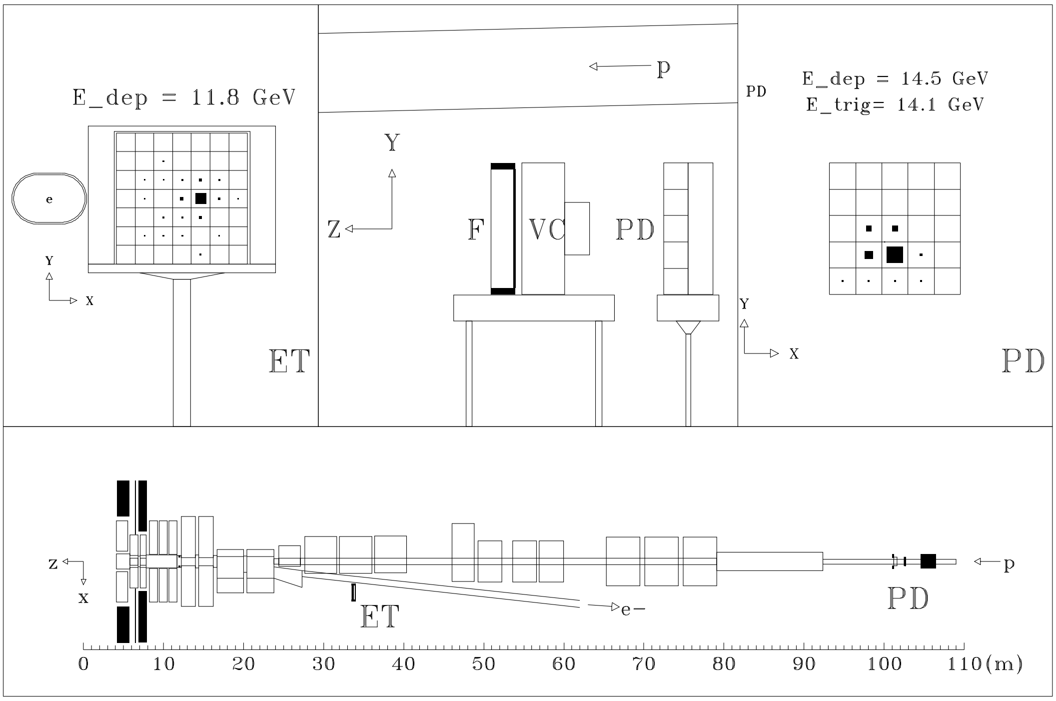

Figure 2.8: *A schematic view from above of the beam transport system and the luminosity monitor (lower figure), showing the position of the Electron Tagger (ET) and the Photon Detector (PD) with respect to the electron and proton beam pipes. Note that the proton beam pipe bends upwards, as can be seen in the figure on top in the middle. In the top left figure, energy depositions in the ET of a typical Bethe-Heitler process is shown. Also indicated is the electron beam pipe. The top right figure shows the energy depositions in the PD of the same event. The top middle figure shows a side view of the PD system, where VC and F stands for the Veto Counter and the lead Filter, respectively. Also shown is the proton beam pipe which bends slightly upward.*

A trigger element may for example be an energy deposition above some threshold in the SPACAL, a reconstructed z-vertex or a ToF requirement. If one of the 128 subtriggers has triggered, the event is kept and passed on to Level 2. However, some subtriggers have a very high trigger rate and must be prescaled, i.e. some triggered events are rejected while the events that are kept are given a weight. The Level 1 trigger system makes the decision to keep or reject the event within 2.3 μs, corresponding to 24 bunch crossings, and reduces the rate from about 100 kHz to 1 kHz. In order to avoid a large dead time, the events from the following bunch crossings are fed into pipelines, until a decision has been made.

Level 2
With a decision time of 20 μs, a more sophisticated analysis of the event can be made at Level 2. Here, two different trigger methods are used: neural network and topological triggers. If the event is kept, a full readout of the detector starts and the event is passed on to Level 3. However, Level 3 was not implemented during the HERA I running period (1992-2000) so the event is therefore passed on directly to Level 4. The typical output rate of Level 2 is 50 Hz.

Level 4
At this level, the full information of the event is used and a fast online reconstruction of the event is performed. Here, the L1 and L2 triggers are verified, and if possible the event is assigned to one or more event classes, e.g. “Electron in SPACAL” or “Jets ($E_T > 5$ GeV)”. If it is not possible to assign the event to a class, the event is either rejected or downscaled. If the triggering of the previous levels can be verified, the output is written to tape and the event is passed on to Level 5. Maximal decision time is 100 ms and the output rate is typically 10 Hz.

Level 5
At Level 5, a complete (offline) reconstruction of the event is made and the event is compressed and written to Data Summary Tapes (DST), which are used for further analyses.

2.3 Combined Objects

The hadronic final state is reconstructed using the complementary information from the trackers and the calorimeters according to the HADROO2 algorithm [110]. First the algorithm selects tracks, removes clusters which are identified as noise and (temporarily) removes tracks and clusters which are associated with leptons. Then the first track in the list (the one with lowest p_T) is extrapolated into the calorimeter. Clusters in the electromagnetic (hadronic) part that lie within a cylinder of radius 25 cm (50 cm) from the track extrapolation are matched to the track. The algorithm then compares the energy resolution of the track obtained from the tracker (assuming that the particle is a pion) and the expected energy resolution of the calorimeter using Equation (2.2), assuming the same energy in the calorimeter as obtained from the measurement on the track. The information which is expected to have the smallest uncertainty is then used to compute the four-vector of the combined object. The track and the matched clusters are removed in order to avoid double counting, and the next track in the list is extrapolated. If there are still clusters left after all the tracks have been extrapolated, HFS objects are defined using these clusters. Since the energy resolution of the tracks decreases with increasing p_T, and the energy resolution of the calorimeters increases with increasing E, the track information is mostly used for $E \lesssim 25$ GeV while the calorimeter is used for $E \gtrsim 25$ GeV (these numbers are for central tracks with $20 < \theta < 160°$).

The HADROO2 method described above uses the track information more often than the FSCOMB algorithm previously applied in H1 [111]. This can be seen by sorting the combined objects in each jet depending on if it is treated as a track or a cluster, calculating the scalar P_T sum of these combined objects and then forming the P_T fractions $P_{T,track}/P_{T,Jet}$ and $P_{T,cluster}/P_{T,Jet}$. In Figure 2.9, this P_T fraction is shown as a function of $P_{T,Jet}$ and η_{Jet} for Monte Carlo events simulated by DJANGO(CDM) and reconstructed using HADROO2 and FSCOMB, respectively. As can be seen, the track information is used for about 60% of the combined objects in a jet in the HADROO2 algorithm, while it is less than 40% when using FSCOMB. This fraction decreases with increasing P_T in agreement with the fact that the uncertainty in the track energy increases with increasing P_T of the track. It is interesting to note that the track fraction decreases more in the FSCOMB scheme compared to HADROO2. Also, the track P_T fraction decreases dramatically in the forward direction (large η_{Jet}) due to the low efficiency of the forward tracker during 1999-2000. The more frequent use of the track information in HADROO2 results in better resolutions of the jet observables compared to FSCOMB (see Figure 4.51).

2.4 Detector Simulation

The response of the H1 detector to an event can be simulated using H1SIM [112], which is based on GEANT [113]. H1SIM includes detailed information about the detector and its components, such as resolutions, inefficiencies, dead material and the exact position of each subdetector. The unfolding of the data can then be performed by using Monte Carlo generated events as input to H1SIM.

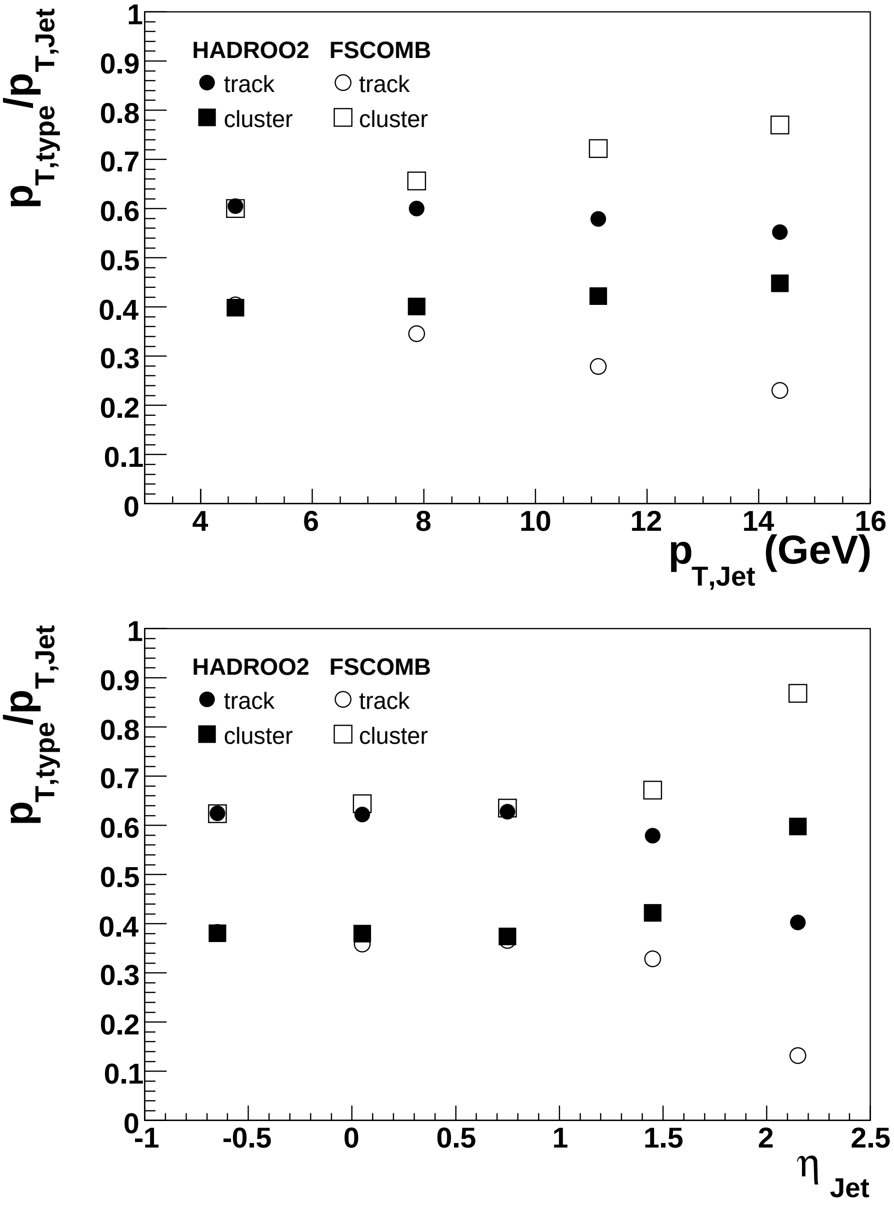

Figure 2.9: *The P_T fraction of combined objects treated as tracks and clusters, as a function of P_T and η of the jet using the FSCOMB and HADROO2 algorithms, respectively.*

Chapter 3

Event Selection and Reconstruction

This chapter presents the selection of runs, DIS events and dijet events. Also, the quality of the DIS and dijet samples are investigated.

3.1 Run Selection

In this analysis, the e^+p data collected by the H1 detector during 1999-2000 are used, corresponding to a luminosity of 64.3 pb^{-1}. The events are grouped into different runs, during which experimental conditions, such as subdetector High Voltage (HV) status, are relatively unchanged. Run conditions may, however, change slightly during a run period. There can for example be a sudden drop of HV for a detector component. For a run to be included in this analysis, it is demanded that the HV is on for the following subdetectors: LAr, SPACAL, CJC1, CJC2, CIP, COP, BDC, ToF and the Luminosity system. Runs with a total luminosity < 0.1 nb^{-1} are rejected, since this is an indication of unstable run conditions. Some runs with poor run quality and shifted z-vertex are also excluded. After this run selection, $3.8 \cdot 10^8$ events remain.

3.2 DIS Selection

The selection of DIS events is almost completely based on a determination of the kinematics from the scattered electrons. However, other cuts also need to be made in order to suppress background and exclude data from non-functioning parts of the detector.

3.2.1 Trigger

As already mentioned in Section 2.2.5 only events satisfying certain trigger conditions are read out and analysed. In the analysis presented here, the events must fulfill the requirements of the S0||S61 triggers, where || means a logical OR. S0 and S61 are defined as

S0 = (SPCLe_IET > 2) && BG
S61 = (SPCLe_IET > 2 || SPCLe_IET_Cen_3) && DCRPh_THig && zVtx_sig && BG

where && means a logical AND. The main trigger element for the S0 trigger is the SPCLe_IET > 2 element, which requires an energy deposition with an energy $E > 6$ GeV in one of the outer[1] SPACAL trigger towers. A trigger tower consists of 4×4 cells, and there are 320 trigger towers, partly overlapping (sliding window method). In addition to this, S61 has also SPCLe_IET_Cen_3 which is similar to SPCLe_IET > 2 but for the central part of the SPACAL. The DCRPh_THig element triggers if there is at least one track candidate in the CJC with a transverse momentum $p_T > 800$ MeV, while zVtx_sig requires a signature for a z-vertex. BG is short for a collection of background rejection trigger elements. The S0 trigger, being very inclusive, triggers on DIS events in the region $1 \lesssim Q^2 \lesssim 100$ GeV^2 with a very high efficiency (the efficiency of the trigger selection is presented in Section 4.2). However, because of the high trigger rate S0 is assigned a large prescale factor, which means that some of the triggered events are not read out, while the events that are read out are weighted. This means a loss in statistics. By combining the S0 trigger with the more exclusive (and less efficient) S61 trigger, one selects some events which otherwise would not be analysed because of the high prescale of the S0 trigger. The mean prescales of the S0 and S61 triggers are 3.32 and 1.15, respectively, for the 1999/2000e^+ period.

Since two subtriggers are used, each one with its own prescale weight (which may change from run to run), one needs to combine these weights in such a way that no events are missed or double counted. If we define r_{ij} as the raw trigger bit for subtrigger i in event j, where r_{ij} can take the values 0 (event is not triggered) or 1 (event is triggered), and d_{ik} as the weight for trigger i in run k, then the probability that trigger i will actually trigger event j in run k is

$$P_{ijk} = \frac{r_{ij}}{d_{ik}}.$$

The probability that it does not fire is then $(1 - P_{ijk})$, and the probability that none of N triggers fires is

$$\prod_{i=1}^{N} (1 - P_{ijk}).$$

The probability that at least one of the N triggers fires is thus

$$P_{jk} = 1 - \prod_{i=1}^{N} (1 - P_{ijk})$$

and the weight of the event j in run k is

$$w_{jk} = \frac{1}{P_{jk}}.$$

However, by averaging over all runs in a run period (in this case all runs during 1999/2000) and taking the integrated luminosity $\int \mathcal{L}_k$ into account, the statistical uncertainties due to

---

[1] The SPCLe_IET trigger is divided into a central ((-16 $< x <$ 8 cm)&&(-8 $< y <$ 16 cm)) and an outer region.

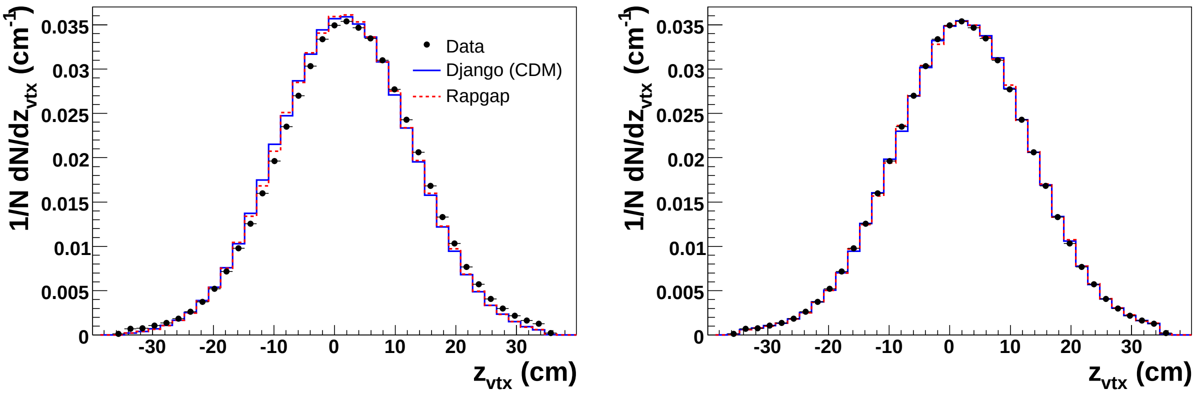

Figure 3.1: *The z-vertex distribution of the data compared to* Rapgap *and* Django(CDM) *before (left) and after (right) reweighting of the z-vertex in the Monte Carlo simulations.*

the changing trigger weights can be reduced. The weight for all events in the run period l will then be [114]

$$w_l = \frac{\sum_{k \in l} \int \mathcal{L}_k}{\sum_{k \in l} \int \mathcal{L}_k P_{jk}}.$$

3.2.2 Vertex Requirement

One of the basic requirements for reconstructing a DIS event is that there should be an interaction vertex reconstructed from tracks. Since the protons in a bunch are distributed according to a Gaussian ($\sim$ 11 cm wide) along the z-direction, it follows that most collisions take place around the nominal interaction point. However, beam-wall and beam-gas collisions will be evenly spread out along the beam direction. Also, electrons colliding with protons in the so-called satellite bunches (small clusters of protons not part of the main bunches) will produce z-vertices far from the nominal interaction point. In order to suppress such backgrounds a cut

$$-35 < z_{\text{vtx}} < 35 \text{ cm}$$

is made. In the MC files used for comparisons to data, the z-vertex was not correctly simulated, and therefore the MC events were reweighted using a polynomial function to fit the data, see Figure 3.1.

3.2.3 $\Sigma(E - p_z)$ Requirement

The sum of $(E - p_z)$ of the initial state particles i (i.e. the electron and the proton) can be written as

$$\begin{aligned} \sum_{i=e,p} E_i - p_{z,i} &= (E_e - p_{z,e}) + (E_p - p_{z,p}) = \\ E_e - (-E_e) + E_p - E_p &= 2E_e \end{aligned}$$

where $p_{z,e} = -E_e$ since the z-axis is defined as the direction of the incoming proton and the mass of the proton and the electron has been neglected. Because of energy and momentum conservation, the sum of $(E - p_z)$ over all final state particles j (including the scattered electron) should give the same result,

$$\sum_j E_j - p_{z,j} = 2E_e.$$

However, because of the limited resolution and acceptance of the detector, one will get a distribution around $2E_e \approx 55$ GeV, rather than a narrow peak. Final state hadrons are mainly lost in the beam pipe hole of the detector, but since these hadrons are close to the beam direction of the proton they only give a small contribution to $\sum_j E_j - p_{z,j}$. In photoproduction events, where the scattered electron leaves through the beam pipe, this sum will be significantly lower than expected. The same thing is true if the scattered electron radiates a highly energetic photon in the beam pipe. Such scenarios can to a large extent be cut away by requiring

$$35 < \sum_j E_j - p_{z,j} < 70 \text{ GeV}.$$

3.2.4 Selection of the Scattered Electron

To ensure that the scattered electron is within the acceptance of the SPACAL and the BDC, a requirement on the polar angle

$$156 < \theta_e < 175^\circ$$

is imposed.

In order to reduce background from photoproduction ($Q^2 \sim 0$ GeV^2), where the scattered electron escapes down the beampipe undetected and a hadron in the SPACAL may fake an electron signal, a cut on the energy of the scattered electrons

$$E_e^{'} > 9 \text{ GeV}$$

is applied. This background can be further suppressed by requiring the (energy weighted) cluster radius to be small,

$$R_{CLUS} < 3.5 \text{ cm},$$

since hadronic clusters are expected to be broader than electromagnetic ones. R_{CLUS} is defined by

$$R_{CLUS} = \frac{\Sigma_i E_i \sqrt{(x_{CLUS} - x_i)^2 + (y_{CLUS} - y_i)^2}}{E_{CLUS}},$$

where x_{CLUS}, y_{CLUS} and E_{CLUS} are the coordinates and energy of the cluster, respectively, and the sum runs over all cells i (with coordinates x_i, y_i and energy E_i) belonging to that cluster.

Also, since the electromagnetic part of the SPACAL is 28 radiation lengths thick, one expects that the scattered electron should be fully absorbed in the electromagnetic part.

Therefore, the energy in the hadronic part behind the electromagnetic cluster is required to fulfill

$$E_{HAD} < 0.5 \text{ GeV}.$$

There is, however, a possibility that a photon in the SPACAL together with a nearby track from a hadron in the BDC is misidentified as an electron. This background can be reduced by requiring the radial distance between the cluster center in the SPACAL and the extrapolated track in the BDC to be

$$\Delta R_{BDC} < 1.5 \text{ cm}.$$

To make sure that all of the scattered electron energy has been detected and that no energy has leaked out of the SPACAL, the energy in the VETO layers (see Section 2.2.2) is demanded to be small,

$$E_{VETO} < 1 \text{ GeV}.$$

3.2.5 Fiducial Cuts

During the 1999-2000 data taking period, some regions of the SPACAL suffered from high background radiation and dead cells. This was not included in the detector simulation, and therefore the following regions had to be excluded:

$$\begin{array}{ccccccccccccccc}
 & x_{SPAC}^2 & & & & + & & y_{SPAC}^2 & & & & < & 15^2 \text{ cm}^2 \\
(& x_{SPAC} & - & (-43.3 \text{ cm}) &)^2 & + & (& y_{SPAC} & - & (-27.5 \text{ cm}) &)^2 & < & 6.7^2 \text{ cm}^2 \\
(& x_{SPAC} & - & (-\ 6.4 \text{ cm}) &)^2 & + & (& y_{SPAC} & - & (-48.3 \text{ cm}) &)^2 & < & 7.3^2 \text{ cm}^2 \\
(& x_{SPAC} & - & (\ 51.2 \text{ cm}) &)^2 & + & (& y_{SPAC} & - & (\ 42.7 \text{ cm}) &)^2 & < & 7.3^2 \text{ cm}^2
\end{array}$$

Here, (x_{SPAC},y_{SPAC}) are coordinates in the SPACAL system. Also, a region where the S0 trigger had a low efficiency was removed

$$(-17 < x_{SPAC} < 9 \text{ cm}) \,\&\&\, (-9 < y_{SPAC} < 17 \text{ cm}). \tag{3.1}$$

Figure 3.2 shows the activity in the SPACAL before and after applying the fiducial cuts. If the scattered electron was identified in one of the regions above, the event was rejected.

3.2.6 Kinematic Phase Space

Having identified the scattered electron, the kinematic variables defined in Section 1.1 can be reconstructed using the Electron method [115]

$$\begin{aligned}
Q^2 &= 4E_eE_e^{'}cos^2(\theta_e/2) \\
y &= 1 - \frac{E_e^{'}}{E_e}sin^2(\theta_e/2) \\
x &= \frac{Q^2}{y \cdot s}.
\end{aligned} \tag{3.2}$$

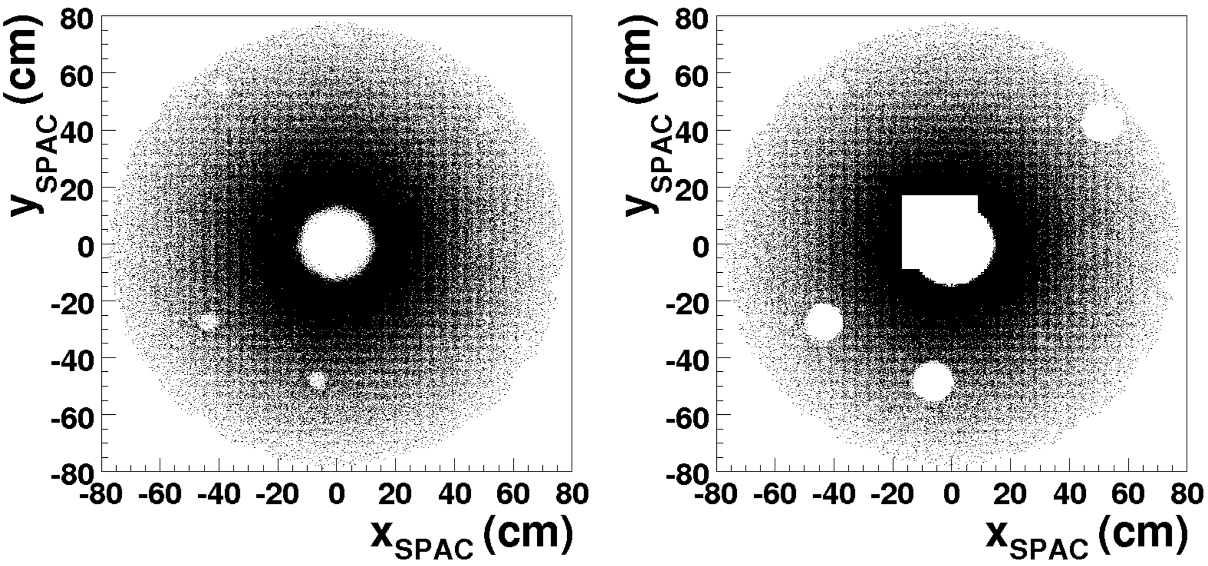

Figure 3.2: *Hits in the SPACAL before (left) and after (right) applying the fiducial cuts.*

Here, $E_e = 27.6$ GeV is the energy of the electron beam and $E_e^{'}$ and θ_e is the energy and polar angle of the scattered electron, respectively. Although these variables are already constrained by the cuts in $E_e^{'}$ and θ_e, additional cuts need to be made in order to avoid unwanted phase space regions. The phase space of this analysis is defined by

$$\begin{aligned} 5 &< Q^2 < 100\ \mathrm{GeV}^2 \\ 0.1 &< y < 0.7. \end{aligned}$$

The lower Q^2 and y cuts remove the photoproduction region, while the upper Q^2 and y cuts are slightly harder than the $E_e^{'}$ and θ_e cuts. From Equation (3.2), this gives the restriction $\sim 8 \cdot 10^{-5} < x_{Bj} <\sim 10^{-2}$. In Figure 3.3 the kinematic region in the (x_{Bj}, Q^2) plane covered in this thesis is shown. After the DIS selection $4.6 \cdot 10^6$ events remain.

It should be mentioned that there are ways of reconstructing the kinematic variables other than the Electron method, e.g. the Hadron method [116] (where all particles except the scattered electron are used), the Double Angle method [115] (where only the angles of all final state particles are used) and the Sigma method [117] (which is a modification of the hadron method). It has, however, been shown [117,118] that the Electron method gives the best reconstruction of the kinematic variables in the phase space region considered in this analysis.

3.3 Dijet Selection

The jet selection was performed using the inclusive k_T algorithm (see Section 1.7) applied to combined objects in the hadronic center of mass frame. The jets are required to be within the acceptance of the LAr calorimeter and the CJC1, CJC2 and FTD,

$$-1 < \eta_j < 2.5.$$

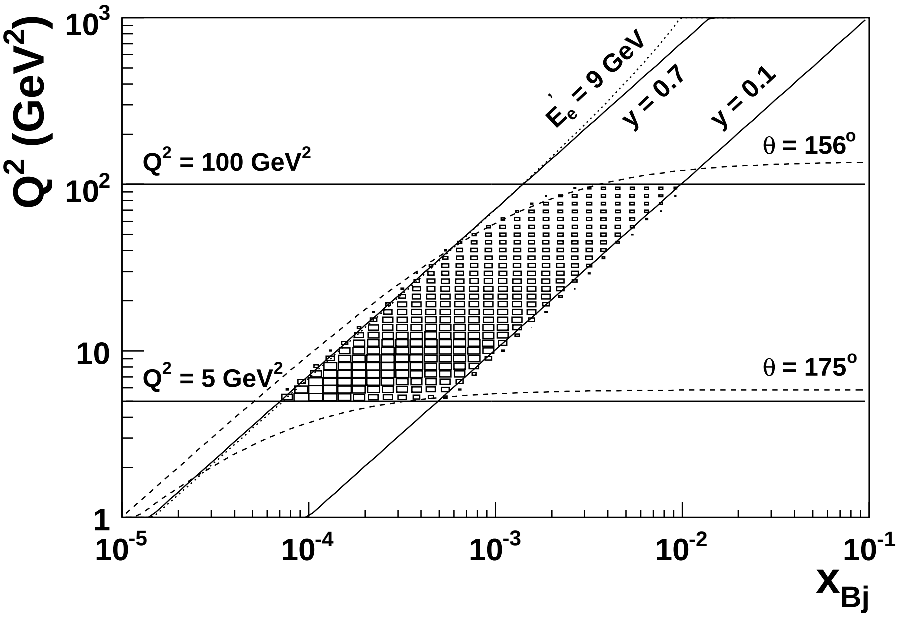

Figure 3.3: *The phase space in* (x_{Bj}, Q^2) *covered in this analysis. Also indicated are the different DIS cuts.*

Here, the pseudo-rapidity is defined as $\eta_j = -\ln(\tan(\theta_j/2))$ where θ_j is the polar angle of the jet in the lab frame. The jets are also required to fulfill

$$E^*_{T,j} > 5 \text{ GeV}.$$

The two jets with lowest η (closest to the scattered electron) are selected as the dijet system, such that jet 1 has the lowest η,

$$\eta_1 < \eta_2.$$

The cuts applied are summarised in Table 3.1. Approximately $1.2 \cdot 10^5$ events pass these cuts.

3.4 DIS and Dijet Selection on the Hadron Level

The cuts presented above have been applied on the measured data and on detector simulated Monte Carlo events. The hadron level DIS phase space is defined by

$$\begin{array}{rcccl} 5 & < & Q^2 & < & 100 \text{ GeV}^2 \\ 0.1 & < & y & < & 0.7 \\ 9 \text{ GeV} & < & E_e^{'} & & \\ 156 & < & \theta_e & < & 175^\circ \end{array}$$

DIS Cuts

5 GeV^2 <	Q^2	< 100 GeV^2
0.1 <	y	< 0.7
9 GeV <	$E_e^{'}$	
156° <	θ_e	< 175°
35 GeV <	$E - p_z$	< 70 GeV
	$\lvert z_{vtx} \rvert$	< 35 cm
	R_{clus}	< 3.5 cm
	E_{had}	< 0.5 GeV
	E_{veto}	< 1.0 GeV

Dijet Cuts

5 GeV <	$E^*_{Tj1,2}$	
−1 <	η_j	< 2.5

Table 3.1: *Summary of event selection cuts on the detector level.*

while the dijet cuts are

$$\begin{aligned} 5\ \text{GeV} &< E^*_{Tj1,2} \\ -1 &< \eta_j < 2.5. \end{aligned}$$

It is often preferred to correct to the hadron level where the electron has not emitted any QED radiation, in order to correct for the mismeasurement of the kinematic variables. This level will in the following be referred to as the non-radiative hadron level. An additional correction is made such that particles with a lifetime $\tau > 0.8 \cdot 10^{-8}$ s are considered to be stable, since most of them will not decay before reaching the calorimeters. This is a standard procedure in H1.

3.5 DIS Event Reconstruction

In Figure 3.4 are shown control distributions for the DIS sample on the detector level of the variables Q^2, x_{Bj}, y, $E_e^{'}$, θ_e and ϕ_e, where ϕ_e is the azimuthal angle of the scattered electron. The data are compared to detector simulated events including initial and final state QED radiation obtained using the RAPGAP and DJANGO(CDM) generators. Also shown are predictions from the PHOJET MC generator, simulating photoproduction background with $Q^2 < 1$ GeV^2. As can be seen, the data are in general well described by the Monte Carlo simulations.

3.6 Dijet Event Reconstruction

In Figure 3.5 control distributions of Q^2, x_{Bj}, $E_e^{'}$ and θ_e for the dijet event sample are shown. The uncorrected data are compared to the detector level distributions obtained using RAPGAP and DJANGO(CDM). Here, the distributions have been normalised to the

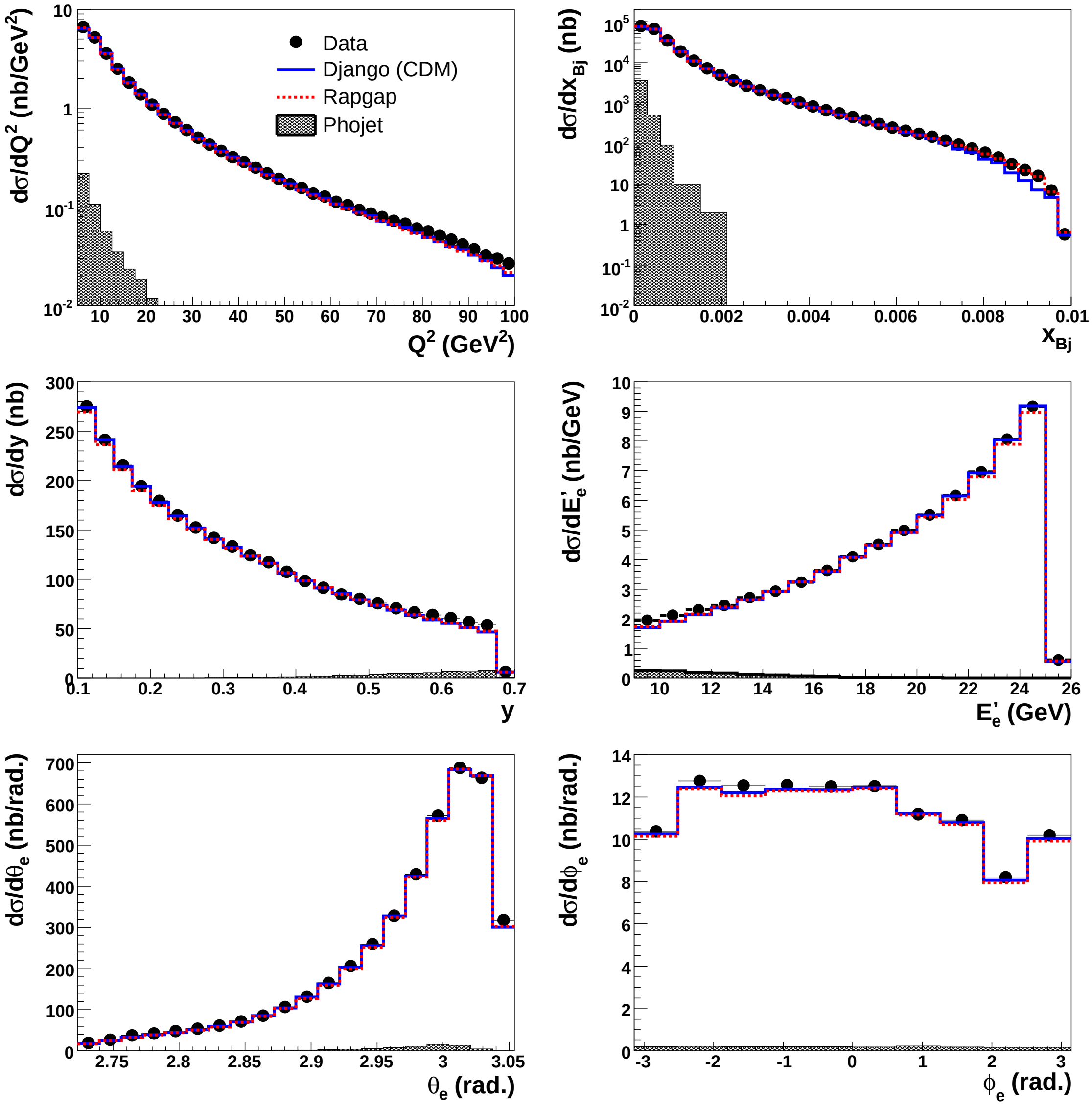

Figure 3.4: *Detector level DIS control distributions of* Q^2, x_{Bj}, y, $E_e^{'}$, θ_e *and* ϕ_e *compared to the predictions of* RAPGAP *and* DJANGO(CDM). *Also shown is the photoproduction background as simulated by* PHOJET.

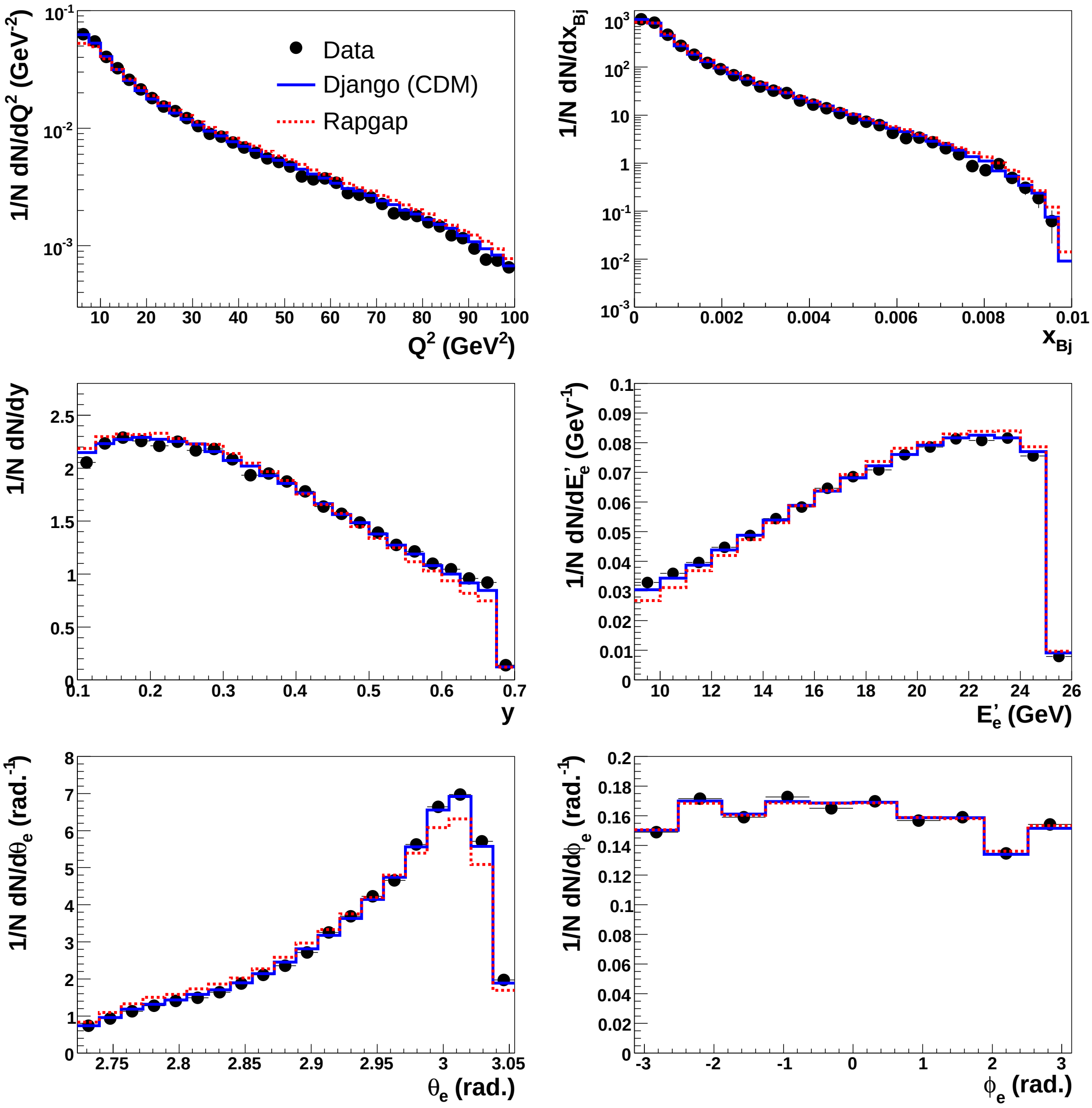

Figure 3.5: *Detector level dijet control distributions of* Q^2, x_{Bj}, y, $E_e^{'}$, θ_e *and* ϕ_e *compared to the predictions of* Rapgap *and* Django(CDM)*. The distributions have been normalised to the total number of events.*

total number of events, since the total dijet cross section is different for Rapgap and Django(CDM). Again, both MC generators are in good agreement with data although Rapgap has some problems with describing the shape of the θ_e distribution. Figure 3.6 shows control distributions of the dijet variables E_T^*, η^* and ϕ^* for jet 1 (left) and jet 2 (right). Also here, both Rapgap and Django(CDM) are in good agreement with data, except for high E_T^* of the second jet, where Django(CDM) overshoots data. This is because of the well known feature of CDM producing too much energy in the forward region [85, 119–121]. The effect of this is only seen in jet 2 since it is always chosen as the more forward going of the two jets. The fact that the Monte Carlo distributions are in good agreement with the experimental data indicates that the detector is well simulated and hence that the MC events can be used when correcting the data for detector effects.

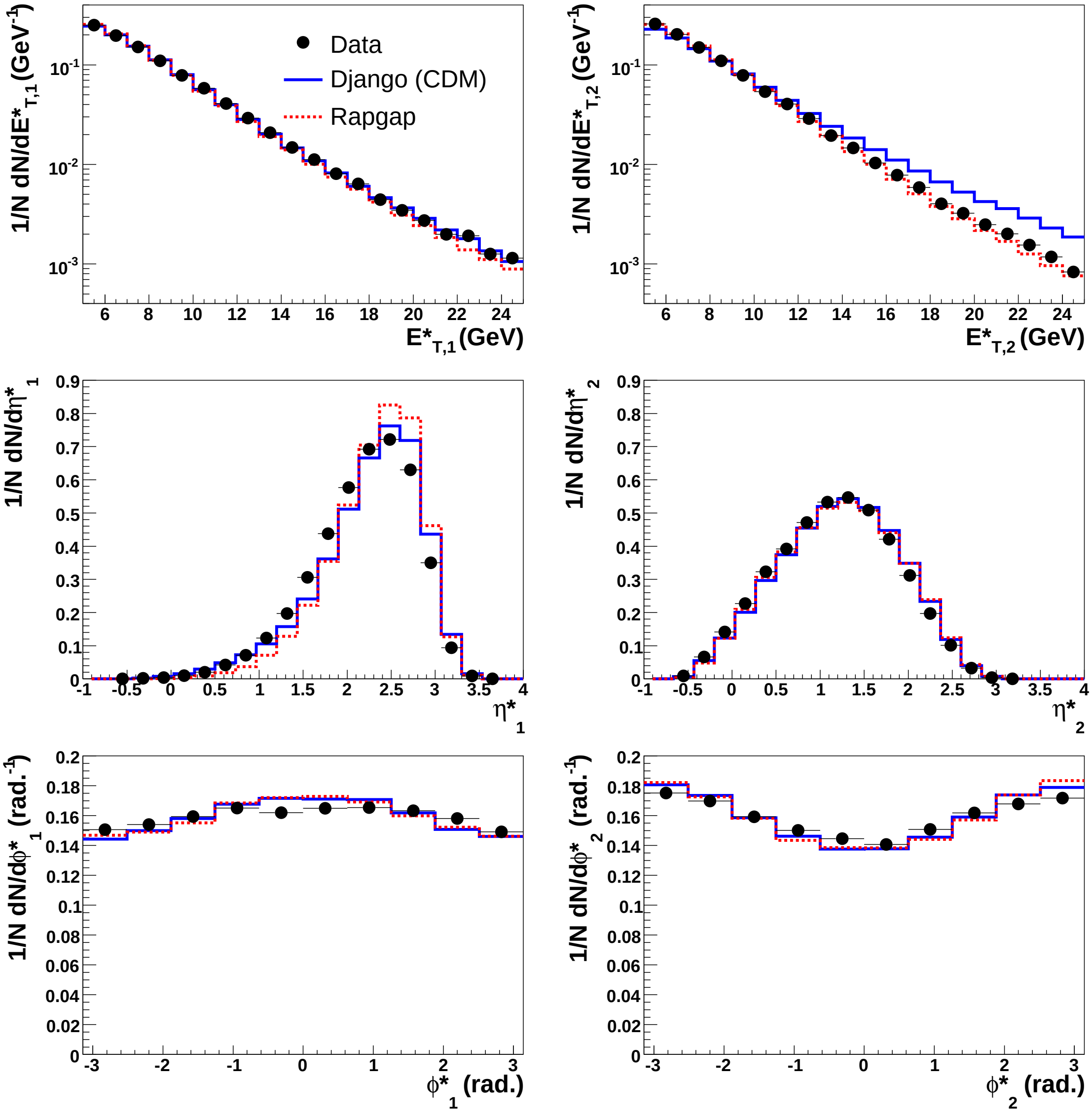

Figure 3.6: *Dijet control distributions of* E_T^*, η^*, ϕ^* *for jet 1 (left) and jet 2 (right) compared to the predictions of* RAPGAP *and* DJANGO(CDM). *The distributions have been normalised to the total number of events.*

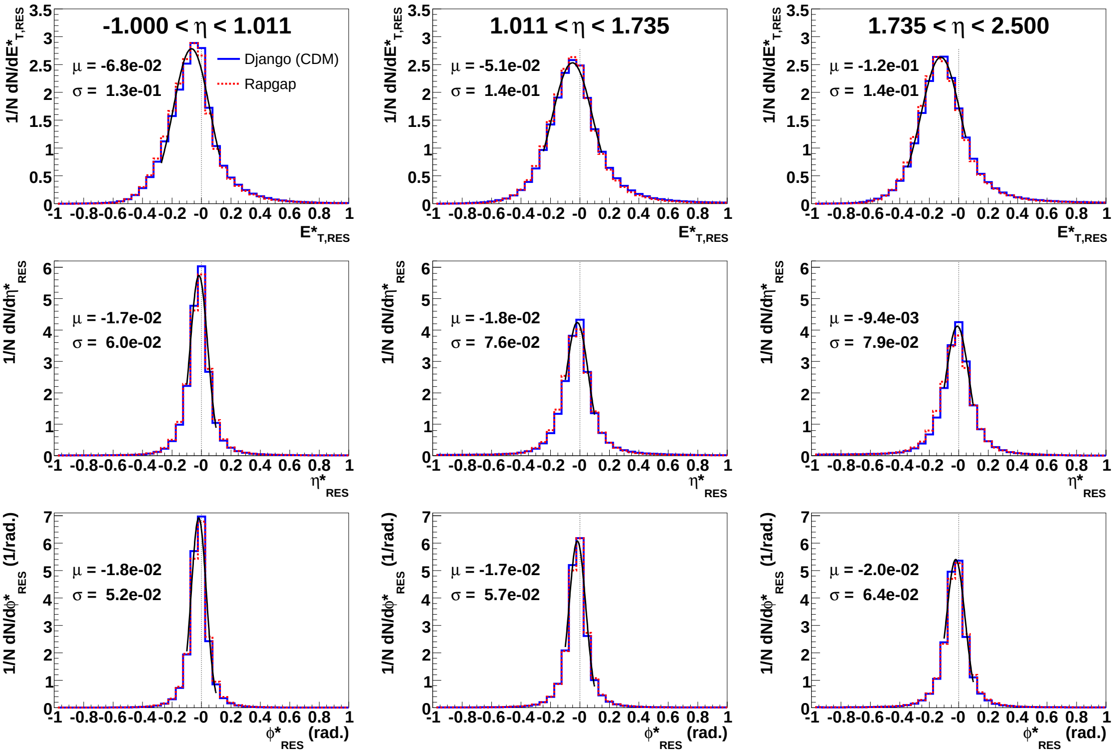

Figure 3.7: *Resolutions of E_T^*, η^* and ϕ^* for the selected jets in bins of η, obtained using* Rapgap *and* Django(CDM)*. Also shown are Gaussian fits to the* Django(CDM) *resolutions, where μ and σ are the mean and width of the Gaussian, respectively.*

Figure 3.7 shows the resolutions of E_T^*, η^* and ϕ^* for the selected jets in bins of η. The resolutions are defined as

$$E^*_{T,RES} = \frac{E^*_{T,DET} - E^*_{T,HAD}}{E^*_{T,HAD}} \tag{3.3}$$

$$\eta^*_{RES} = \eta^*_{DET} - \eta^*_{HAD} \tag{3.4}$$

$$\phi^*_{RES} = \phi^*_{DET} - \phi^*_{HAD} \tag{3.5}$$

where the index DET and HAD mean that the variable is taken on the detector (reconstructed) and the hadron (generated) level, respectively. As seen, the resolution gets worse in the forward direction for all three observables. This is because of the low efficiency of the forward tracker during the 1999/2000 data taking period, with the consequence that the jetfinder is more dependent on clusters in this region. Also, the E_T^* resolution is shifted to negative values, meaning that the measured E_T^* on the detector level is generally too low. This could in the future be corrected for by an improved hadronic energy calibration.

Chapter 4

Analysis Procedure and Results

In this chapter, the analysis procedure is described. Purity and stability, which are measures of data migrations, are defined and the results for the analysis bins are shown. The unfolding procedure which has been used to account for migrations is described and the systematic uncertainties are given. Finally, the measurement is presented in terms of two inclusive dijet cross sections, $\frac{d\sigma}{dx_{Bj}}$ and $\frac{d\sigma}{dQ^2}$, two double differential dijet cross sections, $\frac{d^2\sigma}{dx_{Bj}d\Delta\phi^*}$ and $\frac{d^2\sigma}{dQ^2 d\Delta\phi^*}$, and one triple differential cross section $\frac{d^3\sigma}{dQ^2 dx_{Bj} d\Delta\phi^*}$.

4.1 Purity and Stability

An event generated in one specific bin (e.g. in x_{Bj}) on the hadron level might, due to the limited detector resolution, be reconstructed in another bin on the detector level. The migrations into and out of a bin, when going from the hadron level to the detector level, are measured by the purity (P) and stability (S), respectively. These quantities are defined as

$$\begin{aligned} P &= \frac{N_{HAD\&\&DET}}{N_{DET}} \\ S &= \frac{N_{HAD\&\&DET}}{N_{HAD}} \end{aligned}$$

where $N_{HAD\&\&DET}$ is the number of events which belong to the same bin on the hadron and the detector level, and N_{DET} (N_{HAD}) is the number of events on the detector (hadron) level in that bin. For example, $P = 0.7$ would mean that 70% of the events measured in one bin on the detector level is also in that same bin on the hadron level, while 30% of the events have migrated into that bin. Similarly, $S = 0.7$ would mean that 70% of the events in one bin on the hadron level are also found in that bin on the detector level, while 30% of the events migrate out of that bin. Obviously, P and S should be as close to 1 as possible. Purity and stability have been calculated using both Rapgap and Django(CDM) and the results are shown in Figure 4.1 for the inclusive dijet cross sections, and in Figure 4.2 - 4.7 for the $\Delta\phi^*$ decorrelation cross sections.

For the inclusive cross sections, the purity and stability are, in most bins, above 0.6 and 0.5, respectively while for the double and triple differential cross sections they are above 0.4. The main reason for the large migrations in $\Delta\phi^*$ is the smearing of E_T^* of the jets due

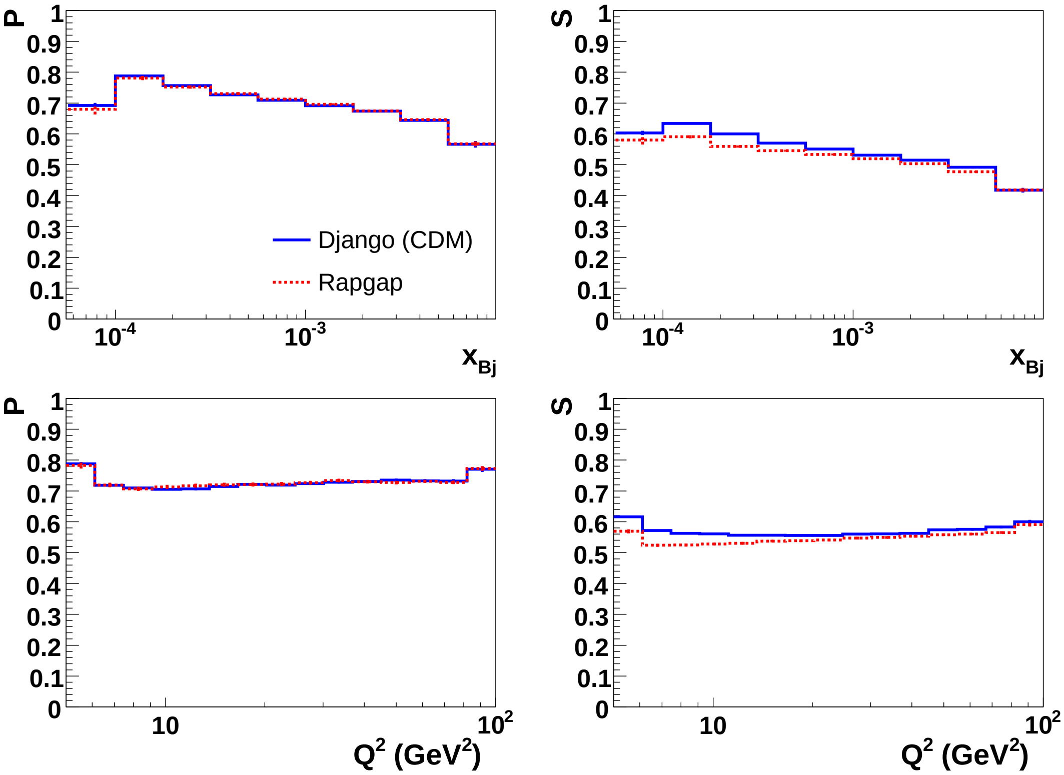

Figure 4.1: *Purity (P) and Stability (S) of* $\frac{d\sigma}{dx_{Bj}}$ *(upper) and* $\frac{d\sigma}{dQ^2}$ *(lower).*

to the limited detector resolution. This can be studied by using MC simulated events and then applying a smearing on the jet variables E_T^*, η and ϕ, and on the kinematic variable Q^2 according to the resolutions obtained using the full detector simulation. The jets after the smearing then define a “toy” detector level where one has full control of the smearing of all variables. A short description of the “toy model” is given in Appendix A. The applied resolutions of E_T^*, η, ϕ and Q^2 in the toy model are seen in Figures 4.8 and 4.9, compared to the resolutions obtained from the full detector simulation. Here, jets with transverse energies as low as $E_T^* > 3$ GeV have been smeared in order to correctly take into account the migrations over the jet cuts given by $E_T^* > 5$ GeV.

Figure 4.10 and 4.11 shows the purity and stability of $d^2\sigma/dQ^2d\Delta\phi^*$ obtained using the toy model and applying smearing on E_T^* (dotted line), E_T^* and η (large-dotted line), E_T^*, η and ϕ (dash-dotted line) and E_T^*, η, ϕ and Q^2 (dashed line) compared to the full detector simulation (full line). It is clear that the largest effect comes from the E_T^* resolution, while the ϕ resolution plays a more significant role at large $\Delta\phi^*$ where the $\Delta\phi^*$ bins are small. The limited resolution in Q^2 gives only a small effect, and the decrease due to the η resolution is almost negligible.

At large $\Delta\phi^*$ the two jets are almost back-to-back and has mostly equal E_T^*, meaning that any additional radiation is soft and does not create a jet. Therefore, at large $\Delta\phi^*$ the probability that different jets are chosen on the detector and the hadron level is small. However, there can still be migrations over the E_T^* jet cut, such that two jets are found on the detector level but only one or no jets on the hadron level, or vice versa, which

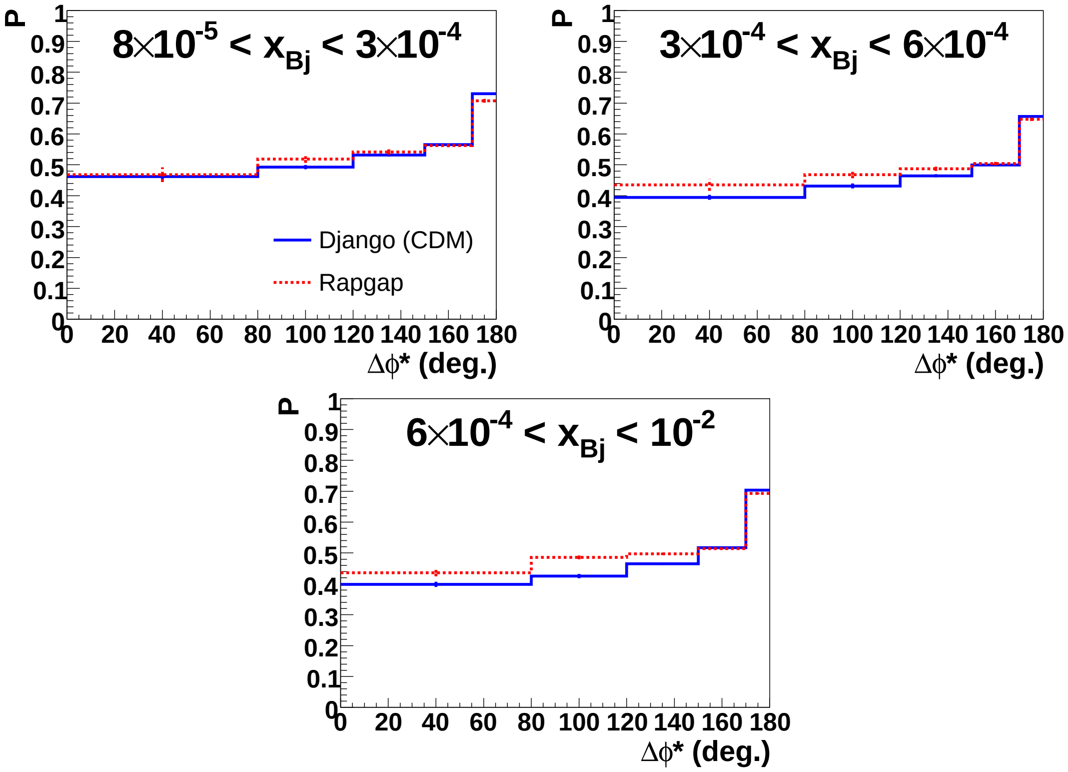

Figure 4.2: *Purity (P) of* $\frac{d^2\sigma}{dx_{Bj}d\Delta\phi^*}$ *obtained using* RAPGAP *and* DJANGO(CDM).

will decrease the purity and stability. At smaller $\Delta\phi^*$ there is a larger probability that three jets pass the cuts, and thus a larger probability that different jets are selected as the dijet system on the detector level and the hadron level. This misidentification leads to additional migrations in $\Delta\phi^*$ and a lower purity and stability. At very small $\Delta\phi^*$, four-jet events begin to play a role, which further decreases P and S. This can be seen in Figure 4.12 where the fraction of dijet events with exactly two, three and four jets satisfying the cuts in Section 3.3 are shown as a function of $\Delta\phi^*$ for the measured data. It is worth pointing out that the migrations are not only between neighbouring $\Delta\phi^*$ bins. In fact, there are migrations between the bin $0 < \Delta\phi^* < 80°$ and all other $\Delta\phi^*$ bins, especially the bin $150 < \Delta\phi^* < 170°$. Often this is due to events where three jets are found on the detector and/or the hadron level, but where different jets are chosen as the dijet system, e.g. because one jet does not pass the E_T^* on one of the levels, or because a jet on the hadron level is clustered into two jets on the detector level. The migrations between all $\Delta\phi^*$ and x_{Bj} bins, as well as over the dijet cuts, are shown for DJANGO(CDM) in Figure 4.13 and 4.14. Each bin corresponds to a $\Delta\phi^*$ bin in each of the x_{Bj} bins on the hadron (x-axis) and the detector level (y-axis), except the first bin which is filled with events that has not passed the DIS and/or dijet cuts. In Figure 4.13, each row has been normalised to the total number of events in that row, and then multiplied by a factor 100; the numbers thus describe, in percentage, the contribution from each bin on the hadron level to each bin on the detector level, and the diagonal elements describe the purity of that bin. Similarly, in Figure 4.14 each column has been normalised to the total number of events in that column. The numbers then describe, in percentage, how many of the events in a certain

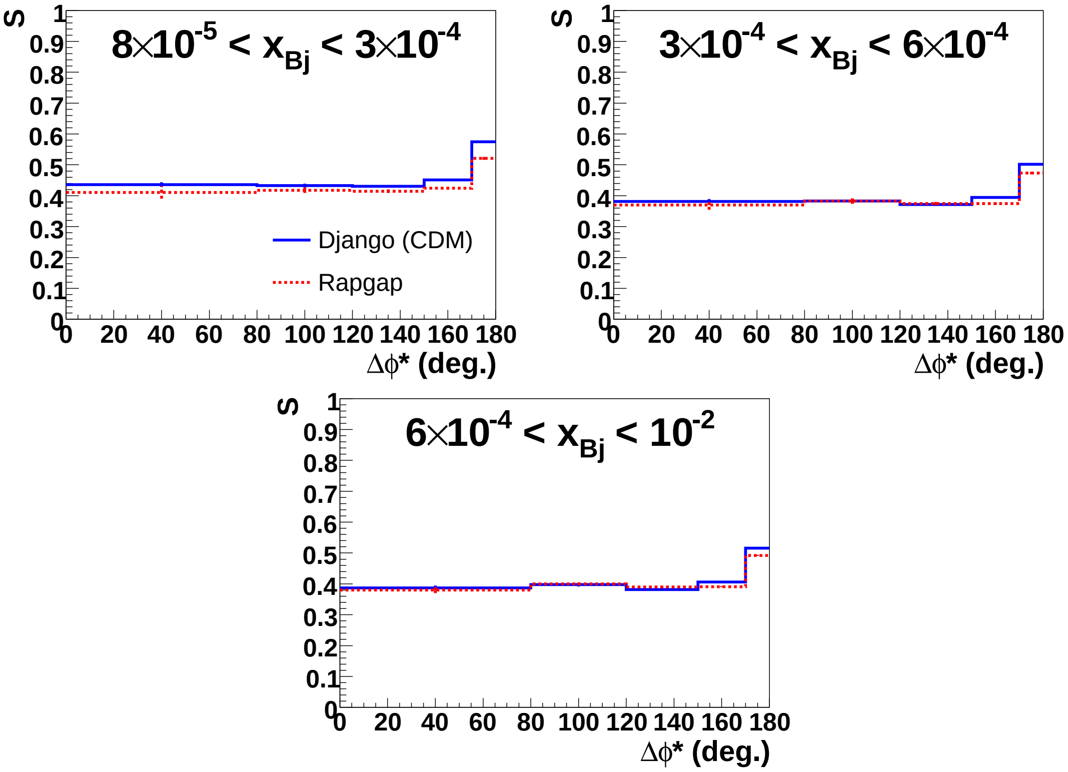

Figure 4.3: *Stability (S) of* $\frac{d^2\sigma}{dx_{Bj}d\Delta\phi^*}$ *obtained using* Rapgap *and* Django(CDM).

bin on the hadron level that end up in a certain bin on the detector level; the diagonal elements describe the stability.

4.2 Correction of the Data

Measured data are most often corrected for detector effects and QED radiation off the electron, i.e. the data are presented at the "non-radiative hadron level". This puts focus on the underlying physical processes and makes it easier to compare published results with those from other analyses and to MC simulations. There are several alternative methods for unfolding the measured distributions, of which the bin-by-bin method is the most straightforward one and among the most used methods at H1. The transition from the "radiative detector level" to the "non-radiative hadron level" is then made by applying the correction factor

$$C_i = \frac{N_{i,Had,Nonrad}}{N_{i,Det,Rad}} \tag{4.1}$$

estimated from the MC to the measured data using a bin-by-bin procedure. Here, $N_{i,Had,Nonrad}$ and $N_{i,Det,Rad}$ are the number of events in bin i on the "non-radiative hadron level" and the "radiative detector level", respectively. This correctly takes into account acceptance effects of the detector. However, to correct for effects of limited resolution, the MC used for the correction must in principle describe the "true" distribution on the hadron level which we are trying to measure. Since this is not known, one may approach this situation

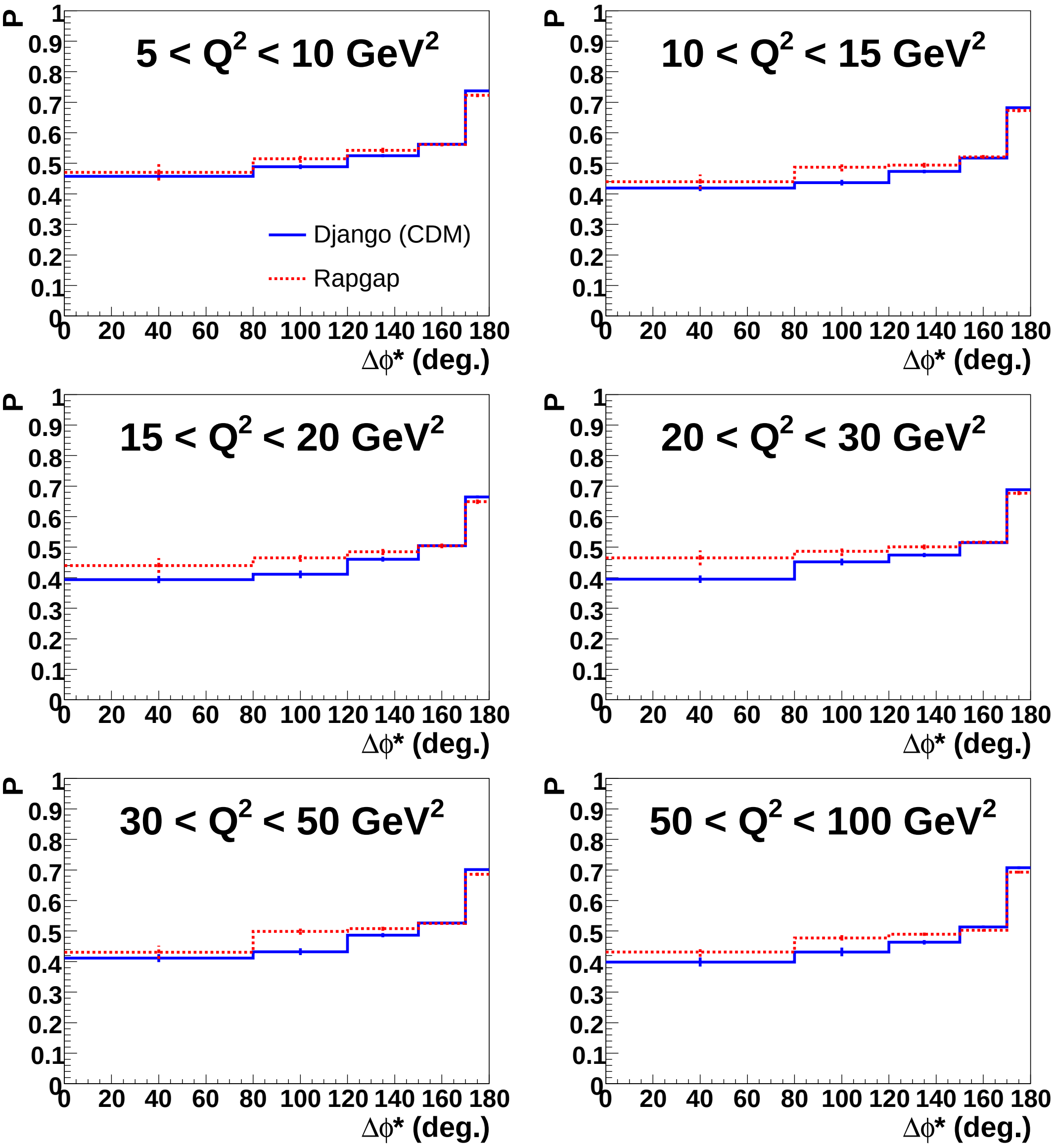

Figure 4.4: *Purity (P) of* $\frac{d^2\sigma}{dQ^2 d\Delta\phi^*}$ *obtained using* Rapgap *and* Django(CDM).

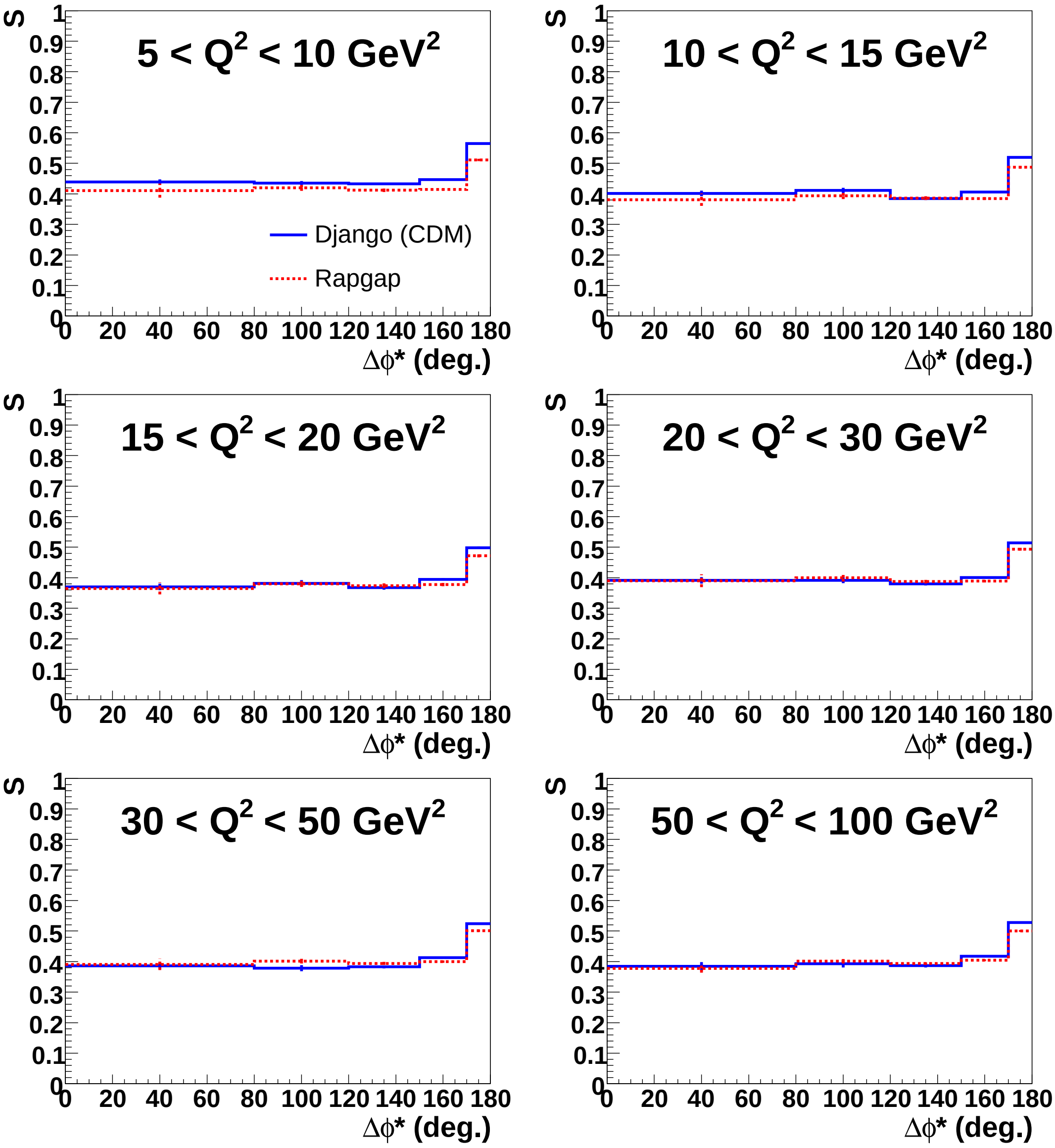

Figure 4.5: *Stability (S) of* $\frac{d^2\sigma}{dQ^2 d\Delta\phi^*}$ *obtained using* Rapgap *and* Django(CDM).

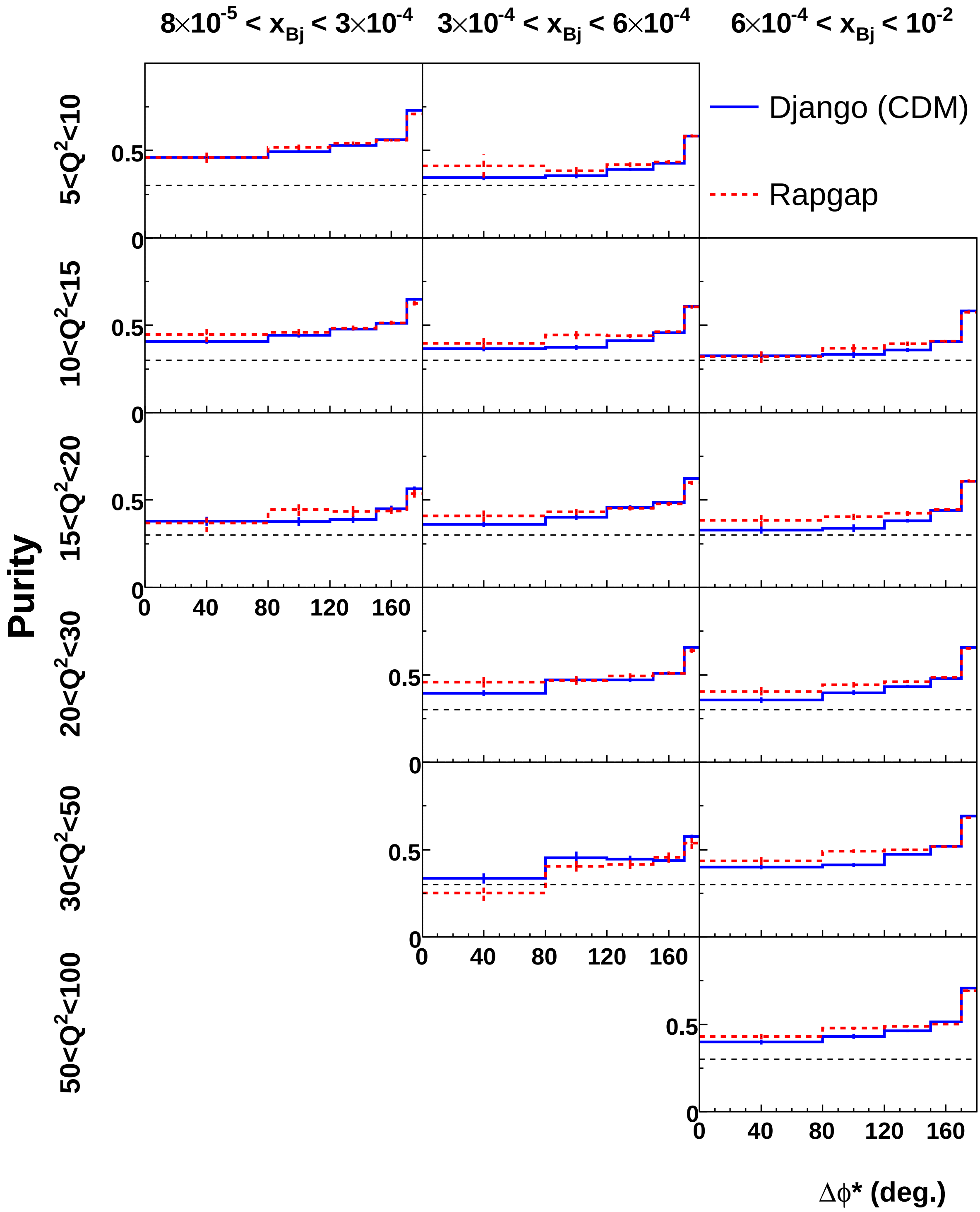

Figure 4.6: *Purity (P) of* $\frac{d^3\sigma}{dQ^2 dx_{Bj} d\Delta\phi^*}$ *obtained using* RAPGAP *and* DJANGO(CDM). *The broken line at* $P = 0.3$ *is shown for reference.*

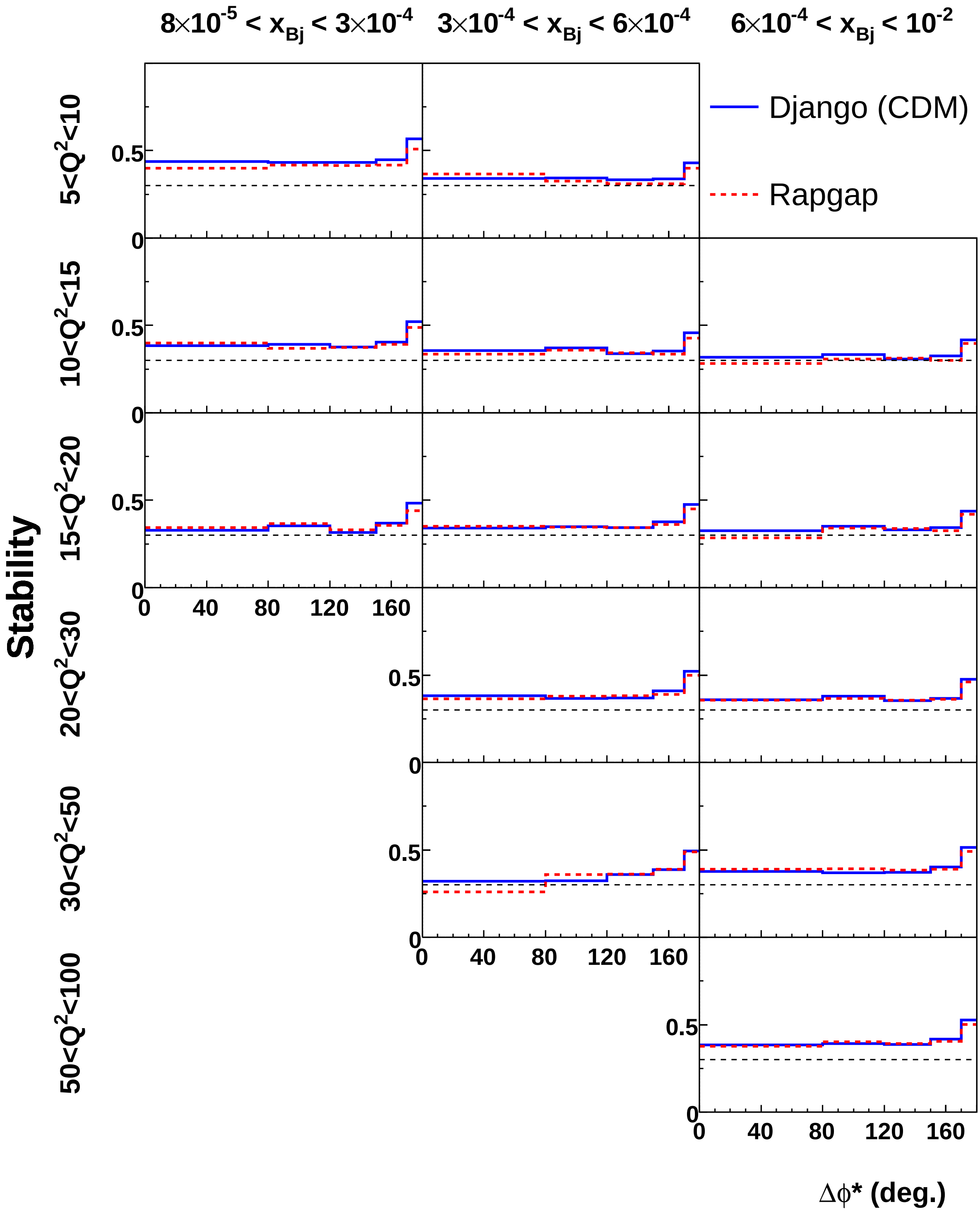

Figure 4.7: *Stability (S) of* $\frac{d^3\sigma}{dQ^2 dx_{Bj} d\Delta\phi^*}$ *obtained using* RAPGAP *and* DJANGO(CDM). *The broken line at* $S = 0.3$ *is shown for reference.*

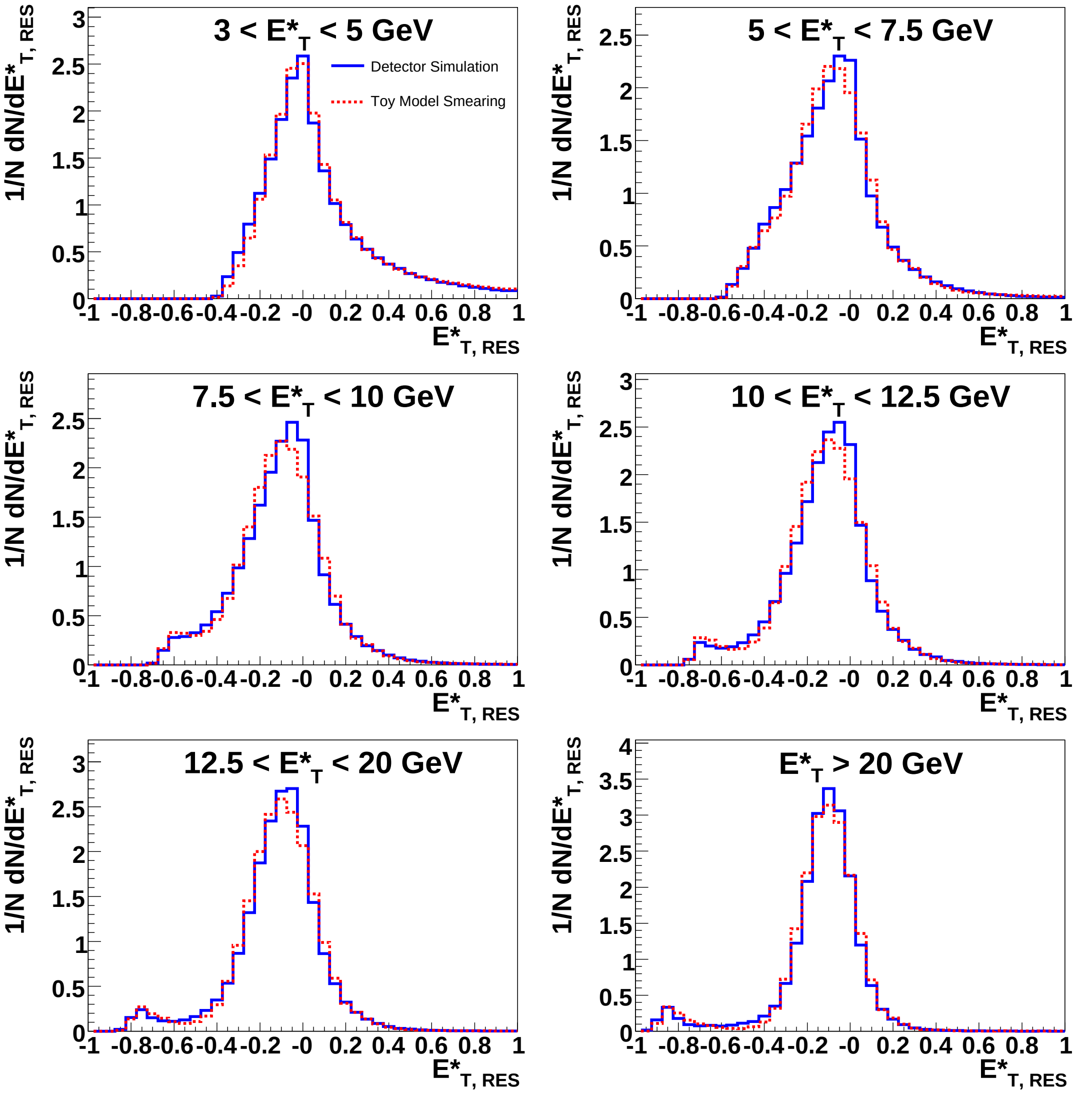

Figure 4.8: *The E_T^* resolutions in bins of E_T^* obtained from the detector simulation compared to the resolutions applied in the toy model. $E_{T,RES}^*$ is defined in Equation (3.3).*

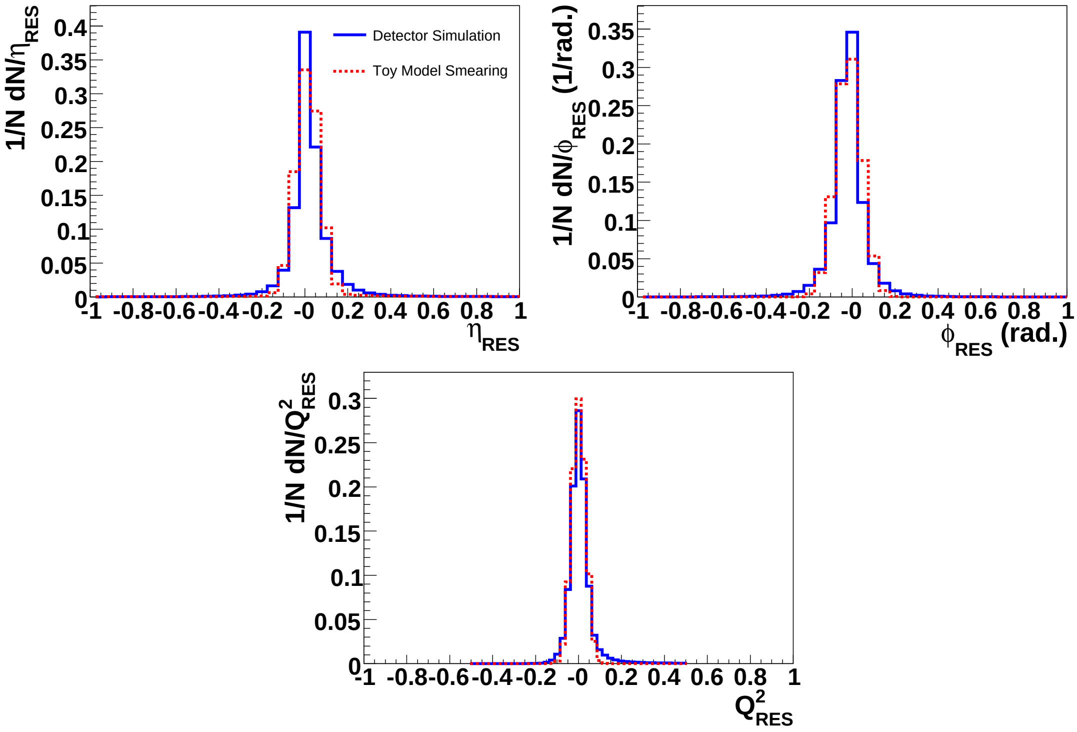

Figure 4.9: *The* η, ϕ *and* Q^2 *resolutions obtained from the detector simulation compared to the resolutions applied in the toy model. Equations (3.4) and (3.5) define* η_{RES} *and* ϕ_{RES}, *while* Q^2_{RES} *is defined in analogy to* $E^*_{T,RES}$ *in Equation (3.3).*

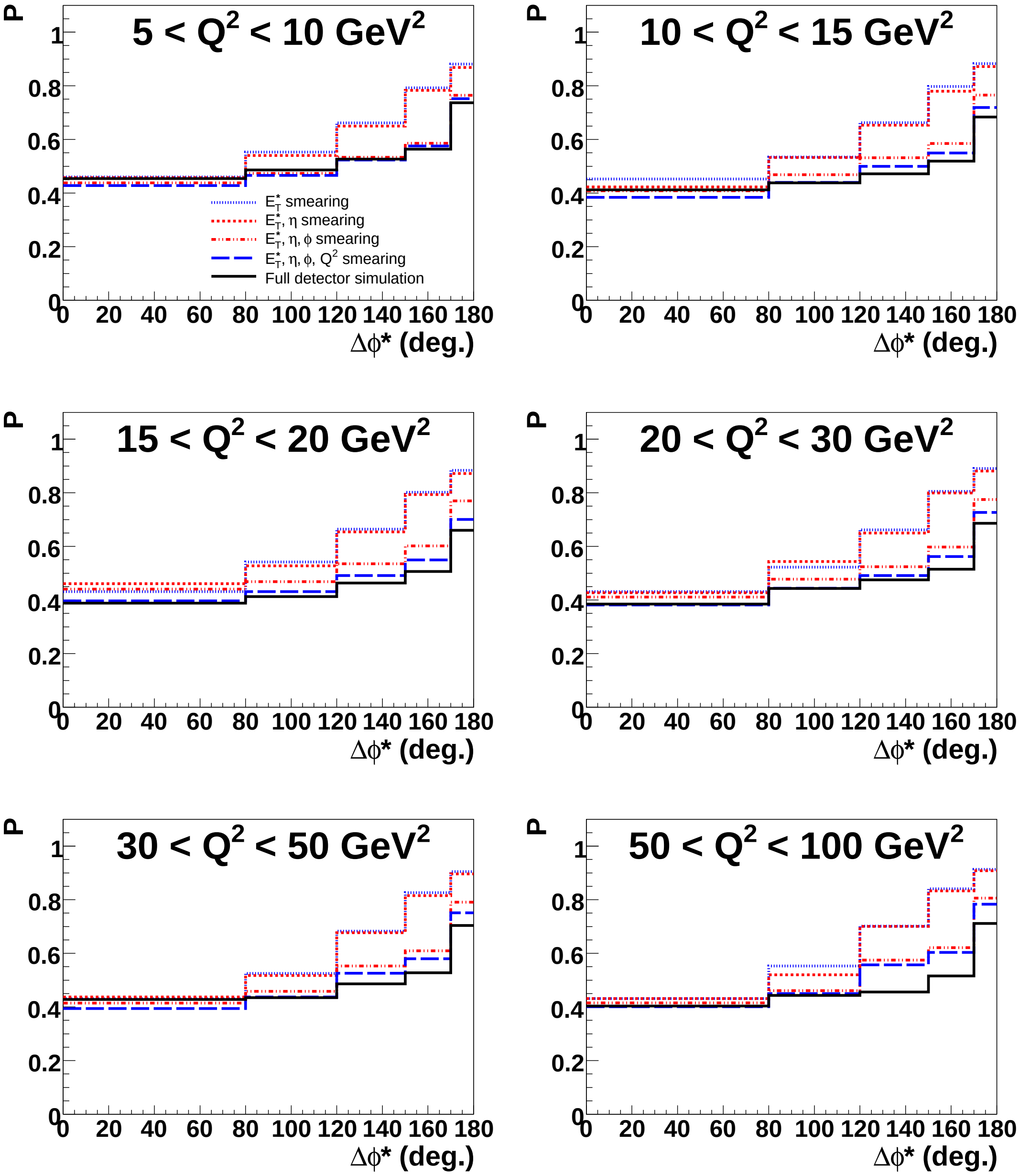

Figure 4.10: *Purity of* $d^2\sigma/dQ^2d\Delta\phi^*$ *obtained using the toy model and applying smearing on* E_T^* *(dotted line),* E_T^* *and* η *(large-dotted line),* E_T^**,* η *and* ϕ *(dash-dotted line),* E_T^**,* η*,* ϕ *and* Q^2 *(dashed line) compared to the full detector simulation (full line).*

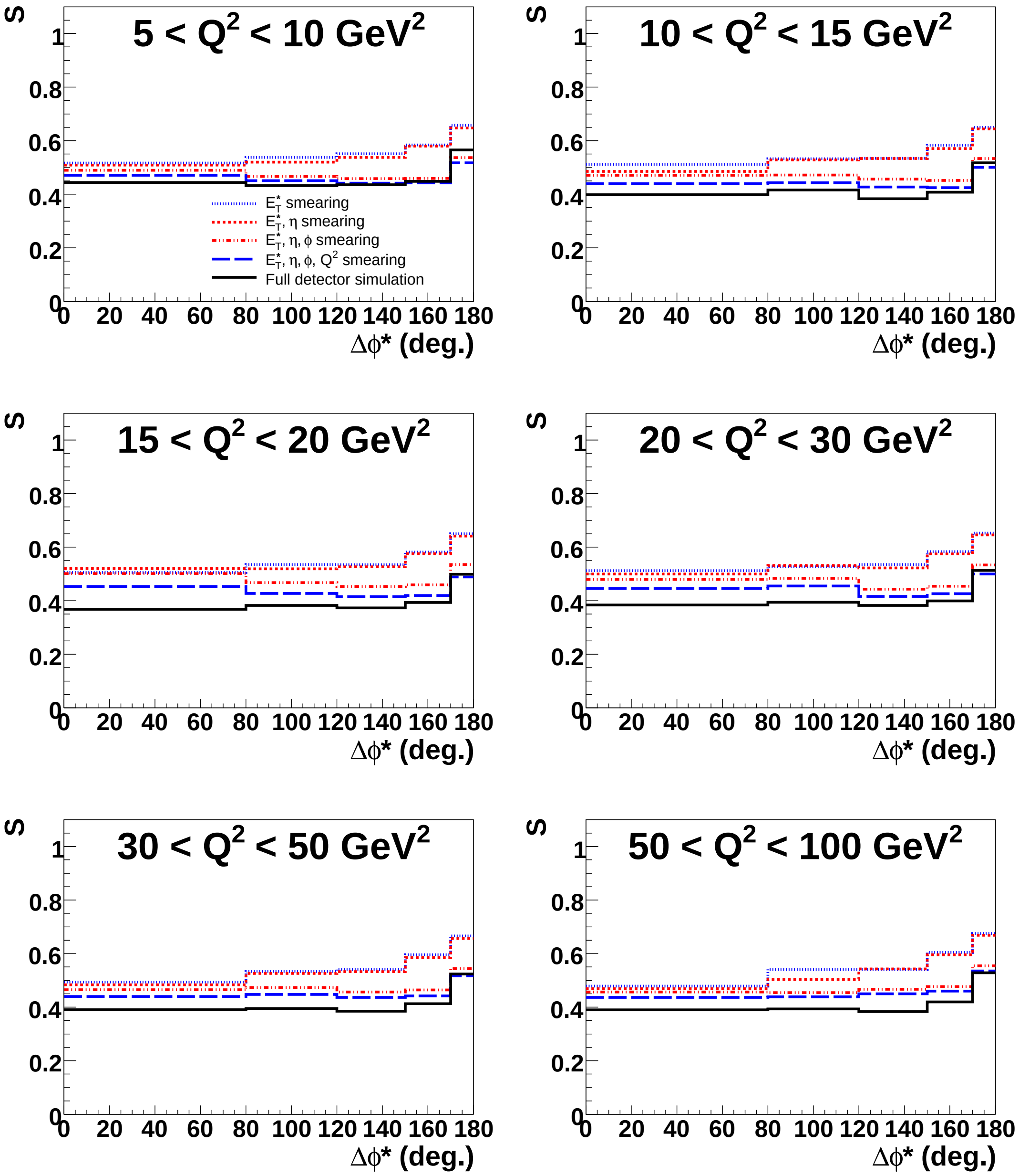

Figure 4.11: *Stability of* $d^2\sigma/dQ^2 d\Delta\phi^*$ *obtained using the toy model and applying smearing on* E_T^* *(dotted line),* E_T^* *and* η *(large-dotted line),* E_T^**,* η *and* ϕ *(dash-dotted line),* E_T^**,* η*,* ϕ *and* Q^2 *(dashed line) compared to the full detector simulation (full line).*

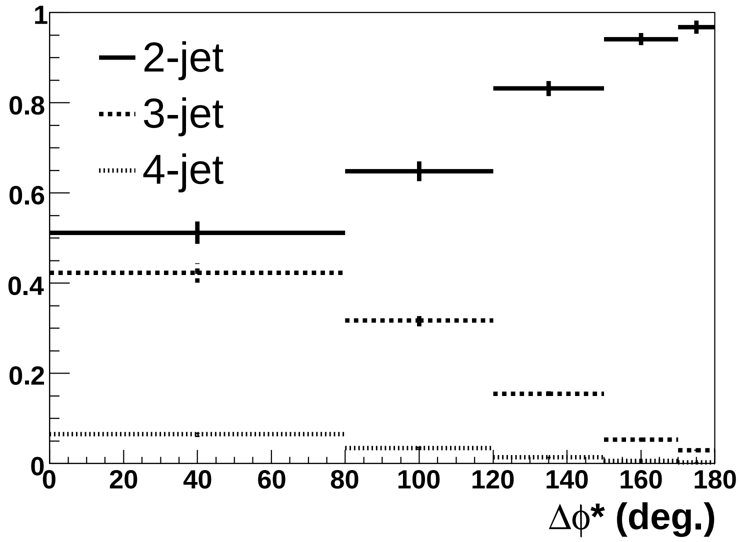

Figure 4.12: *The fraction of dijet events with exactly two, three and four jets satisfying the cuts presented in Section 3.3 as a function of* $\Delta\phi^*$ *for uncorrected data.*

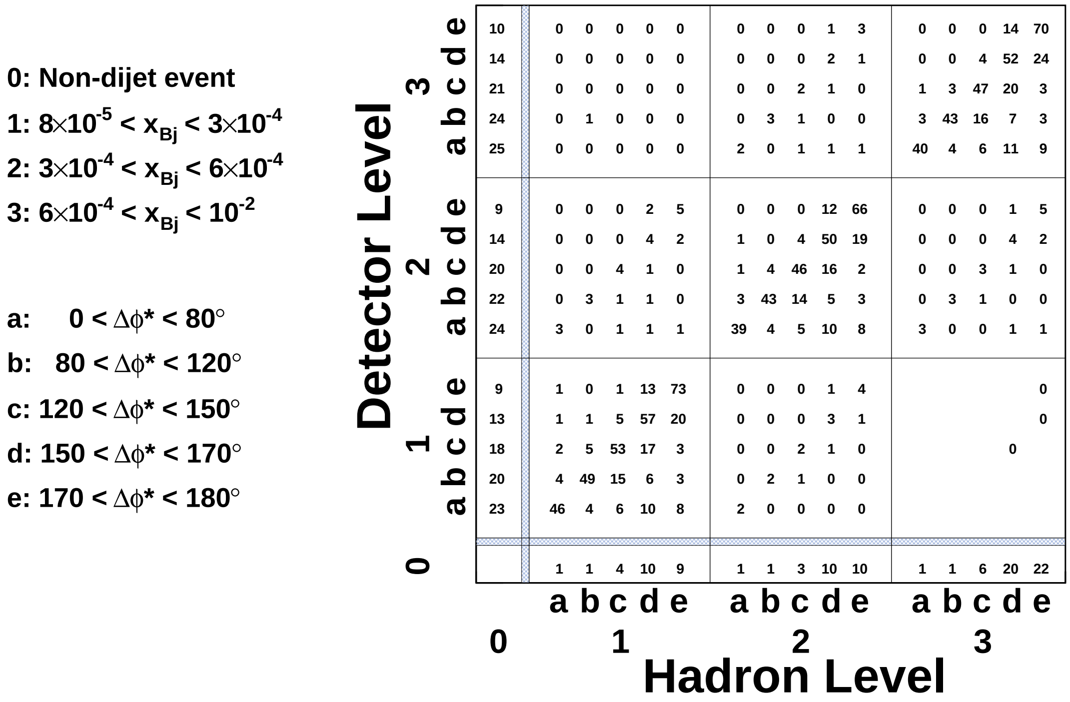

Detector Level \ Hadron Level	0	1 a	1 b	1 c	1 d	1 e	2 a	2 b	2 c	2 d	2 e	3 a	3 b	3 c	3 d	3 e
3 e	10	0	0	0	0	0	0	0	0	1	3	0	0	0	14	70
3 d	14	0	0	0	0	0	0	0	0	2	1	0	0	4	52	24
3 c	21	0	0	0	0	0	0	0	2	1	0	1	3	47	20	3
3 b	24	0	1	0	0	0	0	3	1	0	0	3	43	16	7	3
3 a	25	0	0	0	0	0	2	0	1	1	1	40	4	6	11	9
2 e	9	0	0	0	2	5	0	0	0	12	66	0	0	0	1	5
2 d	14	0	0	0	4	2	1	0	4	50	19	0	0	0	4	2
2 c	20	0	0	4	1	0	1	4	46	16	2	0	0	3	1	0
2 b	22	0	3	1	1	0	3	43	14	5	3	0	3	1	0	0
2 a	24	3	0	1	1	1	39	4	5	10	8	3	0	0	1	1
1 e	9	1	0	1	13	73	0	0	0	1	4					0
1 d	13	1	1	5	57	20	0	0	0	3	1					0
1 c	18	2	5	53	17	3	0	0	2	1	0				0	
1 b	20	4	49	15	6	3	0	2	1	0	0					
1 a	23	46	4	6	10	8	2	0	0	0	0					
0		1	1	4	10	9	1	1	3	10	10	1	1	6	20	22

Figure 4.13: *Migrations of events between all* $\Delta\phi^*$ *and* x_{Bj} *bins. For each bin on the detector level, the numbers give the contribution in percentage from each bin on the hadron level. The diagonal elements thus show the purity. The bin 0 describes events that do not pass the DIS and/or dijet cuts. Empty bins has no entries.*

0: Non-dijet event

1: $8{\times}10^{-5} < x_{Bj} < 3{\times}10^{-4}$

2: $3{\times}10^{-4} < x_{Bj} < 6{\times}10^{-4}$

3: $6{\times}10^{-4} < x_{Bj} < 10^{-2}$

a: $0 < \Delta\phi^* < 80^\circ$

b: $80 < \Delta\phi^* < 120^\circ$

c: $120 < \Delta\phi^* < 150^\circ$

d: $150 < \Delta\phi^* < 170^\circ$

e: $170 < \Delta\phi^* < 180^\circ$

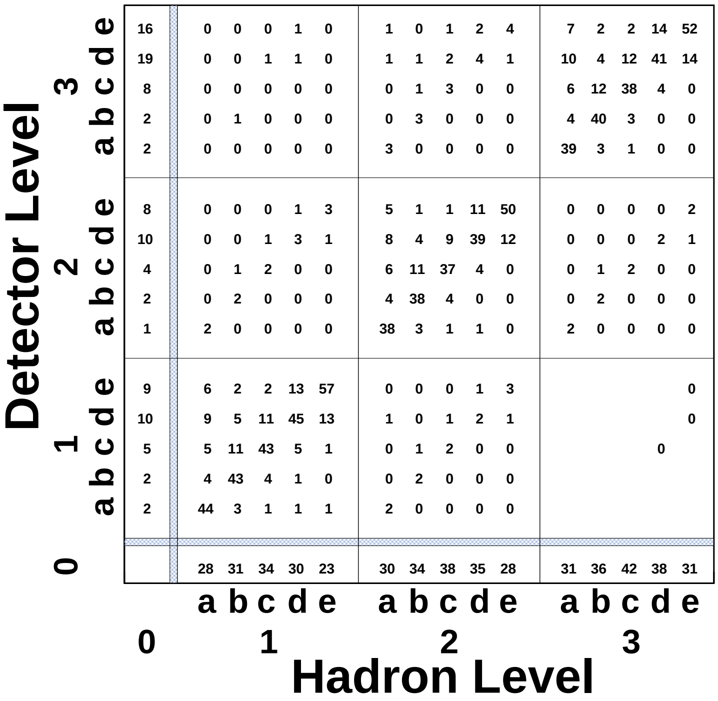

Detector Level \ Hadron Level	0	1 a	1 b	1 c	1 d	1 e	2 a	2 b	2 c	2 d	2 e	3 a	3 b	3 c	3 d	3 e
3 e	16	0	0	0	1	0	1	0	1	2	4	7	2	2	14	52
3 d	19	0	0	1	1	0	1	1	2	4	1	10	4	12	41	14
3 c	8	0	0	0	0	0	0	1	3	0	0	6	12	38	4	0
3 b	2	0	1	0	0	0	0	3	0	0	0	4	40	3	0	0
3 a	2	0	0	0	0	0	3	0	0	0	0	39	3	1	0	0
2 e	8	0	0	0	1	3	5	1	1	11	50	0	0	0	0	2
2 d	10	0	0	1	3	1	8	4	9	39	12	0	0	0	2	1
2 c	4	0	1	2	0	0	6	11	37	4	0	0	1	2	0	0
2 b	2	0	2	0	0	0	4	38	4	0	0	0	2	0	0	0
2 a	1	2	0	0	0	0	38	3	1	1	0	2	0	0	0	0
1 e	9	6	2	2	13	57	0	0	0	1	3					0
1 d	10	9	5	11	45	13	1	0	1	2	1					0
1 c	5	5	11	43	5	1	0	1	2	0	0				0	
1 b	2	4	43	4	1	0	0	2	0	0	0					
1 a	2	44	3	1	1	1	2	0	0	0	0					
0		28	31	34	30	23	30	34	38	35	28	31	36	42	38	31

Figure 4.14: *Migrations of events between all* $\Delta\phi^*$ *and* x_{Bj} *bins. For each bin on the hadron level, the numbers give the contribution in percentage to each bin on the detector level. The diagonal elements thus show the stability. The bin 0 describes events that do not pass the DIS and/or dijet cuts. Empty bins has no entries.*

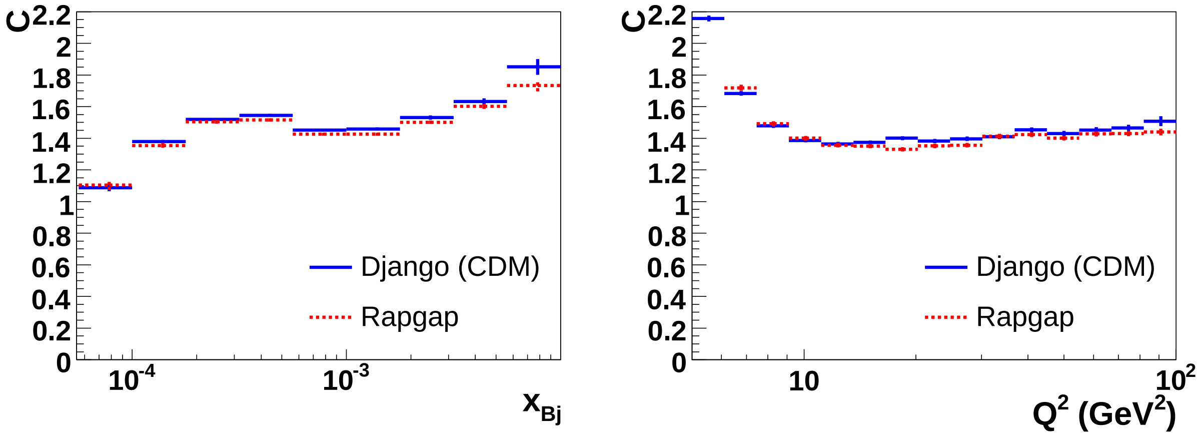

Figure 4.15: *Correction factors as calculated by* RAPGAP *and* DJANGO(CDM) *for the inclusive dijet cross sections* $d\sigma/dx_{Bj}$ *(left) and* $d\sigma/dQ^2$ *(right).*

by reweighting the MC distributions such that the same weight is applied on both the hadron and the detector level to obtain good agreement with data on the detector level. The assumption is then that the MC gives a good description of the observable also on the hadron level. Since this method demands an assumption of the "true" distribution on the hadron level, it should not be used if migration effects are large (low purity and stability) [122]. Furthermore, the bin-by-bin correction only takes into account migrations between neighbouring bins, which is clearly not sufficient for the $\Delta\phi^*$ decorrelations.

The inclusive dijet cross sections, however, do not have significant migrations between non-neighbouring bins and also have large purities and stabilities. Therefore the correction of the inclusive cross sections are made using the bin-by-bin method. The correction factors are shown in Figure 4.15. The large correction factors at low Q^2 are due to the fiducial cuts in the SPACAL (see Chapter 3) which removes many events close to the beampipe, i.e. at low Q^2. This of course also affects the correction factors for $\frac{d\sigma}{dx_{Bj}}$. It has been checked that if the influence of the fiducial cuts is removed, the correction factors are relatively flat around $1.3 - 1.4$ for $\frac{d\sigma}{dQ^2}$, and the peak at small x_{Bj} disappears in the correction factors for $\frac{d\sigma}{dx_{Bj}}$.

In order to cope with large migrations, more sophisticated correction methods have to be used. Another unfolding technique is to define a smearing matrix S, such that

$$\bar{D} = S\bar{H}$$

where $\bar{D}$ and $\bar{H}$ represent vectors of events on the detector and the hadron level, respectively, in each bin. The smearing matrix thus describes the detector response of the true values $\bar{H}$, giving the measured vector $\bar{D}$. S can be estimated by simulating events on the hadron level using a Monte Carlo event generator and then letting these events undergo a detector simulation. The events can then be identified on both the hadron and the detector level, and the migrations are thus known (provided the simulation is correct). If we define the unfolding matrix U as the matrix that gives the hadron level vector if applied on the measured data,

$$\bar{H} = U\bar{D},$$

then a first guess would be to simply invert the smearing matrix such that

$$U = S^{-1}.$$

However, this method has some disadvantages, for instance that the results are unstable with respect to small statistical fluctuations in the determination of the smearing matrix. Also, large statistical fluctuations may give negative number of events, and in extreme cases, the inverse of the smearing matrix might not even exist.

Another way of determining the unfolding matrix U, without having to invert the smearing matrix S, is by using Bayes' theorem [122],

$$P(C_i|E_j) = \frac{P(E_j|C_i) \cdot P(C_i)}{\sum_{l=1}^{n_C} P(E_j|C_l) \cdot P(C_l)}, \tag{4.2}$$

which expresses that the probability $P(C_i|E_j)$ that an observed effect E_j (e.g. an event on the detector level) was produced by a cause C_i (an event on the hadron level) is proportional to the probability of the cause C_i to occur, $P(C_i)$, times the probability that the cause C_i will produce the effect E_j, $P(E_j|C_i)$. The sum in the denominator runs over the total number of causes n_C and ensures that the probabilities are always $\leqslant 1$. The estimation of the number of events of cause C_i, $\hat{n}(C_i)$, is then

$$\hat{n}(C_i) = \frac{1}{\epsilon_i} \sum_{j=1}^{n_E} P(C_i|E_j) \cdot n(E_j) \tag{4.3}$$

where n_E is the total number of effects and $n(E_j)$ is the measured number of effects E_j, i.e. the measured number of events in a certain bin j. Here we have also taken into account the efficiency

$$\epsilon_i = \sum_{j=1}^{n_E} P(E_j|C_i), \tag{4.4}$$

since not all causes need produce an effect. Inserting (4.4) into (4.3) gives

$$\hat{n}(C_i) = \sum_{j=1}^{n_E} U_{ij} \cdot n(E_j), \tag{4.5}$$

where the unfolding matrix U_{ij} is

$$U_{ij} = \frac{P(C_i|E_j)}{\epsilon} = \frac{P(E_j|C_i) \cdot P(C_i)}{\left(\sum_{l=1}^{n_E} P(E_l|C_i)\right)\left(\sum_{l=1}^{n_C} P(E_j|C_l) \cdot P(C_l)\right)}. \tag{4.6}$$

Here, $P(E_j|C_i)$ represents the smearing matrix S which can be estimated using detector simulated MC events. $P(C_i)$, on the other hand, is the probability of having a cause C_i, which is not known. However, by using an iterative procedure the unfolded distribution from iteration k can be seen as a better guess of $P(C_i)$ than the previous guess, and can therefore be used as input for iteration $k+1$. In this way, $P(C_i)$ can be completely unknown from the beginning.

The iterative method relies on the assumption that the unfolded distribution is a better estimator of $P(C_i)$ than obtained in the previous unfolding, such that for each iteration one

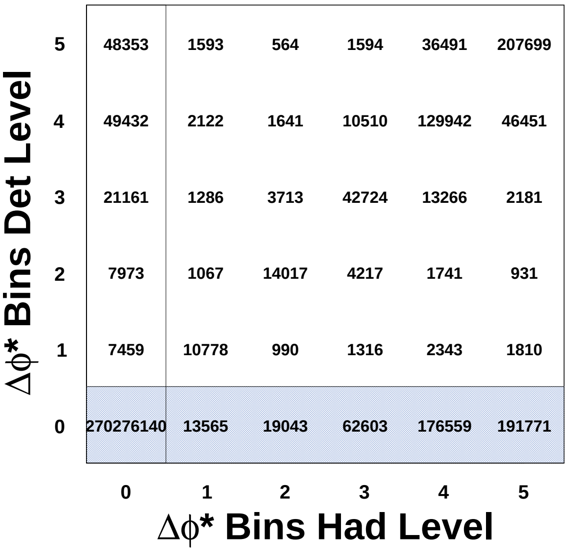

	0	1	2	3	4	5
5	48353	1593	564	1594	36491	207699
4	49432	2122	1641	10510	129942	46451
3	21161	1286	3713	42724	13266	2181
2	7973	1067	14017	4217	1741	931
1	7459	10778	990	1316	2343	1810
0	270276140	13565	19043	62603	176559	191771

Figure 4.16: *The smearing matrix for the lowest x_{Bj} bin, where each column (row) represents a $\Delta\phi^*$ bin on the hadron (detector) level, except the first column (row) which represents events that do not pass the DIS and/or the dijet cuts on the hadron (detector) level. The first row was excluded in the Bayesian unfolding procedure.*

is getting closer and closer to the "true" distribution. This is, however, not quite true. The unfolded distribution does approach the true distribution during the first few iterations, but after this it starts to deviate more and eventually converges. The optimal number of iterations must thus be determined by Monte Carlo simulations.

This Bayesian unfolding technique was used to correct the $\Delta\phi^*$ distributions. For each (x_{Bj} and Q^2) bin a smearing matrix was estimated using detector simulated MC events generated using RAPGAP and DJANGO(CDM). An example for the lowest x_{Bj} bin is shown in Figure 4.16. Each column (row) corresponds to a $\Delta\phi^*$ bin on the hadron (detector) level, except the first ones, which are filled with events not passing the DIS and/or dijet cuts. Due to the large number of events in the bin $(0, 0)$, large fluctuations occur between iterations, not only in shape, but also in normalisation. This bin does not contain any information about the migrations, and could be removed with a cut on the detector level. Since no cut was found that efficiently removes the events in this bin and at the same time keeps the other events in the first row, all events in the lowest row were excluded in the unfolding, but were corrected for bin-by-bin. Thus, the Bayesian unfolding takes into account migrations between all $\Delta\phi^*$ bins and the effect of events that migrate into the dijet sample from the hadron to the detector level, but does not consider migrations out of the dijet sample. The probabilities $P(C_i)$ used as input to the first iteration were chosen to be the (normalised) distributions on the hadron level obtained from the Monte Carlo program.

Having the smearing matrix and a first estimate of $P(C_i)$, the unfolding matrix can be calculated using (4.6) and an unfolded distribution be obtained. Before unfolding the data one must first determine the optimum number of iterations. This is done by unfolding detector simulated events from RAPGAP using the smearing matrix and initial distribution from DJANGO(CDM), and comparing the unfolded distribution to the true (generated)

Trigger	Definition
S0	SPCLe_IET > 2
S61	(SPCLe_IET > 2 || SPCLe_IET_Cen_3) && DCRPh_THig && zVtx_sig
S39	LAr_BR && LAr_electron_2 && FwdRay_T0 && LAr_IF && LAr_2or3_electrons
S64	LAr_IF > 1 && LAr_Etrans > 2
S66	LAr_IF > 1 && LAr_Etmiss > 2
S67	LAr_electron_1
S77	LAr_Etmiss > 1

Table 4.1: *Definition of triggers. Trigger elements for background rejection have been omitted.*

hadron level distribution from Rapgap for each iteration. In Figure 4.17 is shown the cross sections for the two lowest x_{Bj} bins obtained after the first five iterations compared to the true distribution, while Figure 4.18 shows the ratio of the unfolded distributions and the true distribution. Figure 4.18 seems to indicate that the distribution from the second iteration is closest to the true result. To quantify the difference between the distributions, the fractional difference between the unfolded and the true distribution, summed over all bins i in the histogram,

$$\sum_i \frac{|y_{i,unf} - y_{i,true}|}{y_{i,true}} \tag{4.7}$$

is calculated. This variable is shown in Figure 4.19 for the first 30 iterations. As can be seen, the best agreement is achieved after two iterations. Similar results has also been seen in [123, 124] and is consistent with the recommendation in [125]. However, there is no obvious reason why the second iteration should be the optimal choice. This has to be determined in each analysis. Very similar results are also obtained if Django(CDM) is unfolded using the smearing matrix from Rapgap, and also when unfolding $\frac{d^2\sigma}{dQ^2 d\Delta\phi^*}$ and $\frac{d^3\sigma}{dQ^2 dx_{Bj} d\Delta\phi^*}$, although occasionally the first or the third iteration is closest to the true distribution.

4.3 Trigger Efficiencies

It is also necessary to investigate the efficiencies of the trigger selection. The trigger efficiency is calculated using so-called monitor triggers, which should be chosen such that the monitor trigger and the trigger under study do not have any trigger elements in common. However, the monitor triggers must be able to trigger the same type of events as the physics trigger. For the trigger (S0||S61), which depends on the SPACAL calorimeter and the tracking chambers, the combination (S39||S64||S66||S67||S77), which only depends on the LAr calorimeter, is used as monitor trigger. The definition of each trigger is given in Table 4.1, while Appendix B summarizes the definition of each trigger element.

The trigger efficiency is then defined by

$$\epsilon_{Trigger} = \frac{N_{MON\&\&TRIG}}{N_{MON}}$$

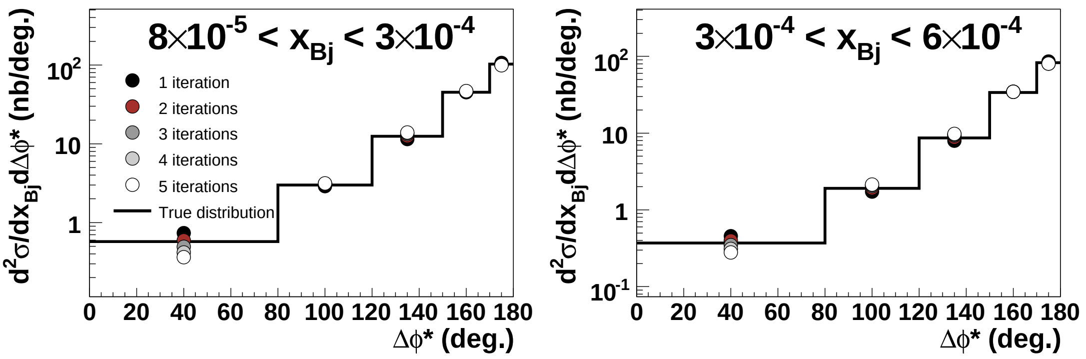

Figure 4.17: *The unfolded distributions obtained when unfolding* Rapgap *using the smearing matrix from* Django(CDM)*. The first five iterations (circles) are compared to the true distribution (black line).*

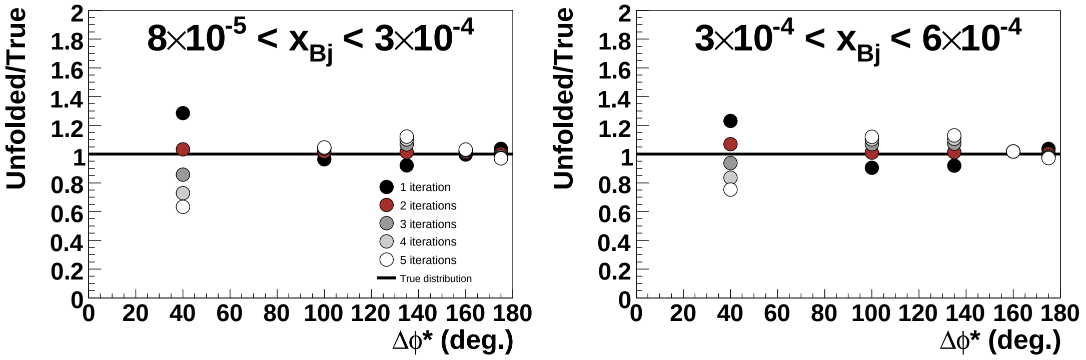

Figure 4.18: *The unfolded distributions obtained when unfolding* Rapgap *using the smearing matrix from* Django(CDM)*. The first five iterations (circles) are divided with the true distribution.*

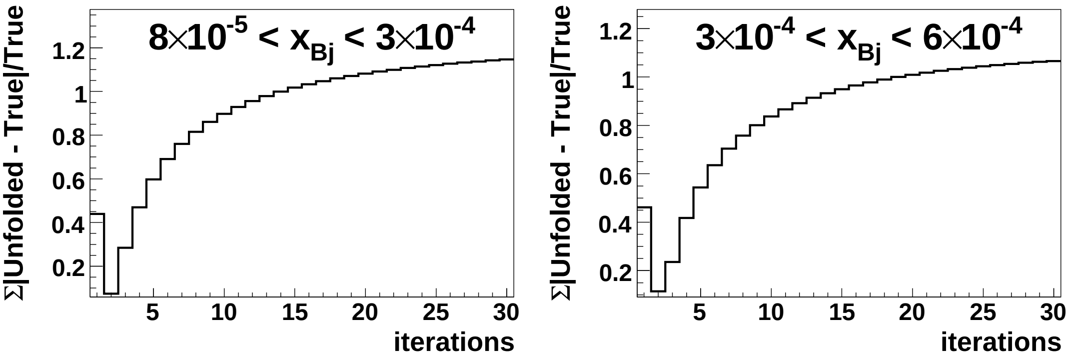

Figure 4.19: *The difference between the unfolded and the true distributions, defined by Equation (4.7), for the first 30 iterations.* Rapgap *was unfolded using the smearing matrix generated by* Django(CDM).

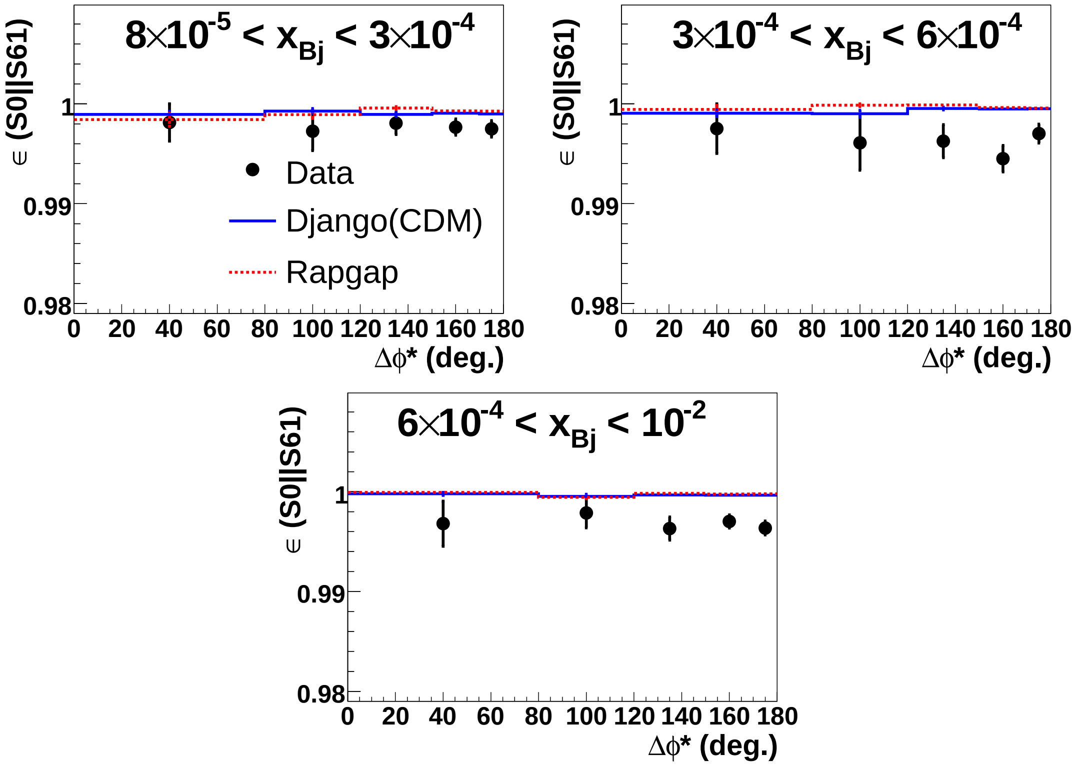

Figure 4.20: *Trigger efficiencies for the (S0||S61) trigger as a function of* $\Delta\phi^*$ *in bins of* x_{Bj}. *Data are compared to the predictions of* Rapgap *and* Django(CDM).

where $N_{MON\&\&TRIG}$ is the number of events triggered by both the selected trigger and the monitor trigger, while N_{MON} is the number of events triggered by the monitor trigger alone. Here, only raw triggers are used, which are defined before any prescaling of the events. In order to study the efficiency for the azimuthal decorrelation measurement, $\epsilon_{Trigger}$ is calculated after the DIS and dijet selection. The trigger efficiency for the (S0||S61) trigger is shown as a function of $\Delta\phi^*$ in bins of x_{Bj} in Figure 4.20 and in bins of Q^2 in Figure 4.21. As can be seen, the efficiency is close to 1 for both data and the Monte Carlo simulations in all analysis bins, although the efficiency of the triggers seem to be slightly overestimated in the simulation. Nevertheless, the differences are small, and no correction factors need to be applied for the trigger efficiency.

4.4 Systematic Errors

In this section, the contributions to the systematic errors are discussed. Table 4.2 and 4.3 summarize the contributions and the typical uncertainties in the inclusive and the $\Delta\phi^*$ dijet decorrelation cross sections, respectively.

Electron Calibration

One contribution to the systematic error is the uncertainty of the SPACAL energy calibration. An uncertainty of the SPACAL energy scale leads to a systematic error of the measured energy of the scattered electron, which in turn leads to uncertainties in the values

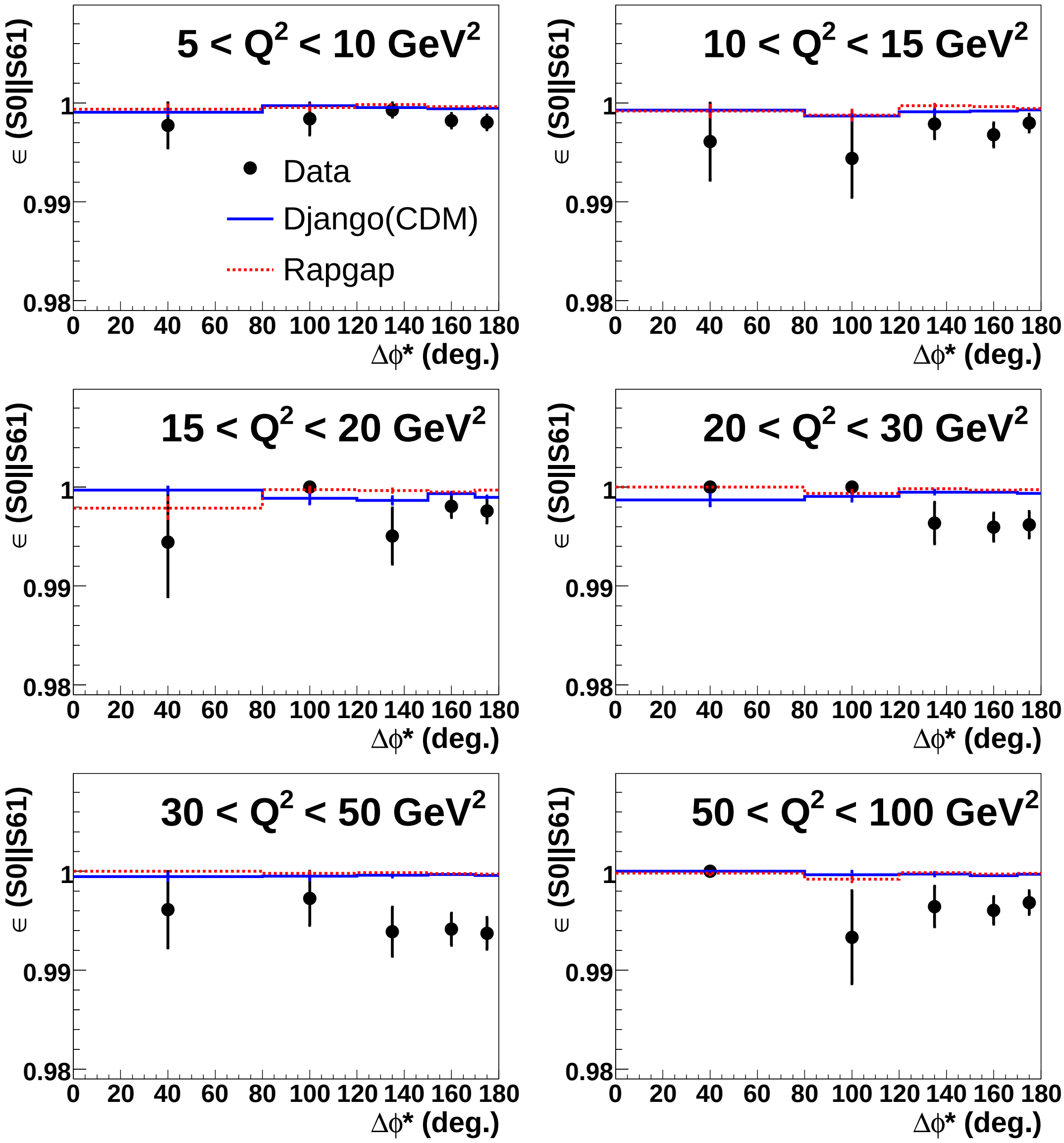

Figure 4.21: *Trigger efficiencies for the (S0||S61) trigger as a function of* $\Delta\phi^*$ *in bins of* Q^2. *Data are compared to the predictions of* RAPGAP *and* DJANGO(CDM).

of the kinematic variables Q^2, x_{Bj} and y, see (3.2). This results in an uncertainty of the four-vector of the exchanged photon and, as a consequence, to an uncertainty of the boost to the HCM frame.

The SPACAL calibration can be studied by comparing the energy of the scattered electron as measured by the SPACAL ($E_e^{'}$) with that measured using the double angle method ($E_{DA}^{'}$) [115]. $E_{DA}^{'}$ is calculated using the polar angles of the electron (θ_e) and the combined four-vector of all other final state particles (γ_H) according to

$$E_{DA}^{'} = \frac{2E_e \cdot \sin\gamma_H}{\sin\gamma_H + \sin\theta_e - \sin(\gamma_H + \theta_e)}$$

where $E_e = 27.6$ GeV is the energy of the incoming electron,

$$\gamma_H = 2 \cdot atan \left(\frac{\sum_i E - \sum_i P_z}{\sum_i P_T} \right)$$

and the sums run over all final state particles except the scattered electron. The double angle is (to lowest order) independent of the energy measured by the SPACAL and may serve as a reference. The distribution of the $E_e^{'}/E_{DA}^{'}$ ratio is shown in Figures 4.22 and 4.23 for data, RAPGAP and DJANGO(CDM) in bins of Q^2 and $E_e^{'}$, respectively. As can be seen, the ratio is shifted towards values below unity and the largest shift is seen for low Q^2. However, this behaviour is well understood as can be seen by the good description of the data by the MC simulations. This is also shown in Figure 4.24, where the ratio of the mean values for data and MC, $< E_e^{'}/E_{DA}^{'} >_{DATA} \ / < E_e^{'}/E_{DA}^{'} >_{MC}$, is shown as a function of Q^2 and $E_e^{'}$. This confirms that the uncertainty of the energy scale of the SPACAL is ±1% [126, 127].

Hadronic Calibration

The calibration of the LAr calorimeter can be studied using the ratio of the transverse momentum of the HFS ($P_{T,HFS}$) and the transverse momentum of the scattered electron ($P_{T,e}$). The HFS is calculated as the sum of the four-momenta of all final state particles, except the scattered electron. In Figures 4.25 and 4.26, the ratio $P_{T,HFS}/P_{T,e}$ is plotted in bins of η and E_T^* of the hardest jet (the jet with the largest transverse momentum in the HCM frame) for data, RAPGAP and DJANGO(CDM). Since the scattered electron and the HFS should balance due to momentum conservation, the ratio $P_{T,HFS}/P_{T,e}$ should peak at 1. Again, the shift and the width are well described by the MC simulations, indicating that the hadronic energy scale is well calibrated. In Figure 4.27, the double ratio $< P_{T,HFS}/P_{T,e} >_{DATA} \ / < P_{T,HFS}/P_{T,e} >_{MC}$ is shown as a function of E_T^* and η of the hardest jet. As can be seen, the variation stays within 4% which is taken as the systematic uncertainty of the hadronic energy scale.

Electron Polar Angle

As described in Section 2.2.1, the polar angle of the scattered electron is measured using the BDC with a precision of ±1 mrad. The uncertainty in the cross sections due to this is relatively small.

Model Dependence

Another source of systematic uncertainties comes from the determination of the cross sections using different Monte Carlo generators. In this analysis, the final cross section

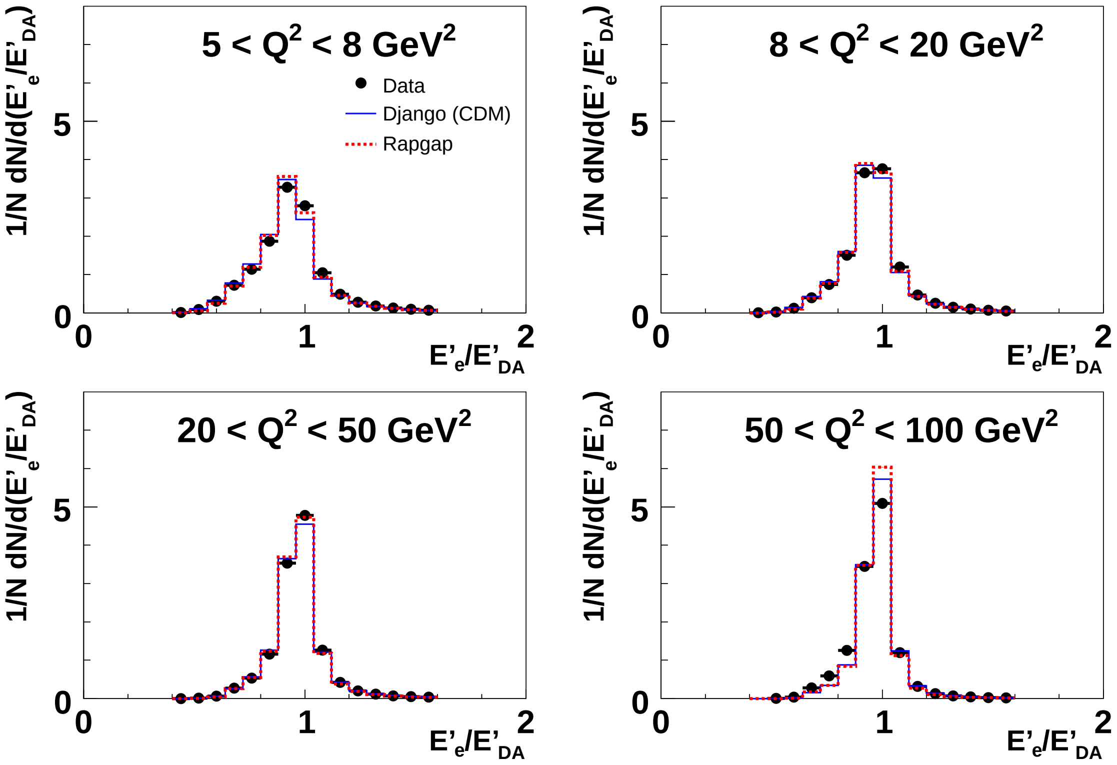

Figure 4.22: *The normalised distributions of the ratio* E'_e/E'_{DA} *in bins of* Q^2*, obtained using* Rapgap *and* Django(CDM)*.*

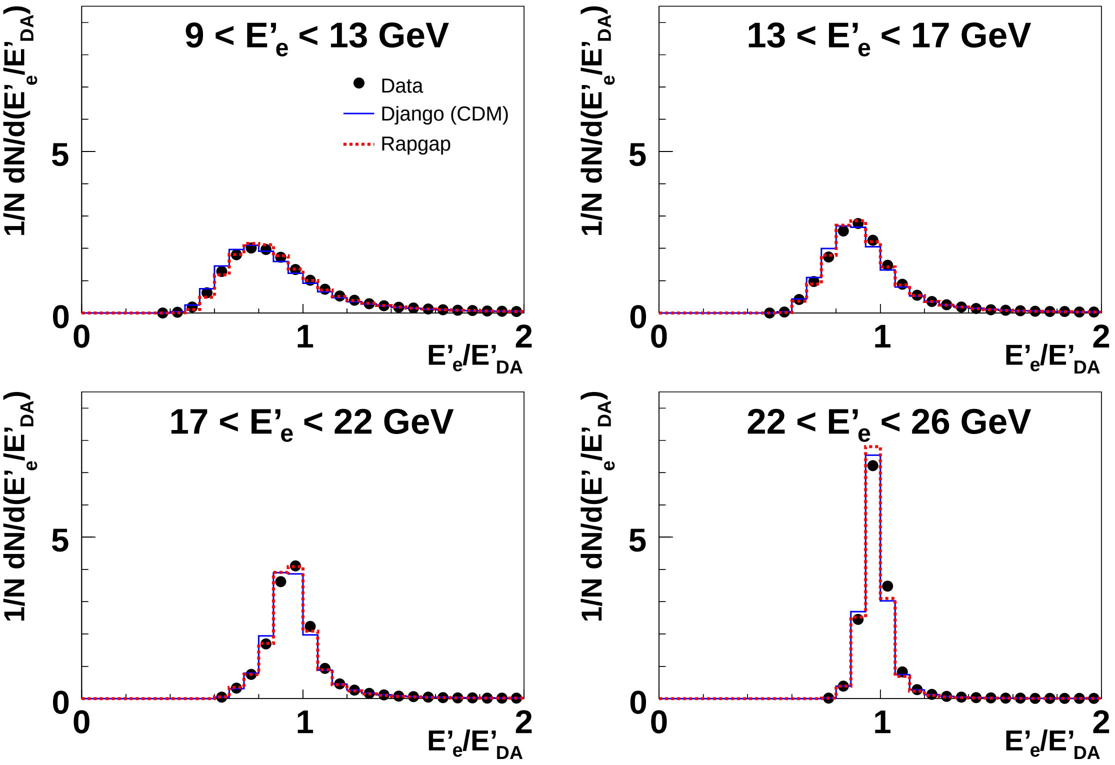

Figure 4.23: *The normalised distributions of the ratio* E_e'/E_{DA}' *in bins of* E_e'*, obtained using* Rapgap *and* Django(CDM)*.*

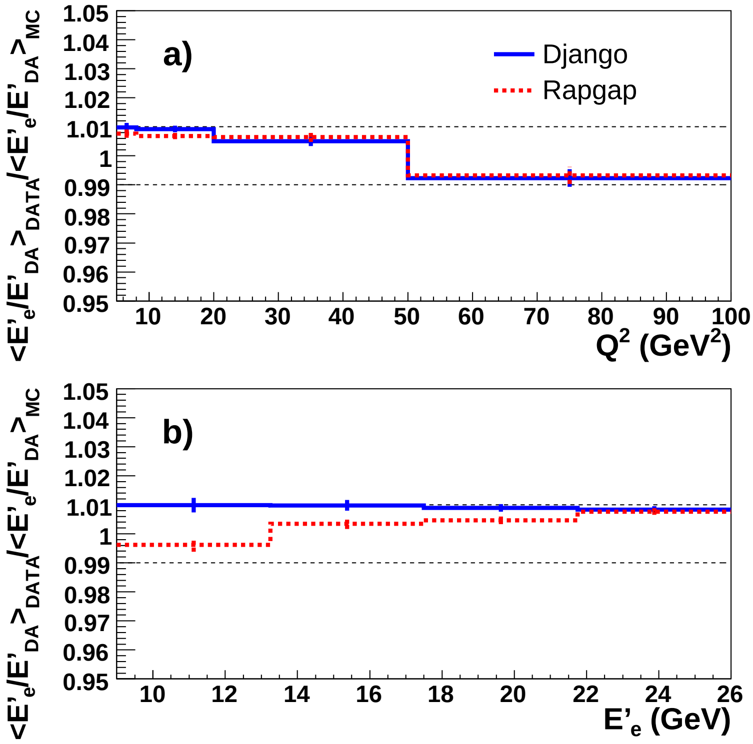

Figure 4.24: *The ratio* $< E_e'/E_{DA}' >_{DATA}$ / $< E_e'/E_{DA}' >_{MC}$ *as a function of* Q^2 *a) and* E_e' *b), obtained using* RAPGAP *and* DJANGO(CDM). *The dashed lines indicate an uncertainty in the SPACAL energy calibration of ± 1%.*

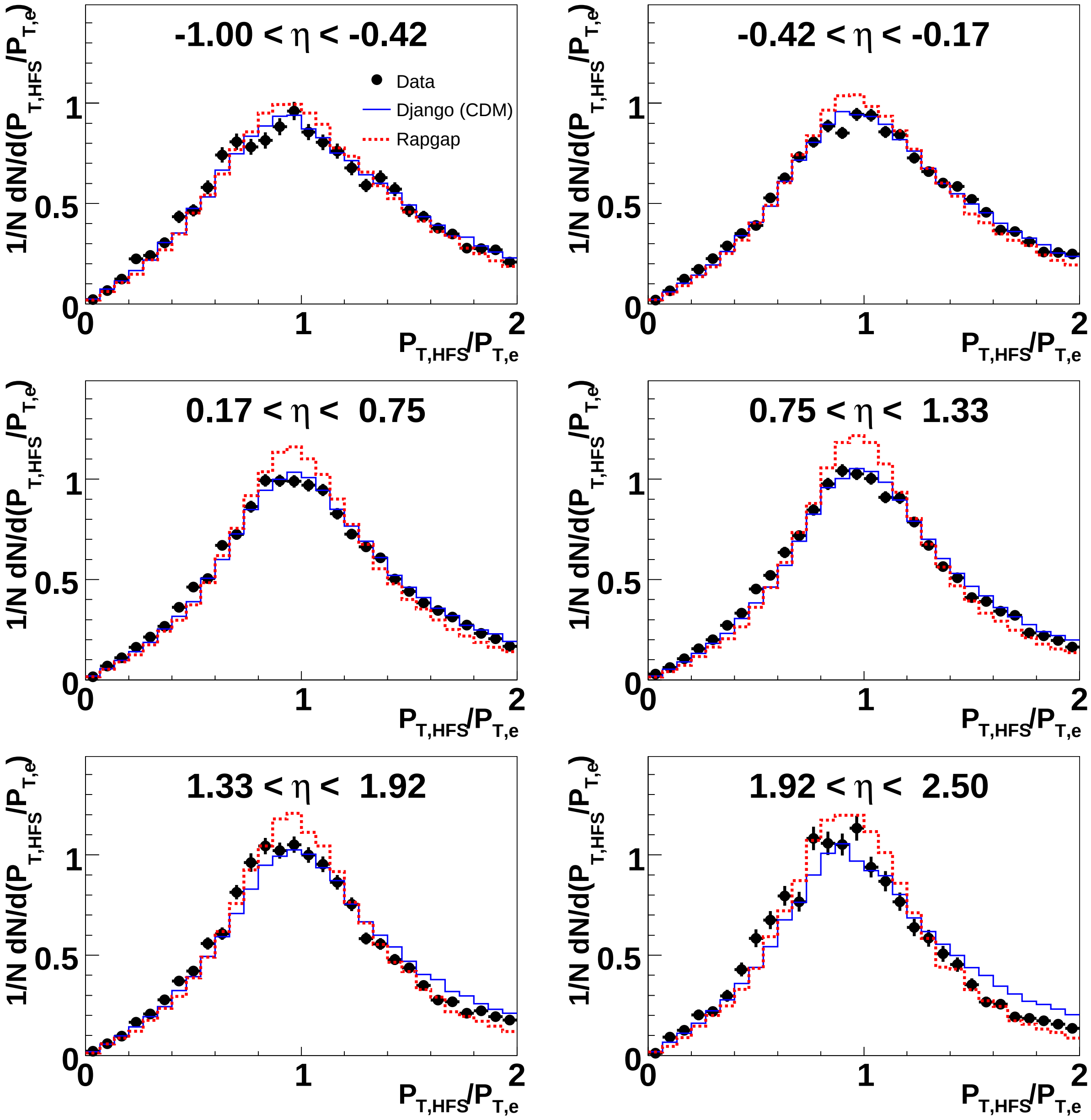

Figure 4.25: *The normalised distributions of the ratio* $P_{T,HFS}/P_{T,e}$ *in bins of* η *of the hardest jet, obtained using* RAPGAP *and* DJANGO(CDM).

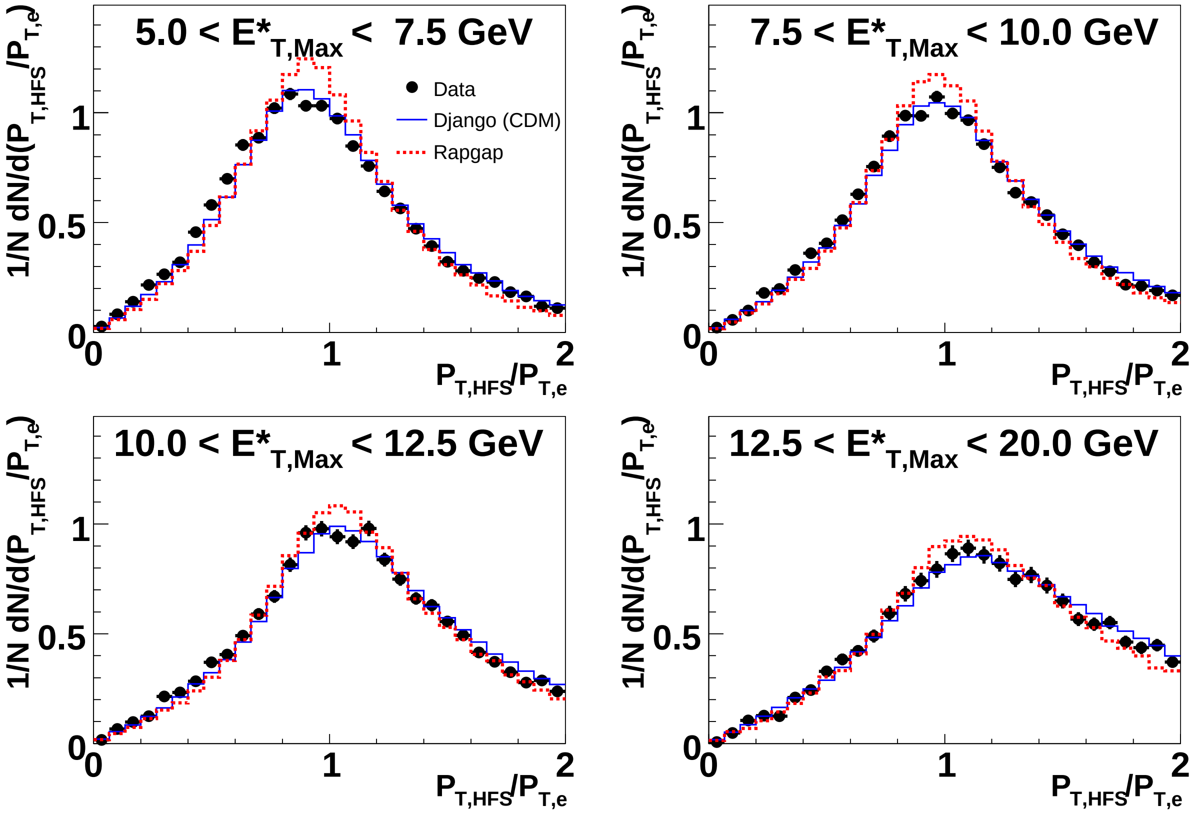

Figure 4.26: *The normalised distributions of the ratio* $P_{T,HFS}/P_{T,e}$ *in bins of* $E^*_{T,Max}$ *of the hardest jet, obtained using* RAPGAP *and* DJANGO(CDM).

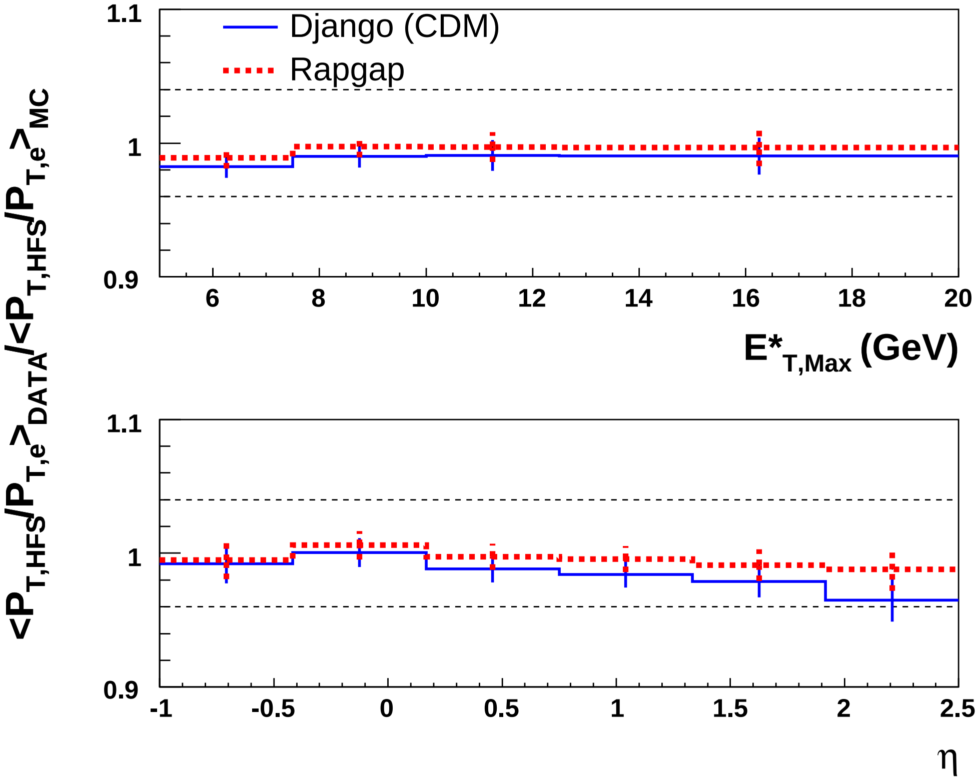

Figure 4.27: *The ratio* $< P_{T,HFS}/P_{T,e} >_{DATA}$ / $< P_{T,HFS}/P_{T,e} >_{MC}$ *as a function of* E_T^* *and* η *of the hardest jet, obtained using* Rapgap *and* Django(CDM)*. The dashed lines indicate an uncertainty in the LAr energy calibration of* $\pm$ *4%.*

is taken as the average of the cross sections obtained by Rapgap and Django(CDM), while half of the difference between these has been added as a systematic error.

Unfolding Bias
The unfolding bias is estimated by unfolding Rapgap using Django(CDM) and then comparing the unfolded distribution to the generated hadron level distribution of Rapgap (and vice versa), as explained in Section 4.2. The mean deviation from the correct distribution in each bin is taken as a systematic uncertainty.

Photoproduction Background
Although specific cuts were made to remove photoproduction events from the sample used in this analysis (see Chapter 3), there might still remain some photoproduction events. This has been investigated using the MC generator Phojet. The contribution to the systematic error from photoproduction background is negligible.

Track Momentum
The uncertainty in the determination of the momentum of a track gives an additional uncertainty in the construction of the combined objects. To investigate the systematic error in the cross sections due to this mismeasurement, the track momentum has been varied by ± 3%. This gives a negligible contribution to the systematic uncertainty.

Luminosity
The luminosity is determined to a precision of ± 1.5%, which is taken as an overall systematic uncertainty.

Source	Uncertainty	Typical $\Delta\sigma$	
		$\frac{d\sigma}{dx_{bj}}$	$\frac{d\sigma}{dQ^2}$
SPACAL electromagnetic energy scale	± 1%	0.5-2%	0.5-2%
Polar angle of scattered electron	± 1 mrad	<1%	<1%
LAr hadronic energy scale	± 4%	2-5%	2-5%
Track momentum	± 3%	$\ll$ 1%	$\ll$ 1%
Model uncertainty	$\frac{\lvert C_{Rapgap}-C_{Django}\rvert}{2}$	1-3%	1-5%
Photoproduction background		$\ll$ 1%	$\ll$ 1%
Luminosity		1.5%	1.5%

Table 4.2: *Summary of systematic errors and their sources for the inclusive dijet cross sections.*

4.5 Results

As previously explained, the aim of this analysis is to measure the azimuthal correlations in dijet events, since the $\Delta\phi^*$ separation between the two jets is directly related to the transverse momentum k_T of the interacting parton. The $\Delta\phi^*$ distributions should thus be sensitive to different parton dynamics in the initial state cascade and also to different

Source	Uncertainty	Typical $\Delta\sigma$		
		$\frac{d^2\sigma}{dx_{bj}d\Delta\phi^*}$	$\frac{d^2\sigma}{dQ^2d\Delta\phi^*}$	$\frac{d^3\sigma}{dx_{bj}dQ^2d\Delta\phi^*}$
SPACAL electromagnetic energy scale	± 1%	0.5-2%	0.5-2%	1-3%
Polar angle of scattered electron	± 1 mrad	<1%	<1%	0.5-2%
LAr hadronic energy scale	± 4%	2-7%	2-7%	2-10%
Track momentum	± 3%	$\ll$ 1%	$\ll$ 1%	$\ll$ 1%
Model uncertainty	$\frac{\lvert C_{Rapgap}-C_{Django}\rvert}{2}$	0.5-2%	0.5-2%	1-4%
Unfolding bias	$\frac{\Delta\sigma_{Rapgap}+\Delta\sigma_{Django}}{2}$	1-4%	1-4%	1-7%
Photoproduction background		$\ll$ 1%	$\ll$ 1%	$\ll$ 1%
Luminosity		1.5%	1.5%	1.5%

Table 4.3: *Summary of systematic errors and their sources for the $\Delta\phi^*$ correlation cross sections.*

parameterizations of unintegrated gluon densities in models using k_T-factorization. First, however, the inclusive dijet cross sections as a function of x_{Bj} and Q^2 are presented.

Inclusive Dijet Cross Sections

The inclusive dijet cross sections as a function of x_{Bj} are presented in Figure 4.28 and 4.29. Below the cross section plots, the ratio of the theoretical predictions and the measured data are also shown. Statistical uncertainties correspond to the inner error bars, while the outer error bars represent the total uncertainty (statistical and systematic uncertainties added in quadrature). In Figure 4.28, the measured data are compared to the predictions of Cascade using two different unintegrated gluon density functions (uGDFs), J2003 set2 and A0 (see Section 1.8). Using the A0 uGDF, Cascade describes the cross section at small x reasonably well, while it undershoots the data in this region with J2003 set2. However, the cross section predicted by Cascade increases with increasing x_{Bj} compared to the measured data, and at large x_{Bj}, both predictions overshoot the data by approximately the same amount. Figure 4.29 compares the same data to cross sections obtained using Rapgap and Lepto(CDM)[1]. If only using the direct component, Rapgap predicts too low a cross section for all x_{Bj} bins except the highest one. By adding the resolved photon component, the cross section increases more at small x_{Bj} than at large x_{Bj}, giving a total cross section which is about 5-10% above the data at all x_{Bj}. The shape of the cross section predicted by Lepto(CDM) resembles the one obtained by Cascade(A0), with the difference that Lepto(CDM) is much closer to the data at large x_{Bj} and overshoots with about 10% at small x_{Bj}.

Figure 4.30 and 4.31 show the inclusive dijet cross section as a function of Q^2 compared to the predictions of Cascade, Rapgap and Lepto(CDM). Since x_{Bj} and Q^2 are correlated, the same tendencies are seen here as in Figure 4.28 and 4.29. Worth noting is that Lepto(CDM) describes the data almost perfectly between $5 < Q^2 < 10$ GeV^2, and also Rapgap DIR+RES does a better job at low Q^2 than at low x_{Bj}. A comparison to fixed order QCD calculations is not meaningful since the NLO 2-jet calculations suffer from incomplete cancellations between real and virtual corrections, while the NLO 3-jet calculations diverge when only demanding two jets, as explained in Section 1.9. However,

---

[1] The data are presented on the non-radiative hadron level. Therefore, Lepto(CDM), which does not include QED corrections, is used for comparisons instead of Django(CDM).

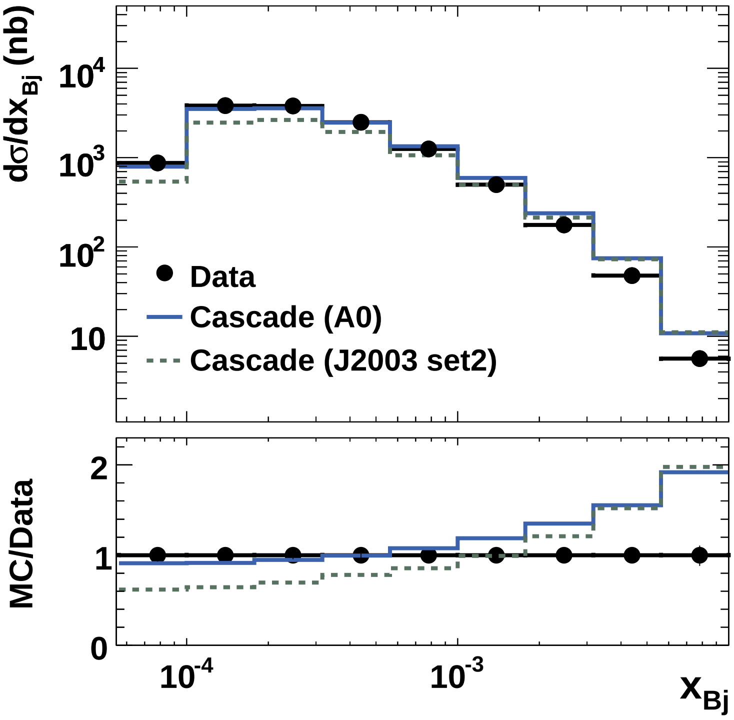

Figure 4.28: *Inclusive dijet cross sections as a function of x_{Bj} compared to the predictions of* Cascade *using two different uGDFs.*

the problematic region is when the two jets are back-to-back, making comparisons to NLO calculations possible if $\Delta\phi^* < 180°$.

Double Differential Dijet Cross Sections

Figure 4.32 gives the dijet cross section as a function of the azimuthal angle $\Delta\phi^*$ in bins of x_{Bj} compared to NLO 2-jet and NLO 3-jet calculations. The renormalisation scale μ_r and factorisation scale μ_f are in these calculations chosen as the average transverse energy of the two jets, $\mu_r = \mu_f = \left(\frac{E^*_{T1}+E^*_{T2}}{2}\right)$. The scale uncertainties, indicated with error bands around the central values, are estimated by varying μ_r and μ_f simultaneously a factor 2 up and 1/2 down. Corrections for hadronisation effects are made bin-by-bin using Cascade with the KMR [128] and A0 uGDFs for the 2-jet and 3-jet case, respectively. The KMR gluon density is evolved using only one gluon emission, and the generated events should therefore, on the parton level, be more similar to the NLO 2-jet calculations. For the NLO calculations, the PDF CTEQ6M [86] is used. In the back-to-back bins ($170 < \Delta\phi^* < 180°$) the predictions of the NLO calculations become meaningless due to infrared sensitivity. The remaining phase space is not covered by LO 2-jet calculations, since the non back-to-back topology requires at least one additional emission, and therefore the NLO 2-jet calculation effectively becomes a LO prediction for the $\Delta\phi^*$ observable. As seen from Figure 4.32 such a description is not sufficient to reproduce the data. The NLO 3-jet calculation, effectively being an NLO prediction, is closer to the data, but is systematically low for $\Delta\phi^* < 150°$. However, the scale uncertainties are large, typically 20 - 50%, and cover the data in most bins. When normalising the distributions to the cross section between $0 < \Delta\phi^* < 170°$ in each x_{Bj} bin, as has been done in Figure 4.33, there is partial cancellation of the scale

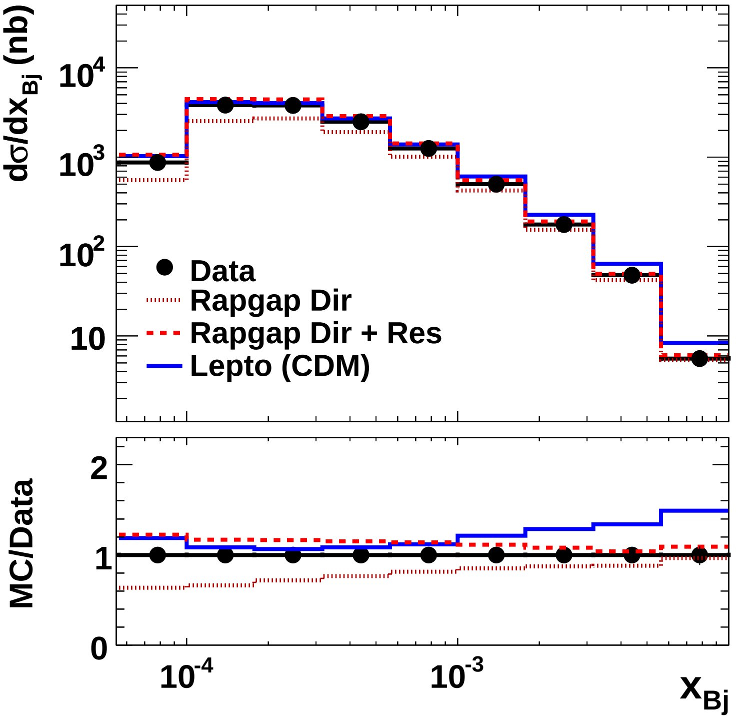

Figure 4.29: *Inclusive dijet cross sections as a function of* x_{Bj}*. Data are compared to* Rapgap DIR *(dotted line),* Rapgap DIR+RES *(dashed line) and* Lepto(CDM) *(full line).*

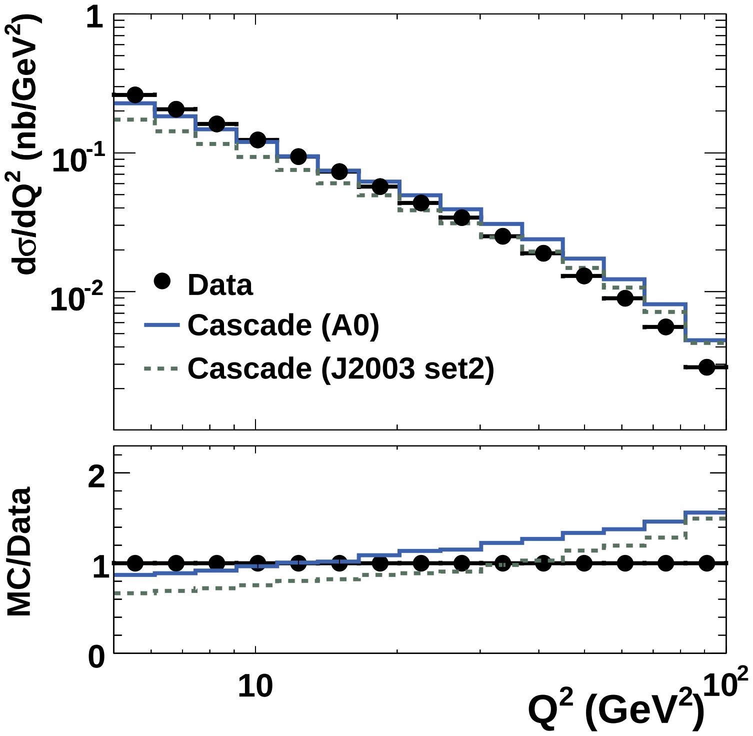

Figure 4.30: *Inclusive dijet cross sections as a function of* Q^2 *compared to the predictions of* CASCADE *using two different uGDFs.*

uncertainties for the NLO calculations. As can be seen, the data are no longer within the scale uncertainties of the NLO 3-jet calculation. Figure 4.34 shows the same data as Figure 4.32 but compared to the predictions of CASCADE using the A0 and J2003 set2 uGDFs. Whereas CASCADE (J2003 set2) describes the data fairly well in all but the lowest x_{Bj} bin, CASCADE (A0) fails to describe the data in all bins, predicting too many jets with small $\Delta\phi^*$. This clearly shows the sensitivity of $\Delta\phi^*$ to the unintegrated gluon density, indicating that the k_T-spectrum of the A0 uGDF is too hard, i.e. it has too many gluons with large k_T.

In Figure 4.35, data are compared to the predictions of RAPGAP DIR, RAPGAP DIR+RES and LEPTO(CDM). RAPGAP DIR predicts about the right amount of back-to-back jets but produces too few dijets with smaller $\Delta\phi^*$. The situation at small $\Delta\phi^*$ is somewhat improved by adding the resolved photon component, but this on the other hand also adds too many back-to-back jets. Also LEPTO(CDM) predicts too many back-to-back jets, but in contrast to RAPGAP DIR+RES, LEPTO(CDM) is closer to data at low x_{Bj} than at high x_{Bj}.

The $\Delta\phi^*$ correlations have also been measured in bins of Q^2, shown in Figures 4.36 - 4.39. In Figure 4.36 we see again that NLO 2-jet (α_s^2) calculations fail to describe the data, whereas NLO 3-jet (α_s^3) calculations improve the situation but are still systematically low for $\Delta\phi^* < 150°$. The data are, however, described within the large scale uncertainties. Normalising the data to the visible cross section between $0 < \Delta\phi^* < 170°$ in each Q^2 bin, shown in Figure 4.37, there is again partial cancellation of the scale uncertainties such that the data are no longer described by the NLO calculations. Figure 4.38 shows the same

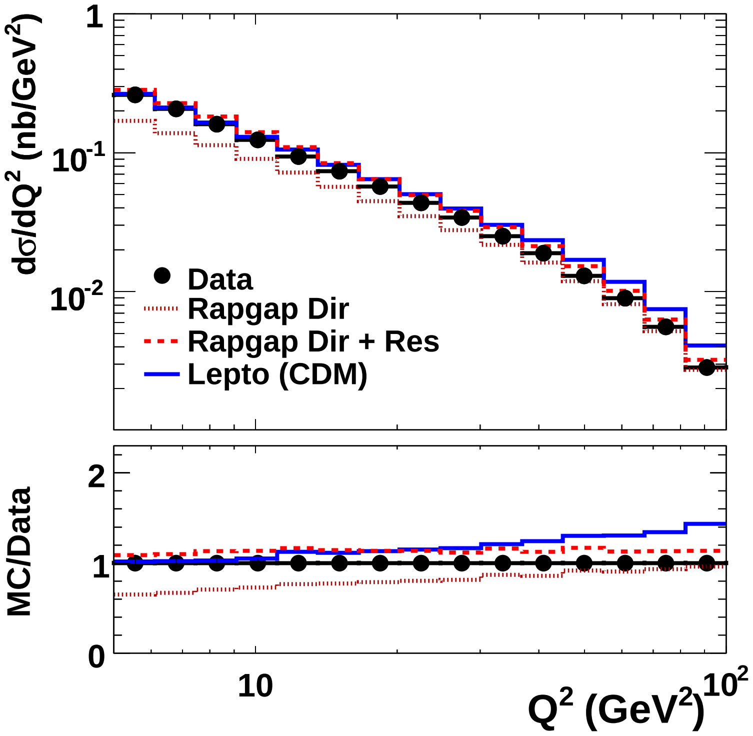

Figure 4.31: *Inclusive dijet cross sections as a function of* Q^2*. Data are compared to* Rapgap DIR *(dotted line),* Rapgap DIR+RES *(dashed line) and* Lepto(CDM) *(full line).*

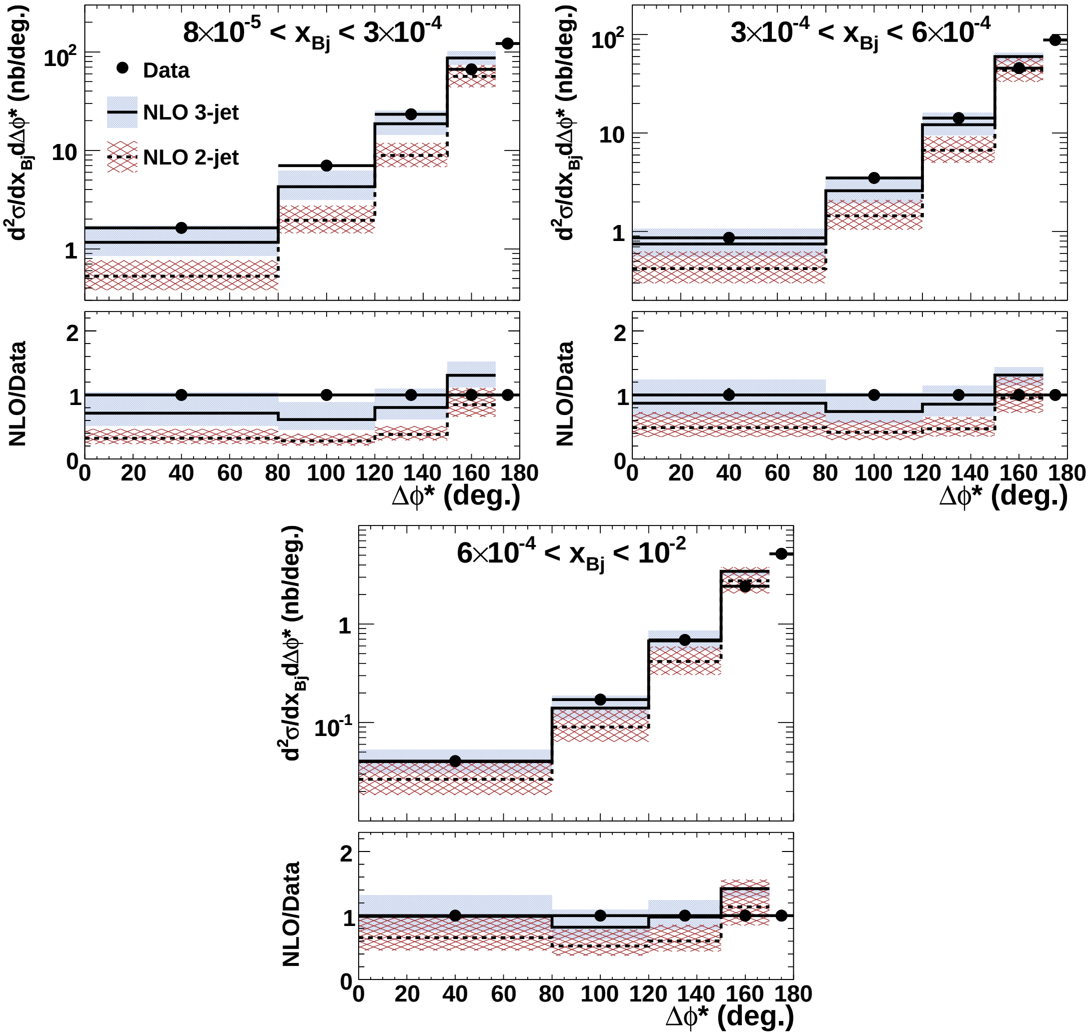

Figure 4.32: *Dijet cross sections as a function of* $\Delta\phi^*$ *in bins of* x_{Bj}. *Data are compared to NLO 3-jet (full line) and NLO 2-jet (dashed line) calculations obtained from the* NLO-JET++ *program. The error bands represent the scale uncertainties as described in the text.*

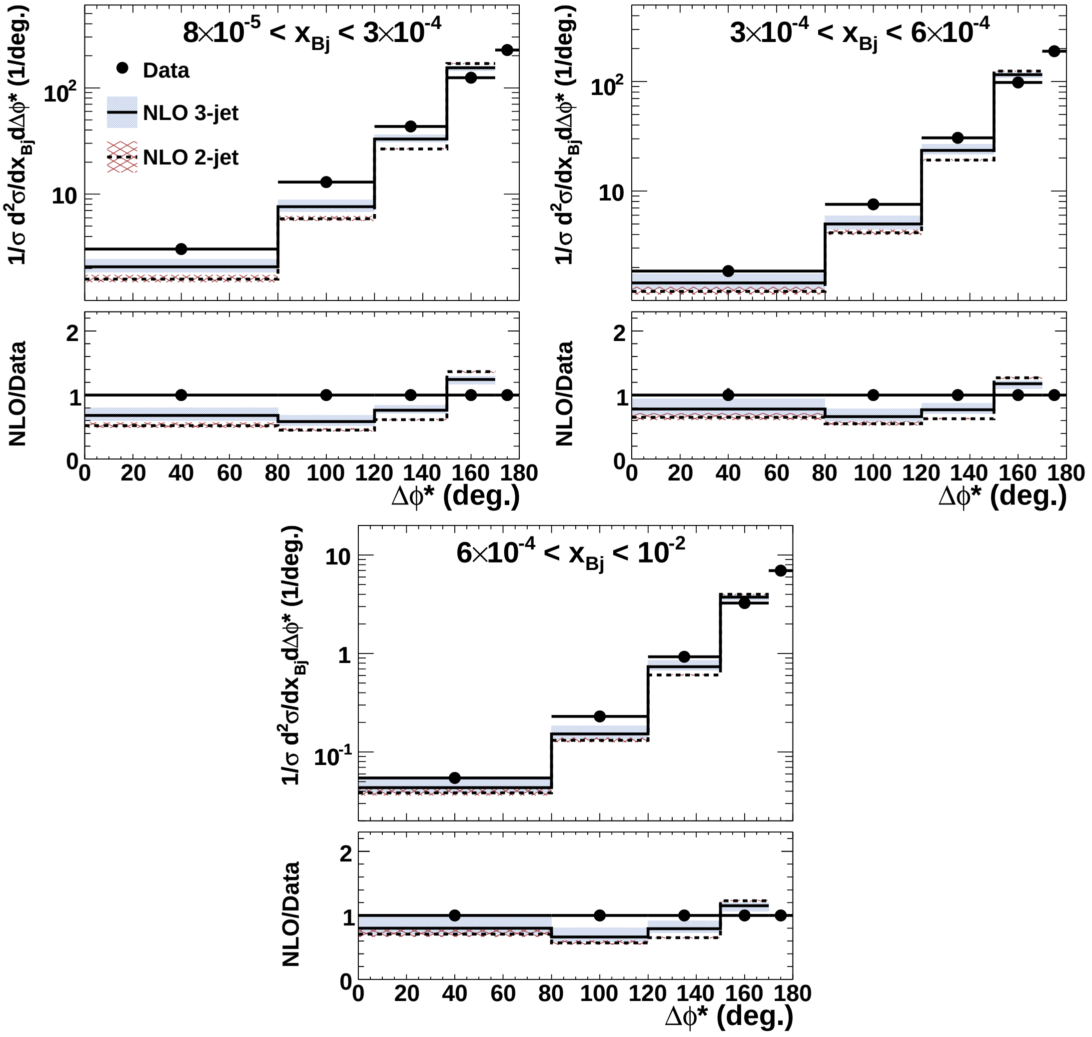

Figure 4.33: *Dijet cross sections as a function of $\Delta\phi^*$ in bins of x_{Bj} normalised to the visible cross section between $0 < \Delta\phi^* < 170^\circ$ in each x_{Bj} bin. Data are compared to NLO 3-jet (full line) and NLO 2-jet (dashed line) calculations obtained from the* NloJet++ *program. The error bands represent the scale uncertainties as described in the text.*

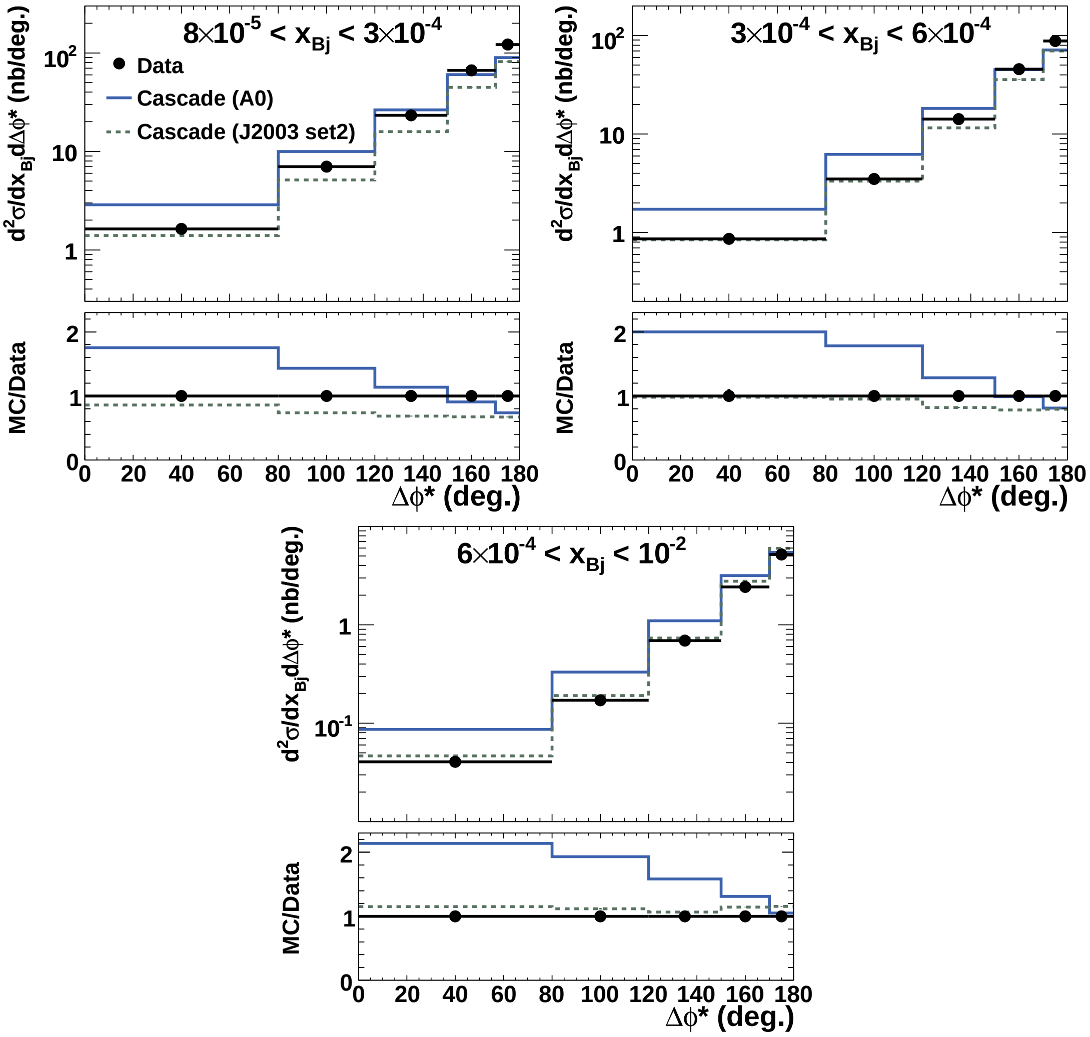

Figure 4.34: *Dijet cross sections as a function of $\Delta\phi^*$ in bins of x_{Bj} compared to the predictions of* CASCADE *using two different uGDFs.*

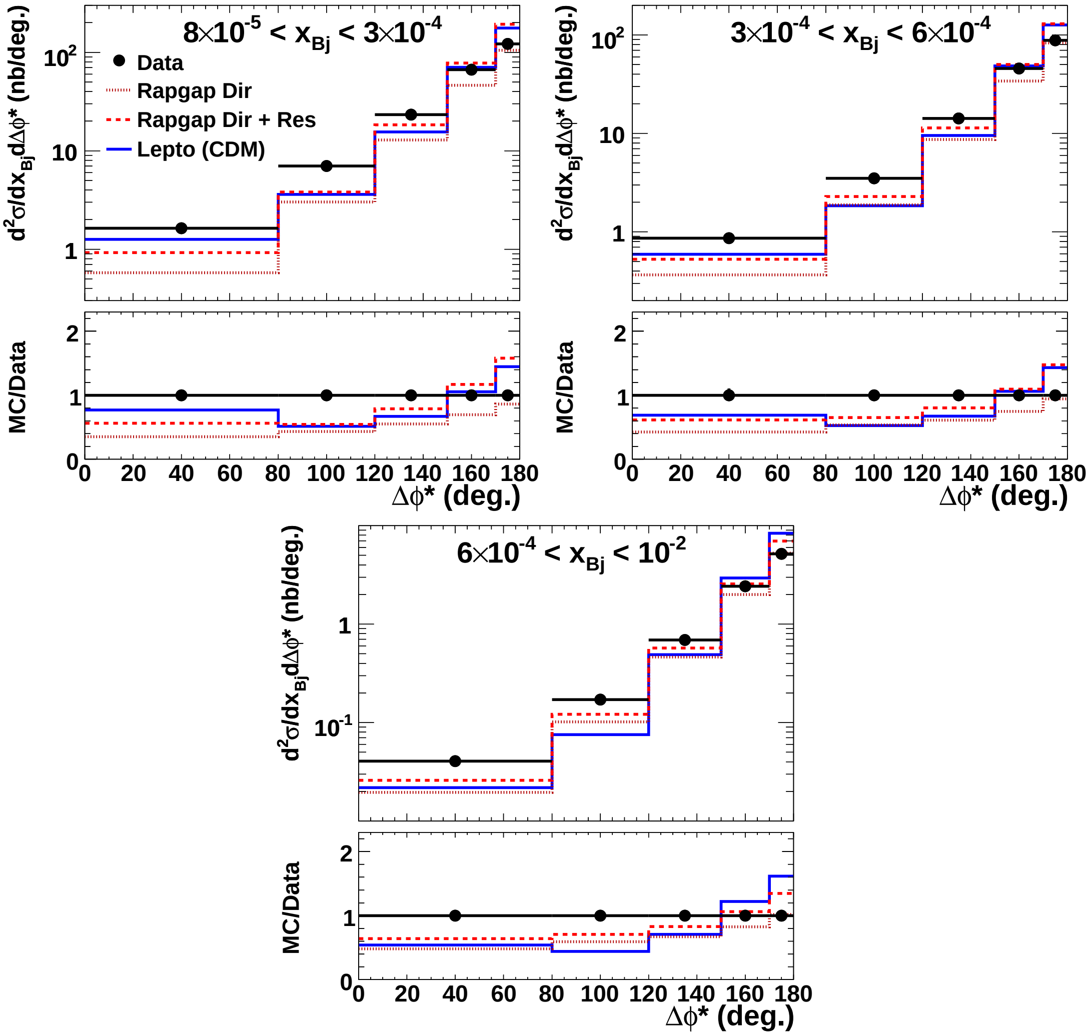

Figure 4.35: *Dijet cross sections as a function of* $\Delta\phi^*$ *in bins of* x_{Bj}. *Data are compared to* Rapgap DIR *(dotted line),* Rapgap DIR+RES *(dashed line) and* Lepto(CDM) *(full line).*

data as Figure 4.36 compared to CASCADE. Using the uGDF J2003 set2, CASCADE is able to describe the data reasonably well, except in the lowest and highest Q^2 bins, while CASCADE(A0) fails in all bins. Comparisons to RAPGAP DIR, RAPGAP DIR+RES and LEPTO(CDM) are shown in Figure 4.39. Again, all models fail to describe the shape of the data, predicting too few dijets with small azimuthal separations and, in the case of RAPGAP DIR+RES and LEPTO(CDM), too many back-to-back jets.

Triple Differential Dijet Cross Sections

The $\Delta\phi^*$ correlations and the ratios between the theoretical predictions and the data are also presented triple differentially in bins of x_{Bj} and Q^2, as shown in Figures 4.40 - 4.47. The same tendencies are seen as in the previous figures: the NLO calculations are systematically low for $\Delta\phi^* < 150°$, as are RAPGAP and LEPTO(CDM), while CASCADE with the A0 uGDF again overshoots the data for small $\Delta\phi^*$. The best description is found with CASCADE J2003 set2, which describes the data well in most bins, although it overshoots the data in the largest x_{Bj} and Q^2 bin and undershoots it in the smallest x_{Bj} and Q^2 bins.

In order to compare the decorrelation in different kinematic regions, the measured $\frac{d^2\sigma}{dx_{Bj}d\Delta\phi^*}$ data are shown in Figure 4.48 for all three x_{Bj} bins normalised to the cross section in each respective back-to-back bin. In addition, the ratio of each cross section and the cross section in the lowest x_{Bj} bin is shown. It is clearly seen that the decorrelation increases as x_{Bj} decreases, in agreement with the expectation that lower x_{Bj} implies more radiation and hence less back-to-back jets. The same tendency is also seen in the theoretical predictions (not shown).

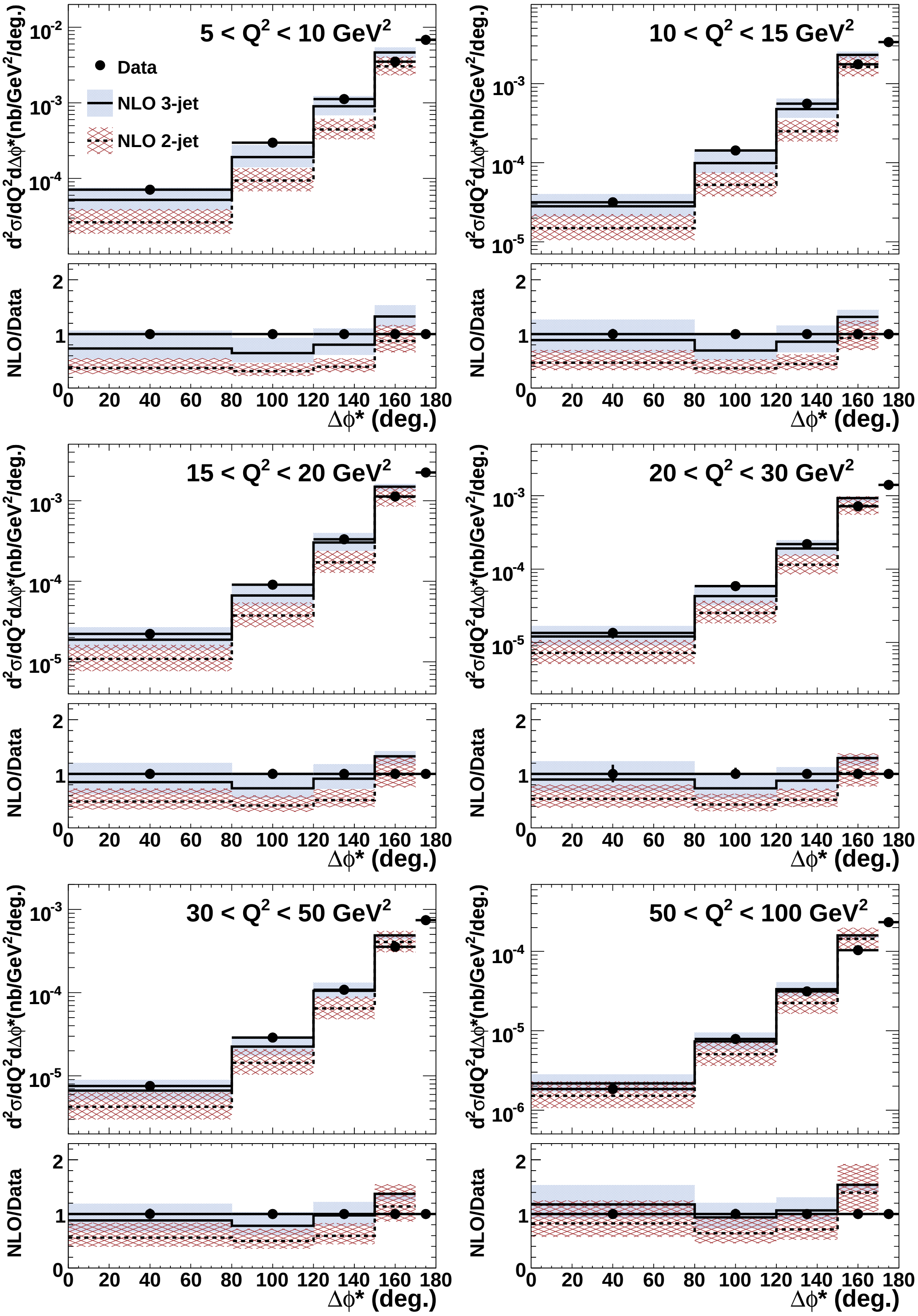

Figure 4.36: *Dijet cross sections as a function of* $\Delta\phi^*$ *in bins of* Q^2*. Data are compared to NLO 3-jet (full line) and NLO 2-jet (dashed line) calculations obtained from the* Nlo-Jet++ *program. The error bands represent the scale uncertainties as described in the text.*

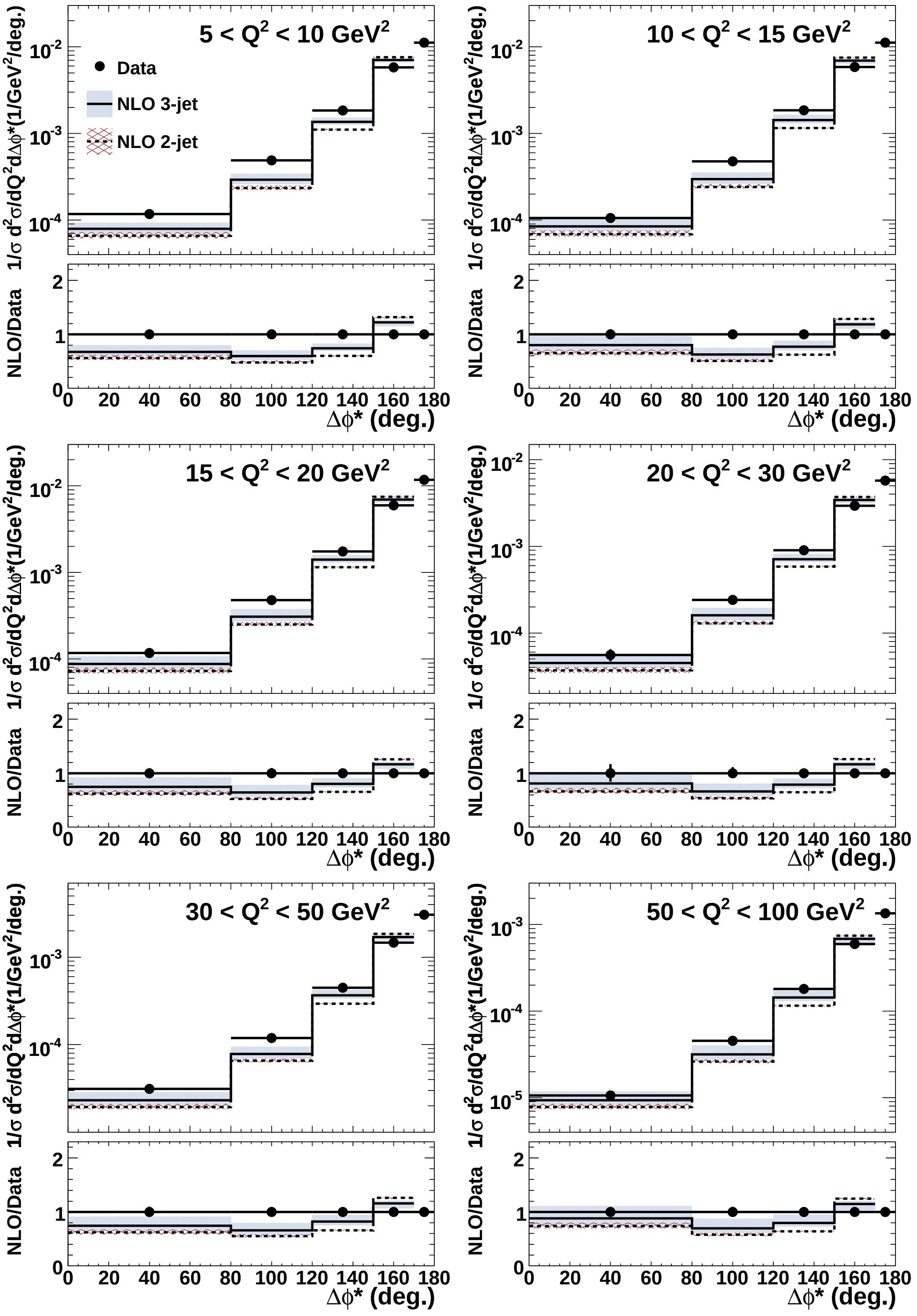

Figure 4.37: *Dijet cross sections as a function of* $\Delta\phi^*$ *in bins of* Q^2 *normalised to the visible cross section between* $0 < \Delta\phi^* < 170°$ *in each* Q^2 *bin. Data are compared to NLO 3-jet (full line) and NLO 2-jet (dashed line) calculations obtained from the* NLOJET++ *program. The error bands represent the scale uncertainties as described in the text.*

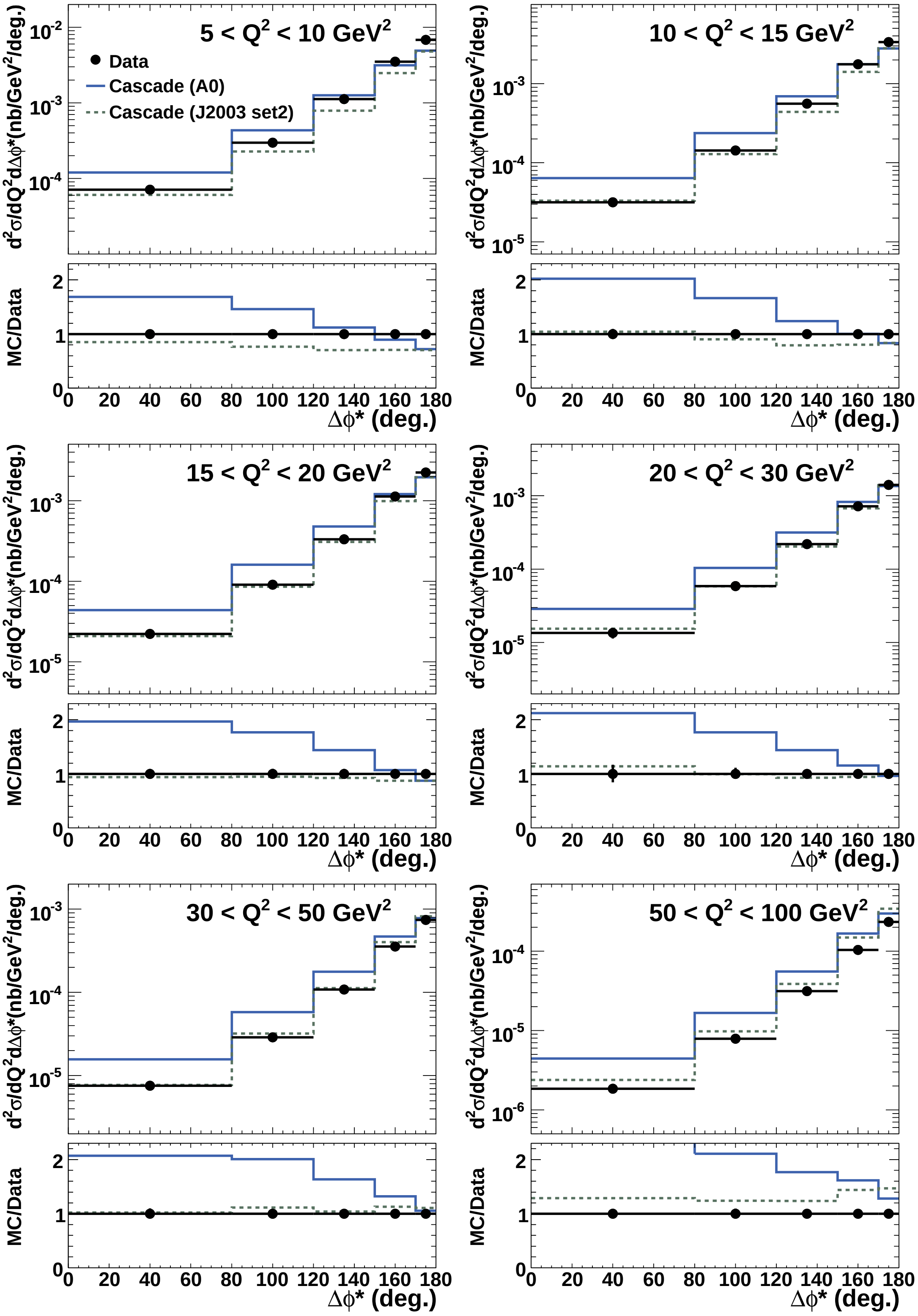

Figure 4.38: *Dijet cross sections as a function of $\Delta\phi^*$ in bins of Q^2 compared to the predictions of* Cascade *using two different uGDFs.*

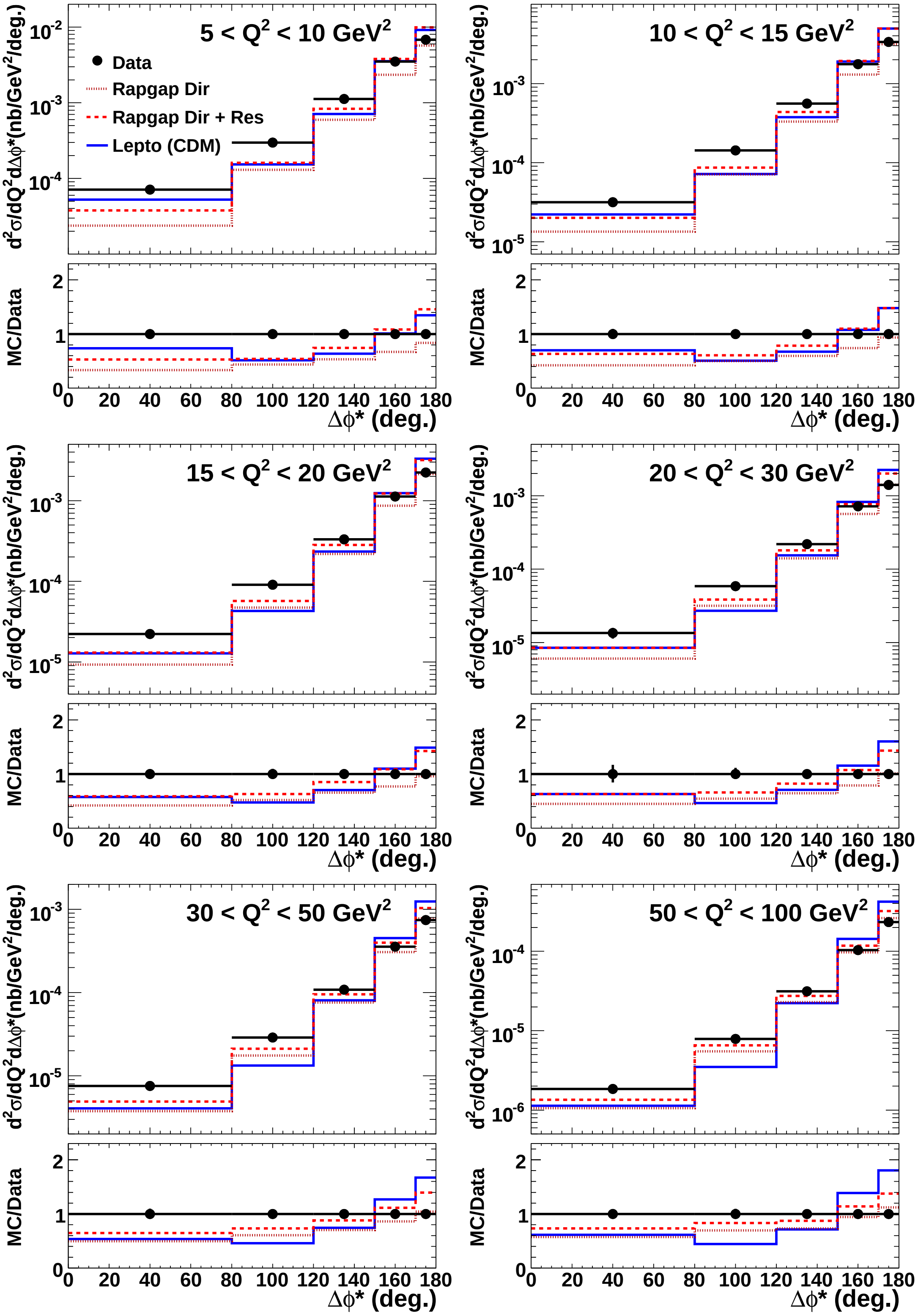

Figure 4.39: *Dijet cross sections as a function of* $\Delta\phi^*$ *in bins of* Q^2*. Data are compared to* RAPGAP DIR *(dotted line),* RAPGAP DIR+RES *(dashed line) and* LEPTO(CDM) *(full line).*

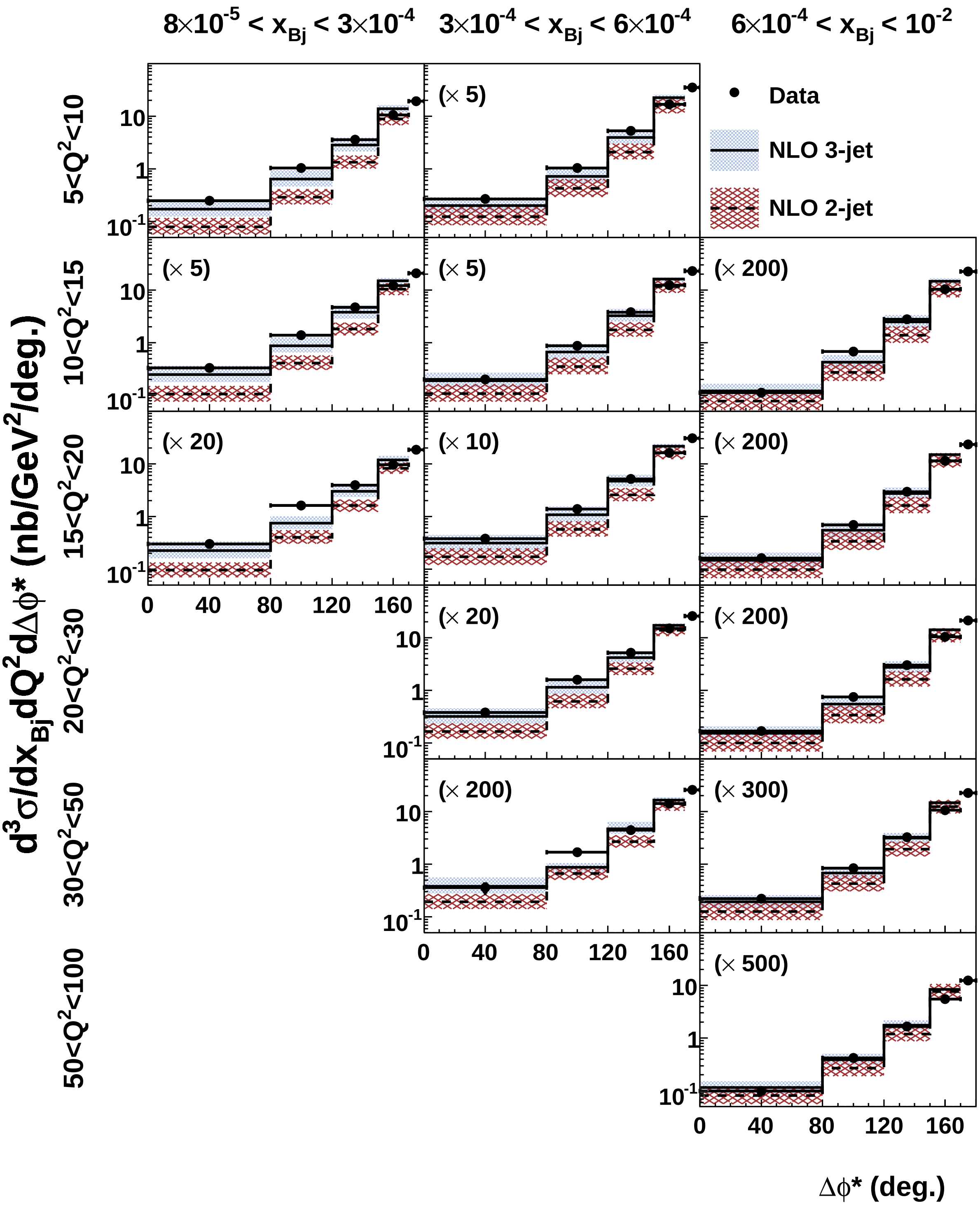

Figure 4.40: *Dijet cross sections as a function of* $\Delta\phi^*$ *in bins of* x_{Bj} *and* Q^2*. Data are compared to NLO 3-jet (full line) and NLO 2-jet (dashed line) calculations obtained from the* NLOJET++ *program. The error bands represent the scale uncertainties as described in the text.*

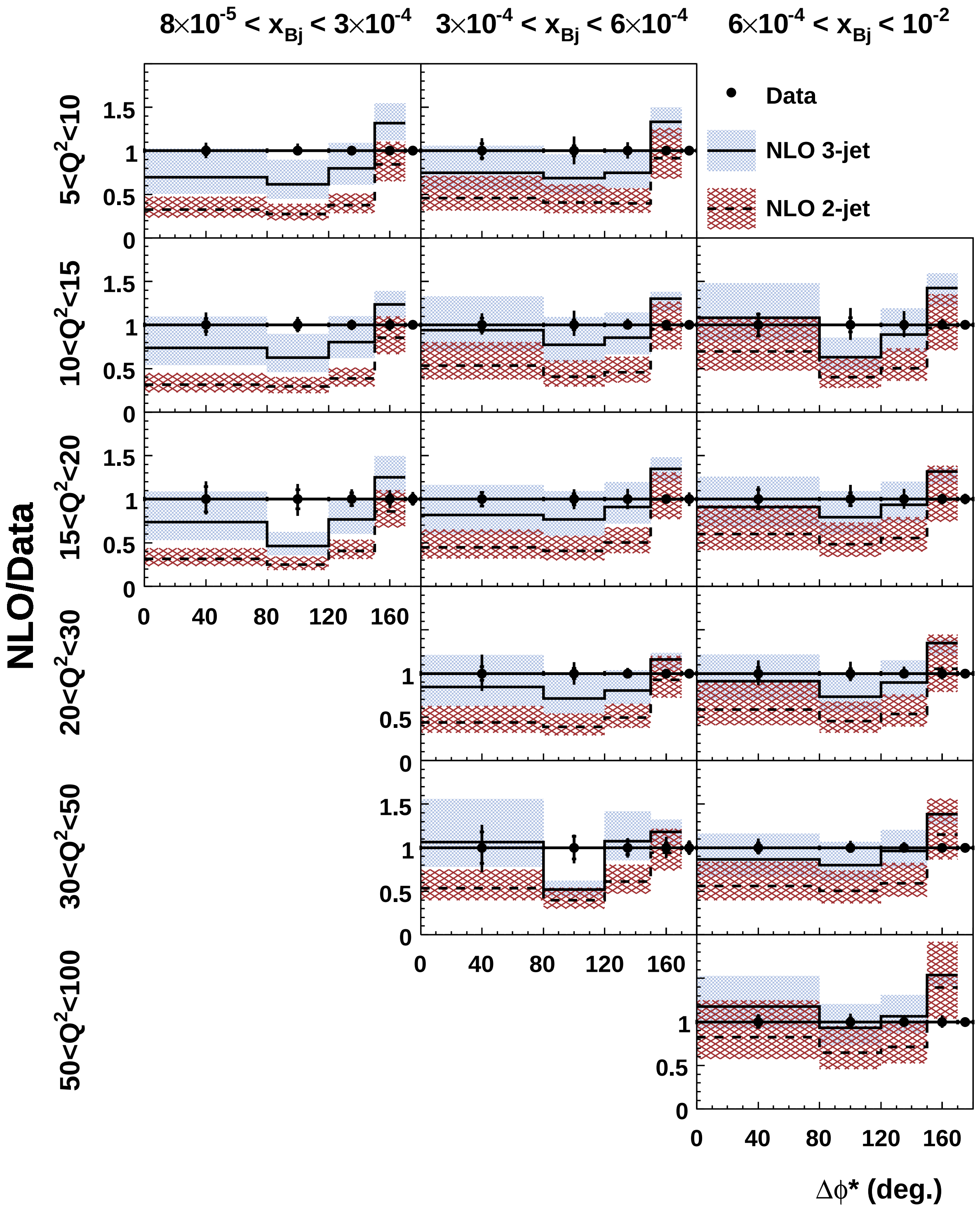

Figure 4.41: *Ratio of the theoretical predictions and the measured dijet cross sections as a function of* $\Delta\phi^*$ *in bins of* x_{Bj} *and* Q^2*. NLO 3-jet (full line) and NLO 2-jet (dashed line) calculations were obtained from the* NloJet++ *program. The error bands represent the scale uncertainties as described in the text.*

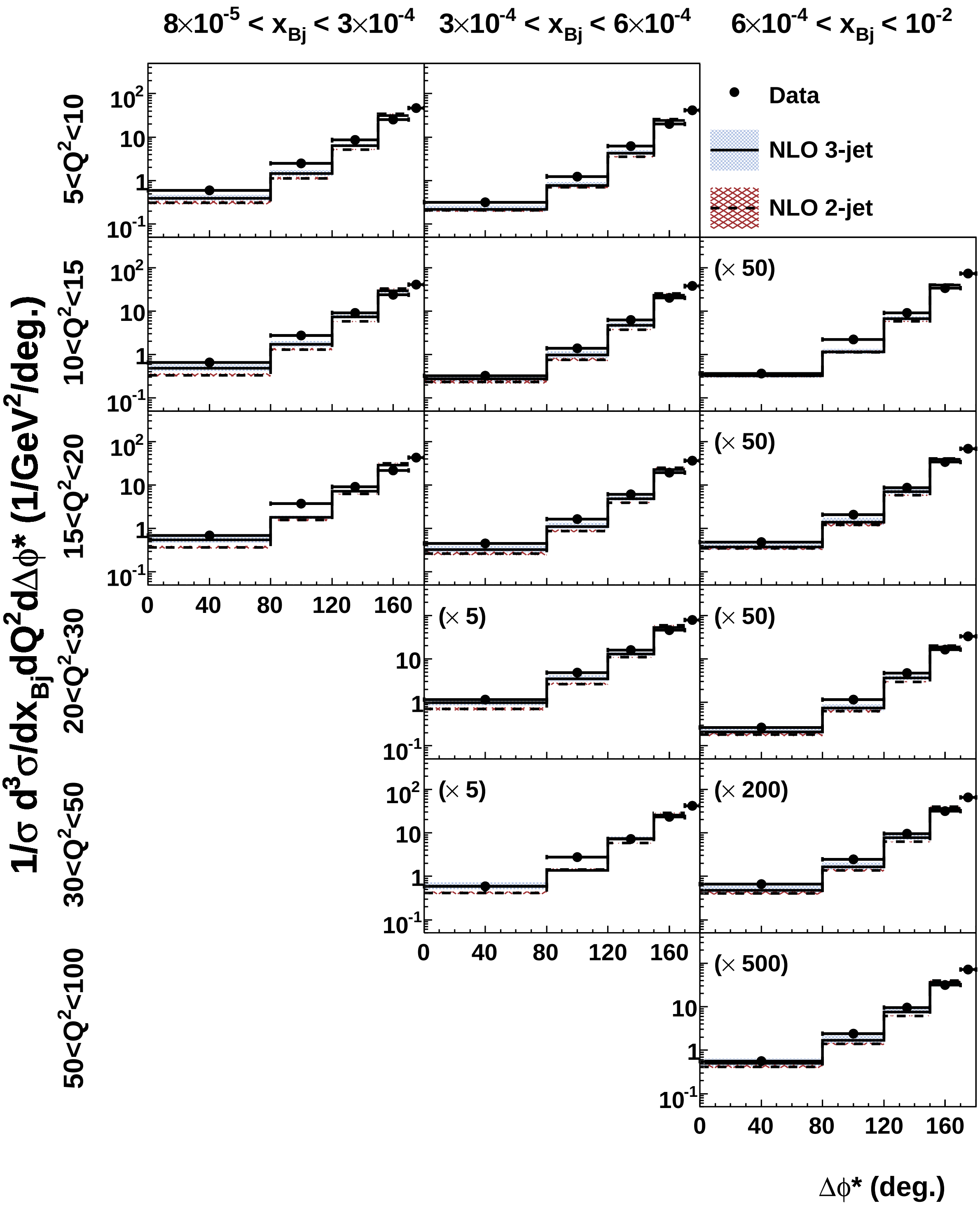

Figure 4.42: *Dijet cross sections as a function of $\Delta\phi^*$ in bins of x_{Bj} and Q^2 normalised to the visible cross section between $0 < \Delta\phi^* < 170^\circ$ in each x_{Bj} and Q^2 bin. Data are compared to NLO 3-jet (full line) and NLO 2-jet (dashed line) calculations obtained from the* NloJet++ *program. The error bands represent the scale uncertainties as described in the text.*

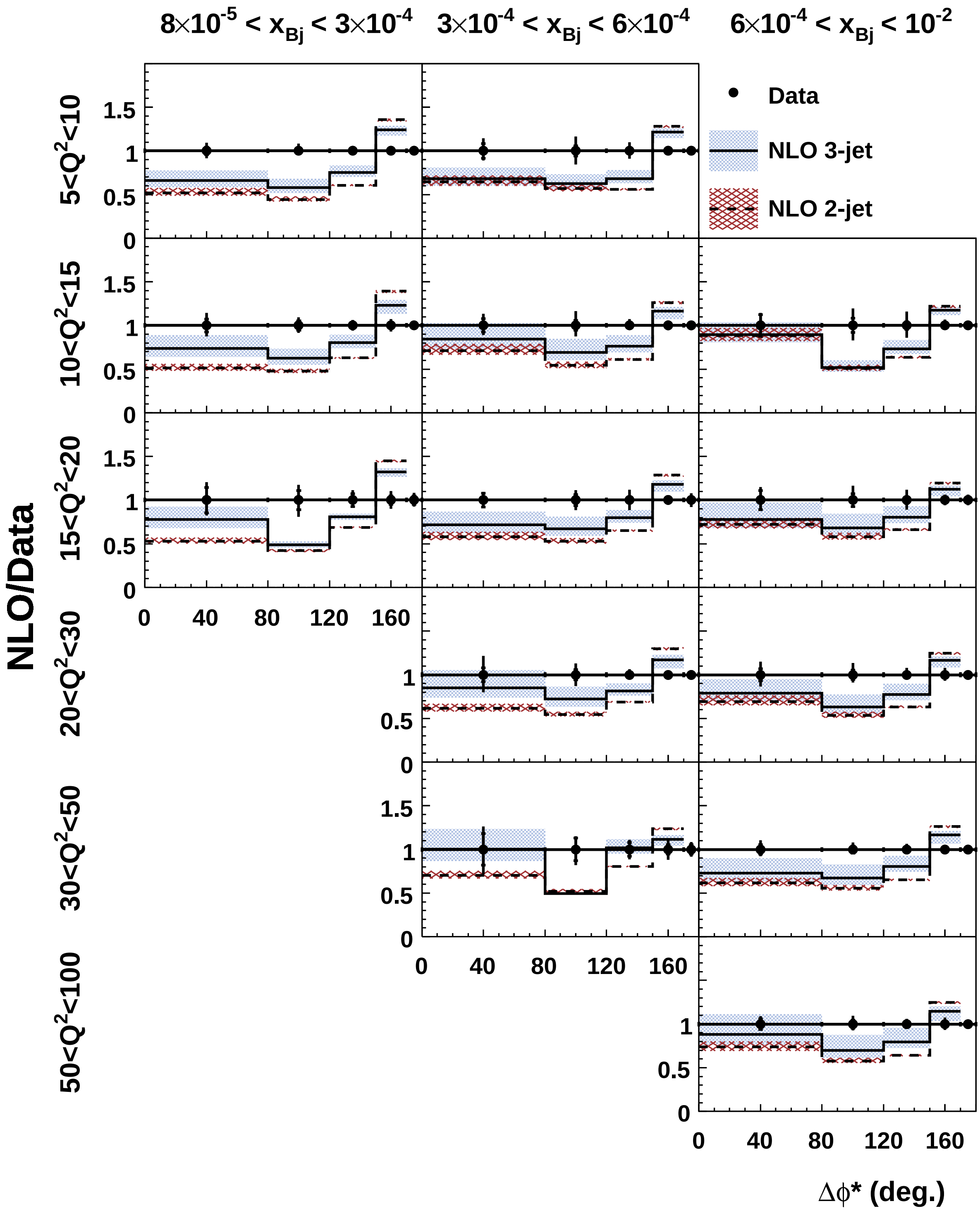

Figure 4.43: *Ratio of the theoretical predictions and the measured dijet cross sections as a function of* $\Delta\phi^*$ *in bins of* x_{Bj} *and* Q^2 *normalised to the visible cross section between* $0 < \Delta\phi^* < 170°$ *in each* x_{Bj} *and* Q^2 *bin. The NLO 3-jet (full line) and NLO 2-jet (dashed line) calculations were obtained from the* NloJet++ *program. The error bands represent the scale uncertainties as described in the text.*

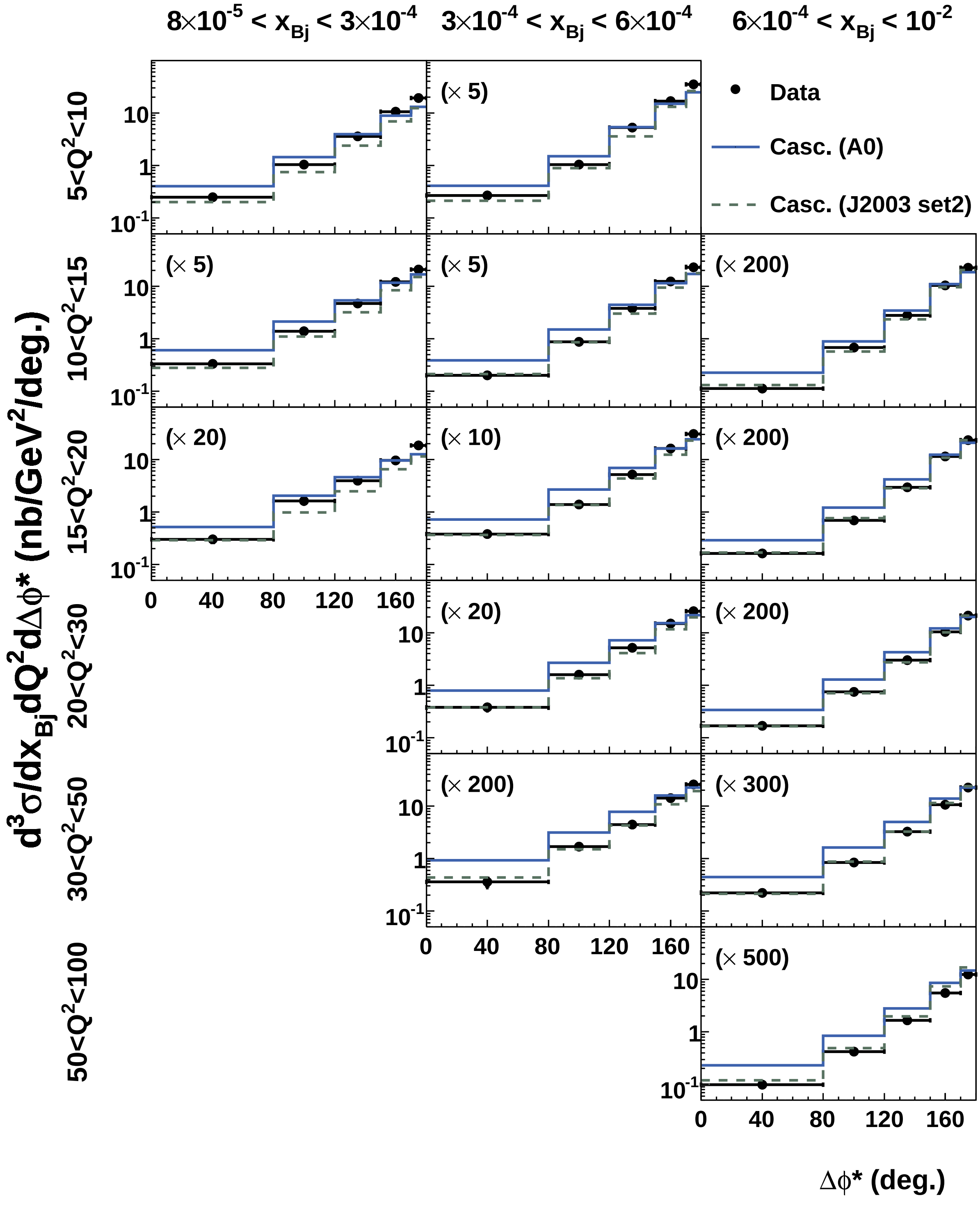

Figure 4.44: *Dijet cross sections as a function of* $\Delta\phi^*$ *in bins of* x_{Bj} *and* Q^2 *compared to the predictions of* CASCADE *using two different uGDFs.*

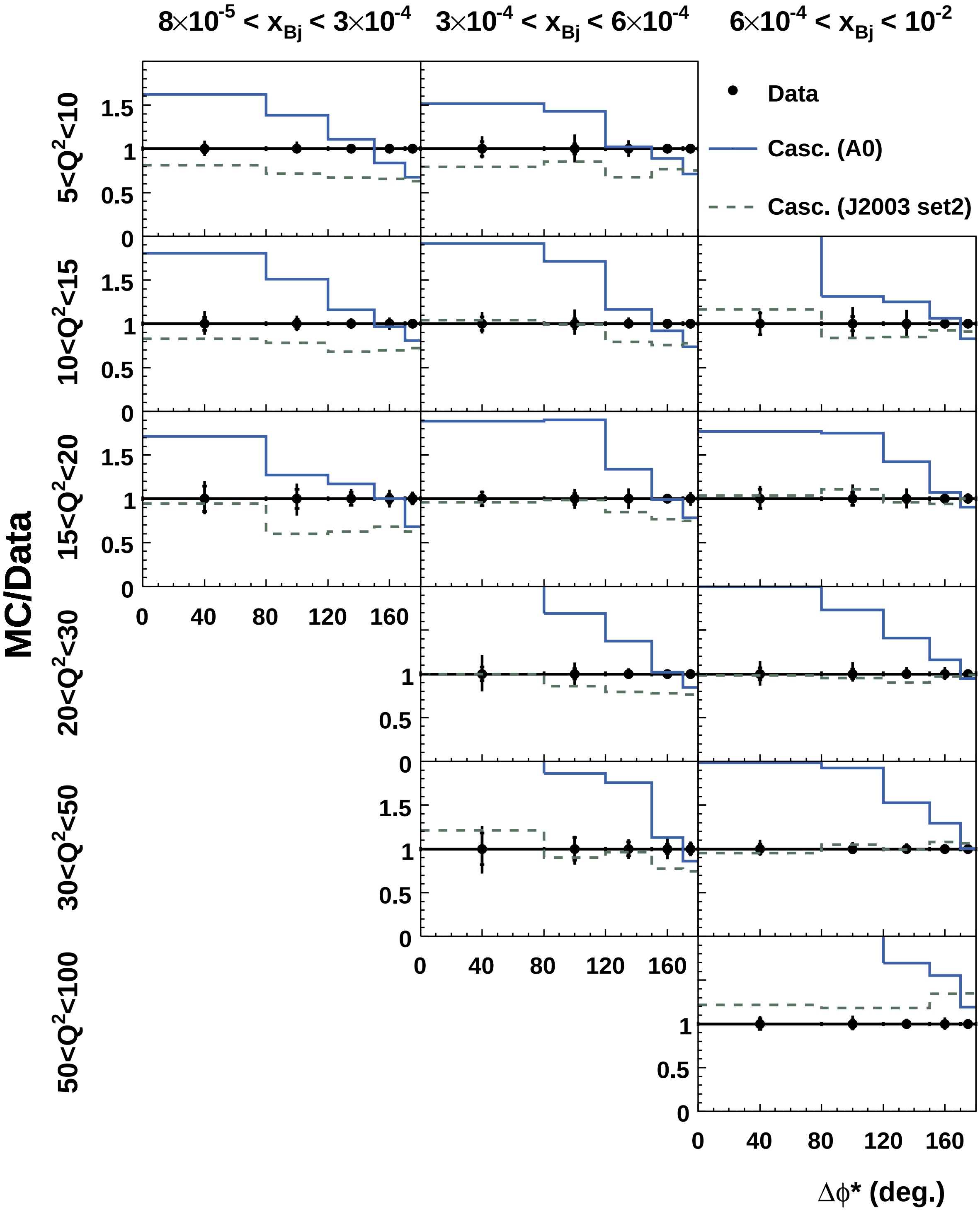

Figure 4.45: *Ratio of the theoretical predictions and the measured dijet cross sections as a function of* $\Delta\phi^*$ *in bins of* x_{Bj} *and* Q^2*. Data are compared to the predictions of* CASCADE *using two different uGDFs.*

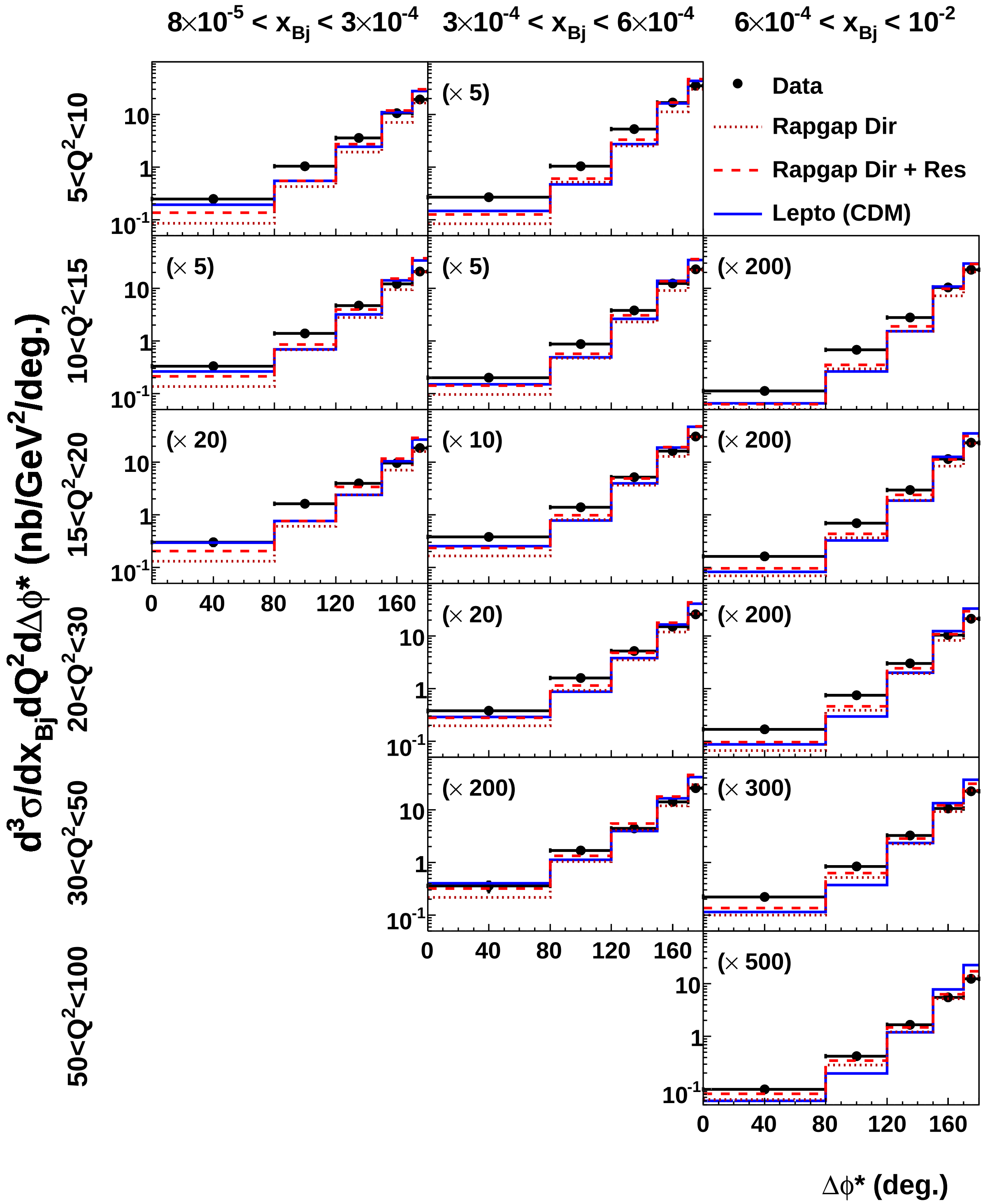

Figure 4.46: *Dijet cross sections as a function of* $\Delta\phi^*$ *in bins of* x_{Bj} *and* Q^2. *Data are compared to* RAPGAP DIR *(dotted line),* RAPGAP DIR+RES *(dashed line) and* LEPTO(CDM) *(full line).*

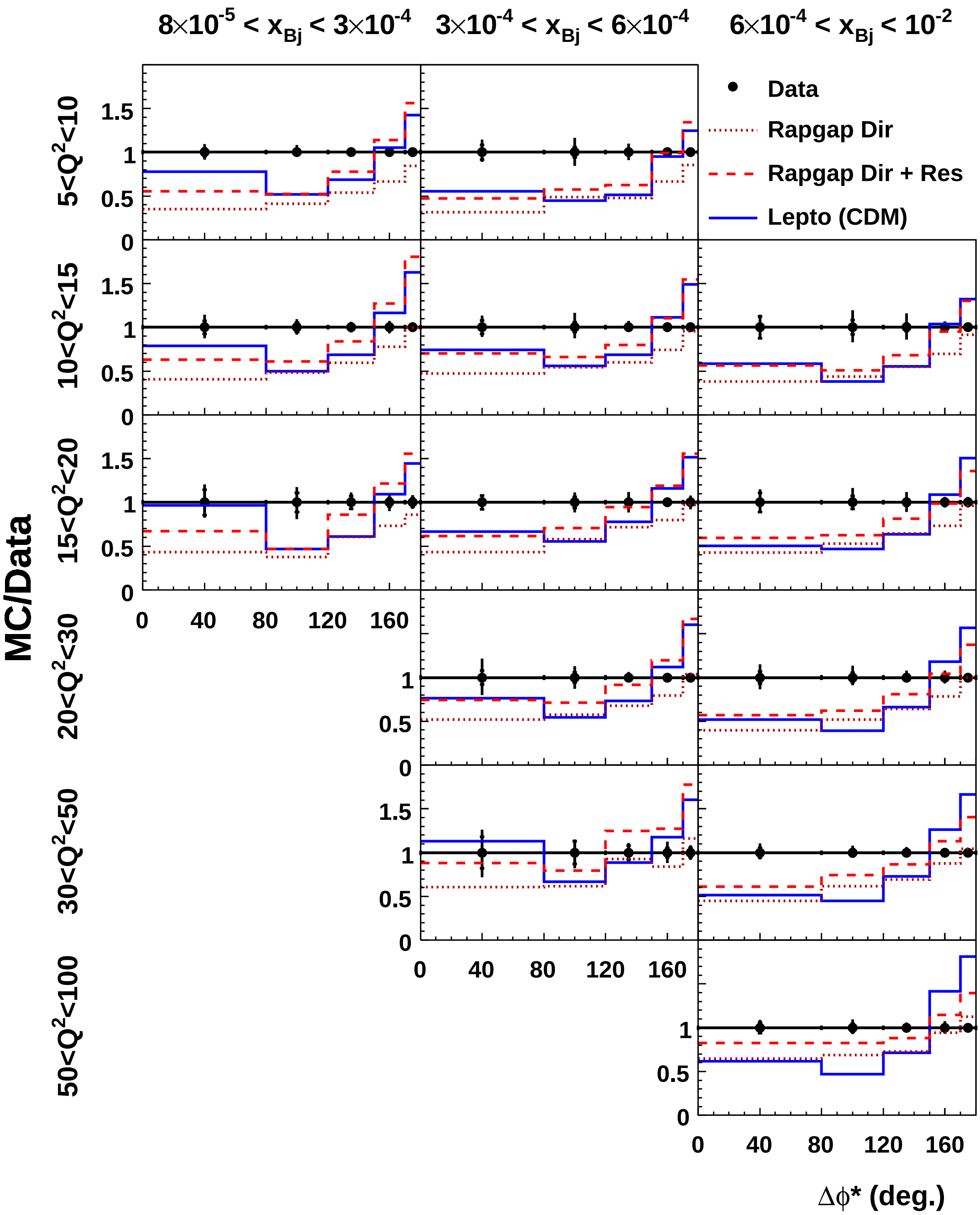

Figure 4.47: *Ratio of the theoretical predictions and the measured dijet cross sections as a function of* $\Delta\phi^*$ *in bins of* x_{Bj} *and* Q^2*. Data are compared to* RAPGAP DIR *(dotted line),* RAPGAP DIR+RES *(dashed line) and* LEPTO(CDM) *(full line).*

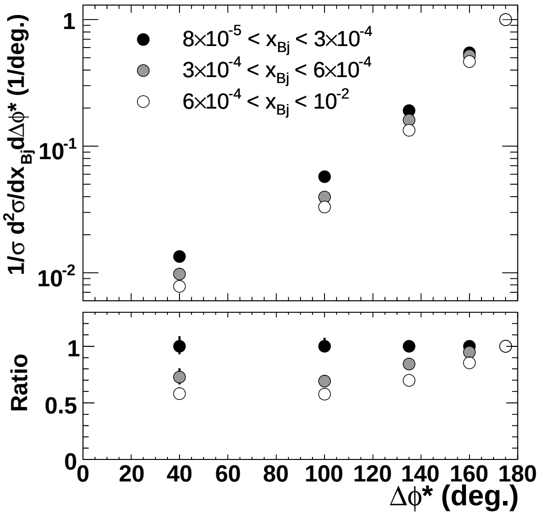

Figure 4.48: *The measured dijet cross sections in bins of* x_{Bj} *normalised to the cross section in each respective back-to-back bin (*$170 < \Delta\phi^* < 180°$*). Also shown is the ratio of each cross section and the cross section in the lowest* x_{Bj} *bin.*

4.6 Comparison with Published Data

The double differential dijet cross section as a function of x_{Bj} in bins of Q^2 was measured in an earlier analysis [12], using 1996-97 data comprising a luminosity of $\mathcal{L} = 21$ pb^{-1}. As a cross check, the analysis presented in this thesis was rerun using the same selection as in [12]:

$$\begin{array}{rcl} E^*_{Tj1} & > & 7 \text{ GeV} \\ E^*_{Tj2} & > & 5 \text{ GeV} \\ -1 \;<\; \eta_{1,2} & < & 2.5 \end{array} \qquad (4.8)$$

where jet 1 and 2 are the two hardest jets. In order to compare the two measurements, the 1999-2000 data had to be corrected for the difference in proton beam energies ($E_p = 820$ GeV in 1996-97 and $E_p = 920$ GeV in 1999-2000). The correction factor is defined as the ratio of the dijet cross sections generated with the two different beam energies, and was obtained using DJANGO(CDM). The low-x bins has the largest correction factors, typically $20-40\%$. The final result for the double differential dijet cross section $\frac{d^2\sigma}{dQ^2 dx_{Bj}}$ corrected for detector effects, QED radiation and the difference in proton beam energies is presented in Figure 4.49, compared to the published result [12]. For the 1999-2000 data, only statistical uncertainties are shown, whereas the total (statistic and systematic uncertainties added in quadrature) is shown for the 1996-97 data. As can be seen, all data points agree within the uncertainties.

In the same publication a measurement of the fraction of dijet events with $\Delta\phi^* < 120°$, i.e.

$$S = \frac{\int_0^{120°} N_{dijet}(\Delta\phi^*, x, Q^2) d\Delta\phi^*}{\int_0^{180°} N_{dijet}(\Delta\phi^*, x, Q^2) d\Delta\phi^*},$$

was performed. The present results in this so-called S-distribution, first proposed in [129], are shown in Figure 4.50 as a function of x_{Bj} in bins of Q^2 and compared to the published data. Again, the 1999-2000 data have been corrected for detector effects, QED radiation and the difference in proton beam energies. Also in this case, there is agreement within the experimental uncertainties. These results altogether give confidence in the present analysis.

The reason for measuring the S-distribution instead of $d\sigma/d\Delta\phi^*$ was the large migrations in $\Delta\phi^*$ due to the mismatching of jets on the detector and the hadron level. This in turn depends largely on migrations in and out of the E^*_T cut on the jets. However, with the HADROO2 algorithm the track information is more often used compared to the cluster information when determining the four-vectors of the combined objects as was the case in the previously used FSCOMB algorithm (see Section 2.3). This results in better jet resolutions for HADROO2 as can be seen in Figure 4.51. The resolutions are shown in the same jet observables as was presented in Figure 3.7. Compared are detector simulated Monte Carlo events reconstructed with HADROO2 and FSCOMB, respectively. In the forward direction, the resolution is not improved because of the low track efficiency in the FTD. In fact, the shift is larger when using HADROO2 compared to FSCOMB, indicating the need for a better hadronic energy calibration. Nevertheless, the improved resolution leads to fewer migrations in $\Delta\phi^*$, as can be seen in Figure 4.52 and 4.53 where purity and stability are shown for detector simulated Monte Carlo events, reconstructed

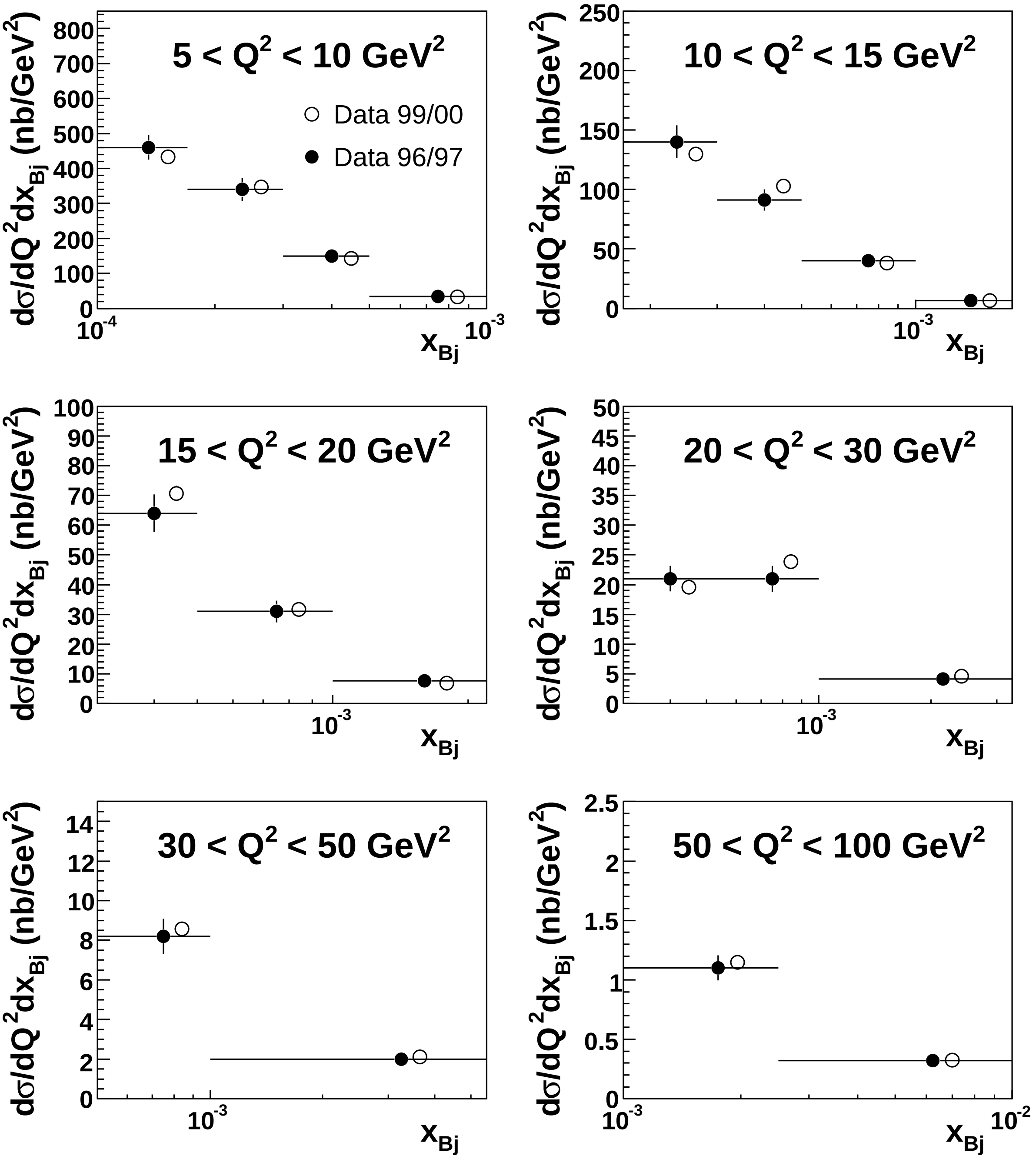

Figure 4.49: *The double differential dijet cross section from the present analysis compared to previously published data [12]. The error bars on the 96/97 data are total (statistical and systematic errors added in quadrature) while the error bars on the 99/00 data are statistical errors only. The 99/00 data have been corrected for the difference in the proton energies between the run-periods. To improve readability the points are shifted in* x_{Bj}.

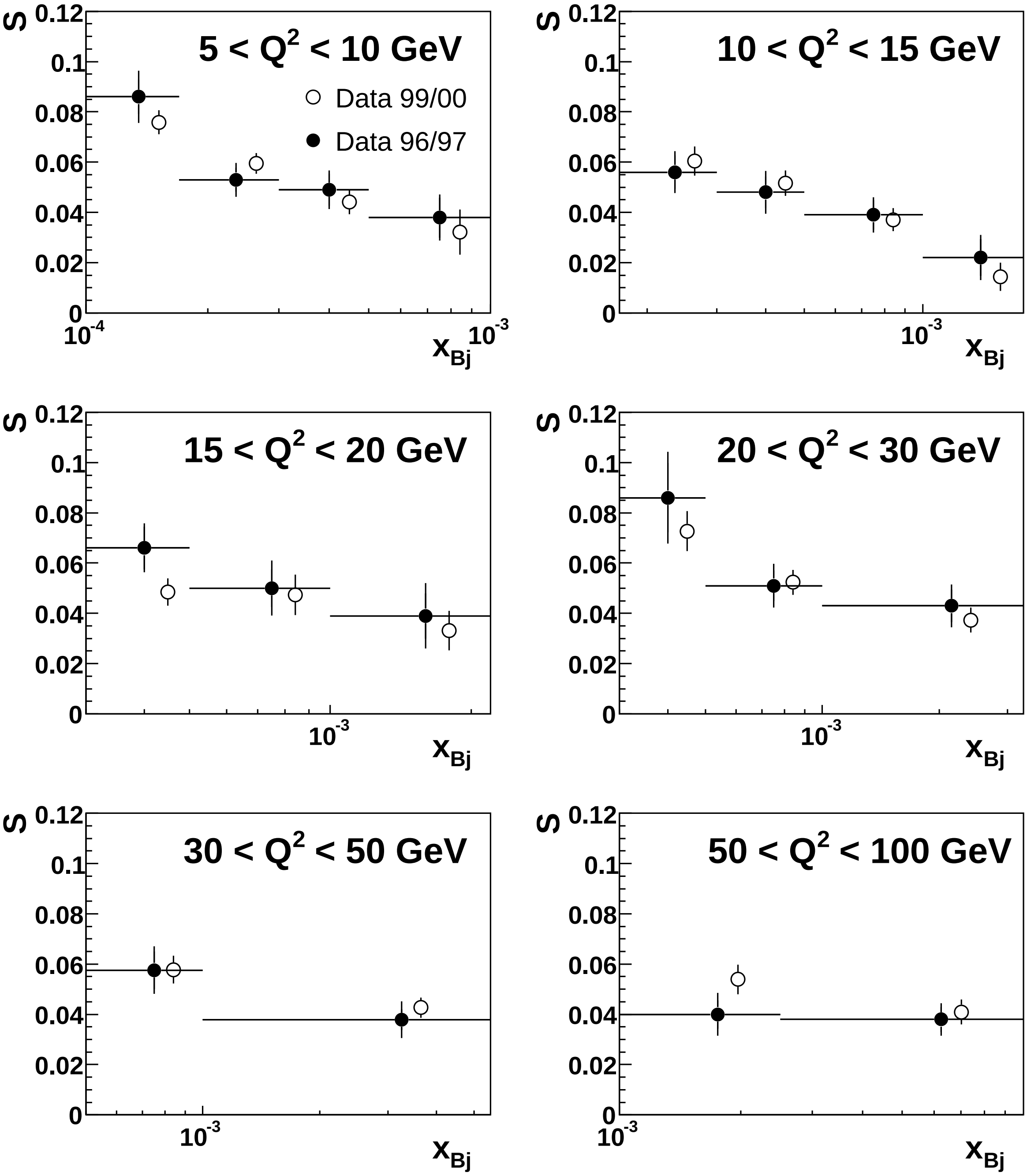

Figure 4.50: *The S-distribution as measured in the present analysis compared to previously published data [12]. The error bars on the 96/97 data are total (statistical and systematic errors added in quadrature) while the error bars on the 99/00 data are statistical errors only. The 99/00 data have been corrected for the difference in the proton energies between the run-periods. To improve readability the points are shifted in* x_{Bj}.

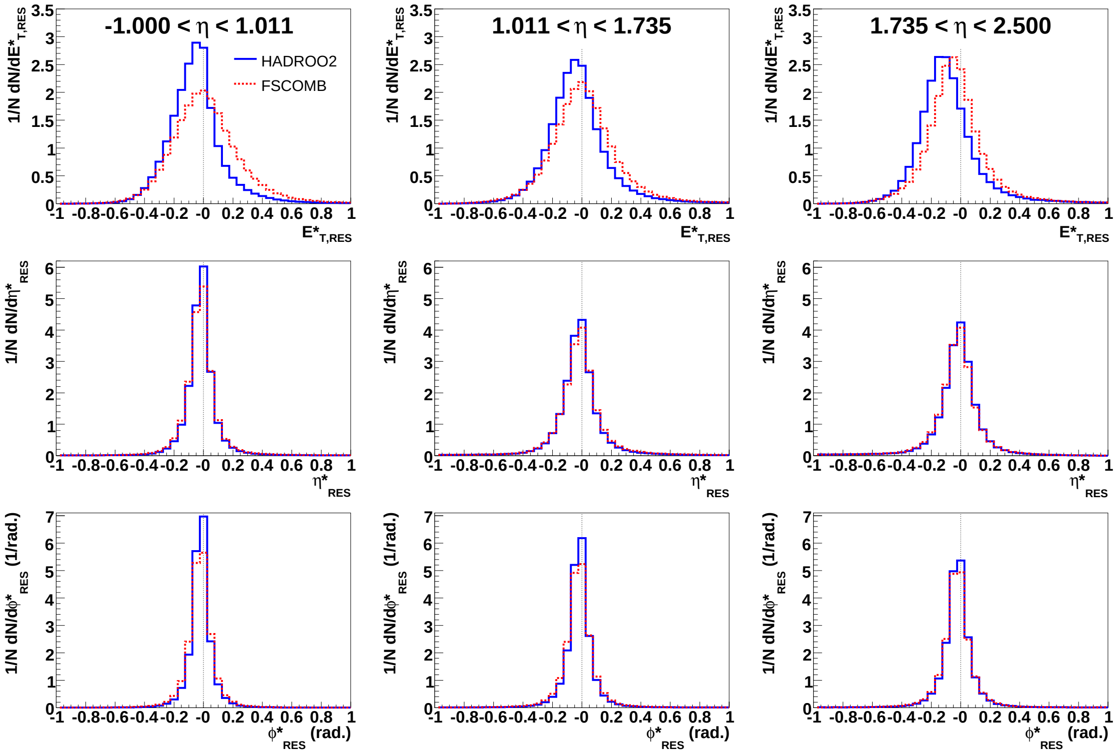

Figure 4.51: *Resolutions in E_T^*, η^* and ϕ^* for the selected jets in bins of η using the HADROO2 (full line) and FSCOMB (dashed line) algorithms, respectively.*

with HADROO2 and FSCOMB, respectively. Also, sorting the jets in η as done in this analysis, instead of E_T^* leads to larger purities, due to less misidentification of the dijet system on the detector level (the η resolution is much better than the resolution in E_T^*, as seen in Figure 3.7 and 4.51).

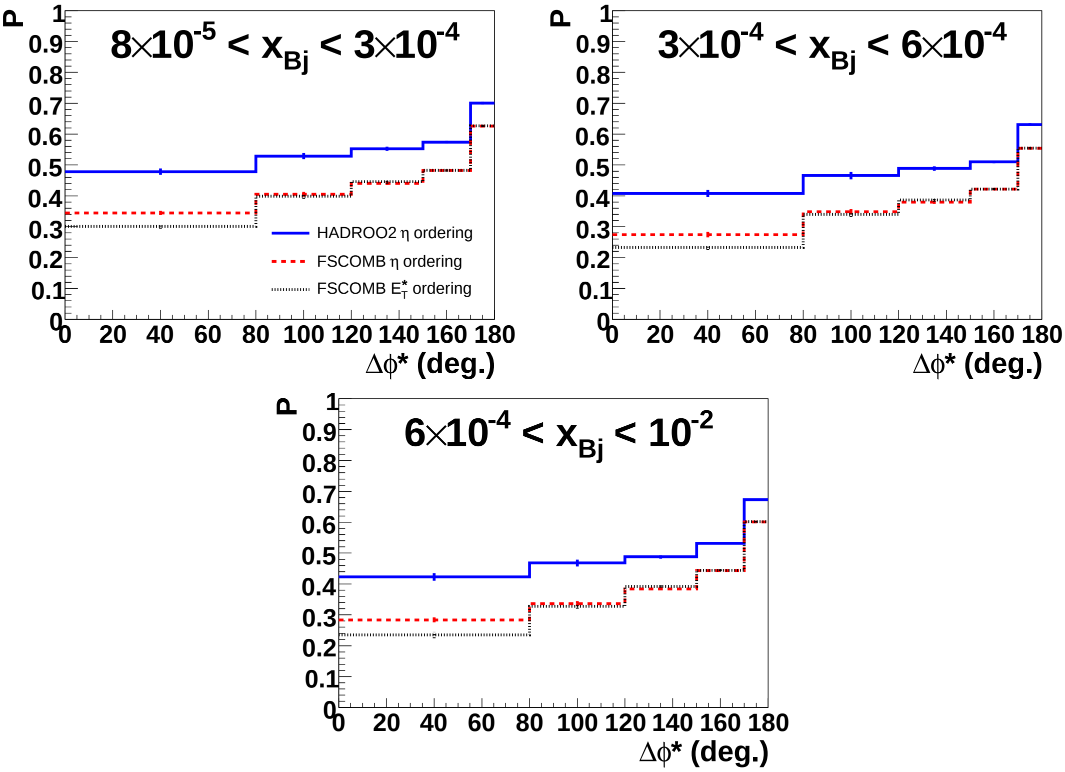

Figure 4.52: *Purity (P) as a function of* $\Delta\phi^*$ *in bins of* x_{Bj} *for detector simulated Monte Carlo events reconstructed with the HADROO2 (full line) and FSCOMB (dashed line) algorithms when ordering the jets in* η*, and with the FSCOMB algorithm when ordering the jets in* E_T^* *(dotted line).*

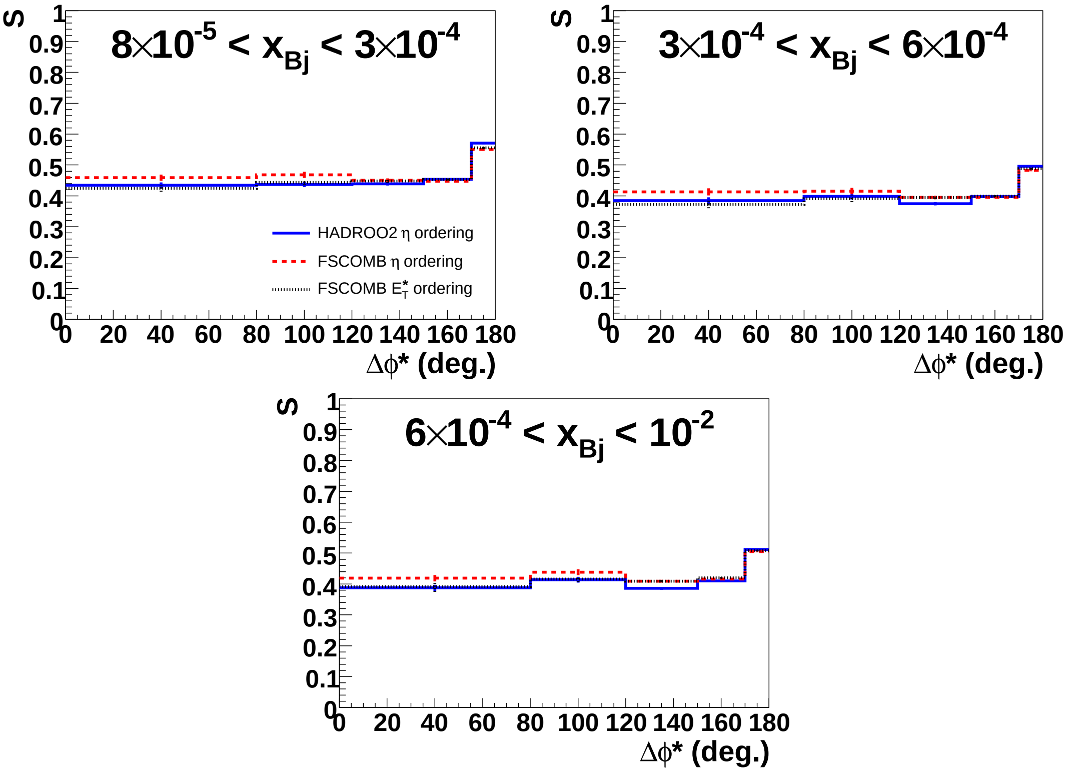

Figure 4.53: *Stability (S) as a function of $\Delta\phi^*$ in bins of x_{Bj} for detector simulated Monte Carlo events reconstructed with the HADROO2 (full line) and FSCOMB (dashed line) algorithms when ordering the jets in η, and with the FSCOMB algorithm when ordering the jets in E_T^* (dotted line).*

Chapter 5

A Determination of the Unintegrated Gluon Density

In the case of k_T-factorization, the cross section of an ep collision can be written as a convolution of a partonic cross section $\hat{\sigma}$ and an unintegrated parton density function (uPDF). In the CCFM approach, the uPDF, $\mathcal{A}$, depends on x, k_T and $\bar{q}$ such that the cross section can be factorized according to

$$\sigma = \int \frac{dx}{x} dk_T^2 \hat{\sigma} \mathcal{A}(x, k_T, \bar{q}). \tag{5.1}$$

While the partonic cross section is perturbatively calculable, the uPDF describes soft and hard multiparton radiation and is not calculable in perturbative QCD, but needs to be determined experimentally at some starting scale $\bar{q}_0$. As soon as this starting distribution $\mathcal{A}_0(x, k_T, \bar{q}_0)$ is known, the uPDF can be evolved to any other scale using the CCFM equation (1.17). The evolution is driven by perturbatively calculable gluon emissions determined by pQCD. In order to avoid the non-perturbative region a k_T cut-off against soft emissions is applied and below this cut-off the value of α_s is kept fixed, whereas otherwise the scale dependence of α_s is considered.

There are some uPDFs available on the market, e.g. [67, 70, 71, 128, 130–133]. However, they are all poorly constrained by experimental data. When studying ep-collisions, a natural starting point is to fit the unintegrated gluon density to describe the inclusive structure function F_2 [70, 71]. However, different uPDFs can give very different predictions for more exclusive observables, while describing F_2 equally well. A clear example of this is given in Chapter 4 where the predictions of Cascade are very dependent on the uPDF used (J2003 set2 or A0). This reflects the fact that the transverse momenta of the gluons are not constrained well enough by F_2. Thus, the fitted unintegrated gluon distributions can have very different k_T dependence and still describe the F_2 distribution. The insufficient constraint from F_2 alone becomes especially clear when exclusive observables dependent on k_T are studied, for example the azimuthal correlation of dijets. Recently, fits of the unintegrated gluon density to the more exclusive observable F_2^c and various dijet cross sections have been performed [134, 135] in order to better constrain the uPDF. In the present analysis the starting distribution $\mathcal{A}_0(x, k_T, \bar{q}_0)$ has been determined from fits to the dijet cross sections presented in Chapter 4, and to the dijet cross section from [12].

These cross sections have been chosen because of their sensitivity to the k_T and x of the gluon, respectively. For the first time, the mean and width of the Gaussian intrinsic k_T distribution are included as free parameters in the fit.

It should be mentioned that PDFs are not observables and thus depend on the evolution scheme used. In this fit the CCFM formalism was used, and hence the uPDF obtained is only valid in this scheme.

5.1 Sensitivity to the Unintegrated Gluon Density

As already mentioned, the azimuthal correlations are sensitive to the transverse momenta of the gluons and thus also to different uPDFs. The sensitivity can be shown more explicitly by studying the x_g and $k_{T,g}$ distributions in the same x_{Bj} and $\Delta\phi^*$ bins as in the measurement (see Chapter 4). CASCADE has been used with the J2003 set2 uPDF to generate x_g and $k_{T,g}$ distributions on the parton level and the results are shown in Figures 5.1 and 5.2. First it can be noted that on the average x_g is larger for larger x_{Bj}, which is not surprising since they are related in LO by

$$x_g = x_{Bj}\left(1 + \frac{M_{ij}^2}{Q^2}\right) \tag{5.2}$$

where M_{ij} is the invariant mass of the dijet system. Also, comparing the large and small $\Delta\phi^*$ bin with the middle ones, one can see a tendency for x_g to reach a minimum for $80 < \Delta\phi^* < 120°$. In the bin $170 < \Delta\phi^* < 180°$ the jets are (almost) back-to-back and the most likely scenario is to have two hard jets and some additional soft radiation. As $\Delta\phi^*$ decreases, the jets get more decorrelated meaning that more soft (or less but harder) radiation is required to balance the two jets. Since energy and momentum are conserved, this leaves on the average less longitudinal momentum accessible for the dijet system, compared to the back-to-back scenario. However, as $\Delta\phi^*$ becomes even smaller, the average x_g increases again. This is due to the fact that, when $\Delta\phi^*$ is forced to be small, $\Delta\eta^*$ can no longer be arbitrarily small since the invariant mass

$$M_{ij} = 2P_{T,1}P_{T,2}(cosh(\Delta\eta^*) + cos(\Delta\phi^*)) \tag{5.3}$$

must be positive. The correlation between $\Delta\phi^*$ and $\Delta\eta^*$ is shown in Figure 5.3. M_{ij} depends strongly on $\Delta\eta^*$ through the $cosh(\Delta\eta^*)$ dependence but only weakly on $\Delta\phi^*$, so by forcing $\Delta\eta^*$ to be large, M_{ij} and hence also x_g will be large. Nevertheless, the x_g dependence on $\Delta\phi^*$ is relatively small, as seen from Figure 5.1.

In Figure 5.2 the $k_{T,g}$ distributions in each x_{Bj} and $\Delta\phi^*$ bin is shown. For fixed $\Delta\phi^*$, the mean value of $k_{T,g}$ decreases with increasing x_{Bj}. This is in agreement with the fact that at small x_{Bj} more additional radiation has been emitted in the gluon ladder, which also increases the $k_{T,g}$ and leads to larger decorrelations of the dijet system, see Figure 4.48. For large $\Delta\phi^*$ where the dijets are almost back-to-back, $k_{T,g}$ peaks at small values (around 1 GeV) which is consistent with the limited phase space for additional radiation from such event topologies. However, the distributions have tails up to larger values which originate

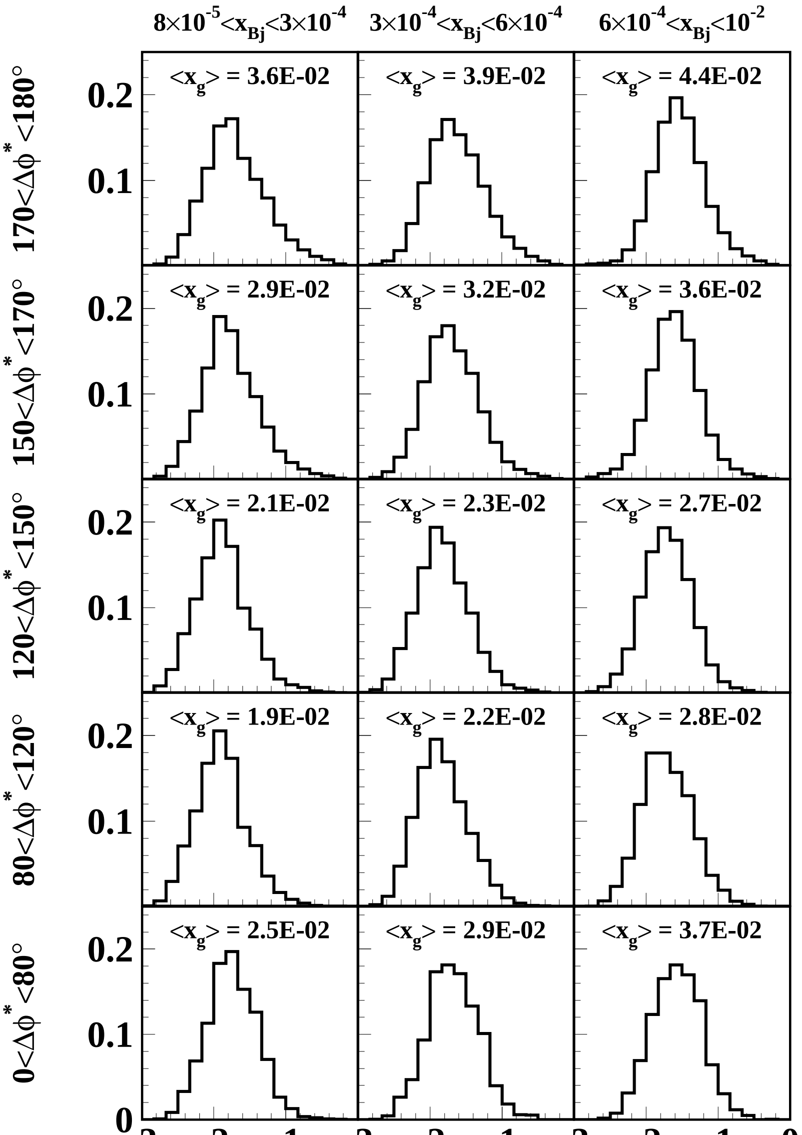

Figure 5.1: *The distribution of* x_g *as generated by* CASCADE *on the parton level using the J2003 set2 uPDF, in different bins of* x_{Bj} *and* $\Delta\phi^*$. *The mean value of* x_g *in each bin is given.*

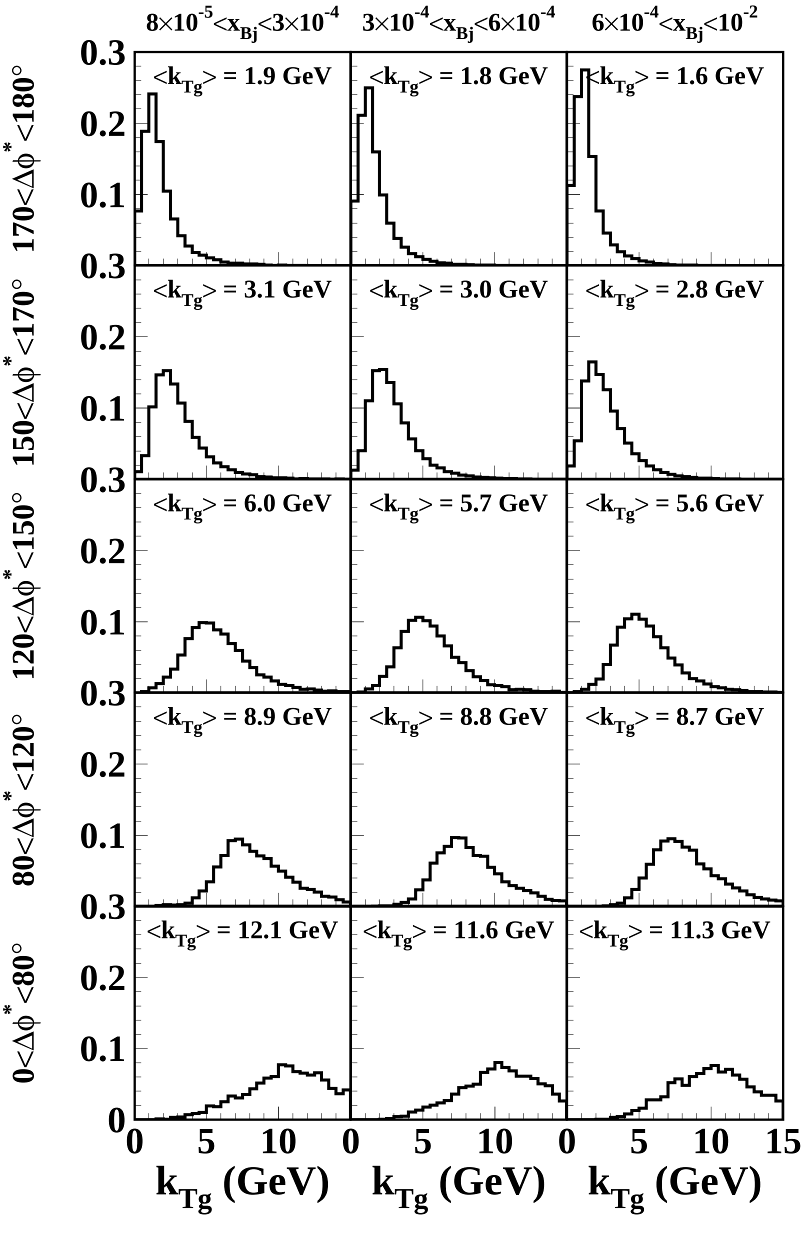

Figure 5.2: *The distribution of* $k_{T,g}$ *as generated by* CASCADE *on the parton level using the J2003 set2 uPDF, in different bins of* x_{Bj} *and* $\Delta\phi^*$*. The mean value of* $k_{T,g}$ *in each bin is given.*

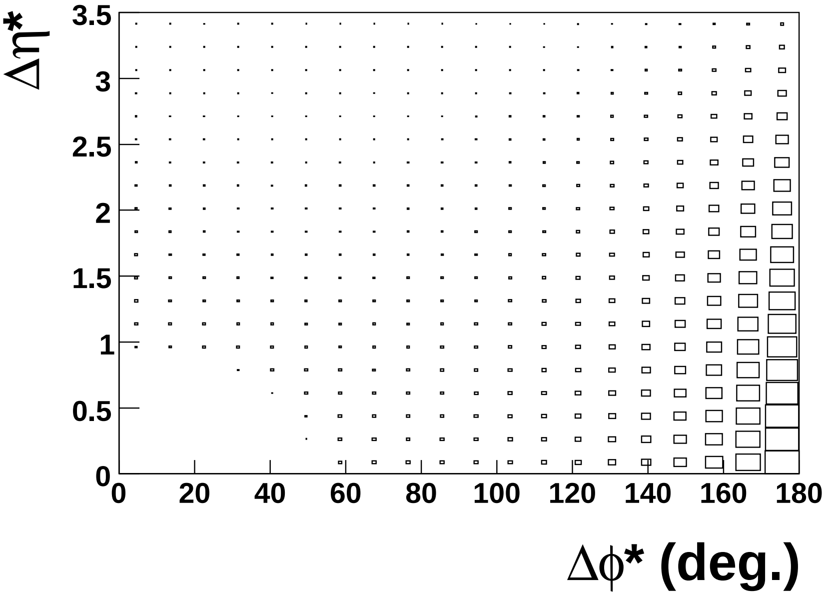

Figure 5.3: *The correlation between* $\Delta\phi^*$ *and* $\Delta\eta^*$ *on the hadron level as generated by* Django(CDM).

from events with very high P_T jets, where even at large $\Delta\phi^*$, $k_{T,g}$ can reach high values, as can be realized from

$$k_{T,g}^2 = P_{T,1}^2 + P_{T,2}^2 + 2P_{T,1}P_{T,2}cos(\Delta\phi^*).$$

For smaller values of $\Delta\phi^*$, the transverse momentum $k_{T,g}$ increases significantly, as expected.

In an attempt to better constrain the x_g dependence, the triple differential dijet cross sections $\frac{d^3\sigma}{dx_{Bj}dQ^2dE^*_{T,Max}}$ from [12] are also included in the fit of the unintegrated gluon density. Here, $E^*_{T,Max}$ is the transverse momentum of the hardest jet in the HCM frame. The DIS and dijet cuts of the analysis are explained in Chapter 4. In Figure 5.4, the x_g distribution in the lowest Q^2 bin, $5 < Q^2 < 10$ GeV^2, is shown for different x_{Bj} and $E^*_{T,Max}$ bins. As can be observed, x_g is fairly well constrained by the dijet measurement and is highly sensitive to $E^*_{T,Max}$. This is due to the fact that $E^*_{T,Max}$ is directly related to the invariant mass M_{ij} of the dijet system according to Equations (5.2) and (5.3). From Figure 5.5 it is obvious that $k_{T,g}$ is less well constrained by this measurement.

5.2 Fit Procedure

The fit of the unintegrated gluon density to the data discussed in this analysis is performed using the Cascade Monte Carlo generator together with HzTool [136] and the downhill simplex method [137] as implemented in the Minuit [138] package. The simplex method is used because it only relies on the calculation of function values and is therefore less sensitive

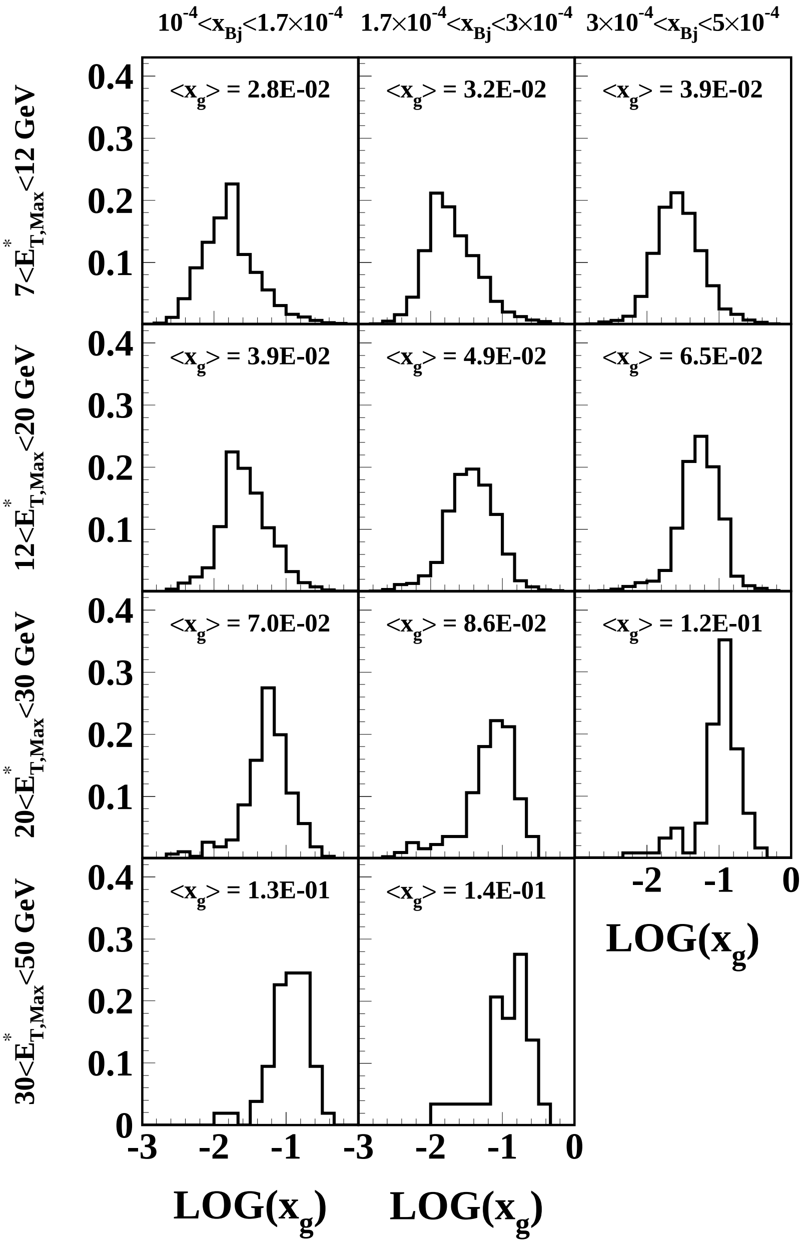

Figure 5.4: *The distribution of x_g as generated by* CASCADE *on the parton level using the J2003 set2 uPDF, in different bins of x_{Bj} and $E^*_{T,Max}$ for $5 < Q^2 < 10$ GeV^2. The mean value of x_g in each bin is given.*

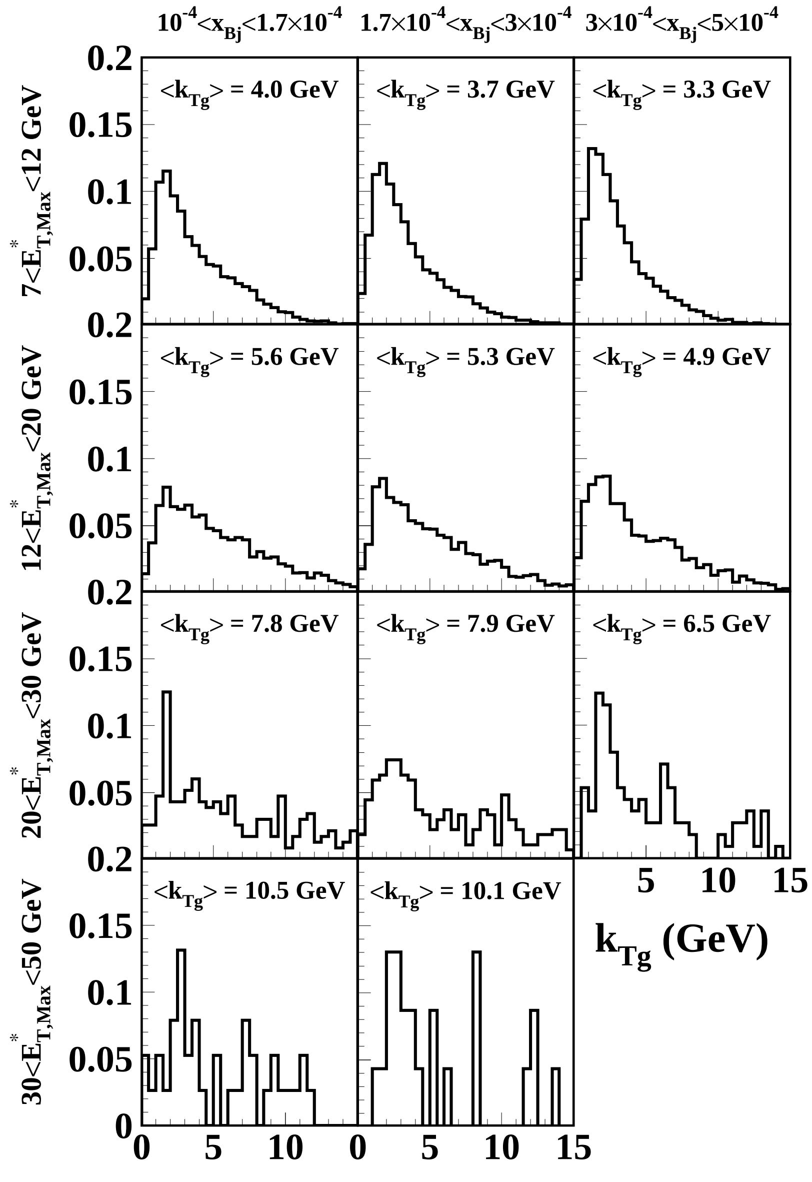

Figure 5.5: *The distribution of* $k_{T,g}$ *as generated by* CASCADE *on the parton level using the J2003 set2 uPDF, in different bins of* x_{Bj} *and* $E^*_{T,Max}$ *for* $5 < Q^2 < 10$ GeV^2. *The mean value of* $k_{T,g}$ *in each bin is given.*

to statistical fluctuations than methods using derivatives. The starting distribution is parameterized as

$$x\mathcal{A}_0(x, k_T, \bar{q}_0) = N \cdot x^{-B} \cdot (1-x)^4 \cdot exp\left(-\frac{(k_T-\mu)^2}{2\sigma^2}\right) \tag{5.4}$$

where N, B, μ and σ are free parameters, and the starting scale is chosen as $\bar{q}_0 = 1.2$ GeV. N is an overall normalisation factor, B determines the small-x behaviour while μ and σ are the mean value and the width (standard deviation) of the Gaussian intrinsic k_T distribution, respectively. The factor $(1-x)^4$ mostly affects the large-x region and only shows a small sensitivity to the cross sections. The exponent is therefore kept fixed at 4, which is the same as in earlier fits to F_2 and F_2^c [70, 71, 134]. A set of starting parameters is chosen for $x\mathcal{A}_0(x, k_T, \bar{q}_0)$, which is used as input to CASCADE. With this parameter setting CASCADE generates full DIS events on the hadron level by convoluting the starting distribution $\mathcal{A}_0$ with the CCFM evolution kernel $\tilde{\mathcal{A}}$,

$$x\mathcal{A}(x, k_T, \bar{q}) = \int dx' \mathcal{A}_0(x, k_T, \bar{q}_0) \cdot \frac{x}{x'} \tilde{\mathcal{A}}(\frac{x}{x'}, k_T, \bar{q}).$$

$\tilde{\mathcal{A}}$ contains the splitting function which, in this analysis, includes both the singular and non-singular terms (for details, see [71, 72]). The generated events are fed through the analysis code where dijet events are selected according to the cuts in Chapters 3 and 4, and predictions on the hadron level for $\frac{d^3\sigma}{dx_{Bj}dQ^2d\Delta\phi^*}$ and $\frac{d^3\sigma}{dx_{Bj}dQ^2dE^*_{T,Max}}$ are obtained. Using the HZTOOL package, the predictions are then compared to the measured data, and a χ^2 is calculated according to

$$\chi^2 = \sum_{i=1}^{n} \frac{\left(\sigma_{i,MC} - \sigma_{i,Data}\right)^2}{\delta^2_{i,MC} + \delta^2_{i,Data}} \tag{5.5}$$

where $\sigma_{i,MC}$, $\sigma_{i,Data}$, $\delta_{i,MC}$ and $\delta_{i,Data}$ are the theoretical predictions and the measured cross sections with the corresponding uncertainties for bin i. Here, $\delta_{i,Data}$ is the total error (statistical and systematic errors added in quadrature), while $\delta_{i,MC}$ only contains the statistical error from the MC event generation. The sum runs over all bins $i = 1, 2, \ldots, N$. A new parameter setting for the starting distribution is then chosen according to the rules of the downhill simplex method (see Appendix C) and the procedure is iterated until a minimum is found.

5.3 Results

Before performing a simultaneous fit of the triple differential $\Delta\phi^*$ correlation data presented in Chapter 4, $\frac{d^3\sigma}{dx_{Bj}dQ^2d\Delta\phi^*}$, and the triple differential dijet cross sections $\frac{d^3\sigma}{dx_{Bj}dQ^2dE^*_{T,Max}}$ from [12], the unintegrated gluon density is first fitted to each sample separately. Apart from studying the sensitivities to different values of μ and σ, it is also interesting to investigate the sensitivities to the parameter B, since in a recent study [134], the value $B = 0.0278$ was obtained from a fit to F_2 while a fit to F_2^c gave $B = 0.2860$. The B parameter determines the slope of the starting uPDF as a function of x (see Eqution 5.4), where a larger value gives a steeper rise toward small x. The parameters of the Gaussian

	χ^2/ndf	χ^2	ndf	N	B	σ (GeV)	μ (GeV)
$\frac{d^3\sigma}{dx_{Bj}dQ^2d\Delta\phi^*}$	3.0	186	61	0.25	0.29	1.1	1.5
	5.3	325	61	0.47	0.04	1.1	1.5
	6.9	421	61	0.20	0.29	0.7	0.0
	10.0	613	61	0.47	0.04	0.7	0.0
$\frac{d^3\sigma}{dx_{Bj}dQ^2dE^*_{T,Max}}$	1.6	53	34	0.25	0.29	1.1	1.5
	1.3	44	34	0.47	0.04	1.1	1.5
	2.2	75	34	0.19	0.30	0.7	0.0
	2.1	71	34	0.47	0.04	0.7	0.0
Combined Fit	2.5	245	99	0.25	0.29	1.1	1.5
	4.4	440	99	0.47	0.03	1.1	1.5

Table 5.1: *The obtained χ^2 and χ^2/ndf, where ndf is the number of degrees of freedom, found for different parameter settings, when fitting the two data sets separately and when fitting to both sets simultaneously (Combined Fit).*

k_T distribution were not included in the fit of [134], but set to $\mu = 0$ GeV and $\sigma = 0.7$ GeV. It is therefore natural to use these parameter values of B, μ and σ as starting values in the fit procedure. However, the effects of larger values of μ and σ are also investigated here. As seen in Table 5.1, the triple differential azimuthal correlation data clearly prefer a large value of B, and also larger values of μ and σ than previously used. However, the χ^2/ndf is still large for the best fit, which is mainly due to the largest x_{Bj} and Q^2 bin contributing $\chi^2 = 89$. Also the $\frac{d^3\sigma}{dx_{Bj}dQ^2dE^*_{T,Max}}$ data prefer larger values of μ and σ but not as significantly. In contrast to the azimuthal correlation cross sections, these data seem to prefer a less steep gluon density. However, also $B = 0.29$, in combination with $\sigma = 1.1$ and $\mu = 1.5$, gives a reasonable description of the data, as seen in Table 5.1.

The simultaneous fit to the two data sets yields an unintegrated gluon density with the parameters $N = 0.252$, $B = 0.292$, $\sigma = 1.06$ GeV and $\mu = 1.50$ GeV, giving a χ^2/ndf= 2.5. The uPDF with this parameter setting will in the following be called uPDF1. The combined fit thus gives a very similar unintegrated gluon density as the fit to the $\Delta\phi^*$ correlation data alone. Apparently, the errors in the $\frac{d^3\sigma}{dx_{Bj}dQ^2dE^*_{T,Max}}$ measurement are not small enough to have sufficient influence on the fit in order to lower the B value. A local minimum is, however, found with a smaller value of B, but with a significantly larger χ^2/ndf, see Table 5.1.

Figure 5.6 shows the cross section of the measured data and the obtained fit result (uPDF1), in addition to the predictions of CASCADE with A0 and J2003 set2 already shown in Chapter 4, while Figure 5.7 shows the ratio of the predictions and the data. As previously noticed, A0 overshoots the data for $\Delta\phi^* < 150°$ in almost all bins, while J2003 set2 gives a reasonable description of the data. The largest improvement of uPDF1 compared to J2003 set2 is seen at small x_{Bj} where uPDF1 describes all $\Delta\phi^*$ bins fairly well. There is also a slight improvement at medium x_{Bj} for the large $\Delta\phi^*$ bins, while both J2003 set2 and uPDF1 give similar results at large x_{Bj}. In the largest x_{Bj} and Q^2 bin, both J2003 set2 and uPDF1 give too large a cross section, especially at large $\Delta\phi^*$. In Figure 5.8 is shown the cross sections measured in [12] compared to the predictions of

	Total χ^2	χ^2 contributions from	
		$\frac{d^3\sigma}{dx_{Bj}dQ^2d\Delta\phi^*}$	$\frac{d^3\sigma}{dx_{Bj}dQ^2dE^*_{T,Max}}$
uPDF1	245	184	61
J2003 set2	861	762	99
A0	2056	1974	82

Table 5.2: *The total χ^2 values and the contributions from the separate data sets obtained using* CASCADE *with uPDF1, J2003 set2 and A0.*

CASCADE using the same uPDFs as above, and Figure 5.9 shows the ratio of the CASCADE predictions and the data. Here, A0 gives a better description than J2003 set2 at small x_{Bj} while it is worse at large x_{Bj}. Although the uPDF1 gives quite a good agreement with data in the lowest $E^*_{T,Max}$ bin, the deviation increases with increasing $E^*_{T,Max}$. This tendency is observed in most x_{Bj} and Q^2 bins. However, the errors on both the data and the generated distributions are large, such that the data are described within the errors in almost all $E^*_{T,Max}$ bins. Even though the χ^2/ndf obtained in the combined fit is somewhat large, it is still an improvement compared to J2003 set2 and A0. This can be seen in Table 5.2, where the χ^2 values obtained from uPDF1, J2003 set2 and A0 are given, also showing the separate contributions from $\frac{d^3\sigma}{dx_{Bj}dQ^2d\Delta\phi^*}$ and $\frac{d^3\sigma}{dx_{Bj}dQ^2dE^*_{T,Max}}$. In general, the largest contribution to the χ^2 values comes from the $\Delta\phi^*$ correlation data. For uPDF1, it is in particular the largest x_{Bj} and Q^2 bin which contributes the most ($\chi^2 = 85$). If this bin is excluded in the fit, the same minimum is found but with χ^2/ndf$= 151/94 = 1.6$. Such problems do not appear if $\frac{d^3\sigma}{dx_{Bj}dQ^2dE^*_{T,Max}}$ is fitted in combination with the double differential cross section $\frac{d^2\sigma}{dx_{Bj}\Delta\phi^*}$. Such a fit results in a χ^2/ndf$= 84/49 = 1.7$ with in principle the same parameters as uPDF1 ($N = 0.253$, $B = 0.293$, $\sigma = 1.06$ GeV and $\mu = 1.50$ GeV).

In order to study the sensitivity of the fit to the free parameters, a scan around the minimum is performed for each parameter separately, while all other parameters are kept fixed at the values obtained in the fit (uPDF1). The result of this scan is shown in Figure 5.10. The large sensitivity to the parameters N and B is clearly seen, and the χ^2 function shows one clear minimum. The parameters μ and σ have less influence on χ^2 but shows a more complex behaviour, with local minima.

Figure 5.11 shows the unintegrated gluon densities uPDF1, A0 and J2003 set2 as a function of x for two different values of k_T^2, and as a function of k_T^2 for two different values of x. The factorization scale is $\bar{q} = 4$ GeV in all plots. For $k_T^2 = 1$ GeV^2, both A0 and J2003 set2 are almost flat at low x, while uPDF1 rises as x decreases. The small-x behaviour is determined by the parameter B, which in the fit is found to be $B = 0.292$. For A0 and J2003set2, this parameter was set to $B = 0$. For $k_T^2 = 10$ GeV^2, A0 and J2003 set2 still have very similar shapes. However, A0 is everywhere higher, which is consistent with the conclusion in Chapter 4 that A0 has a harder k_T spectrum. Again, uPDF1 has a steeper rise at small x given by the higher B value, but in the large-x tail uPDF1 is similar to J2003 set2.

Looking at the k_T dependence of the uPDFs at different values of x, one can see a separation between the low and high k_T region. In the low k_T region, $k_T^2 \lesssim 1.5$ GeV^2, the

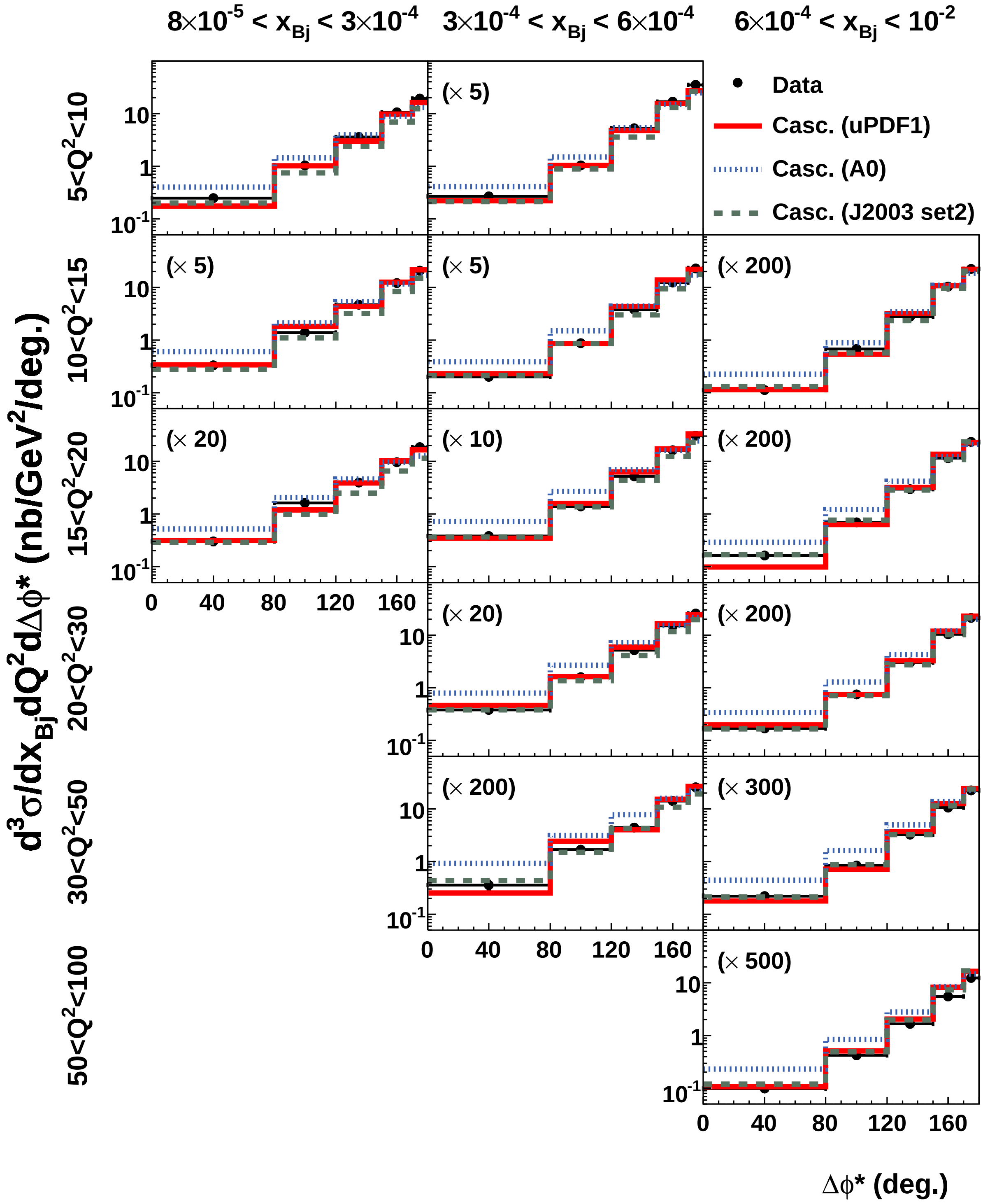

Figure 5.6: *Dijet cross sections as a function of* $\Delta\phi^*$ *in bins of* x_{Bj} *and* Q^2 *compared to the predictions of* CASCADE *using the uPDFs A0, J2003 set2 and uPDF1 obtained from the fit.*

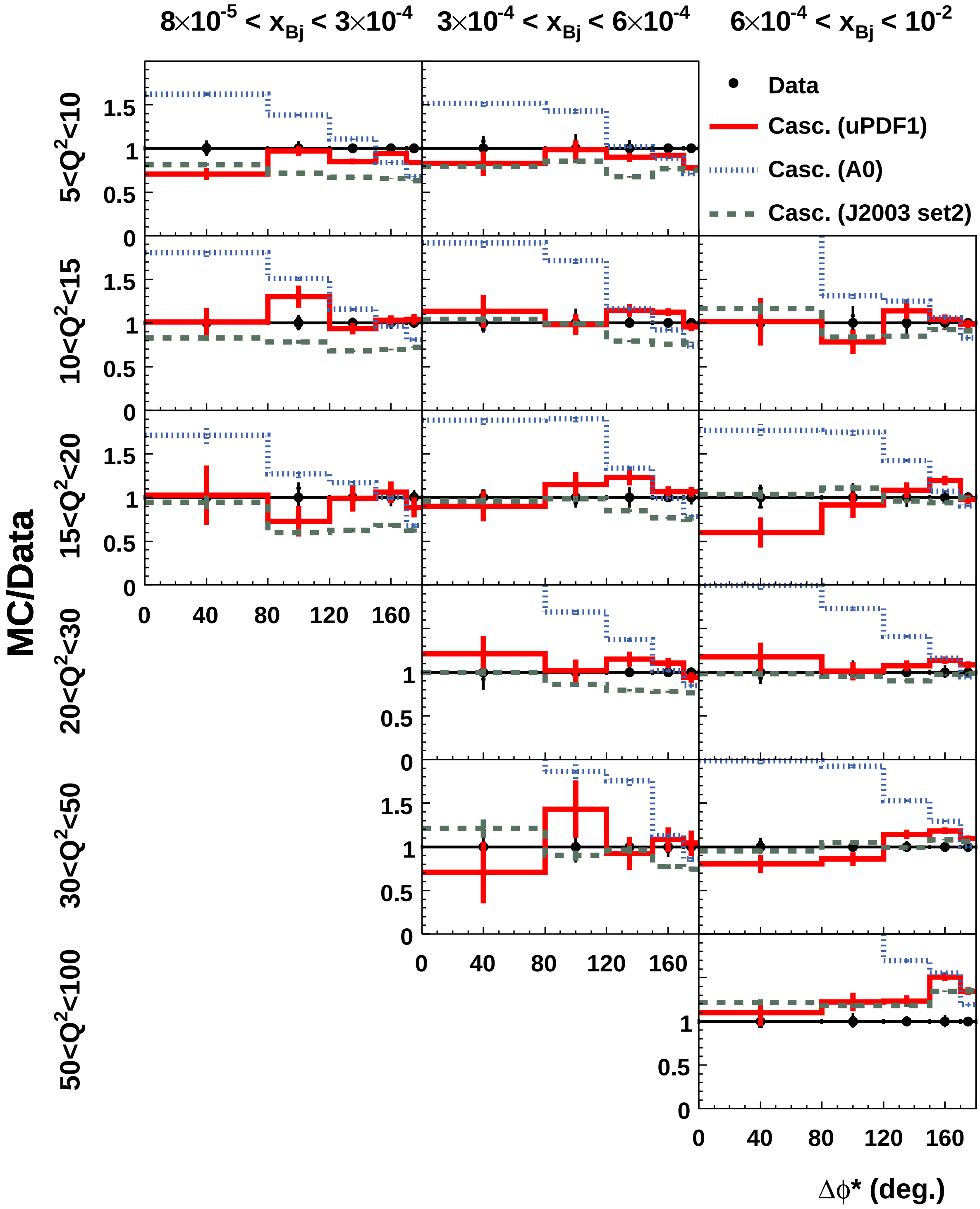

Figure 5.7: *Ratio of the theoretical predictions and the measured dijet cross sections as a function of* $\Delta\phi^*$ *in bins of* x_{Bj} *and* Q^2*. Data are compared to the predictions of* CASCADE *using the uPDFs A0, J2003 set2 and uPDF1 obtained from the fit.*

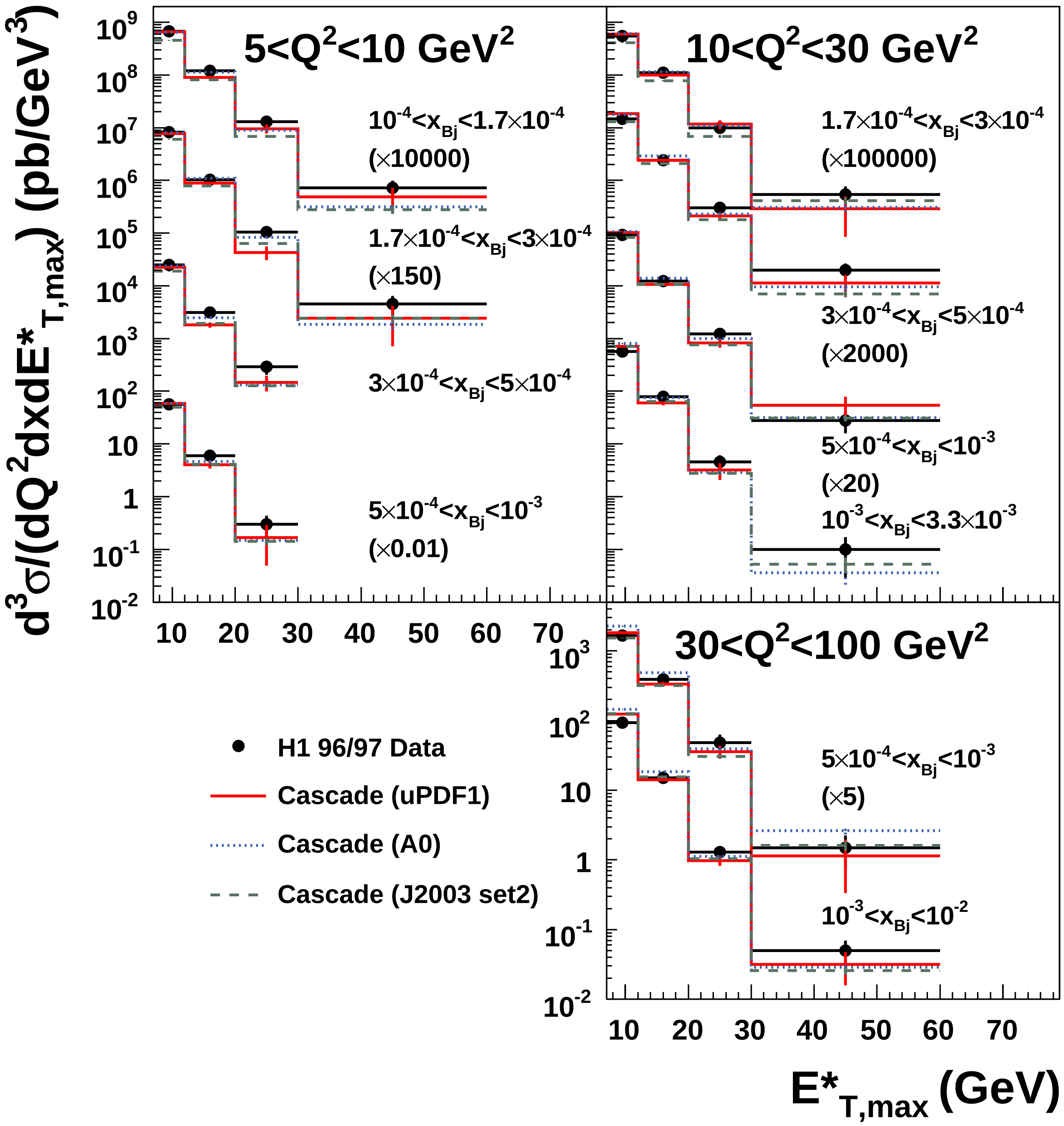

Figure 5.8: *The dijet cross sections as a function of* $E^*_{T,Max}$ *in bins of* x_{Bj} *and* Q^2 *from [12] compared to the predictions of* CASCADE *using the uPDFs A0, J2003 set2 and uPDF1 obtained from the fit.*

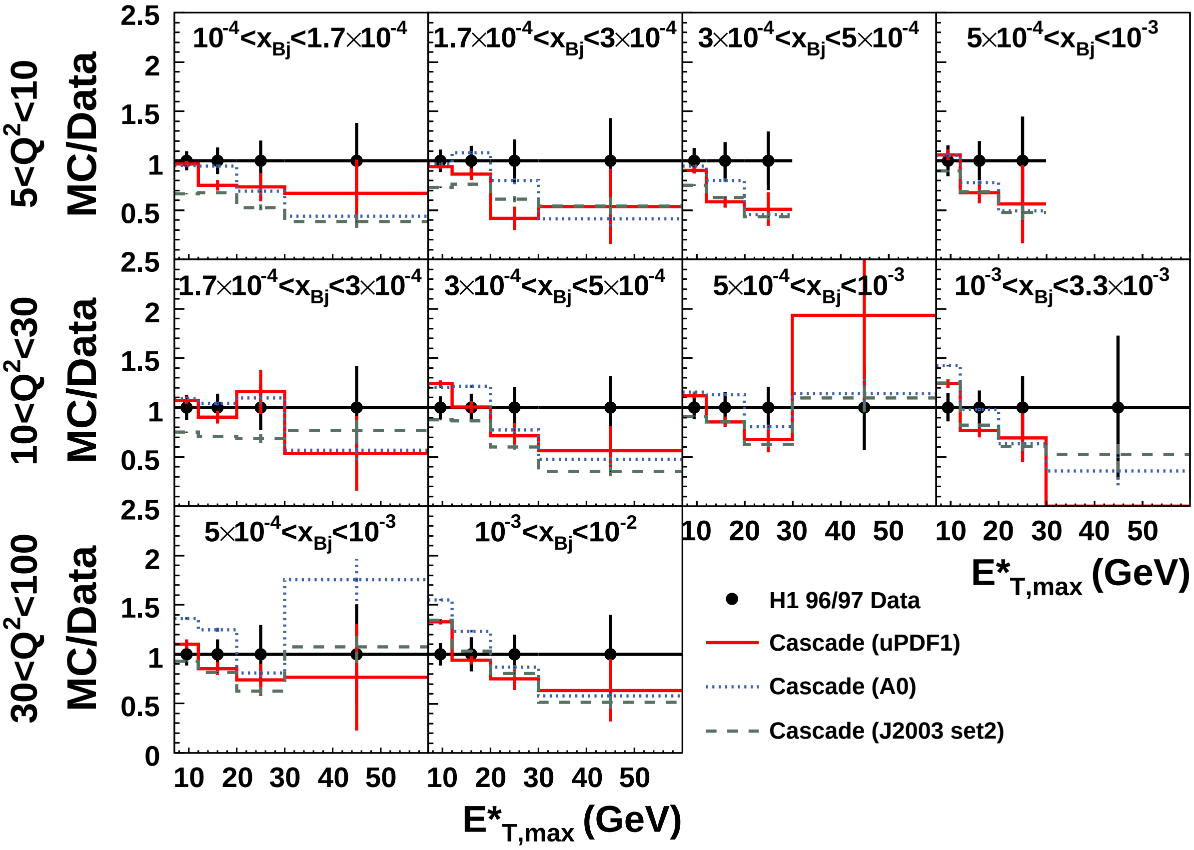

Figure 5.9: *Ratio of the theoretical predictions and the measured dijet cross sections as a function of* $E^*_{T,Max}$ *in bins of* x_{Bj} *and* Q^2 *from [12]. Data are compared to the predictions of* CASCADE *using the uPDFs A0, J2003 set2 and uPDF1 obtained from the fit.*

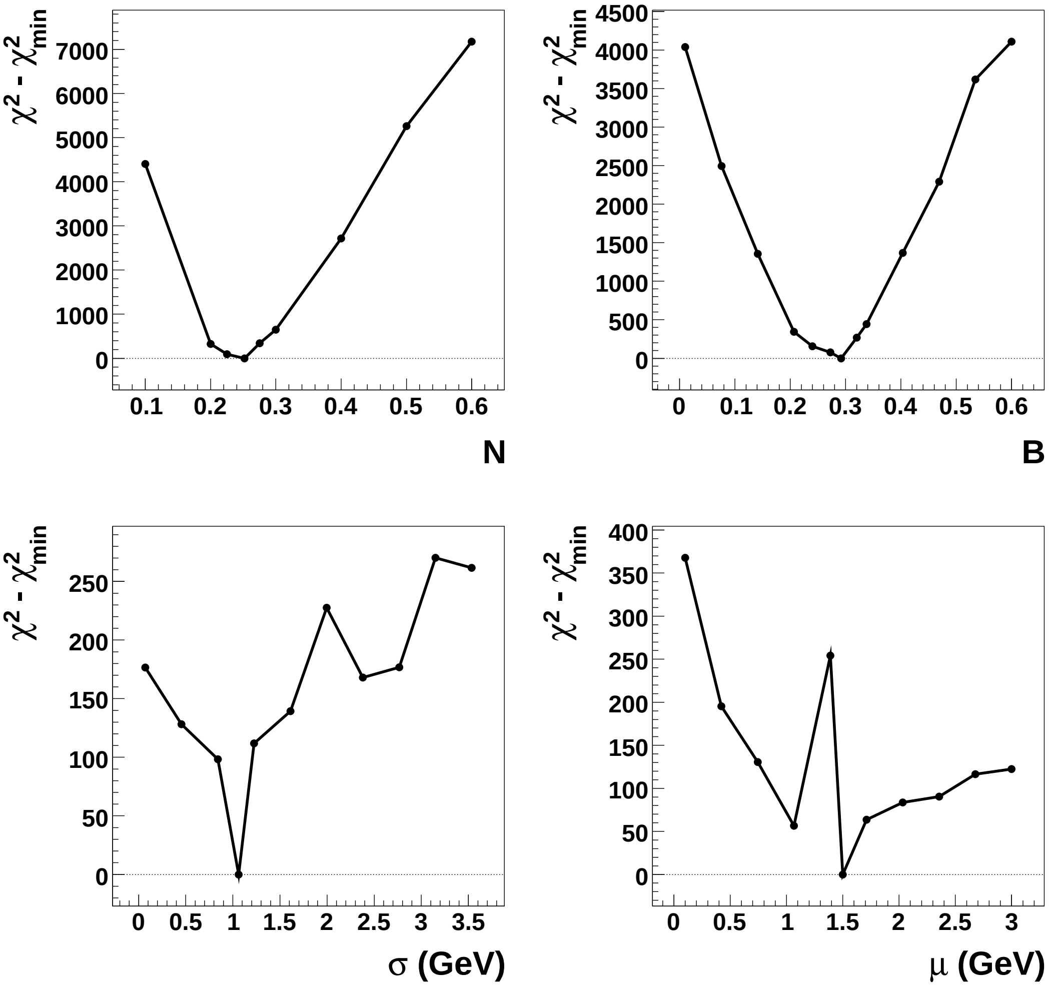

Figure 5.10: *The* χ^2 *profile as a function of the various parameters,* N*,* B*,* σ *and* μ*, in the fit of the unintegrated gluon density. Plotted on the vertical axis is the difference between the total* χ^2 *and the minimum* χ^2 *obtained from the fit (uPDF1).*

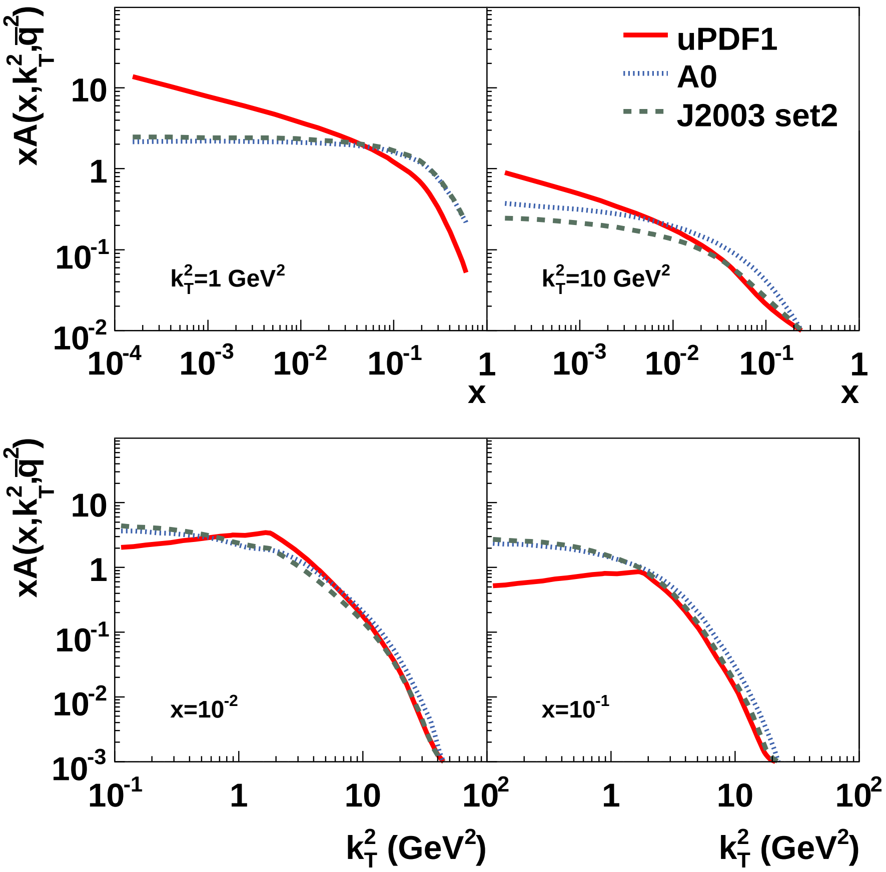

Figure 5.11: *A comparison of the unintegrated gluon densities uPDF1, A0 and J2003 set2. The uPDFs are plotted as a function of* x *for two different values of* k_T^2 *(upper), and as a function of* k_T^2 *for two different values of* x *(lower). A factorization scale* $\bar{q} = 4$ *GeV has been used.*

shape of the uPDF is determined by the Gaussian intrinsic k_T distribution chosen for the starting density function. The impact of choosing different mean values μ of the Gaussian intrinsic k_T distribution is clearly seen: A0 and J2003 set2 both have $\mu = 0$ GeV (with $\sigma = 0.94$ GeV and 0.83 GeV, respectively), leading to uPDFs that rise toward $k_T^2 = 0$ GeV^2, while uPDF1 with $\mu = 1.5$ GeV peaks at $k_T^2 \sim 1.5$ GeV^2 and decreases for smaller k_T^2. A similar behaviour is expected in the saturation model (GBW) [132]. In the high k_T region, the uPDF is mostly determined by the perturbative evolution and should be less sensitive to the non-perturbative input distribution. Indeed, uPDF1, A0 and J2003 set2 are very similar for large k_T^2, although A0 is slightly higher than the others for large k_T^2, as expected.

Chapter 6

Summary and Outlook

Summary
In this thesis, a measurement of dijet events in deep inelastic *ep*-scattering at HERA is presented. The analysis was performed using data collected by the H1 experiment during 1999-2000 with an integrated luminosity of $\mathcal{L} = 64.3$ pb^{-1}. The DIS events were selected with $5 < Q^2 < 100$ GeV^2 and $0.1 < y < 0.7$, while the jets where required to have a transverse momentum $E_T^* > 5$ GeV in the hadronic center-of-mass frame and be within $-1 < \eta < 2.5$ in the lab frame.

Inclusive dijet cross sections are presented as a function of x_{Bj} and Q^2, and compared to predictions of QCD models implementing LO matrix elements, parton showers and hadronisation effects. The best agreement is found with Rapgap when incorporating the resolved photon contribution, while Lepto(CDM) and Cascade, with the A0 unintegrated gluon density, describe the data at low x_{Bj} and low Q^2 but overshoot the data for larger values of x_{Bj} and Q^2. With the J2003 set2 unintegrated gluon density, the predictions of Cascade are too low at low x_{Bj} and Q^2 but are becoming too high at high x_{Bj} and Q^2.

A measurement of azimuthal correlations of dijets is presented double differentially in bins of x_{Bj} and in bins of Q^2, respectively, and triple differentially in bins of x_{Bj} and Q^2. The data are compared to fixed order QCD calculations corrected for hadronisation effects, and to the same QCD models as for the inclusive cross sections. The NLO 2-jet ($\mathcal{O}(\alpha_s^2)$) calculations are not able to describe the data, but are consistently too low for $\Delta\phi^* < 150°$. The discrepancy is largest for low x_{Bj} and/or low Q^2. The NLO 3-jet ($\mathcal{O}(\alpha_s^3)$) calculations are also lower than data for $\Delta\phi^* < 150°$, but due to the large uncertainties connected to the variation of the renormalization and factorization scales, μ_r and μ_f, the NLO 3-jet calculations are able to describe the data in most bins within the errors. By normalising the cross sections with the total cross section between $0 < \Delta\phi^* < 170°$ in each x_{Bj} and Q^2 bin, some of the scale uncertainties are cancelled and the NLO calculations are no longer able to describe the data. Comparing the data to predictions of Cascade one can clearly see the sensitivity of the azimuthal correlations to the choice of uPDF. The J2003 set2 uPDF gives approximately the correct shape but falls somewhat below data at low x_{Bj} and low Q^2, whereas it slightly overshoots data in the highest x_{Bj} and Q^2 bin. In the intermediate region the description is reasonably good. On the other hand, Cascade with the A0 uPDF predicts a completely different $\Delta\phi^*$ dependence where the cross section is much too high for small $\Delta\phi^*$ but approaches data as $\Delta\phi^*$ increases. This behaviour is typical for all kinematic bins but the absolute magnitude of the cross section increases with increasing x_{Bj} and Q^2, compared to data. The colour dipole model in combination with LO matrix elements, Lepto(CDM), generally predicts less decorrelation of the dijets compared to data, i.e. too many back-to-back jets and too few dijet events with low $\Delta\phi^*$. It is, however, closer to the data at low x_{Bj} and Q^2 than at high x_{Bj} and Q^2. Rapgap DIR is able to describe the back-to-back bin in almost all x_{Bj} and Q^2 bins, but undershoots the data for lower $\Delta\phi^*$. Adding the contribution from resolved photons, Rapgap DIR+RES is closer to the data for low $\Delta\phi^*$ compared to Rapgap DIR, but predicts too many back-to-back jets. In contrast to Lepto(CDM), both Rapgap DIR and Rapgap DIR+RES do a better job at high x_{Bj} and Q^2 compared to low x_{Bj} and Q^2.

The measurement thus shows that neither the direct DGLAP approximation nor models breaking the transverse momentum ordering in the parton ladder satisfactorily describe the azimuthal correlations. The best description is found using a model implementing the CCFM approximation, but this, on the other hand, shows a large sensitivity to the choice of the unintegrated PDF. Fixed order NLO calculations of $\mathcal{O}(\alpha_s^2)$ and $\mathcal{O}(\alpha_s^3)$ are also not able to fully describe the data, indicating that higher order corrections are important for this observable. This is in agreement with the measurement of [12], but in contrast to the recently published measurement of [89], where good agreement with $\mathcal{O}(\alpha_s^3)$ calculations was found.

A combined fit of the unintegrated gluon density in the CCFM approach to the triple differential dijet data $\frac{d^3\sigma}{dx_{Bj}dQ^2d\Delta\phi^*}$ presented in this analysis and the triple differential dijet data $\frac{d^3\sigma}{dx_{Bj}dQ^2dE^*_{T,Max}}$ from [12] has been performed. The dijet correlation cross section is directly sensitive to the $k_{T,g}$ of the interacting gluon and in a limited range also sensitive to its longitudinal momentum fraction x_g. The dijet data from [12], however, shows a large sensitivity to x_g but a limited sensitivity to $k_{T,g}$. By combining the two, a better constraint of the unintegrated gluon density $\mathcal{A}(x, k_T, \bar{q})$ is expected. The starting distribution is parameterized as $x\mathcal{A}_0(x, k_T, \bar{q}_0) = N \cdot x^{-B} \cdot (1-x)^4 \cdot exp\left(-\frac{(k_T-\mu)^2}{2\sigma^2}\right)$, where N, B, μ and σ are free parameters in the fit. By excluding the highest x_{Bj} and Q^2 bin in the azimuthal correlation data, a reasonable fit with χ^2/ndf= 150.85/93 = 1.62 is found. The unintegrated gluon density obtained is very similar to that found when fitting to the azimuthal correlation data alone, indicating that the data from [12] has a small influence on the result. The gluon density found in the fit rises more steeply towards low x compared to A0 and J2003 set2, but is similar to the uPDF found in a previous fit to F_2^c [134]. Also, the data fitted in this analysis prefer a mean $\mu \neq 0$ GeV for the Gaussian intrinsic k_T distribution resulting in a decreasing uPDF as $k_T \rightarrow 0$. It should be noted that the k_T distribution is assumed to be a Gaussian in the fit, and that this assumption is not constrained.

Outlook

In a possible continuation of this analysis, an improved hadronic calibration would decrease the migrations significantly and make possible a finer binning in $\Delta\phi^*$. A related variable to $\Delta\phi^*$ which would be interesting to measure, is the vectorial P_T sum of the two dijets, $|\sum_{j=1,2}\bar{P}_{T,j}|$. This variable was measured in [89]. Another variable, proposed in [107], is $f(P^2_{T,Max} > k \cdot P^2_{T,Min}) = \frac{\sigma_{Dijet}(P^2_{T,Max} > k \cdot P^2_{T,Min})}{\sigma_{Dijet}}$ where $P^2_{T,Max} = max(P^2_{T,1}, P^2_{T,2})$, $P^2_{T,Min} = min(P^2_{T,1}, P^2_{T,2})$ and k is a positive number. This variable is a measure of the spread in the $P_{T,1}^2 \times P_{T,2}^2$ space, which should differ significantly between DGLAP and non-DGLAP approximations, and also between different uPDFs. It would also be interesting to extend the analysis by measuring the azimuthal correlation between the most forward jet and the scattered electron [88,102,103,106] similar to the analysis in hadron-hadron colliders where the azimuthal correlation between the two jets most separated in rapidity is measured [90].

Regarding the fit of the unintegrated gluon density, more work is needed to clarify why different densities are obtained for different data sets. The next steps would also include fitting the uPDF with uncorrelated and correlated errors separated, so that an uncertainty in the uPDF can be estimated. There is ongoing work to develop a framework in which a more precise fit can be performed [139,140]. In such a procedure, errors of the parameters could be obtained.

Acknowledgement

These four and a half years would surely not have been such a pleasure without the commitment and support from my supervisor, Prof. Leif Jönsson. With his continuous encouragement and willingness to share his great experience, I have always felt privileged to be a part of the H1 Lund group. I could not have wished for a better supervisor. I would like to thank Dr. Hannes Jung for official supervision during the first years, and for his continued engagement in the analysis also during the last years. Always being positive and full of ideas, suggestions and solutions, Hannes has been of invaluable help throughout the course of my PhD. I thank my partners in crime, Albert Knutsson and Sakar Osman, for creating a stimulating atmosphere in the office, where all questions and problems are taken seriously (but never too seriously, of course). Many thanks to all who read and commented the thesis. Apart from Leif, Hannes, Albert and Sakar, who were more or less forced to read it, I would also like to thank Prof. Evert Stenlund, the thesis inspector, Dr. Dave Milstead, Dr. Stephen J. Maxfield and Lena for many valuable corrections, comments and suggestions. I really appreciate all the time and effort you have spent on improving the thesis.

As I have been part of a large international collaboration, there are many people who have helped me with a number things, from general analysis issues to technical complications. To name you all would be impossible, so a big “Thank You” to the whole H1 collaboration, and especially to the HaQ group. I have also much appreciated the company of the staff at the Division of Experimental High-Energy Physics in Lund.

Kungliga Fysiografiska Sällskapet is kindly acknowledged for financial support.

Last, but not least, I am grateful to

PPM2, for constantly reminding me that there are other things in life than physics.

Magnus, for designing the cover of the thesis.

Lena, Mamms, Sofia, Andreas, family and friends.

Bibliography

[1] H. Geiger and E. Marsden, 1909, Proc. R. Soc. London **82**, 495

[2] E. Rutherford, 1911, Philos. Mag. **21**, 669

[3] R. Hofstadter and R. W. McAllister, 1955, Phys. Rev. **98**, 217

[4] R. Hofstadter, 1956, Rev. Mod. Phys. **28**, 214

[5] R. E. Taylor, Rev. Mod. Phys. **63** (1991) 573

[6] H. W. Kendall, Rev. Mod. Phys. **63** (1991) 597

[7] J. I. Friedman, Rev. Mod. Phys. **63** (1991) 615

[8] V. Gribov and L. Lipatov, Sov. J. Nucl. Phys. **15** (1972) 438 and 675

[9] L. Lipatov, Sov. J. Nucl. Phys. **20** (1975) 94

[10] G. Altarelli and G. Parisi, Nucl. Phys. **B 126** (1977) 298

[11] Y. Dokshitzer, Sov. Phys. JETP **46** (1977) 641

[12] A. Aktas *et al.* [H1 Collaboration], Eur. Phys. J. C **33** (2004) 477 [arXiv:hep-ex/0310019]

[13] F. Halzen and A. D. Martin, Quarks and Leptons: An Introductory Course in Modern Particle Physics, Wiley 1984

[14] R. N. Cahn and G. Goldhaber, The Experimental Foundations of Particle Physics, Cambridge University Press, 1989

[15] J. D. Bjorken and E. A. Paschos, Phys. Rev. **185** (1969) 1975

[16] R. P. Feynman, Phys. Rev. Lett. **23** (1969) 1415

[17] C. G. Callan and D. J. Gross, Phys. Rev. Lett. **22** (1969) 156

[18] E. D. Bloom *et al.*, Phys. Rev. Lett. **23** (1969) 930

[19] M. Breidenbach *et al.*, Phys. Rev. Lett. **23** (1969) 935

[20] W. Albrecht *et al.*, PRINT-94-0179, DESY-69-46 (1969)

[21] R. E. Taylor and F. J. Gilman, Proc. of the 4th Int. Symposium on Electron and Photon Interactions at High Energies, Liverpool (1969)

[22] D. J. Fox *et al.*, Phys. Rev. Lett. **33** (1974) 1504

[23] Y. Watanabe *et al.*, Phys. Rev. Lett. **35** (1975) 898

[24] C. Chang *et al.*, Phys. Rev. Lett. **35** (1975) 901

[25] H. L. Anderson *et al.*, Phys. Rev. Lett. **38** (1977) 1450

[26] C. Adloff *et al.* [H1 Collaboration], Eur. Phys. J. C **30** (2003) 1 [arXiv:hep-ex/0304003]

[27] W.-M. Yao *et al.*, J. Phys. G **33**, 1 (2006)

[28] G. Altarelli, Phys. Rept. **81** (1982) 1

[29] J. R. Andersen *et al.* [Small x Collaboration], Eur. Phys. J. C **35** (2004) 67 [arXiv:hep-ph/0312333]

[30] E. Kuraev, L. Lipatov and V. Fadin, Sov. Phys. JETP **44** (1976) 443

[31] E. Kuraev, L. Lipatov and V. Fadin, Sov. Phys. JETP **45** (1977) 199

[32] Y. Balinsky and L. Lipatov, Sov. J. Nucl. Phys. **28** (1978) 822

[33] B. Andersson *et al.* [Small x Collaboration], Eur. Phys. J. C **25** (2002) 77 [arXiv:hep-ph/0204115]

[34] M. Ciafaloni, Nucl. Phys. B **296** (1988) 49

[35] S. Catani, F. Fiorani and G. Marchesini, Phys. Lett. B **234** (1990) 339

[36] S. Catani, F. Fiorani and G. Marchesini, Nucl. Phys. B **336** (1990) 18

[37] G. Marchesini, Nucl. Phys. B **445** (1995) 49

[38] G. Gustafson, Phys. Lett. B **175** (1986) 453

[39] G. Gustafson and U. Pettersson, Nucl. Phys. B **306** (1988) 746

[40] B. Andersson *et al.*, Z. Phys. C **43** (1989) 625

[41] B. Andersson G. Gustafson and L. Lönnblad, Nucl. Phys. B **339** (1990) 393

[42] L. Lonnblad, Z. Phys. C **65** (1995) 285

[43] A. H. Mueller, Nucl. Phys. B **415** (1994) 373

[44] L. Lonnblad, CERN-TH/95-95

[45] L. Lonnblad, Z. Phys. C **70** (1996) 107

[46] R. D. Field and R. P. Feynman, Phys. Rev. D **15** (1977) 2590

[47] R. D. Field and R. P. Feynman, Nucl. Phys. B **136** (1978) 1

[48] R. D. Field and S. Wolfram, Nucl. Phys. B **213** (1983) 65

[49] B. R. Webber, Nucl. Phys. B **238** (1984) 492

[50] X. Artru and G. Mennessier, Nucl. Phys. B **70** (1974) 93

[51] M. G. Bowler, Z. Phys. C **11** (1981) 169

[52] B. Andersson, G. Gustafson and B. Soderberg, Z. Phys. C **20** (1983) 317

[53] B. Andersson, G. Gustafson, G. Ingelman and T. Sjostrand, Phys. Rept. **97** (1983) 31

[54] B. Andersson, G. Gustafson and B. Soderberg, Nucl. Phys. B **264** (1986) 29

[55] W. Bartel *et al.* [JADE Collaboration], Z. Phys. C **33** (1986) 23

[56] M. H. Seymour, Z. Phys. C **62** (1994) 127

[57] S. Catani, Y. L. Dokshitzer and B. R. Webber, Phys. Lett. B **285** (1992) 291

[58] S. Catani, Y. L. Dokshitzer, M. H. Seymour and B. R. Webber, Nucl. Phys. B **406** (1993) 187

[59] S. D. Ellis and D. E. Soper, Phys. Rev. D **48** (1993) 3160 [arXiv:hep-ph/9305266]

[60] M. H. Seymour, Nucl. Phys. B **513** (1998) 269 [arXiv:hep-ph/9707338]

[61] M. Wobisch and T. Wengler, To be published in the proceedings of Workshop on Monte Carlo Generators for HERA Physics (Plenary Starting Meeting), Hamburg, Germany, 27-30 Apr 1998 [arXiv:hep-ph/9907280]

[62] J. Huth *et al.*, FERMILAB-CONF-90 249-E (1990)

[63] H. Jung, Comput. Phys. Commun. **86** (1995) 147

[64] A. Kwiatkowski *et al.* Proc. of the Workshop on Physics at HERA, eds. W. Buchmüller and G. Ingelmann, Hamburg (1992) 1294

[65] T. Sjostrand, Comput. Phys. Commun. **39** (1986) 347

[66] T. Sjostrand, Comput. Phys. Commun. **82** (1994) 74

[67] H. Jung and G. P. Salam, Eur. Phys. J. C **19** (2001) 351 [arXiv:hep-ph/0012143]

[68] H. Jung, Comp. Phys. Comm. **143** (2002) 100 [arXiv:hep-ph/0109102]

[69] T. Sjostrand et al., Comp. Phys. Comm. **135** (2001) 238

[70] H. Jung, arXiv:hep-ph/0411287

[71] M. Hansson and H. Jung, arXiv:hep-ph/0309009

[72] H. Jung, Acta Phys. Polon. B **33** (2002) 2995 [arXiv:hep-ph/0207239]

[73] L. Lönnblad, Comp. Phys. Comm. **71** (1992) 15

[74] G. Ingelman, A. Edin and J. Rathsman, Comput. Phys. Commun. **101** (1997) 108 [arXiv:hep-ph/9605286]

[75] G.A. Schuler, H. Spiesberger, Proc. of the Workshop on Physics at HERA, eds. W. Buchmüller and G. Ingelman, Hamburg (1992) 1419

[76] R. Engel, Z. Phys. C **66** (1995) 203

[77] R. Engel and J. Ranft, Phys. Rev. D **54** (1996) 4244

[78] Z. Nagy and Z. Trocsanyi, Phys. Rev. Lett. **87** (2001) 082001 [arXiv:hep-ph/0104315]

[79] M. Klasen and G. Kramer, Phys. Lett. B **366** (1996) 385 [arXiv:hep-ph/9508337]

[80] S. Frixione and G. Ridolfi, Nucl. Phys. B **507** (1997) 315 [arXiv:hep-ph/9707345]

[81] A. Banfi and M. Dasgupta, JHEP **0401** (2004) 027 [arXiv:hep-ph/0312108]

[82] C. Duprel, T. Hadig, N. Kauer and M. Wobisch, arXiv:hep-ph/9910448

[83] B. Potter, Comput. Phys. Commun. **133** (2000) 105 [arXiv:hep-ph/9911221]

[84] J. Chyla and K. Sedlak, arXiv:hep-ph/0308116

[85] A. Knutsson, Ph.D. Thesis, Forward Jet Production in *ep*-collisions at HERA, 2007

[86] J. Pumplin, D. R. Stump, J. Huston, H. L. Lai, P. Nadolsky and W. K. Tung, JHEP **0207** (2002) 012 [arXiv:hep-ph/0201195]

[87] G. A. Schuler and T. Sjostrand, Phys. Lett. B **376** (1996) 193 [arXiv:hep-ph/9601282]

[88] C. Adloff *et al.* [H1 Collaboration], Nucl. Phys. B **538** (1999) 3 [arXiv:hep-ex/9809028]

[89] S. Chekanov *et al.* [ZEUS Collaboration], arXiv:0705.1931 [hep-ex]

[90] S. Abachi *et al.* [D0 Collaboration], Phys. Rev. Lett. **77** (1996) 595 [arXiv:hep-ex/9603010]

[91] V. M. Abazov *et al.* [D0 Collaboration], Phys. Rev. Lett. **94** (2005) 221801 [arXiv:hep-ex/0409040]

[92] A. J. Askew, D. Graudenz, J. Kwiecinski and A. D. Martin, Phys. Lett. B **338** (1994) 92 [arXiv:hep-ph/9407337]

[93] E. Mirkes and S. Willfahrt, Phys. Lett. B **414** (1997) 205 [arXiv:hep-ph/9708231]

[94] J. Kwiecinski, A. D. Martin and A. M. Stasto, Phys. Lett. B **459** (1999) 644 [arXiv:hep-ph/9904402]

[95] A. Banfi, G. Marchesini and G. Smye, JHEP **0204** (2002) 024 [arXiv:hep-ph/0203150]

[96] A. Banfi, G. Marchesini and G. Smye, Acta Phys. Polon. B **33** (2002) 3323 [arXiv:hep-ph/0207072]

[97] Y. Delenda, arXiv:0706.2172 [hep-ph]

[98] A. S. Vera and F. Schwennsen, arXiv:0707.0256 [hep-ph]

[99] A. S. Vera and F. Schwennsen, arXiv:hep-ph/0702158

[100] A. S. Vera and F. Schwennsen, arXiv:hep-ph/0611151

[101] E. Cuautle, I. Dominguez and G. Paic, AIP Conf. Proc. **857** (2006) 283 [arXiv:hep-ph/0604257]

[102] J. Bartels, V. Del Duca and M. Wusthoff, Z. Phys. C **76** (1997) 75 [arXiv:hep-ph/9610450]

[103] F. Schwennsen, arXiv:hep-ph/0703198

[104] A. Szczurek, A. Rybarska and G. Slipek, arXiv:0704.3537 [hep-ph]

[105] C. Marquet and C. Royon, arXiv:0704.3409 [hep-ph]

[106] A. S. Vera and F. Schwennsen, arXiv:0708.0549 [hep-ph]

[107] M. Luszczak and A. Szczurek, Phys. Lett. B **594** (2004) 291 [arXiv:hep-ph/0404210]

[108] I. Abt *et al.* [H1 Collaboration], Nucl. Instrum. Meth. A **386** (1997) 310

[109] I. Abt *et al.* [H1 Collaboration], Nucl. Instrum. Meth. A **386** (1997) 348

[110] M. Peez, B. Portheault and E. Sauvan, *An Energy Flow Algorithm for Hadronic Reconstruction In OO: Hadroo2*, H1 internal note (2005). H1-IN-616. M. Peez, B. Portheault, E. Sauvan, CPPM Marseille, LAL Orsay

[111] C. Adloff *et al.* [H1 Collaboration], Z. Phys. C **74** (1997) 221 [arXiv:hep-ex/9702003]

[112] H1 Collaboration, Guide for the H1 simulation program H1SIM, H1 Software Note 3 (1989)

[113] R. Brun, R. Hagelberg, M. Hansroul and J. C. Lassalle, "Geant: Simulation Program For Particle Physics Experiments. User Guide And Reference Manual", CERN-DD-78-2-REV

[114] S.Egli *et al.*, H1 Internal Note H1-IN-517(04/1997)

[115] S. Bentvelsen, J. Engelen and P. Kooijman, Reconstruction of (x,Q^2) and Extraction of Structure Functions in Neutral Current Scattering at HERA, in *Proc. of the Workshop on Physics at HERA. Vol. 1*, edited by W. Buchmüller and G. Ingelman, page 23, Hamburg, 1991, DESY, NIKHEF-H-92-02

[116] F. Jacquet and A. Blondel, Proceedings of the Study for an ep Facility for Europe, U. Amaldi (ed.), p. 391. Hamburg, Germany (1979). Also in DESY-79-048 (1979) 377

[117] U. Bassler and G. Bernardi, Nucl. Instrum. Meth. A **361** (1995) 197 [arXiv:hep-ex/9412004]

[118] U. Bassler and G. Bernardi, Nucl. Instrum. Meth. A **426** (1999) 583 [arXiv:hep-ex/9801017]

[119] R. Pöschl, Ph.D. Thesis, Dortmund (2000)

[120] T. Schoerner-Sadenius, Ph.D. Thesis, München (2001)

[121] C. Adloff *et al.* [H1 Collaboration], Phys. Lett. B **542** (2002) 193 [arXiv:hep-ex/0206029]

[122] G. D'Agostini, A Multidimensional Unfolding Method Based on Bayes' Theorem, DESY 94-099

[123] K. Sedlak, Ph.D. Thesis, Measurement of Dijet Production at Low Q^2 at HERA, 2004

[124] T. Kluge, Ph.D. Thesis, Measurement and QCD Analysis of Event Shape Variables in Deep-Inleastic Electron-Proton Collisions at HERA, DESY-THESIS-2004-024

[125] G. D'Agostini, Comments on the Bayesian unfolding, ZEUS-Note 95-166

[126] A. A. Glazov, Ph.D. Thesis, Berlin (1998), DESY-THESIS-1998-005

[127] E. Tzamariudaki, Talk given at the 7th International Conference on Calorimetry in High-Energy Physics (ICCHEP97), Tucson, AZ, (1997)

[128] M. A. Kimber, A. D. Martin and M. G. Ryskin, Phys. Rev. D **63** (2001) 114027 [arXiv:hep-ph/0101348]

[129] A. Szczurek, N. N. Nikolaev, W. Schafer and J. Speth, "Mapping the proton unintegrated gluon distribution in dijets correlations in real and virtual photoproduction at HERA," Phys. Lett. B **500** (2001) 254 [arXiv:hep-ph/0011281]

[130] J. Blumlein, arXiv:hep-ph/9506403

[131] J. Kwiecinski, A. D. Martin and A. M. Stasto, Phys. Rev. D **56** (1997) 3991 [arXiv:hep-ph/9703445]

[132] K. Golec-Biernat and M. Wusthoff, Phys. Rev. D **60** (1999) 114023 [arXiv:hep-ph/9903358]

[133] G. Gustafson, L. Lonnblad and G. Miu, JHEP **0209** (2002) 005 [arXiv:hep-ph/0206195]

[134] H. Jung, A. V. Kotikov, A. V. Lipatov and N. P. Zotov, arXiv:hep-ph/0611093

[135] M. Hansson and H. Jung, arXiv:0707.4276 [hep-ph]

[136] J. Bromley *et al.*, Hamburg 1995/96, Future physics at HERA, vol. 1, 611-612

[137] J.A. Nelder and R. Mead, Computer Journal, vol. 7 (1965) 308-313

[138] F. James and M. Roos, Comput. Phys. Commun. **10** (1975) 343

[139] H. Hoeth, Parameter Optimisation in Monte Carlo Event Generators, Talk given at the 1st MCnet School, IPPP Durham, 18-20th April 2007

[140] H. Jung, A. Knutsson and K. Kutak, Fitting of gluon density with Monte Carlo, Talk at the LHC-D workshop on QCD and electroweak physics at the LHC, MPI Munich, July 2007

Appendix A

The Toy Model

This appendix describes the toy model used for performing a detailed study of the migrations in the azimuthal correlation measurement (see Section 4.1).

The starting point is to determine the resolutions of the relevant observables (E_T^*, η, ϕ, Q^2) using detector simulated Monte Carlo events. The resolutions for η, ϕ and Q^2 are obtained inclusively by fitting Gaussian distributions to each resolution plot. The E_T^* resolutions, however, are determined in six bins of $E_{T,HAD}^*$ with the lower limit $E_{T,HAD}^* >$ 3 GeV, by fitting a combination of a Gaussian and two Landau distributions to each resolution histogram. The results on the mean value, μ, for the Gaussian distribution, the most probable value, mpv, for each of the Landau distributions and their standard deviations, σ, are given in Table A.1. The events are then passed through the analysis code again, and if an event passes the DIS selection on the hadron level, one or more of the observables E_T^*, η, ϕ and Q^2 will be smeared according to Table A.1. This leads to two event samples, one of which contains the original set of hadron level observables and the other a set of smeared observables, constituting a "toy detector level". The dijet selection can then be applied to both these levels, and purities and stabilities can be calculated. In this way, one can study the migrations in detail by "turning on" and "off" the smearing of the observables in different combinations.

Since all the smearing is applied after the DIS selection, migrations over the DIS cuts are neglected in this toy model. The smearing of Q^2 is only applied to investigate the effect of migrations between different Q^2 bins.

	Bin	Landau 1		Gauss		Landau 2	
		mpv $(/10^{-1})$	σ $(/10^{-2})$	μ $(/10^{-2})$	σ $(/10^{-1})$	mpv $(/10^{-1})$	σ $(/10^{-2})$
E_T^*	$3.0 < E_T^* < 5.0$ GeV	-2.23	10.8	-10.7	0.87	0.21	5.43
	$5.0 < E_T^* < 7.5$ GeV	-4.45	8.49	-7.18	1.45	3.02	5.00
	$7.5 < E_T^* < 10$ GeV	-6.07	6.34	-9.14	1.55	3.24	4.65
	$10 < E_T^* < 12.5$ GeV	-7.08	4.54	-9.67	1.53	3.13	4.23
	$12.5 < E_T^* < 20$ GeV	-7.86	4.52	-9.59	1.41	2.90	3.44
	$E_T^* > 20$ GeV	-8.81	3.12	-10.1	1.14	2.27	2.56
η	–	–	–	1.2	0.54	–	–
ϕ	–	–	–	-1.7	0.60	–	–
Q^2	–	–	–	0.1	0.32	–	–

Table A.1: *The mean μ (for the Gaussian distributions), the most probable value, mpv, (for the Landau distributions) and σ used in the toy model.*

Appendix B

Definition of Trigger Elements

In this appendix, the definition of each trigger element present in either the physics triggers (S0, S61) or in the monitor triggers (S39, S64, S66, S67, S77) is given. The triggers are defined in Table 4.1.

Trigger element	Definition
SPCLe_IET > 2	An energy deposition with E > 6 GeV in the outer SPACAL region.
SPCLe_IET_Cen_3	An energy deposition with E > 6 GeV in the inner SPACAL region.
DCRPh_THig	At least one track candidate in the CJC with a $p_t > 800$ MeV.
zVtx_sig	A signature for the z-vertex found.
LAr_IF	Sum over all Big Towers[1] (BT) lying in the inner forward modules of the LAr calorimeter (labelled IF2H and IF1E in Figure 2.5) above threshold.
LAr_BR	A track is found in the MWPCs (CIP, COP, FPC) pointing to a Big Tower with an energy deposit exceeding 1 GeV in the LAr calorimeter.
LAr_Etmiss > 1(2)	Missing transverse energy $E_{T,miss} \geqslant 4.5(6)$ GeV as calculated using Big Towers.
LAr_electron_1	An EM energy deposition above threshold in any LAr BT. The threshold is 6 GeV in the backward region and increases in the forward direction due to large beam-induced background.
LAr_electron_2	Same as LAr_electron_1 but with higher threshold (7.5 GeV in the backward region).
LAr_2or3_electrons	Two or three electrons found in the LAr calorimeter.
FwdRay_T0	One or more tracks found in the MWPCs with any topology in the $r - \phi$ plane.

---

[1] The LAr is segmented into Big Towers radially outward from the interaction point, as seen in Figure 2.5.

Appendix C

The Downhill Simplex Method

This appendix summarizes the downhill simplex method. For a more detailed description, see [1,2].

The downhill simplex method needs $N+1$ starting points for the minimization of a function with N free parameters. In this analysis, four parameters were used, so the first step in the minimisation procedure is to calculated five function (χ^2-) values. If each point in the four-dimensional parameter space is labelled P, while e_i and λ_i denote the unit vector and a characteristic length scale of parameter i, and P_0 is the original starting point of the unintegrated gluon density, then the first five points are chosen as P_0 and four points P_i defined by

$$P_i = P_0 + \lambda_i e_i.$$

Using these points, a geometric figure called a simplex can be constructed by connecting the points with lines. The simplex then encloses a four-dimensional volume. For example, with two free parameters, the three starting points can be connected to a triangle which encloses a two-dimensional surface. The idea of the downhill simplex method is then to replace the point with the highest χ^2 value with a new point, thus forming a new simplex. The procedure to find a new point relies on three operations: reflection, contraction and expansion, and is summarised below:

1. Determine which point has the highest (P_{hi}), next-to-highest (P_{nhi}) and lowest (P_{lo}) χ^2 value. Let y_{hi}, y_{nhi} and y_{lo} denote the function values in these points.
2. Reflect the highest point P_{hi} through the centroid of the simplex and evaluate $y_{new,1}$ at the new point $P_{new,1}$.
3. If $y_{new,1} < y_{lo}$ then extrapolate $P_{new,1}$ even further away from P_{hi}, to $P_{new,2}$.
    (a) If $y_{new,2} < y_{lo}$, then replace P_{hi} with $P_{new,2}$ and start over from 1.
    (b) If $y_{new,2} > y_{lo}$, then replace P_{hi} with $P_{new,1}$ and start over from 1.
4. If $y_{new,1} > y_{lo}$, but $y_{new,1} < y_{nhi}$, then replace P_{hi} with $P_{new,1}$ and start over from 1.
5. If $y_{new,1} > y_{lo}$, and $y_{new,1} > y_{nhi}$ then
    (a) If $y_{new,1} < y_{hi}$ then replace P_{hi} with $P_{new,1}$.

(b) Contract P_{hi} trough the centroid to a new point $P_{new,3}$.

(c) If $y_{new,3} < y_{hi}$ then replace P_{hi} with $P_{new,3}$ and start over from 1.

(d) If $y_{new,3} > y_{hi}$ then contract all points toward P_{lo} and start over from 1.

Using this algorithm, the simplex "falls" down the slope towards a (local or global) minimum. The advantage of this method is that it only uses function values and not derivatives, making it less sensitive to statistical fluctuations in the calculation of the function values compared to e.g. MIGRAD [138]. However, it does not give any error estimations of the parameters or information about correlations between the parameters.

References

[1] J.A. Nelder and R. Mead, Computer Journal, vol. 7 (1965) 308-313

[2] W.H. Press *et al.*, Numerical Recipes in C: The Art of Scientific Computing, 2nd ed. (1992) Cambridge University Press

Appendix D

Paper I

Proceedings of the 14th International Workshop on Deep Inelastic Scattering (DIS 2006), Tsukuba, Japan, 20-24 Apr 2006.

DECORRELATION OF DIJETS AT LOW x AND Q^2

M. HANSSON*
Lund University,
Box 118, SE-221 00 Lund, Sweden
E-mail: magnus.hansson@hep.lu.se

Correlations in the azimuthal angle between dijets produced in deep inelastic e^+p scattering events have been investigated. Cross sections are presented as a function of the azimuthal separation between the two jets in the hadronic center of mass frame, $\Delta\phi^*$, in different regions of the photon virtuality Q^2 and in different regions of the Bjorken scaling variable x_{Bj}. The results are compared to the predictions of QCD models implementing LO matrix elements, matched parton showers and hadronisation as well as to NLO di-jet (α_s^2) and NLO three-jet (α_s^3) parton level calculations corrected for hadronisation effects.

1. Introduction

Dijet production in deep inelastic ep-scattering is at low x dominated by the boson gluon fusion process. In the DGLAP approximation, the dijets are in LO produced back-to-back in the hadronic center of mass (HCM) frame, i.e. the azimuthal angle between the two jets is[a] $\Delta\phi^* = 180°$, and configurations with $\Delta\phi^* < 180°$ can only originate from higher order initial or final state radiation. At low x, initial state radiation is in the DGLAP approximation ordered in k_t which implies that the transverse momentum of the interacting gluon is restricted. However, at low x there may be non-ordering in k_t such that the gluon interacting with the photon may take any kinematically allowed transverse momentum. This would give a broader $\Delta\phi^*$ spectrum[1] compared to that predicted by DGLAP. Also, in approximations using unintegrated gluon densities the gluon has an initial transverse momentum already in LO. Hence, azimuthal correlations at low x could be used to distinguish between various models describing parton dynamics and also to constrain the unintegrated gluon density.

---

*On behalf of the H1 Collaboration

[a] Observables in the HCM frame are labeled with a *

2. Event Selection

In this analysis, positron-proton data collected by the H1 experiment during 1999-2000 are used, corresponding to an integrated luminosity of $\mathcal{L}_{int} = 64.3\ \mathrm{pb}^{-1}$. Deep inelastic scattering (DIS) events are selected by requiring $E_e^{'} > 9$ GeV, $156° < \theta_e < 175°$, $5 < Q^2 < 100\ \mathrm{GeV}^2$ and $0.1 < y < 0.7$ where $E_e^{'}$ and θ_e is the energy and polar angle of the scattered positron, Q^2 is the virtuality of the exchanged photon and y is the inelasticity. Jets are found using the inclusive k_t-algorithm[2] in the HCM frame and must fulfill $-1 < \eta_j < 2.5$ and $E_{T,j}^{*} > 5$ GeV. If more than two jets are found, the two jets closest to the scattered positron in η are chosen as the dijet system. The data are corrected for limited detector resolution and acceptance using detector simulated QED radiative events generated with the Monte Carlo (MC) programs DJANGOH[3] (with ARIADNE[4]) and RAPGAP[5].

3. Results

The dijet cross section as a function of the azimuthal angle $\Delta\phi^*$ in bins of x_{Bj} is compared to the NLO 2-jet (α_s^2) and NLO 3-jet (α_s^3) calculations obtained using the NLOJET++[6] program. The CTEQ6M[7] PDF is used and the renormalisation and factorisation scales are chosen as $\mu_r = \mu_f = \left(\frac{E_{T1}^{*}+E_{T2}^{*}}{2}\right)$. Scale uncertainties are estimated by varying μ_r and μ_f simultaneously a factor 2 up and 1/2 down. The calculations are corrected for hadronisation effects using CASCADE[8]. Because of infrared sensitivity, the NLO calculations give no meaningful predictions in the back-to-back bin ($170° < \Delta\phi^* < 180°$). As seen in Figure 1 the NLO 2-jet calculation, which effectively is a LO prediction for this observable, is clearly not sufficient to describe the data. The NLO 3-jet calculation, effectively being an NLO prediction, is closer to the data, but is systematically low for $\Delta\phi^* < 150°$. However, the scale uncertainties are large, typically 20 - 50%, and cover the data in most bins. When normalising the data to the total cross section between $0° < \Delta\phi^* < 170°$ in each x_{Bj} bin, there is partial cancellation of the scale uncertainties for the NLO calculations. As can be seen in Figure 2, the data is no longer within the scale uncertainties of the NLO 3-jet calculation.

Figure 3 shows the same data as in Figure 1 compared to the predictions of the CCFM based CASCADE MC generator, using A0[9] and J2003 set2[10] for the unintegrated gluon density. Whereas CASCADE (J2003 set2) describes the data fairly well in all but the lowest x_{Bj} bin, CASCADE (A0) fails to describe the data in all bins, predicting too many jets with small

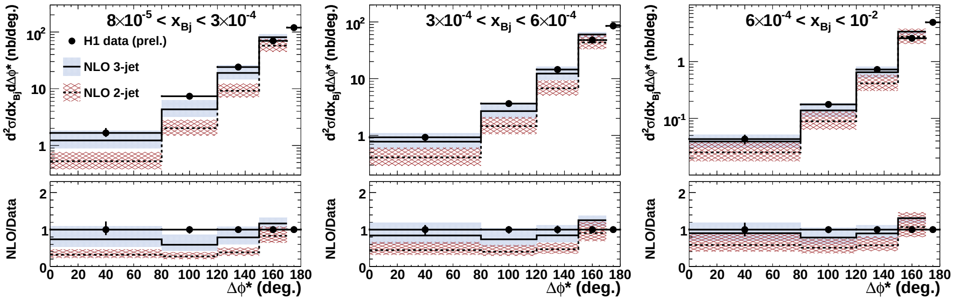

Figure 1. *Dijet cross sections as a function of* $\Delta\phi^*$ *in bins of* x_{Bj}*. Data are compared to NLO 3-jet (full line) and NLO 2-jet (dashed line) calculations.*

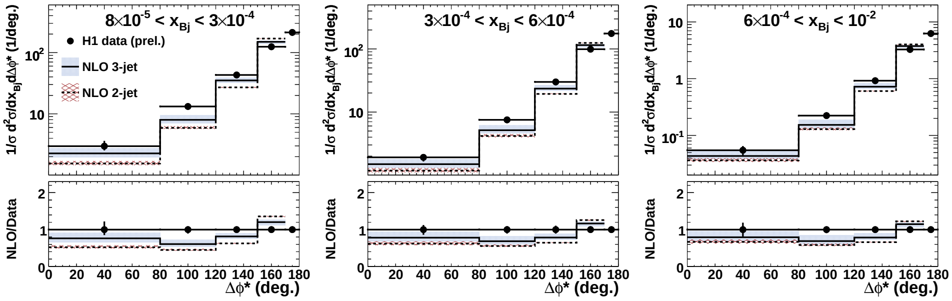

Figure 2. *Dijet cross sections as a function of* $\Delta\phi^*$ *in bins of* x_{Bj} *normalised to the visible cross section between* $0^\circ < \Delta\phi^* < 170^\circ$ *in each* x_{Bj} *bin. Data are compared to NLO 3-jet (full line) and NLO 2-jet (dashed line) calculations.*

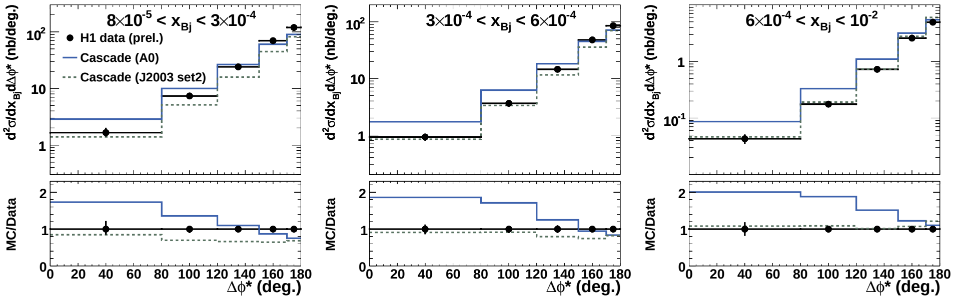

Figure 3. *Dijet cross sections as a function of* $\Delta\phi^*$ *in bins of* x_{Bj} *compared to the predictions of CASCADE using two different unintegrated gluon densities.*

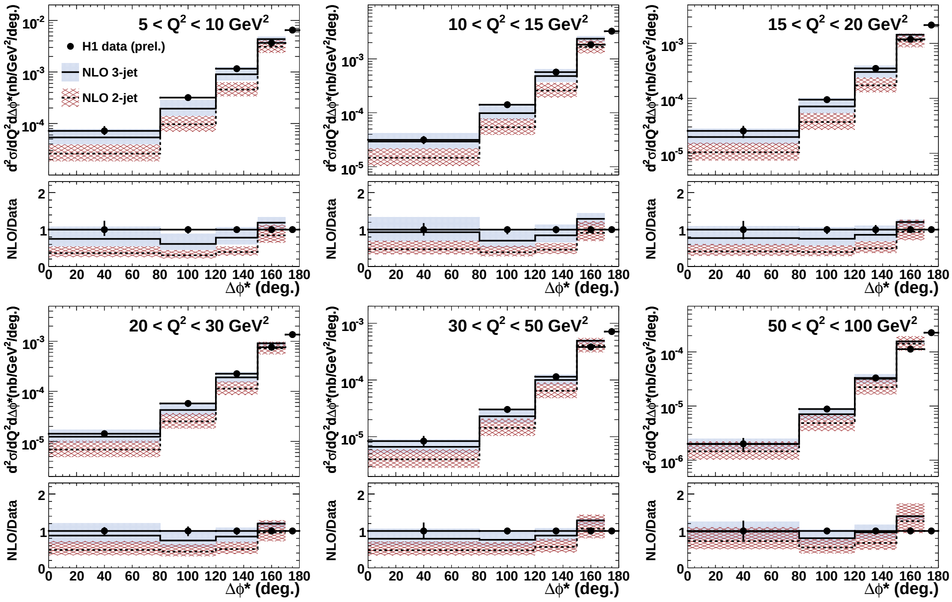

Figure 4. *Dijet cross sections as a function of $\Delta\phi^*$ in bins of Q^2. Data are compared to NLO 3-jet (full line) and NLO 2-jet (dashed line) calculations.*

$\Delta\phi^*$. This indicates that the k_t-spectrum of the gluon distribution of A0 is too hard. In addition to the dijet cross sections in bins of x_{Bj}, the same observable has also been measured in bins of Q^2, shown in Figure 4. The same tendencies are seen as above, also when comparing to CASCADE (not shown).

To summarise, NLO 3-jet calculations are not sufficient to describe the azimuthal decorrelation of dijets at low $\Delta\phi^*$, indicating the need for higher orders. Also, a sensitivity to the unintegrated gluon density is observed.

References

1. A. J. Askew *et al.*, Phys. Lett. B **338** (1994) 92 [arXiv:hep-ph/9407337]
2. S. D. Ellis and D. E. Soper, Phys. Rev. D **48** (1993) 3160
3. K. Charchula *et al.* Comput. Phys. Commun. **81** (1994) 381
4. L. Lönnblad, Comput. Phys. Commun. **71** (1992) 15
5. H. Jung, Comput. Phys. Commun. **86** (1995) 147
6. Z. Nagy and Z. Trocsanyi, Phys. Rev. Lett. **87** (2001) 082001
7. J. Pumplin *et al.* JHEP **0207** (2002) 012 [arXiv:hep-ph/0201195]
8. H. Jung and G. P. Salam, Eur. Phys. J. C **19** (2001) 351
9. H. Jung, [arXiv:hep-ph/0411287]
10. M. Hansson and H. Jung, [arXiv:hep-ph/0309009]

Appendix E

Paper II

To appear in the proceedings of the 15th International Workshop on Deep-Inelastic Scattering and Related Subjects (DIS2007), Munich, Germany, 16-20 Apr 2007.

Towards precision determination of uPDFs

Magnus Hansson[1] and Hannes Jung[2]

1- Lund University
2- DESY, FRG

The unintegrated Parton Density Function of the gluon is obtained from a fit to dijet production in DIS as measured at HERA. Reasonable descriptions of the measurements are obtained, and a first attempt to constrain the intrinsic transverse momentum distribution at small $k_\perp$ is presented [1].

1 Introduction

Unintegrated parton density functions (uPDFs) are best suited to study details of the hadronic final state in high energy *ep* and also in *pp* collisions (for a review see [2–8]). In general, the production cross section for jets, heavy quarks or gauge bosons can be written as a convolution of the uPDF $\mathcal{A}(x, k_\perp^2, \bar{q})$ with the partonic off-shell cross section $\hat{\sigma}(x_i, k_\perp^2)$, with $x_i, k_\perp$ being the longitudinal momentum fraction and the transverse momentum of the interacting parton i and $\bar{q}$ being the factorization scale. For example the cross section for $ep \rightarrow \text{jets} + X$ can be written as:

$$\frac{d\sigma^{jets}}{dE_T d\eta} = \sum_i \int\int\int dx_i \; dQ^2 d \ldots \cdot \left[dk_\perp^2 x_i \mathcal{A}(x_i, k_\perp^2, \bar{q}) \right] \hat{\sigma}(x_i, k_\perp^2)$$

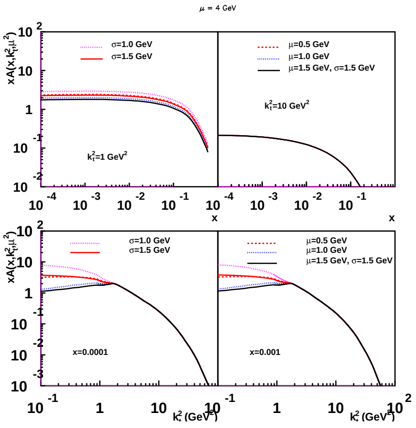

Figure 1: The unintegrated gluon distribution at a scale $\bar{q} = 4$ GeV for different values of μ and σ of the intrinsic $k_\perp$ distribution as a function of x for fixed $k_\perp$(top) and as a function of $k_\perp$ (bottom) for fixed x

At high energies, the gluon density is dominating for many processes, therefore here only the gluon uPDF is considered. It has already been shown in [9], that the predictions of the total cross section as well as differential distributions for heavy quark production at HERA and the LHC agree well in general with those coming from fixed NLO calculations. However, the details depend crucially on a precise knowledge of the uPDF. Therefore precision fits to inclusive and exclusive measurements have to be performed to determine precisely the free parameters of the uPDF: the starting distribution function at a low scale $Q_0 \sim 1$ GeV as well as parameters connected with α_s and details of the splitting functions for the perturbative evolution.

An overview and discussion of uPDFs is given in [4–6]. In a previous paper [10] the uPDF was determined from a pQCD fit using the CCFM evolution equation [11–14] to the structure function F_2 and F_2^c with acceptable χ^2/ndf. However, the small x behavior of the uPDF obtained from F_2^c was very different compared to the one obtained from F_2.

Here also measurements of high p_t-dijet production in DIS at HERA [15–17] are investigated.

2 The method

The unintegrated gluon density is determined by a convolution of the non-perturbative starting distribution $\mathcal{A}_0(x)$ and the CCFM evolution denoted by $\tilde{\mathcal{A}}\,(x, k_\perp, \bar{q})$:

$$x\mathcal{A}(x, k_\perp, \bar{q}) \quad = \quad \int dx' \mathcal{A}_0(x', k_\perp) \cdot \frac{x}{x'} \tilde{\mathcal{A}} \left(\frac{x}{x'}, k_\perp, \bar{q} \right)$$

In the perturbative evolution the gluon splitting function P_{gg} including non-singular terms (as described in detail in [18, 19]) is applied.

The distribution $\mathcal{A}_0$ is parameterized at the starting scale Q_0 by:

$$\begin{aligned} x\mathcal{A}_0(x, k_\perp) \quad &= \quad N x^{-B_g} \cdot (1-x)^{C_g} \, (1 - D_g x) \\ & \quad \cdot \exp\left[- \frac{(\mu - k_\perp)^2}{\sigma^2} \right] \qquad (1) \end{aligned}$$

The parameters N_g, B_g, C_g, D_g as well as μ, σ of $\mathcal{A}_0$ are free parameters which have to be constrained by measurements. It turns out, that C_g, D_g are not sensitive to the data considered here, and are therefore fixed to $C_g = 4$ and $D_g = 0$. The other parameters are determined by a fit [20] to measurements such to minimize the χ^2 defined by:

$$\chi^2 = \sum_i \left(\frac{(T - D)^2}{\sigma_i^{2\ stat} + \sigma_i^{2\ sys}} \right)$$

with T being the theory value and D the measurement with the corresponding statistical and systematic uncertainty.

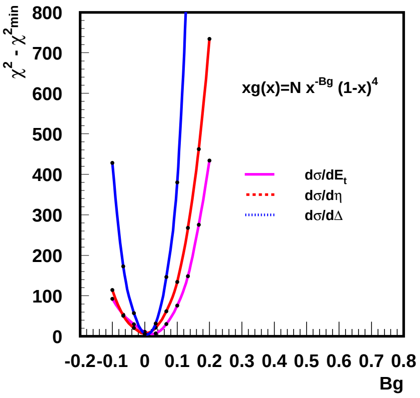

Figure 2: A scan in the parameter space of B_g for $\frac{d^3\sigma}{dQ^2 dx dE_t}$, $\frac{d^3\sigma}{dQ^2 dx d\Delta}$ and $\frac{d^3\sigma}{dQ^2 dx d\Delta\eta}$ as measured in [15].

3 The intrinsic $k_\perp$distribution

The Gaussian form with $\mu = 0$ and a width of $\sigma \sim 1.0$ GeV of the intrinsic $k_\perp$distribution in eq.(1) is an assumption to parameterize our ignorance about the small $k_\perp$behavior. In the saturation model of GBW [21] the uPDF vanishes for small $k_\perp$. Such a behavior can be mimicked by a Gaussian distribution with $\mu \sim Q_0$. The effect of choosing different μ is illustrated in Fig. 1.

4 Dijets in DIS

The sensitivity of the shape in x and the intrinsic $k_\perp$ was studied for dijets in DIS [15] in the kinematic range of $5 < Q^2 < 100$ GeV^2, $10^{-4} < x < 10^{-2}$, $0.1 < y < 0.7$ and two jets with at least $E_t > 5$ GeV in the range $-1 < \eta < 2.5$. The differential cross sections $\frac{d\sigma}{dE_t}$, $\frac{d\sigma}{d\Delta\eta}$, with $\Delta\eta$ being the rapidity difference between the highest E_t jets are mainly sensitive to the x dependence of the uPDF. The same is observed for the cross section $\frac{d\sigma}{d\Delta}$ with $E_t > E_{t\ min} + \Delta$ and $E_{t\ min} = 5$ GeV. A scan over the parameter space of Bg is shown in Fig 2. With this choice of parameters the cross sections are well described, giving a reasonable χ^2/ndf. In Tab. 1 the χ^2/ndf are given for different values of Bg and the mean μ of the intrinsic $k_\perp$ distribution.

		χ^2/ndf		
Bg	μ [GeV]	$\frac{d\sigma}{dE_t}$	$\frac{d\sigma}{d\Delta\eta}$	$\frac{d\sigma}{d\Delta}$
0.025	1.5	68/37=1.8	102/35=2.3	267/89=3.0
0.25	1.5	95/37=2.5	113/35=2.5	306/89=3.4
0.025	0	63/37=1.7	93/35=2.1	284/89=3.2
0.25	0	99/37=2.7	123/35=2.7	345/89=3.9

Table 1: Quality of the description of the different differential cross sections using $Bg = 0.025$ and $Bg = 0.25$ together with $\sigma = 1.5$ GeV.

From Tab. 1 it is seen, that a value of $Bg = 0.025$ is preferred, and that the sensitivity of these measurements to the intrinsic $k_\perp$ distribution is very small.

However, the cross section as a function of $\Delta\phi$, where $\Delta\phi$ is the difference in azimuthal angle between the two leading jets in the hadronic center-of-mass frame, is directly sensitive to the transverse momentum of the incoming parton, and thus a crucial test of the uPDF.

In Fig. 3 we show a comparison of the measurement of [17] with the prediction of CASCADE using the uPDF determined before. A reasonable description of the measurement is achieved. Table 2 shows the χ^2/ndf obtained for these data and also to the azimuthal correlations from [16].

		χ^2/ndf	
Bg	μ [GeV]	$\frac{d\sigma}{dQ^2 d\Delta\phi}$ (H1 prel) [16]	$\frac{d\sigma}{d\Delta\phi}$ (dijets ZEUS) [17]
0.025	1.5	163/29=5.6	332/19=17.5
0.25	1.5	128/29=4.4	234/19=12.3
0.025	0	200/29=6.9	417/19=22.0
0.25	0	237/29=8.2	338/19=17.8

Table 2: Quality of the description of $\frac{d\sigma}{d\Delta\phi}$ using $Bg = 0.025$ and $Bg = 0.25$ together with $\sigma = 1.5$ GeV.

It is interesting to observe, that $\frac{d\sigma}{d\Delta\phi}$ gives also access to Bg, now with a preference to a much steeper initial gluon distribution. The measurement prefers a distribution which decreases for very small transverse momenta $k_\perp$. However it should be noted, that the form of the intrinsic $k_\perp$ distribution is not constrained.

5 Conclusion

The shape of the starting gluon distribution in x and $k_\perp$ has been investigated with dijet events in DIS. Whereas the cross sections as a function of E_t prefer a soft gluon distribution ($Bg \sim 0.025$) and show little sensitivity to the intrinsic $k_\perp$ distribution, the cross sections as a function of $\Delta\phi$ prefer a much steeper gluon ($Bg \sim 0.25$) and show a clear preference to a intrinsic $k_\perp$ distribution which decreases for small $k_\perp$. The different x-slope of the initial gluon distribution, as already observed in fits to F_2 and F_2^c, is also observed in di-jet cross section measurement. Further investigations are obviously needed.

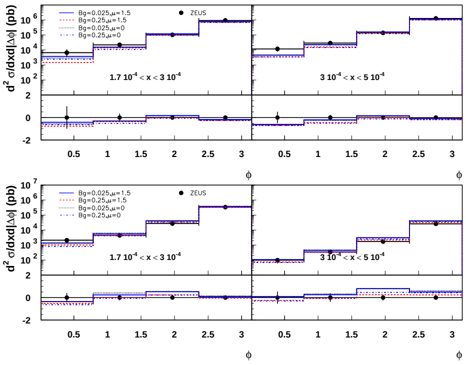

Figure 3: The cross section $\frac{d\sigma}{d\Delta\phi}$ as measured by [17] compared to predictions using CASCADE and the uPDF as in Tab. 2. The lower plots always show the ratio $R = \frac{theory - data}{data}$.

Acknowledgments

Many thanks go to the the organizers of this very interesting workshop.

References

[1] Slides:
`http://indico.cern.ch/contributionDisplay.py?contribId=54&sessionId=6&confId=9499`

[2] H. Jung, *Phys. Rev.* **D 65**, 034015 (2002). [hep-ph/0110034]

[3] H. Jung, *Mod. Phys. Lett.* **A19**, 1 (2004). [hep-ph/0311249]

[4] Small X Collaboration; B. Andersson *et al.*, *Eur. Phys. J.* **C 25**, 77 (2002). [hep-ph/0204115]

[5] Small X Collaboration, J. R. Andersen *et al.*, *Eur. Phys. J.* **C35**, 67 (2004). [hep-ph/0312333]

[6] Small X Collaboration, J. R. Andersen *et al.* (2006). [hep-ph/0604189]

[7] H. Jung. DIS 2004, Strbské Pleso, Slovakia, [hep-ph/0411287]

[8] J. Collins and H. Jung, *Need for fully unintegrated parton densities*, 2005. [hep-ph/0508280]

[9] S. Alekhin *et al.*, *Hera and the LHC - a workshop on the implications of HERA for LHC physics: Proceedings Part A and B*, 2005. [hep-ph/0601012,hep-ph/0601013], J. Baines *et al.* (2006). [hep-ph/0601164]

[10] H. Jung, A. V. Kotikov, A. V. Lipatov and N. P. Zotov, [hep-ph/0611093].

[11] M. Ciafaloni, *Nucl. Phys.* **B 296**, 49 (1988)

[12] S. Catani, F. Fiorani, and G. Marchesini, *Phys. Lett.* **B 234**, 339 (1990)

[13] S. Catani, F. Fiorani, and G. Marchesini, *Nucl. Phys.* **B 336**, 18 (1990)

[14] G. Marchesini, *Nucl. Phys.* **B 445**, 49 (1995)

[15] A. Aktas *et al.* [H1 Collaboration], Eur. Phys. J. C **33** (2004) 477 [hep-ex/0310019].

[16] M. Hansson [H1 Collaboration], "Decorrelation Of Dijets At Low X And Q**2," *Prepared for 14th International Workshop on Deep Inelastic Scattering (DIS 2006), Tsukuba, Japan, 20-24 Apr 2006*

[17] S. Chekanov *et al.* [ZEUS Collaboration], [hep-ex/0705.1931] .

[18] H. Jung, *Acta Phys. Polon.* **B33**, 2995 (2002). [hep-ph/0207239]

[19] M. Hansson and H. Jung. DIS 2003, St. Petersburg, Russia, [hep-ph/0309009]

[20] F. James and M. Roos, *Comput. Phys. Commun.* **10**, 343 (1975)

[21] K. Golec-Biernat and M. Wusthoff, Phys. Rev. D **60** (1999) 114023 [hep-ph/9903358].